POLYTECHNIQUE MONTRÉAL
affiliée à l'Université de Montréal

Investigation of the CO_2 Thermal Network Connected to Local Heat Pumps for Heating and Cooling of Buildings

SEPEHR GHOLAMREZAIE
Département de génie mécanique

Thèse présentée en vue de l'obtention du diplôme de *Philosophiæ Doctor*
Génie mécanique

Mai 2026

POLYTECHNIQUE MONTRÉAL
affiliée à l'Université de Montréal

Cette thèse intitulée :

Investigation of the CO_2 Thermal Network Connected to Local Heat Pumps for Heating and Cooling of Buildings

présentée par **Sepehr GHOLAMREZAIE**
en vue de l'obtention du diplôme de *Philosophiæ Doctor*
a été dûment acceptée par le jury d'examen constitué de :

Michaël KUMMERT, président
Massimo CIMMINO, membre et directeur de recherche
Parham ESLAMI-NEJAD, membre et codirecteur de recherche
Cédric BÉGUIN, membre
Etienne SALOUX, membre externe

DEDICATION

To those who choose hope and action,
protecting Earth for tomorrow. . .

ACKNOWLEDGEMENTS

I would like to express my deepest and most sincere gratitude to my supervisors, Prof. Massimo Cimmino and Dr. Parham Eslami-Nejad, for their exceptional guidance, unwavering support, and constant encouragement throughout my Ph.D. journey. My relationship with them was never limited to academic and professional matters alone; their influence extended deeply into my personal life as well. When I first arrived in Canada and was learning how to adapt to a new country and a new way of life, knowing that I could always rely on their warm support gave me a profound sense of reassurance and belonging.

Through their example, they taught me that being a researcher is not only about acquiring knowledge, but also about discipline, integrity, honesty, and consistency. These lessons helped me grow not only as a scholar, but also as a person who hopes to contribute meaningfully to society. I learned from them the importance of remaining committed and dedicated to one's responsibilities, even during difficult times. I witnessed this through their own lives: regardless of the challenges they themselves may have been facing, they were always available to support me and always gave priority to my progress and my work. Five years is not a short time, and through all the ups and downs of this journey, I came to feel a strong bond with them. For all of this, I am profoundly grateful.

I would also like to express my heartfelt gratitude to my mother, my father, and my sister, who have always been my greatest source of strength. They were my refuge in difficult moments and the first to celebrate every success with me. Their love, encouragement, and unwavering belief in me carried me through many of the challenges of this journey.

My deepest thanks also go to my partner, who stood by me throughout this path, through both the joyful and the difficult moments. Thank you for always being there to lift my spirits during my lowest times and to share in my happiness and achievements with genuine love and care.

I would also like to extend my sincere gratitude to the members of the BEE Lab, whose presence made these years far richer both professionally and personally. In particular, I would like to thank Prof. Michaël Kummert, whose remarkable ability to bring people together made the lab feel like a family. The many gatherings, 5 à 7 events, and moments of shared laughter created some of my most cherished memories during these years. From my first biking experience with him and the group to the many beautiful gatherings, picnics, and hikes, these moments brought joy, balance, and friendship to my Ph.D. life.

I would also like to thank Prof. Michel Bernier, who was always present at these gatherings, generously sharing his stories and experiences. His presence made these occasions not only enjoyable, but also enriching, and even in informal moments there was always something valuable to learn from him.

My sincere thanks also go to my dear friends in the lab, who became much more than colleagues over the years. I would especially like to thank Geoffrey Viviescas, who was always there for me through both the difficult and happy moments, always ready to listen, to support, and to make me feel at home. We shared some of the best moments of these years, and I will always be grateful for his friendship, kindness, and positive spirit. I would also like to thank Aziz Mbye, Giulio Tonellato, Gabriel Sabbagh, Guillaume Ingelaere, and many others whose friendship, joy, and companionship made this journey far more meaningful and memorable.

Beyond the university environment, I would like to express my gratitude to CanmetENERGY in Varennes, which hosted me first as an intern and later as a research engineer during my Ph.D. This opportunity greatly enriched my doctoral experience and made possible a more comprehensive study in this thesis through the valuable experimental data provided from their test bench. I would especially like to thank Dr. Arash Bastani for his supervision during my internship and for his support throughout this important part of my journey.

I would also like to gratefully acknowledge the financial support of the Natural Sciences and Engineering Research Council of Canada (NSERC) through a Discovery Grant, which contributed to funding the Ph.D. research presented in this thesis.

To all those who supported me professionally, personally, and emotionally throughout this journey, thank you. This thesis would not have been possible without you.

RÉSUMÉ

Le réseau thermique au CO_2 (CO_2TN) est une architecture à l'échelle du bâtiment dans laquelle une boucle de CO_2 à un seul tuyau fournit une source/puits commun à un ensemble de pompes à chaleur locales (LHP) desservant plusieurs zones. En faisant circuler le CO_2 dans un état près de la saturation, le réseau peut offrir à l'ensemble des LHPs une température de source quasi-uniforme, tout en permettant des échanges d'énergie entre zones. Toutefois, une évaluation crédible des performances et une supervision exploitable requièrent : (i) des modèles validés expérimentalement, fiables en régimes sous-critique et transcritique, et (ii) des stratégies de supervision coordonnant les décisions au niveau réseau (pression de boucle et fonctionnement de l'unité de circulation) avec l'activation des zones, tout en respectant les contraintes de faisabilité et les limites d'exploitation des équipements.

Cette thèse répond à ces exigences au travers de quatre objectifs : développer un modèle numérique du CO_2TN et de ses principaux composants, valider expérimentalement le modèle aux échelles composant et système, formuler des stratégies de supervision visant à réduire la consommation électrique sous contraintes d'exploitation, et évaluer annuellement les performances dans un bâtiment multi-zones représentatif.

Premièrement, un modèle stationnaire du CO_2TN est développé et implémenté dans TRNSYS à l'aide de TYPES dédiés pour l'unité de circulation, les échangeurs de chaleur et les interfaces de couplage avec les LHP. Le modèle est validé à partir de mesures issues d'un prototype de CO_2TN. Au niveau composant, le modèle de compresseur reproduit le débit massique de CO_2 avec une erreur absolue moyenne en pourcentage (MAPE) de 7.24% (écart maximal 14%) et la puissance du compresseur avec une MAPE de 0.96% (écart maximal de 2%). Pour les échangeurs à plaques eau–CO_2 fonctionnant en régions surchauffée ou supercritique, le refroidisseur de gaz présente une MAPE de 1.37% (écart maximal de 3%) et le désurchauffeur une MAPE de 8.36% (écart maximal 9%). En régime sous-critique, le modèle d'évaporateur atteint une MAPE de 8.10% (écart maximal de 12%) et le modèle de condenseur une MAPE de 4.05% (écart maximal de 5.5%). L'échangeur interne (CO_2–CO_2) est validé en comparant les flux de chaleur côté aspiration et côté refoulement, ce qui conduit à une MAPE de 9.45% et à une erreur maximale de 11%, tout en respectant la surchauffe d'aspiration visée. Au niveau système, le modèle prédit la puissance totale avec des erreurs relatives comprises entre 1.45% et 7.89% et la capacité en chauffage et refroidissement avec des erreurs comprises entre 4.48% et 7.80%, et avec un écart maximal de 16.9% sur le COP pour les cas de validation. La validation quantifie également la pénalité de performance associée aux pertes de charge

du prototype : la suppression des pertes de charge mesurées augmente le COP du système de 21% en mode refroidissement, de 7% en mode chauffage et de 20% en mode équilibré, ce qui met en évidence la réduction des pertes de charge comme un enjeu de conception.

Deuxièmement, le modèle validé est utilisé pour formuler et comparer deux stratégies de commande conçues via la génération hors ligne de cartes et une consultation en ligne. La stratégie à débit massique minimal (MM) impose un fonctionnement strictement diphasique de la boucle et sélectionne le plus faible débit de circulation de CO_2 satisfaisant la faisabilité pour chaque pression de boucle candidate. La stratégie à température bornée (TB) relâche l'exigence de diphasique strict et contraint plutôt les températures de boucle dans une bande de ± 10 K autour de la saturation, autorisant des excursions monophasique bornées tout en maintenant une bande de température serrée du côté source des LHP. La co-simulation annuelle TRNSYS–MATLAB pour un immeuble de bureaux à cinq zones à Montréal montre que la méthode TB améliore systématiquement les performances saisonnières par rapport à la méthode MM. Le COP moyen du système augmente de 3.07 (MM) à 3.75 (TB), le COP médian augmente de 2.95 à 4.27, et la fraction de pas de temps avec $\text{COP}_{sys} > 4$ passe de 8% à 55%. Sur l'année complète, le facteur de performance saisonnier global augmente de $\text{SPF}_{sys,ann} = 2.98$ (MM) à $\text{SPF}_{sys,ann} = 3.65$ (TB). Le gain de performance est maximal durant les périodes dominées par le refroidissement en régime transcritique, où la méthode TB réduit à la fois le débit massique de CO_2 et le rapport de pression du compresseur de circulation.

Globalement, cette thèse fournit : (i) une plateforme de modélisation validée du CO_2TN, adaptée à la simulation annuelle des bâtiments et aux études de commande, et (ii) des stratégies de commande supervisoire visant un fonctionnement efficace du système, et (iii) des éléments montrant que la commande à température bornée peut surpasser un fonctionnement strictement diphasique à débit massique minimal en élargissant la région de fonctionnement faisable à haut rendement sous des charges multi-zones réalistes.

ABSTRACT

The CO_2 thermal network (CO_2TN) is a building-scale thermal system in which a single-pipe CO_2 loop supplies a shared source/sink to an array of packaged local heat pumps (LHPs) serving multiple zones. By circulating CO_2 mainly in the two phase region, the network can provide a nearly uniform source temperature to all LHPs while allowing energy exchange between zones. However, performance assessment and practical control require (i) experimentally validated models that remain reliable across different operating conditions, and (ii) supervisory strategies that coordinate network-level decisions (loop pressure and circulation-unit operation) with zone-level activation while respecting feasibility constraints and equipment envelopes.

This thesis addresses these requirements through four objectives: development of a numerical model of the CO_2TN and its key components, experimental validation at component and system levels, formulation of supervisory strategies to control and optimize performance under operational constraints, and annual performance evaluation in a representative multi-zone building.

First, a steady-state, CO_2TN model is developed and implemented in TRNSYS using dedicated component TYPES for the circulation unit, heat exchangers, and LHP coupling interfaces. The model is validated using measurements from a CO_2TN prototype. At the component level, the compressor model reproduces the CO_2 mass flow rate with a mean absolute percentage error (MAPE) of 7.24% (maximum deviation of 14%) and compressor power with a MAPE of 0.96% (maximum deviation of 2%). For water-to-CO_2 plate heat exchangers operating in superheated or supercritical regions, the gas cooler achieves a MAPE of 1.37% (maximum deviation of 3%) and the desuperheater a MAPE of 8.36% (maximum deviation of 9%). For subcritical operation, the evaporator model yields a MAPE of 8.10% (maximum deviation of 12%) and the condenser model a MAPE of 4.05% (maximum deviation of 5.5%). The internal heat exchanger (CO_2–CO_2) is validated by comparing suction-side and discharge-side heat-transfer rates, resulting in a MAPE of 9.45% and a maximum error of 11%, while consistently meeting the target suction superheat. At the system level, the model predicts total power with relative errors between 1.45% and 7.89% and heating/cooling capacity with errors between 4.48% and 7.80%, with a maximum COP deviation of 16.9% across the validation cases. The validation also quantifies the performance penalty associated with prototype pressure drops: removing measured pressure losses increases system COP by 21% in cooling mode, 7% in heating mode, and 20% in balanced mode, highlighting

pressure-drop reduction as a primary design lever.

Second, the validated model is used to formulate and compare two supervisory control strategies designed for execution through offline map generation and online lookup. The minimum-mass-flow (MM) strategy enforces strictly two-phase loop operation and selects the smallest CO_2 circulation rate that satisfies feasibility for each candidate loop pressure. The temperature-bounded (TB) strategy relaxes strict two-phase operation and instead constrains loop temperatures within a ± 10 K band around saturation, permitting bounded single-phase excursions while maintaining a tight temperature band for the LHP source side. Annual TRNSYS–MATLAB co-simulation for a five-zone office building in Montréal shows that the TB method systematically improves seasonal performance relative to the MM method. The mean system COP increases from 3.07 (MM) to 3.75 (TB), the median increases from 2.95 to 4.27, and the fraction of time steps with $\text{COP}_{sys} > 4$ rises from 8% to 55%. Over the full year, the overall seasonal performance factor increases from $\text{SPF}_{sys,ann} = 2.98$ (MM) to $\text{SPF}_{sys,ann} = 3.65$ (TB). The performance advantage is largest during cooling-dominant, transcritical operation, where the TB method reduces both CO_2 mass flow rate and circulation-compressor pressure ratio.

Overall, this thesis provides (i) an experimentally validated CO_2TN model for annual building simulation and supervisory studies, (ii) supervisory control strategies to operate the system efficiently, and (iii) evidence that temperature-bounded supervision can outperform strictly two phase, minimum-mass-flow operation by expanding the feasible high-efficiency operating region under realistic multi-zone loads.

TABLE OF CONTENTS

LIST OF TABLES

LIST OF FIGURES

LIST OF SYMBOLS AND ACRONYMS

Acronyms

AHRI	Air-Conditioning, Heating, and Refrigeration Institute
ASHRAE	American Society of Heating, Refrigerating and Air-Conditioning Engineers
CO_2TN	CO_2 thermal network
COND	Condenser
COP	Coefficient of performance
DSPHTR	Desuperheater
EV	Expansion valve
EVAP	Evaporator
FS	Fixed-speed
GC	Gas cooler
GWP	Global warming potential
HCF	Heat carrier fluid
HFC	Hydrofluorocarbon
HP	Heat pump
HVAC	Heating, ventilation, and air conditioning
IHE	Internal heat exchanger
LHP	Local heat pump
LMTD	Logarithmic mean temperature difference
MAPE	Mean absolute percentage error
MM	Minimum-mass-flow supervisory method
MPC	Model predictive control
NTU	Number of transfer units
ODP	Ozone depletion potential
OU	Outdoor unit
PFD	Process flow diagram
PHE	Plate heat exchanger
PRV	Pressure regulating valve

R-744	Refrigerant designation for carbon dioxide
RV	Reversing valve
RVCC	Reversible vapor compression cycle
SPF	Seasonal performance factor
TB	Temperature-bounded supervisory method
UA	Overall conductance
VS	Variable-speed
VRF	Variable refrigerant flow
WLHP	Water-loop heat pump

Symbols

A	Area [m^2]
b	Corrugation depth of the plate heat exchanger [m]
Bo	Boiling number [-]
C	Thermal capacitance [kJ/K]
c_p	Specific heat capacity [kJ/(kg K)]
D_h	Hydraulic diameter [m]
h	Specific enthalpy [kJ/kg]
k	Thermal conductivity [W/(m K)]
$\dot{m}$	Mass flow rate [kg/s; kg/hr for compressor maps]
NC	Number of channels in the plate heat exchanger [-]
Nu	Nusselt number [-]
P	Pressure [MPa]
Pr	Prandtl number [-]
$\dot{Q}$	Heat transfer rate [kW]
$\dot{q}$	Heat transfer rate per cell or local segment [kW]
Re	Reynolds number [-]
S	Compressor speed [Hz]
T	Temperature [°C or K]
U	Overall heat transfer coefficient [W/(m^2 K)] or control input [-], depending on context

$\dot{W}$	Power input [kW]
x	Vapor quality [-]
X	Generic compressor-map output [kW or kg/hr]
X_{tt}	Martinelli parameter [-]
α	Convective heat transfer coefficient [W/(m^2 K)]
β	Chevron angle of the plate heat exchanger [°]
ϵ	Heat exchanger effectiveness [-]
η	Efficiency [-]
μ	Dynamic viscosity [Pa s]
ρ	Density [kg/m^3]
ϕ	Enlargement factor of the plate heat exchanger [-]
Θ	Supervisory decision vector [-]

Subscripts

ann	Annual
C	Cooling
$comp$	Compressor
cr	Critical state
dis	Discharge
f	Saturated liquid state
g	Saturated vapor state
H	Heating
HP	Heat pump
i	Cell or control-volume index
in	Inlet
$isen$	Isentropic
$loop$	Distribution loop
max	Maximum
min	Minimum
sat	Saturation condition
sub	Subcooled region or condition

suc	Suction
sup	Superheated region or condition
sys	System level
2ϕ	Two phase region
v	Volumetric
w	Water side
z	Zone

LIST OF APPENDICES

CHAPTER 1 INTRODUCTION

Buildings account for roughly one-third of global energy use and about one-quarter of CO_2 emissions, making the sector a central lever for decarbonization [1, 2]. In cold and mixed climates, the demand is dominated by thermal end uses, especially space heating and domestic hot water. In Canada, these services represent about 63% and 18% of residential energy use, respectively [3]. As jurisdictions pursue deep decarbonization, electrification of these end uses—primarily through high efficiency heat pumps—has become a major pathway, although performance and design constraints in cold climates remain important considerations [2]. At the same time, widespread electrification can amplify winter peak demand and, in some regions, shift electricity systems from summer- to winter-peaking, increasing the value of flexibility and coordinated operation [1]. This context has motivated growing interest in thermal network concepts (e.g. low-temperature ambient temperature loops) that enable energy sharing between simultaneous heating and cooling demands and facilitate integration of renewable and waste heat sources [4, 5]. Efficient integration and supervisory control of heat pumps in multi-zone buildings is therefore a key challenge for meeting climate targets at reasonable cost while managing peak electrical demand.

Common multi-zone HVAC architectures include hydronic water-loop heat pump (WLHP) systems and variable refrigerant flow (VRF) systems. In WLHP systems, decentralized water-to-air or water-to-water heat pumps are connected to a common water loop that is typically maintained within a moderate temperature range by a boiler and a chiller. This arrangement offers individual zone control and can recover heat between zones when heating and cooling demands occur at the same time. It is especially well suited to larger buildings with diversified core and perimeter loads, and it can also be combined with thermal storage or geothermal sources. VRF systems provide another important reference for multi-zone conditioning. These systems are direct expansion multi zone systems in which one or more outdoor units are connected through refrigerant piping to multiple indoor fan coil units distributed across the building. Their main feature is that the refrigerant flow rate is adjusted to match the thermal demand of the connected zones. In practice, this is achieved by combining variable-speed compressor operation in the outdoor unit with electronic expansion valves at the indoor units, allowing each zone to be regulated individually through a common control network. Because refrigerant is delivered directly to the terminal units, VRF systems offer compact distribution, good zoning flexibility, and effective part-load capacity modulation. In buildings with diverse loads, some VRF configurations can also transfer heat between zones through heat recovery operation. However, that capability generally requires additional refrigerant routing components and more involved control than standard heating-only or cooling-only operation.

Beyond efficiency and system integration, refrigerant choice has also become an important part of HVAC system design. International policy has increased pressure to reduce the use of high-global-warming-potential refrigerants, most notably through the Montréal Protocol framework [6] and its Kigali Amendment [7], which introduced a global phasedown of HFCs. In this context, natural refrigerants have received growing attention. Among them, carbon dioxide (CO_2, R-744) is attractive because it is non-flammable and has a global warming potential of 1. Transcritical CO_2 heat pumps have been widely studied for domestic hot water and space heating applications. However, most of these works have focused on stand alone units or relatively small systems. Extending CO_2 technology to large multi-zone thermal networks therefore raises additional questions related to system architecture, modelling, and supervisory control.

1.1 CO_2-based thermal network

Several authors have investigated CO_2-based thermal networks in which two phase CO_2 is used to transport energy between a central plant and distributed local units. In these concepts, the network does not act as a conventional sensible heat water loop. Instead, it uses the phase change of CO_2 to transfer thermal energy at low temperature, while local devices provide the temperature lift or temperature reduction required by the end users. This architecture combines a shared thermal carrier with decentralized conditioning, which makes it relevant to applications where heat recovery, load diversity, and integration of low-temperature sources are important. Early work on this idea was developed mainly at district scale and showed that CO_2 can provide high volumetric energy transport capacity, reduced circulation effort, and effective coupling with distributed energy conversion technologies compared with conventional water-based distribution [8–11].

The building-scale CO_2 thermal network (CO_2TN) extends this idea to a single building and is therefore a distinct concept. In the proposed configuration, near-saturated two phase CO_2 circulates through a single-pipe loop that connects multiple local heat pumps in series distributed throughout the building. The concept is patented by Eslami Nejad et al. [12] and further described in a study by Eslami Nejad and Bastani [13] as a thermal energy system that distributes and recovers energy through a common two phase refrigerant loop.

As shown in Fig. 1.1, the system includes a central circulation mechanism implemented as a reversible vapor compression cycle (RVCC). The role of the RVCC is to circulate two phase

CO_2 through the main loop and deliver it at the required mass flow rate and vapor quality to serve the local heat pumps. Because the loop operates mainly in two phase region, its pressure largely determines its temperature level, which provides a nearly uniform source temperature for the connected units. The vapor compression based circulation system also enables integration of external balancing stations operating at different temperature levels, such as ground heat exchangers, air-source units, solar thermal collectors, or thermal storage. Furthermore, the concept is intended to operate the CO_2 loop near room temperature, which helps minimize heat losses from the distribution loop and, in indoor applications, can avoid the need for pipe insulation [12, 13].

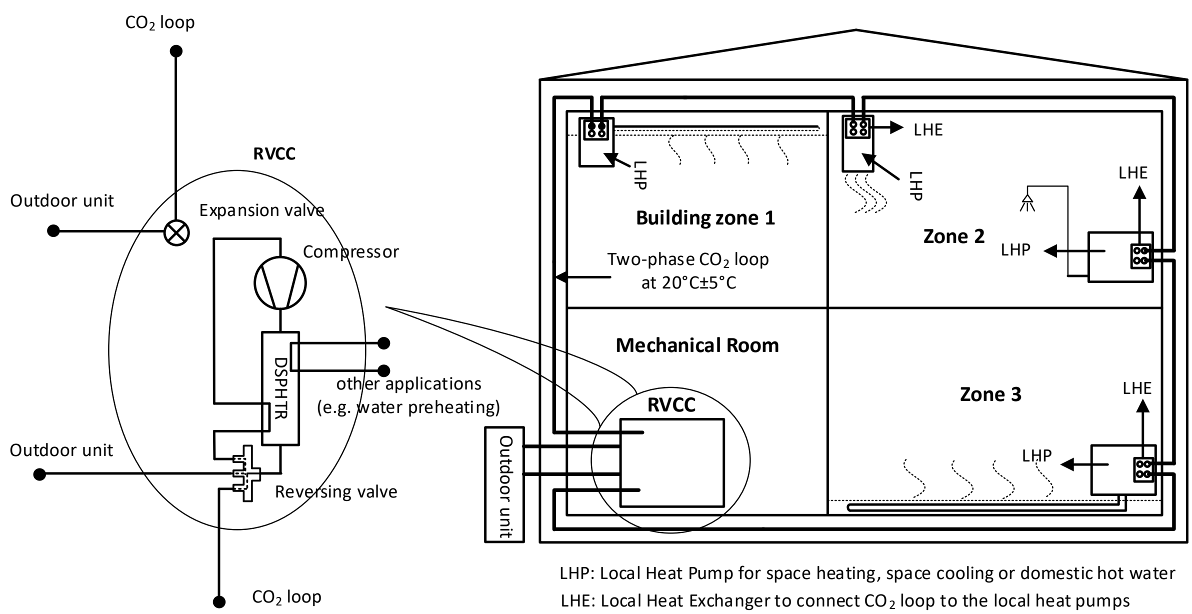

Figure 1.1 CO_2TN concept [13]

In this architecture, the CO_2 loop acts as a common source and sink for the local heat pumps, while each local heat pump serves the heating or cooling demand of its own thermal zone. Because the same CO_2 stream flows through the local units, heat exchanged at one unit affects the thermodynamic state entering the next one. As a result, the refrigerant enthalpy and vapor quality evolve along the loop, even though the loop temperature remains approximately uniform over most operating conditions. This sequential interaction allows heat rejected by units operating in cooling mode to be used directly by units operating in heating mode through the same loop, thereby supporting inter-zone heat recovery.

1.2 Modelling and control challenges

Realizing the full potential of CO_2TN system requires a detailed understanding of its behavior under realistic operating conditions and over extended time periods. This, in turn, raises important modelling and control challenges.

On the modelling side, a reliable model is needed to quantify the efficiency of the CO_2TN under realistic operating conditions, support the development of supervisory control strategies, and eventually provide a basis for component sizing and system design. This modelling problem has two levels: component-level modelling and system-level modelling. At the component level, the main elements of the system must be represented with sufficient fidelity, including the circulation unit and the main heat exchangers such as the gas cooler (GC), evaporator (EVAP), condenser (COND), internal heat exchanger (IHE), and desuperheater (DSPHTR), as well as the distributed local heat pumps (LHP). Thermodynamically, the system can operate in either subcritical or transcritical regimes. The model must therefore capture the strong property variations of CO_2 near the critical point, the transition in transcritical operation, and the effects of varying mass flow rate and pressure. Heat exchangers that may operate in supercritical, superheated, two phase, or subcooled regimes are particularly sensitive to modelling assumptions and to the choice of heat transfer correlations. Beyond individual components, the full CO_2TN must also be represented at the system level. This requires connecting the component models into a complete network model that captures the interactions between the building loads, the LHPs, the CO_2 loop, and the circulation unit, and coupling that network to building-zone models subjected to weather-driven loads and occupancy schedules. Such integrated simulation is necessary to predict seasonal performance and to evaluate how supervisory strategies affect annual efficiency. These modelling requirements motivate the first part of this thesis, which develops a comprehensive CO_2TN model and validates it against experimental data.

On the control side, the efficiency of the CO_2TN depends strongly on a small set of network-level operating variables that affect all active LHPs simultaneously. In particular, the loop pressure determines the saturation temperature of the common CO_2 loop and therefore the source conditions seen by the LHPs, while the circulation unit operation affects refrigerant flow and the overall thermodynamic state of the network. For a given set of zone heating and cooling demands, these variables must be selected so that the system operates efficiently while respecting pressure, temperature, and equipment limits. The supervisory control problem is therefore to determine the network operating conditions that maximize overall system performance, typically expressed through system COP, under coupled and nonlinear interactions between the local units and the shared loop.

1.3 Problem statement and thesis context

The CO_2TN is a promising architecture for multi-zone buildings, but its adoption and credible assessment require modelling tools and supervisory control methods that remain undeveloped. In particular, the limited body of published work to date highlights several gaps that motivate the present thesis:

- **Validated modelling for annual simulation:** There is a lack of fully validated CO_2TN models that represent the circulation unit, LHPs, and heat exchangers with sufficient fidelity to capture the transcritical operation.
- **Supervisory control under constraints:** Reported control approaches often rely on simplified assumptions or address only a subset of the available degrees of freedom. Therefore, the definition of appropriate decision variables and supervisory control strategies for such a system remains largely unexplored and is addressed in this thesis.

In this context, the overarching research question addressed in this thesis is:

> *How can a single-pipe, two phase CO_2 thermal network serving multiple local heat pumps be modelled and controlled to provide efficient building heating and cooling under realistic operating conditions and constraints?*

This thesis adopts a paper-based format and is built around two peer-reviewed journal articles. The first article develops a modular numerical model of a single-pipe CO_2TN connected to local heat pumps and validates component- and system-level performance against experimental data from a prototype installation [14]. The second article uses the validated model as a platform to develop and evaluate two supervisory control strategies for a five-zone office building.

The detailed research objectives and the structure of the thesis are presented in Chapter 3.

CHAPTER 2 LITERATURE REVIEW

This chapter reviews building-scale thermal networks and multi-zone heat pump architectures, with emphasis on CO_2-based secondary loops and the single-pipe CO_2 thermal network (CO_2TN) coupled to local heat pumps (LHPs). It begins by positioning CO_2 thermal networks within the broader transition toward low-GWP working fluids and by summarizing district- and building-scale CO_2 distribution approaches. It then surveys CO_2 thermal network concepts and prior CO_2TN studies, followed by modeling and co-simulation approaches used to evaluate component interactions and annual performance. Finally, control strategies are reviewed at both device and supervisory levels, leading to the research gaps that frame the contributions developed in the subsequent chapters.

2.1 CO_2-based thermal network

The ongoing transition away from high global warming potential (GWP) fluorinated refrigerants has intensified research and deployment of low-GWP alternatives in heating, cooling, and refrigeration systems. A central driver is the global phase-down of hydrofluorocarbons (HFCs) under the Montréal Protocol, which introduces a long-term reduction schedule for HFC production and consumption. These policy signals also have a measurable climate motivation, as assessments of the Montréal Protocol indicates that strong compliance can substantially reduce projected warming attributable to future HFC emissions [15].

Within the set of low-GWP options, carbon dioxide (CO_2, R744) is frequently classified as a natural refrigerant with zero ozone depletion potential (ODP) and a GWP of 1 by definition. In addition, CO_2 is non-flammable and is listed in the highest safety group (A1) in standard refrigerant safety classifications, although it must be treated as a simple asphyxiant at elevated concentrations [16, 17]. From a thermophysical perspective, CO_2 also has high vapor density and favorable transport properties relative to many conventional refrigerants, which can translate into high volumetric capacity and compact components in vapor compression systems [17]. The renewed interest in CO_2 can be traced to the modern re-introduction of CO_2 refrigeration concepts in the 1990s and the subsequent body of work that established transcritical cycle fundamentals, component requirements, and control sensitivities [18, 19].

At the same time, CO_2 imposes distinct thermodynamic and engineering constraints that strongly influence system design. Because the critical temperature of CO_2 is near typical ambient conditions, heat rejection processes in air-conditioning and heat pump applications often occur in a supercritical regime, where supercritical CO_2 rejects heat via a gas cooler rather than condensed at a fixed saturation temperature. The critical temperature and pressure, together with the resulting high operating pressures, require dedicated high pressure components and careful attention to pressure control, pressure drops, and safety devices [17].

While the preceding body of work primarily concerns stand-alone CO_2 devices, building- and district-scale performance depends not only on the vapor compression unit but also on how thermal energy is distributed among multiple users and how sources and sinks are coordinated. Thermal networks address this system-level requirement by circulating a heat carrier fluid through a piping network that links multiple loads and multiple interface devices. At both building and district scales, such networks can enable heat exchange between users with simultaneous heating and cooling demands and can facilitate integration of heat sources and sinks such as ambient air, ground, or waste heat [4, 20, 21]. For multi-zone buildings, these network interactions affect seasonal efficiency, peak electrical demand, and operational stability, which motivates studying distribution architecture rather than treating the heat pump as an isolated component.

CO_2 can enter a thermal network architecture in two distinct ways: (i) as the refrigerant confined within local vapor compression devices that exchange with a secondary loop heat carrier, or (ii) as the circulating fluid of the network itself. The second option is of particular interest when CO_2 circulates near saturation, because two phase transport can provide a near constant temperature associated with saturation pressure and can reduce the systematic temperature drift along the flow direction that is typical of sensible heat secondary loops. Building on this idea, a single-pipe CO_2 thermal network has been proposed in which a two phase CO_2 line connects multiple local heat pumps in series and allows heat recovery between zones through the loop [12]. The remainder of this section reviews CO_2-based thermal networks at (i) the district scale and (ii) the building scale, and then focuses on the single-pipe CO_2 thermal network (CO_2TN) concept that underpins this thesis.

2.1.1 CO_2-based district thermal networks

District-scale CO_2 thermal networks have been proposed as an alternative to conventional water-based district heating and cooling networks in order to (i) reduce distribution pumping requirements through the favorable transport properties of CO_2 and (ii) enable heat exchange at nearly uniform temperature when the distribution loop operates close to saturation. A common feature of many concepts is the use of two distribution lines that carry CO_2 in different phases (typically saturated vapor in one line and saturated liquid in the other). End users interface with the network through heat exchangers and/or local heat pumps that adjust the delivered temperature to the required heating or cooling level.

Weber and Favrat [9] proposed a subcritical two pipe CO_2 district energy system that is particularly relevant to the present thesis because it uses CO_2 as a shared distribution fluid between a central plant and multiple users. The main idea is to replace conventional water-based heating and cooling networks with a refrigerant network composed of one liquid line and one vapor line. This arrangement aims to reduce pipe space requirements and to lower exergy losses associated with large temperature differences in water networks. To preserve the latent-heat benefit of CO_2 while avoiding transcritical operation, the network is operated below the critical point at an intermediate temperature level. The authors indicate an average pressure corresponding to a saturation temperature in the range of about 12 to 18 °C. As shown in Fig. 2.1, the proposed system includes a central heating/cooling plant, a two pipe CO_2 network, and several possible user-side conversion processes. For heating and domestic hot water, the authors consider two options. In the open CO_2 heat pump mode, vapor CO_2 taken from the vapor line is compressed to the temperature level required by the building, rejects heat to the building heating or hot water network, and is then expanded and separated, with the liquid phase returned to the liquid line. In the closed loop option, the CO_2 network acts as the source side of a conventional local heat pump, which is considered more suitable when the required heating temperature glide is small. For cooling, liquid CO_2 is drawn from the liquid line, evaporates in a building-side heat exchanger while absorbing heat from the building, and returns to the vapor line. Because the liquid line is kept at a slightly higher pressure than the vapor line, this cooling process can take place without a dedicated local pump. The paper also shows that the roles of the two lines are not fixed in the same way as supply and return pipes in conventional water networks. Their functions depend on the district-wide balance between heating and cooling demands. When heating and hot water demands dominate, the vapor line acts as the supply line and the liquid line as the return line, so the central plant evaporates CO_2 and sends vapor to the users. When cooling demands dominate, the liquid line becomes the supply line and the vapor line becomes the return line, so the plant condenses CO_2 and sends liquid to the users. The central plant is therefore the main balancing element of the network. The authors further note that, when available, lake water, river water, or wastewater can serve as a plant-side heat source in heating mode or a heat sink in cooling mode. Additional options such as geothermal borehole or unglazed solar collectors are presented as ways to support this balance: in winter they can help generate additional vapor CO_2 for heating and hot water, while in summer they can help condense vapor CO_2 to provide enough liquid for daytime cooling. The concept is evaluated against a conventional water-based district energy system in a small virtual district using a quasi-steady multi-period model. In that comparison, the reference system uses separate hot- and cold-water networks, whereas the CO_2 case assumes closed loop heat pumps at the consumers' place for heating and domestic hot water. Under these assumptions, the CO_2 system gave smaller pipe dimensions, lower annualized pipe costs, slightly higher exergy efficiency, and lower annual operating cost than the water-based reference.

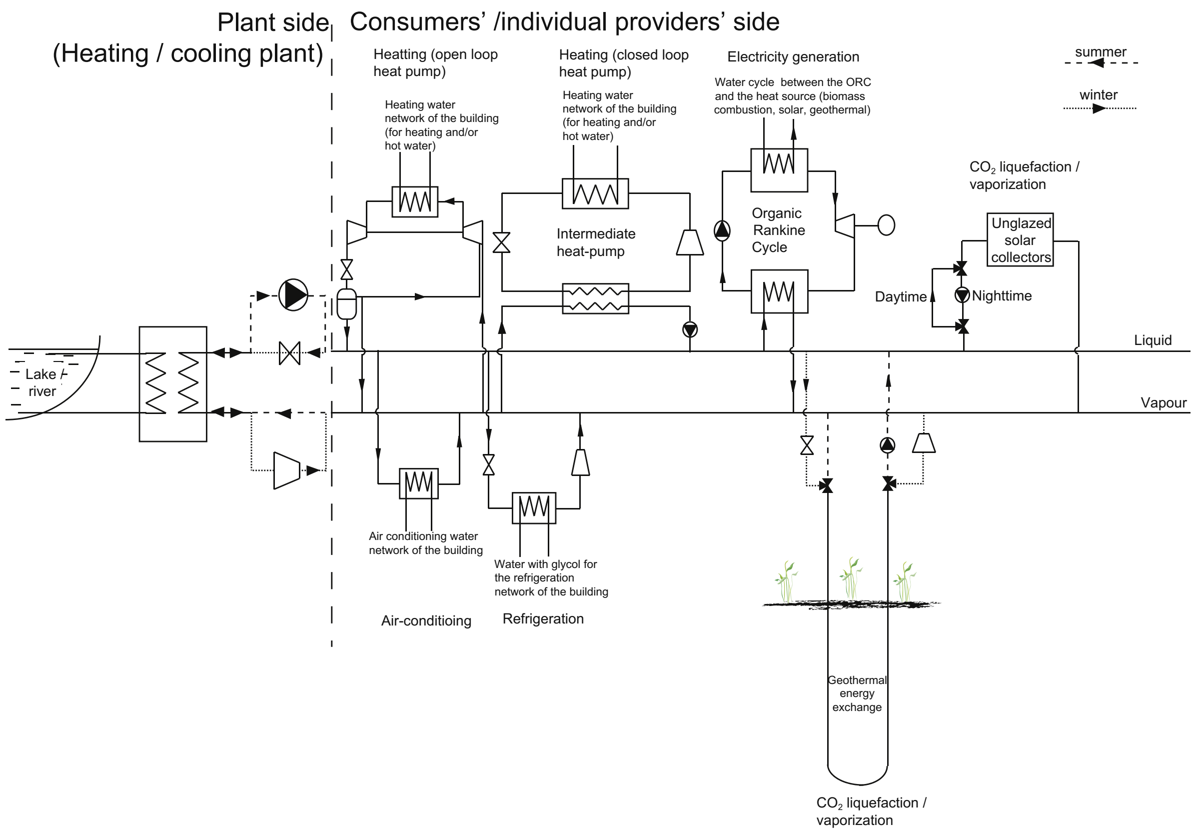

Figure 2.1 Schematic representation of the CO_2 based district energy system [9]

Henchoz et al. [10] extended the concept to a techno-economic case study for an urban district in Geneva (Rues Basses) and evaluated both performance and profitability under practical design constraints. The authors design the CO_2 network at a saturation temperature of 15°C with an imposed pressure drop of 1 bar, and they introduce explicit distribution constraints on maximum fluid velocity (5 m/s for liquid and 20 m/s for gas) to size the two pipes. Under these constraints, the required pipe diameters are reported as 265 mm for the liquid line and 330 mm for the vapor line, and the mass flow rate required at peak conditions is on the order of 74 kg/s. Using an hourly simulation framework for the district loads and plant operation, the authors report an annual electricity consumption of 10,968 MWh for the CO_2-based system, with a peak electric demand of 5.98 MW. They further quantify the electricity-use breakdown (38.2% for heating, 34.4% for cooling, and 27.4% for distribution/compression) and show that pumping losses remain a small fraction of the annual electricity use (about 1.6%). In addition to the performance assessment, the paper provides an investment analysis and reports a short payback (about 5.5 years), highlighting that economic outcomes are sensitive to local energy prices and to the availability of an effective environmental sink/source for network heat exchange.

More recently, Fiaschi et al. [22] investigated a CO_2-based district heating concept in which the distribution network is coupled to a geothermal resource and local heat pumps at the user substations lift the temperature to the required heating level. The authors compare a conventional water-based district heating layout to a CO_2 network in which the grid operates near CO_2 saturation and heating delivery relies on latent-heat transport, while the substation heat pumps use regenerative CO_2 cycles with high discharge pressures (up to 300 bar) to achieve the required temperature lift. The study performs a combined thermodynamic and economic optimization and shows that the design optimum is governed by a trade-off between (i) higher heat pump COP at the surface plant and (ii) geothermal drilling and heat-extraction costs. For the Gavorrano (Italy) case study considered, the authors report an illustrative reduction of the levelized cost of heat from about 0.21 to 0.16 €/kWh when moving from the water-based to the CO_2-based configuration, together with a reduction of the optimal drilling depth from 5 to 4 km under their assumptions. They also show that the economic optimum can correspond to a moderate COP (around 3) rather than the maximum achievable COP, because pushing COP higher requires increased heat extraction from the geothermal source and thus higher drilling costs.

Taken together, district-scale studies show that CO_2 distribution near saturation can reduce the temperature drop associated with sensible-heat transport and can potentially reduce distribution pumping requirements, while enabling heat-pump-based conversion at the user interface. At the same time, these studies identify constraints that become increasingly important as the network footprint grows, including refrigerant charge management, pressure control over long pipe runs, phase management (separation and the avoidance of uncontrolled two phase flow), and safety provisions for a refrigerant loop that spans public and occupied spaces. These considerations motivate interest in building-scale CO_2 thermal networks, where distribution lengths are shorter, interfaces can be standardized, and refrigerant-based components can be concentrated in controlled mechanical spaces.

2.1.2 CO_2-based building thermal networks

Following the concept introduction of CO_2-based building thermal networks, Bastani and Eslami-Nejad [23] performed an initial feasibility study of the CO_2TN using a quasi-steady hourly simulation driven by zone-load profiles for three Canadian locations: Montréal, Vancouver, and Whitehorse. As shown in Fig. 2.2, the model represents the system with a variable-speed compressor, three heat exchangers, three expansion valves, a receiver, auxiliary heater and cooler devices, and n connected local heat pumps (LHPs). The component models are intentionally simplified. The compressor is represented by volumetric and isentropic efficiency relations derived from manufacturer data at 60 Hz and corrected for other operating speeds through a frequency-ratio relation over an assumed speed range of 0 to 70 Hz. The heat exchangers are modeled with ε-NTU relations and assumed adiabatic, the expansion valves are assumed isenthalpic, and the receiver pressure is imposed through a setpoint equivalent to the desired saturated temperature in the two phase distribution loop. The model further assumes that the system is appropriately sized and uses outdoor air as the balancing source in the case study. Under these assumptions, the authors reported a strong climate dependence of annual performance. Vancouver, which has the mildest climate among the three cities, gave the highest annual seasonal performance factor, reported as 3.85, which is 20% and 25% higher than the values obtained for Montréal and Whitehorse, respectively. The study also showed that performance improves during periods with simultaneous heating and cooling, because heat rejected by one zone can be recovered by another through the common loop. In the shoulder season, this internal recovery reduces the net energy that must be added to or removed from the network and leads to reported COP values up to 6.

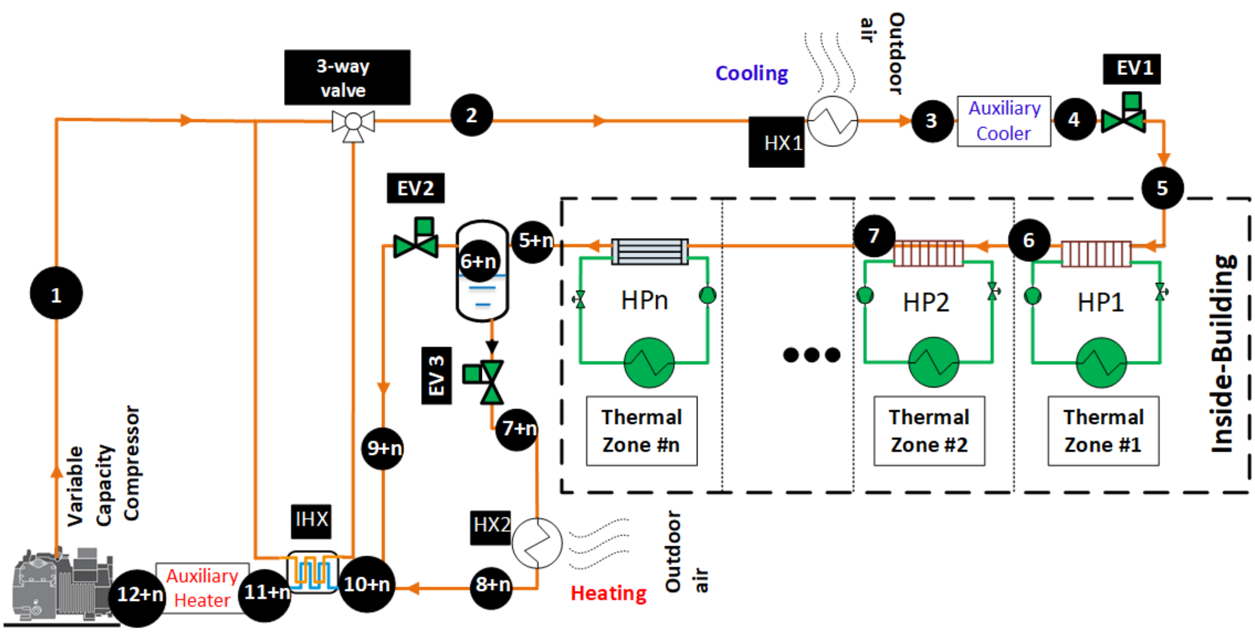

Figure 2.2 Bastani and Eslami-Nejad [23] system configuration

However, the conclusions of this study remain limited for several reasons. First, the system operation is governed by prescribed operating logic rather than by a control strategy. Although the model includes a variable-speed compressor and three expansion valves, the operating pressures are imposed through selected operating rules and receiver setpoints. Second, the component models rely on several simplifying assumptions. The heat exchangers are modeled with simplified ε-NTU relations, assumed adiabatic, and combined with isenthalpic expansion valves. These assumptions are acceptable for an initial feasibility study, but they do not fully capture CO_2 behavior in operating regions where the thermophysical properties vary strongly with pressure and temperature. The compressor model is also simplified, since volumetric and isentropic efficiencies are obtained from manufacturer-based relations as functions of pressure ratio and then corrected for speed. In addition, the local heat pumps are represented as ideal low-lift units with a fixed COP of 10. As a result, the study cannot quantify how terminal capacity, efficiency, and electricity use vary with source condition, sink condition, and temperature lift. Third, the building representation remains simplified, since the model is driven by prescribed hourly zone-load profiles rather than being coupled to a dynamic building model. As a result, the analysis does not explicitly account for the transient response of zones and the effect of different thermal capacitances. Fourth, the paper does not report an experimental validation of either the component models or the overall system model, which limits confidence in the numerical predictions. The results are further influenced by the imposed boundary conditions. Whenever outdoor air cannot provide the required heating or cooling effect, the model restores the energy balance with an auxiliary boiler of 90% efficiency or an auxiliary cooler with COP = 1. Since the system is also assumed to be appropriately sized, the predicted seasonal performance becomes strongly dependent on the assumed auxiliary characteristics and on the climate data.

This early work is therefore best viewed as a first climate-sensitivity and feasibility study. Its main contribution was to show that the single-pipe CO_2TN concept is especially promising in buildings and climates with frequent simultaneous heating and cooling. At the same time, it left several essential developments for later work, including detailed component modeling, experimental validation, and control.

Bastani and Gholamrezaie [24] presented a pilot-scale CO_2 thermal network (CO_2TN) prototype at CanmetENERGY–Varennes[1] to demonstrate physical feasibility and to quantify system behavior under controlled multi-unit operating conditions. The experimental installation is shown in Fig. 2.3, and the corresponding process-flow diagram (PFD) with state-point definitions is shown in Fig. 2.4. The test bench consists of: (i) a reversible CO_2 vapor com-

[1]This work was carried out during the author's Ph.D. internship at CanmetENERGY as part of the effort to establish an experimental platform for the CO_2TN concept.

pression cycle (RVCC) that circulates CO_2 and sets the loop pressure levels; (ii) a secondary water–30% glycol loop that acts as the heat source/sink for the RVCC and whose temperature is stabilized by a balancing unit (i.e. a constant-temperature bath); and (iii) a zone section comprising three demonstrated zones equipped with LHPs (one CO_2-to-water LHP and two CO_2-to-air LHPs) connected in series to the CO_2 loop. The PFD defines CO_2 state points along the refrigerant line and water–glycol state points along the secondary loop, providing a consistent reference for reporting operating regimes, control actions, and measured performance.

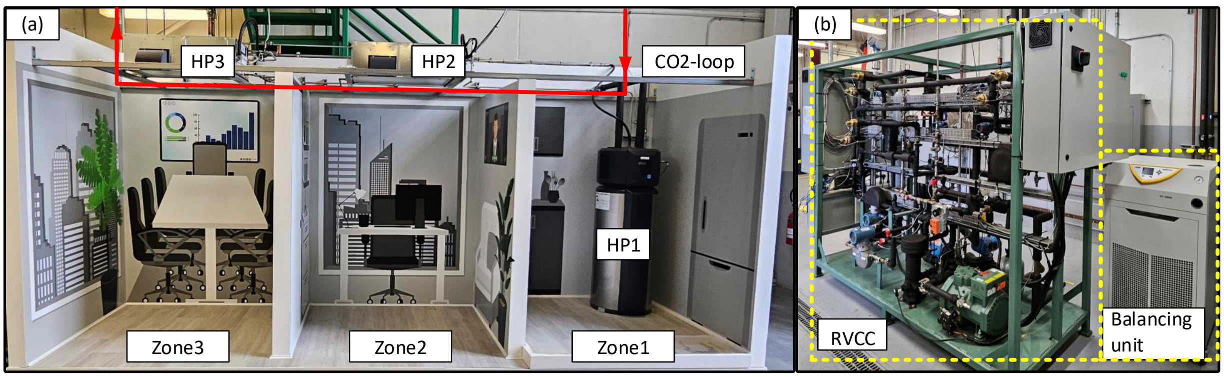

Figure 2.3 Experimental setup from [24]: (a) circulation mechanism and balancing unit; (b) CO_2 loop and local heat pumps (LHPs)

The prototype uses a single stainless-steel CO_2 loop (inner diameter 0.013 m) designed for pressures up to 14 MPa. This pressure envelope enables subcritical operation in the distribution loop while allowing transcritical operation in the high-pressure section when required. A variable-speed, semi-hermetic reciprocating compressor provides the circulation driving force, with frequency modulation between 30 and 60 Hz. Downstream of compression, the discharge stream is routed through a desuperheater (HX1) to control discharge-line temperature, and an internal heat exchanger (HX2) is used to manage suction superheat and support receiver liquid handling. Excess heat is rejected to the secondary loop through the gas cooler (HX4) when the net effect of the connected local units is heat injection into the CO_2 loop. High-side pressure is controlled by EV1: when EV1 is fully open, the discharge side operates close to receiver/loop pressure (enabling subcritical operation), whereas transcritical operation is obtained by modulating EV1 to increase the discharge pressure above the loop pressure.

Downstream of EV1, CO_2 enters the distribution loop that connects the LHPs in series (Fig. 2.4). The distribution loop is designed to operate below the critical pressure so that CO_2 can circulate near saturation (two phase or near-saturated conditions) at the receiver pressure.

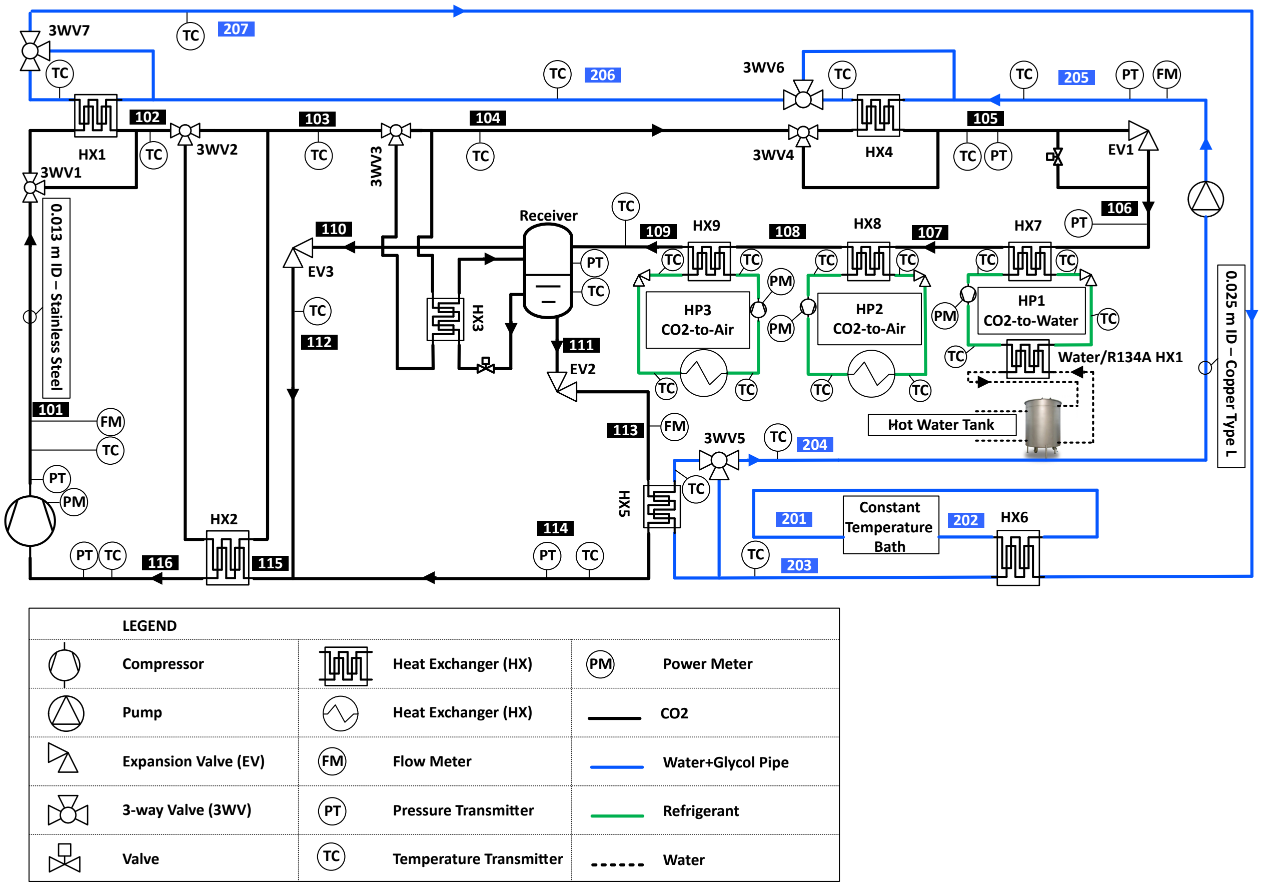

Figure 2.4 Test bench process flow diagram from [24]

CO_2 exiting the last LHP returns to the receiver, which functions as a phase separator that separates liquid and vapor. Receiver pressure is regulated by a flash-gas valve (EV3). Liquid from the receiver is expanded by EV2 and directed to the evaporator heat exchanger (HX5), and EV2 is modulated to satisfy compressor suction superheat requirements. Together, the receiver separation and the coordinated control of EV2 (superheat) and EV3 (receiver pressure) define the boundary conditions of the two phase section and therefore strongly influence whether the loop remains near saturation under varying load combinations.

The balancing unit is implemented using a secondary loop filled with water and 30% glycol connected to a constant-temperature bath. This loop imposes repeatable boundary conditions and compensates the net thermal imbalance of the RVCC, allowing the prototype to emulate heating-dominant and cooling-dominant conditions without reliance on actual outdoor equipment. When the connected LHPs inject net heat into the CO_2 loop, the balancing unit removes this surplus primarily through HX4 (and through the discharge-side heat exchanger as required). When the connected units extract net heat from the loop, HX5 transfers heat from the water–glycol loop to the CO_2 loop to compensate the deficit. This configuration is useful for systematically exploring operating points because it decouples the imposed zone-load combinations from weather variability and isolates the network-level thermodynamic interactions.

Three commercially available LHPs were integrated and modified to exchange heat with CO_2 on the source side. HP1 is a CO_2-to-water unit intended to represent hydronic terminals; it was originally an air-to-water unit using R134a and was retrofitted with a brazed-plate CO_2 heat exchanger (HX7). HP2 and HP3 are CO_2-to-air units intended to represent space-conditioning terminals; they were originally R410A water-to-air units and their water-side heat exchangers were replaced by pipe-in-pipe CO_2–to–R410A heat exchangers (HX8 and HX9). This approach preserves the native load-side heat exchangers and control logic of the commercial units while enabling controlled coupling to a CO_2 distribution loop, which is appropriate for isolating source-side and network-level behavior.

The main component specifications reported for the test bench are summarized in Table 2.1. These specifications define the feasible operating envelope (pressure limits and valve ratings), the expected approach temperatures and pressure drops across heat exchangers (heat-transfer areas and geometries), and the controllability of discharge and receiver pressures via EV1–EV3 and compressor speed. The prototype is also instrumented to measure temperature, pressure, mass flow rates, and electrical power; the paper reports calculated uncertainties on the order of $\pm 2.6\%$ for heat-transfer rate and $\pm 2.7\%$ for COP, supporting the use of the dataset for model calibration and validation in subsequent studies.

In summary, prior work established the CO_2TN concept, identified potential energy benefits, and demonstrated prototype feasibility. Nevertheless, the literature at the start of this Ph.D. lacked (i) detailed, experimentally validated dynamic models suitable for annual co-simulation with buildings, and (ii) practical supervisory control strategies that coordinate loop pressure, mass flow, and compressor operating points across changing zone activity and boundary conditions. The remainder of this chapter therefore reviews modeling approaches for transcritical CO_2 systems and thermal networks, followed by control strategies at both device and supervisory levels, to position the contributions of this thesis.

2.2 Modeling

Modeling of refrigeration systems and thermal networks is commonly approached in a modular way because these systems are composed of several strongly coupled components, each governed by different thermodynamic processes. Compressors determine refrigerant mass

Table 2.1 CO_2TN prototype main components specifications [24]

Component	Specification
Compressor	Semi-hermetic reciprocating; variable capacity; 8.90 kW nominal cooling capacity at 30 Hz.
CO_2 receiver	Volume: 2.3×10^{-2} m^3; design pressure: 9.0 MPa
Electronic expansion valves	
EV1	Discharge pressure control valve; design pressure: 14.0 MPa
EV2	Suction superheat control valve; design pressure: 14.0 MPa
EV3	Flash-gas (receiver pressure) valve; design pressure: 14.0 MPa
CO_2 heat exchangers	
HX1	CO_2 to water brazed-plate HX; heat-transfer area: 0.43 m^2
HX2	CO_2 to CO_2 brazed-plate HX; heat-transfer area: 0.46 m^2
HX3	CO_2 to CO_2 brazed-plate HX; heat-transfer area: 0.18 m^2
HX4	CO_2 to water brazed-plate HX; heat-transfer area: 0.47 m^2
HX5	water to CO_2 brazed-plate HX; heat-transfer area: 0.54 m^2
HX6	water to water brazed-plate HX; heat-transfer area: 0.30 m^2
HX7	CO_2 to R134a brazed-plate HX; heat-transfer area: 0.20 m^2
HX8	CO_2 to R410A pipe-in-pipe HX; length: 3.18 m; CO_2 side ID/OD: 0.015/0.016 m; R410A side ID/OD: 0.021/0.022 m
HX9	CO_2 to R410A pipe-in-pipe HX; length: 3.18 m; CO_2 side ID/OD: 0.015/0.016 m; R410A side ID/OD: 0.021/0.022 m

flow rate, power consumption, and discharge conditions; heat exchangers govern heat transfer, pressure drop, and outlet states; and receivers, separators, or distribution lines define inventory and pressure levels. Since the outlet state of one component becomes the inlet condition of the next, system behavior emerges from the interaction of these component models.

A modular formulation is especially useful for studying refrigeration cycles and shared thermal networks because it allows each component to be modeled at an appropriate level of fidelity and then coupled into a closed system solver. This approach facilitates calibration and validation at the component level, and makes it possible to replace or refine individual submodels without reformulating the whole system. It is therefore widely used in simulation studies of heat pumps, refrigeration cycles, and networked thermal systems, particularly when the objective is to evaluate performance over broad operating envelopes or under changing boundary conditions.

The need for such a structure becomes stronger in transcritical CO_2 systems, where thermophysical properties vary sharply near the critical region and simplified whole-system representations can become inaccurate or numerically fragile. In these systems, predictive performance depends mainly on how well the compressor and heat-exchanger models reproduce off-design behavior, since these components largely determine refrigerant mass flow rate, heat transfer, pressure levels, and outlet states. For this reason, the literature commonly reviews modeling approaches first at the component level and then considers how these submodels are assembled into a complete system representation.

At the component level, the modeling objective is to relate boundary conditions and control inputs to quantities such as exchanged heat rate, pressure drop, power consumption, and outlet state, while maintaining numerical robustness over a wide operating range. In practice, model selection balances three competing requirements: accuracy, generality, and computational cost (compatible with annual simulation and control co-simulation). The following subsections therefore review the main modeling approaches for compressors and plate heat exchangers, which are the two component classes most often identified as critical to the accuracy of transcritical CO_2 heat pump simulations.

2.2.1 Compressor modeling

In vapor compression heat pump models, the compressor submodel provides the refrigerant mass flow rate $\dot{m}$, the compressor electrical power $\dot{W}_{comp}$, and the discharge state (e.g. T_{dis} or h_{dis}) that couples directly to downstream heat exchanger models. This role is important in transcritical CO_2 heat pumps because the compressor operates over a wide envelope, cycle performance is sensitive to suction density and pressure ratio, and compressor model errors can affect the capacity, power demand, and optimal high-side pressure [25, 26].

Compressor models are commonly classified into three broad categories: black-box, gray-box, and white-box models [27]. In this classification, black-box models represent input–output relations without explicitly resolving the underlying physical processes, gray-box models combine fitted relations with simplified physical structure, and white-box models aim to describe the internal processes entirely from first principles [27].

In general, model complexity and computational cost increase as the representation moves from black-box to white-box formulations. More detailed models can better represent internal compressor processes, but they require more information, more parameters, and higher computational cost. The appropriate model should therefore be selected according to the objective of the study. When the objective is compressor design, diagnostics, or analysis of internal loss mechanisms, higher fidelity gray-box or white-box formulations may be justified. By contrast, in vapor compression cycle simulations especially in system level studies of transcritical CO_2 heat pumps where the main focus is the overall cycle rather than the compressor itself, black-box compressor models are used more often because they retain the key input–output behavior at much lower computational cost [27].

For positive-displacement compressors, the most widely used black-box form is the standardized temperature indexed map in CAN/ANSI/AHRI Standard 540 [28]. For operating conditions that can be represented with meaningful saturation (dew-point) temperatures, each compressor output X (typically $\dot{m}$ or $\dot{W}_{comp}$, each with its own coefficient set) is written as a bi-cubic polynomial in the suction and discharge saturation temperatures T_s and T_d,

$$\begin{aligned} X = {} & C_{1,n} + C_{2,n}T_s + C_{3,n}T_d + C_{4,n}T_s^2 + C_{5,n}T_sT_d + C_{6,n}T_d^2 \\ & + C_{7,n}T_s^3 + C_{8,n}T_s^2T_d + C_{9,n}T_sT_d^2 + C_{10,n}T_d^3 \end{aligned} \tag{2.1}$$

where the subscript n denotes the modulation step when multiple steps are provided. AHRI 540 specifies a single coefficient set for fixed-displacement compressors and multiple coefficient sets for modulating compressors. Since each set contains ten coefficients, at least ten test points are required to identify the map for one modulation step. A recent review and comparison by Hjortland and Crawford [29] notes that using only the minimum number of points makes the fitted map sensitive to measurement noise and reduces prediction quality at conditions not used in fitting, therefore, more than the minimum number of points is commonly used in practice. This is consistent with the manufacturer survey findings reported in the AHRI-sponsored work by Aute et al. [30], where most manufacturers reported using more than fourteen test points when developing maps.

For continuous variable-speed compressors, fitting many separate ten coefficient maps across speed can be inconvenient. As an alternative, Guo et al. [31] proposed an extended 20 coefficient regression that includes compressor rotational frequency S (Hz) directly as follows:

$$\begin{aligned} X = {} & c_0 + c_1T_s + c_2T_d + c_3S + c_4T_s^2 + c_5T_d^2 + c_6S^2 + c_7T_sT_d \\ & + c_8T_sS + c_9T_dS + c_{10}T_s^3 + c_{11}T_d^3 + c_{12}S^3 + c_{13}T_s^2T_d \\ & + c_{14}T_s^2S + c_{15}T_sT_d^2 + c_{16}T_d^2S + c_{17}T_sS^2 + c_{18}T_dS^2 \\ & + c_{19}T_sT_dS \end{aligned} \tag{2.2}$$

This model has twenty coefficients for each output and therefore requires at least twenty test points, with additional points used to reduce sensitivity to noise and to improve prediction at unseen conditions.

A second practical issue with AHRI-style maps is that they are generated under standardized suction conditions, typically constant suction superheat or constant suction temperature. In a system simulation, the suction state varies with heat exchanger performance and control, so map outputs are often corrected before they are used in the cycle solver. Hjortland and Crawford [29] summarize the commonly used correction proposed by Dabiri and Rice [32], which adjusts the mapped mass flow rate using the ratio of actual suction density to the map suction density as follows:

$$\frac{\dot{m}_{corr}}{\dot{m}_{map}} = 1 + F_V \left(\frac{\rho_{suc}}{\rho_{map}} - 1 \right) \tag{2.3}$$

where $\dot{m}_{map}$ is the mass flow rate predicted by the map at the rating convention, ρ_{map} is the suction density at the map suction condition, ρ_{suc} is the actual suction density in the system simulation, and F_V is a volumetric efficiency correction factor. Under the assumption that isentropic efficiency is not a function of suction superheat, Dabiri and Rice also propose a compatible correction for compressor power as follows:

$$\frac{\dot{W}_{corr}}{\dot{W}_{map}} = \frac{\dot{m}_{corr}}{\dot{m}_{map}} \cdot \frac{\Delta h_{isen,corr}}{\Delta h_{isen,map}} \tag{2.4}$$

where $\dot{W}_{map}$ is the mapped power, $\dot{W}_{corr}$ is the corrected power, and Δh_{isen} is the specific isentropic compression work evaluated at the actual and map suction states [32].

An example of AHRI-style mapping in a variable speed heat pump model is given by Viviescas and Bernier [33]. They use an AHRI-like regression for $\dot{m}$ and $\dot{W}_{comp}$ and include compressor speed explicitly. They also apply the suction state correction when suction conditions deviate from the map convention and show that omitting the correction increases the mass flow error in their validation [33]. This example illustrates the usual role of AHRI maps in system models: they are convenient interpolators inside the calibrated domain, but they are used together with correction relations when suction conditions do not follow the rating convention.

A complementary perspective is provided by Sanchez et al. [34], who evaluate a standard ten coefficient polynomial form against transcritical CO_2 data and then modify the regression when deviations are observed. They write the standard form for an output X as a polynomial in evaporating temperature T_{ev} and discharge pressure P_{dis},

$$\begin{aligned} X = A_1 + A_2 T_{ev} + A_3 P_{dis} + A_4 T_{ev}^2 + A_5 (T_{ev} P_{dis}) + A_6 P_{dis}^2 \\ + A_7 T_{ev}^3 + A_8 (T_{ev}^2 P_{dis}) + A_9 (P_{dis}^2 T_{ev}) + A_{10} P_{dis}^3 \end{aligned} \tag{2.5}$$

and they report larger deviations for mass flow prediction in their data set. They then replace T_{ev} by suction pressure P_{suc} and include suction temperature T_{suc}, which yields a reduced nine coefficient regression,

$$
\begin{aligned}
X = {} & A_1 + A_2 P_{suc} + A_3 P_{dis} + A_4 P_{suc}^2 + A_5 (P_{suc} P_{dis}) + A_6 P_{dis}^2 \\
& + A_7 T_{suc} + A_8 T_{suc}^2 + A_9 (P_{dis} P_{suc} T_{suc})
\end{aligned}
\tag{2.6}
$$

which improves agreement with their measurements [34]. For transcritical CO_2, this type of pressure based description is often preferred because high side heat rejection occurs in a gas cooler and there is no unique condensing temperature. A temperature indexed map therefore requires a choice of surrogate high side temperature, and the fitted coefficients depend on that choice.

Overall, AHRI-style polynomial maps remain convenient when operation stays within a well sampled calibration domain and when the saturation temperature representation is meaningful [28, 30]. For transcritical CO_2 operation, pressure based correlations are often used because there is no unique condensing temperature on the high side and because pressure variables match discharge pressure control [34–36].

2.2.2 Plate heat exchanger modeling

Plate heat exchangers (PHEs), especially brazed plate heat exchangers, are widely used in CO_2 heat pumps because they provide high heat transfer performance within a compact footprint. Their corrugated chevron plates promote strong mixing and thin thermal boundary layers, which is attractive for both sensible heat exchange and phase-change duties. In CO_2 applications, however, the same compact exchanger can be required to operate in fundamentally different thermodynamic regimes, ranging from supercritical single-phase cooling to subcritical condensation and evaporation. This operating diversity is central to the modeling problem, because the CO_2 thermophysical properties can change rapidly near the critical region and because phase-change segments may appear or disappear as operating conditions shift. Consequently, a model structure and correlation set that is adequate in one regime may become inaccurate or numerically fragile in another, and it is often necessary to select modeling formulations that remain valid as the heat exchanger crosses the critical point or transitions into and out of the two phase dome. This requirement is particularly important for CO_2 because its critical point is at $T_{cr} = 31.1\,°\mathrm{C}$ and $P_{cr} = 7.38\,\mathrm{MPa}$, so transcritical gas cooler operation occurs in a supercritical region where thermophysical properties can vary sharply over a narrow temperature change.

Figure 2.5 illustrates this behavior for CO_2 at 8, 9, and 10 MPa. For a given supercritical pressure, the pseudo-critical temperature (T_{pc}) is defined here as the temperature at which the specific heat reaches a maximum. As shown in the figure, this temperature increases with pressure over the range considered. In the vicinity of the pseudo-critical temperature, density and dynamic viscosity decrease sharply, the specific heat exhibits a peak, and thermal conductivity also varies noticeably. The modeling implication is that even a small local temperature change can strongly modify the refrigerant side heat capacity rate, heat transfer coefficient, and pressure drop. As a result, simplified constant property or single UA representations may become inaccurate when a CO_2 heat exchanger operates near the pseudo-critical region, especially in transcritical gas coolers.

The literature commonly organizes PHE and heat-exchanger models into three families that trade fidelity for computational cost as follows [37]:

- Lumped-parameter models
- Moving-boundary models
- Finite-volume models

At the simplest end, lumped-parameter models represent the exchanger by a single overall conductance, typically through a constant UA paired with an logarithmic mean temperature difference (LMTD) or ε–NTU relation. This choice remains common in building energy and system simulations because it is numerically robust, fast, and easy to calibrate to steady state data or manufacturer ratings [37]. When the heat exchanger operates in a narrow regime and the temperature profiles remain "well behaved" (for example, as an evaporator, or condenser), a tuned lumped model can reproduce heat transfer with acceptable accuracy for annual performance studies. The main limitation is that a single calibrated UA represents an effective (lumped) behavior of the exchanger at the calibration point. Because it treats the heat exchanger as a single averaged element, this approach cannot capture variations in local heat transfer and thermophysical properties along the flow path. Therefore, its accuracy may degrade when operating conditions depart from the calibration range. In CO_2 heat pump applications this matters most when the exchanger spans regions with strongly changing heat capacity rate on the refrigerant side, because the local temperature glide and pinch behavior are no longer captured by a single average conductance. In supercritical cooling, for instance, the pseudo-critical peak in c_p reshapes the temperature profile and shifts where most of the heat is rejected, so a constant-UA model may match total heat transfer at one condition yet drift in outlet temperature prediction as conditions change. A common "middle ground" reported in practice is to retain the lumped structure but introduce regime-aware averaging (different effective UA values for distinct operating modes) or a small number of serial lumps, which preserves speed while reducing the bias associated with a single global average [38].

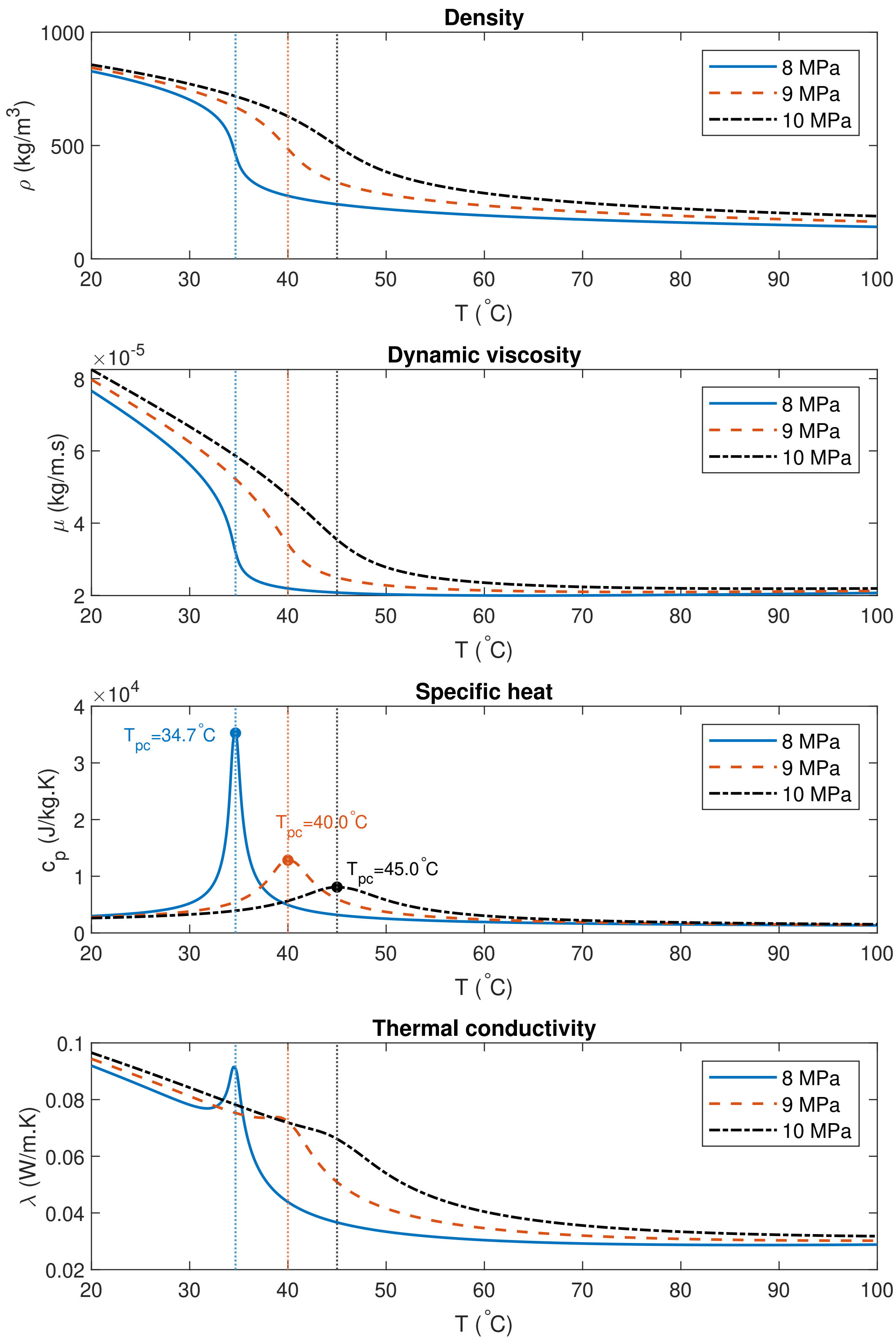

Figure 2.5 CO_2 (R744) thermophysical properties near the critical region ($P_{cr} = 7.38\,\mathrm{MPa}$ $T_{cr} = 31.1\,°\mathrm{C}$)

Moving-boundary (MB) models add the missing structure of lumped UA approaches by treating each thermodynamic region as a separate control volume whose length (or heat-transfer area fraction) varies with operating condition. In subcritical condensers and evaporators, the natural decomposition into superheated, two phase, and subcooled zones makes MB formulations especially attractive: within each zone, property variations are typically smoother than across the full exchanger, while the moving interfaces capture how the available area reallocates between zones as load and inlet conditions vary. This region-based view is also consistent with experimental CO_2 plate exchanger studies. For example, Hayes et al. [39] analyze CO_2 condensation in a chevron plate heat exchanger by explicitly separating the exchanger into superheated-vapor, saturated two phase, and subcooled-liquid sections, and by allocating area based on regime-specific heat-transfer balances. This type of analysis aligns directly with the MB assumption that region boundaries move as operating conditions change, and it supports MB modeling as a physically meaningful reduced-order representation for subcritical CO_2 PHE duties. For system-level vapor compression modeling, MB models are therefore widely used as a control-oriented and annual-simulation-capable compromise, offering substantially lower computational cost than fine discretization while retaining zone migration and phase-change structure [40]. The main limitations are numerical. As operating conditions change, one or more regions can shrink to nearly zero length or reappear, so the model must switch between different region configurations. Without robust switching logic, this can lead to oscillations or convergence difficulties. In addition, the standard MB partitioning is defined by phase boundaries and does not apply directly to supercritical gas coolers, where high-pressure CO_2 remains single phase and no phase boundary exists. A large body of work has therefore focused on making MB models robust across arbitrary region configurations and pinch behavior, and on extending the MB idea to supercritical gas coolers by redefining "regions" within the supercritical domain using criteria related to the pseudo-critical neighborhood and local heat-capacity-rate behavior rather than phase [41–43]. These developments clarify the best-use region of MB models: they are most transparent and reliable for subcritical heat exchangers that pass through superheated, two phase, and subcooled regions, and they remain a strong compromise for system simulation and supervisory-control evaluation when the study requires outlet states that respond correctly to zone migration but cannot justify a fully discretized model at every time step.

Finite-volume (FV) models provide the most general 1-D framework used in heat pump simulations. By discretizing the flow direction, they evaluate properties locally and apply region-appropriate closure relations cell-by-cell, which allows them to represent sharp gradients, internal pinch points, and non-uniform temperature glide without imposing a fixed region structure a priori. This capability is particularly valuable for supercritical CO_2 gas coolers where steep property variations near the pseudo-critical region can localize heat transfer into a relatively small portion of the exchanger and strongly influence outlet temperatures and optimal high-side operating conditions [44, 45]. In the PHE context, FV ideas appear either as true cell-by-cell solvers or as “sliced” formulations that decouple channels by assuming locally constant wall temperature per slice and iterating the slices to convergence. Such approaches can handle generalized flow configurations and phase change, which is important when the same PHE family is used as condenser, evaporator, or gas cooler under different operating modes [46]. The critical review point for FV models is that their apparent fidelity depends on two external factors: (i) the suitability of the selected heat-transfer correlations for the specific PHE geometry and for CO_2 in the relevant regimes, and (ii) the discretization strategy (number of cells and how property evaluation is performed). Correlation performance scatter has been repeatedly documented in plate exchangers, with accuracy that can vary markedly across datasets and conditions; this is why many authors recommend correlation screening against plate exchanger databases and, when possible, calibration to the targeted exchanger family [47, 48].

In the CO_2TN context of this thesis, the modeling choice can therefore be justified by matching each exchanger’s dominant thermodynamic pattern to the simplest formulation that remains region-consistent. When an exchanger operates predominantly in a single, relatively narrow regime, a calibrated lumped UA or effectiveness-based model can be adequate and keeps the annual simulations lightweight. When subcritical operation induces a clear superheated/two phase/subcooled sequence, an MB model provides a natural way to represent zone migration with modest computational cost and good interpretability for control studies. When transcritical operation near the pseudo-critical region is central to the results—especially when outlet temperature prediction affects supervisory decisions—FV discretization becomes the defensible choice, because it preserves the effect of sharp property gradients on the temperature profile and avoids embedding that physics into a single fitted average.

2.3 Control and supervision of CO_2 thermal networks

The supervisory problem has two coupled goals. The first goal is feasibility: the supervisor must select operating conditions that satisfy equipment envelopes and feasibility constraints. The second goal is performance: within the feasible region, the supervisor seeks operating points that maximize a system metric such as COP_{sys} under changing boundary conditions and LHP activation patterns. The remainder of this section reviews supervisory methods used for constraint-rich vapor compression systems and shared-source plants.

Supervisory coordination strategies for vapor compression systems can be organized into two main categories: online optimal control and, offline optimal control. These categories differ in how supervisory decision variables are generated and updated under changing operating conditions. The following subsections review each category and summarize their main characteristics, advantages, and limitations in the context of vapor compression and CO_2-based systems.

2.3.1 Online optimal control

Online optimal control refers to supervisory approaches in which the optimization problem is solved during system operation using current measurements or estimated states. In the transcritical CO_2 literature, this category can be grouped into two main streams: online model-based optimal control and online model-free optimal control. In the first stream, an explicit steady-state or dynamic model is embedded in the optimizer to evaluate candidate supervisory decisions under performance and feasibility constraints. In the second stream, the supervisory input is adapted directly from measured performance without relying on a calibrated plant model.

Within online model-based optimal control, one line of work focuses on optimization of the current operating condition. In transcritical CO_2 systems, this problem is most often formulated as online determination of the optimal high-side or discharge pressure, since system performance is highly sensitive to this variable. Cecchinato et al. [49] addressed the optimal energy efficiency and high pressure problem in single stage transcritical CO_2 vapor compression units and developed a real-time model-based optimization algorithm to determine the optimal, or near-optimal, pressure from measured boundary conditions and a model of system performance. More recently, Li et al. [50] presented model-based optimal-control approaches for a water-to-water CO_2 heat pump for domestic hot water use. Their controller combines an optimization strategy with system models to identify optimal setpoints for discharge pressure and gas cooler outlet water temperature, showing how online model-based optimization can be extended beyond single-setpoint pressure tuning to coordinated adjustment of multiple operating variables.

A second line of work adopts model predictive control (MPC). At each control update, MPC uses a predictive model to estimate future system behavior over a finite horizon and then solves an optimization problem to determine the control actions that optimize a chosen objective while satisfying constraints. Only the first control action is applied, and the optimization is repeated at the next update using new measurements. Wang et al. [51] proposed MPC for a transcritical CO_2 air-source heat pump water heater. They first built a high-fidelity physical model in Dymola, then identified a control-oriented dynamic model from the generated data, and finally designed the MPC to maximize COP under model equations and operating constraints. Their work is particularly useful because it explicitly distinguishes MPC from earlier online pressure optimization methods: instead of searching only for the current optimal heat rejection pressure, the controller predicts future operating conditions and computes the optimal manipulated inputs accordingly.

Subsequent studies extended MPC to other transcritical CO_2 applications and control structures. Zhang et al. [52] developed an MPC strategy for a transcritical CO_2 air conditioning system used in railway vehicles. Their controller combines physical knowledge and data in the predictive model and optimizes discharge pressure together with air-side actuation while maintaining passenger comfort. Wang et al. [53] proposed a data-driven nonlinear MPC for a transcritical CO_2 cabin thermal management system in cooling mode, where the controller simultaneously adjusts the compressor, throttle valve, and indoor fan to reduce power consumption while satisfying comfort requirements. Cui et al. [54] further extended the MPC framework to a transcritical CO_2 heat pump water heater. In that work, the optimization problem is complicated by the presence of an additional medium-pressure level and stronger internal coupling among variables. To keep the online problem tractable, the authors first identified a relation between the optimal medium pressure and the suction and discharge pressures, then used this intrinsic relation to reduce the decision space before constructing the MPC. Taken together, these studies show that MPC has become the common dynamic realization of online model-based optimal control in transcritical CO_2 systems, especially when several actuators and operational constraints must be coordinated simultaneously.

Although directly analogous online optimal-control studies for CO_2 thermal networks remain limited, related work on shared-source refrigeration systems and thermal networks is still relevant because it highlights the optimization structures that arise once several terminals share common pressure or temperature levels. Hovgaard et al. [55, 56] studied a multi-zone refrigeration system in which several cooling units share a common compressor and formulated a supervisory MPC that allocates cooling capacity to the zones while selecting a common evaporation temperature. Their results show that even when the system dynamics and constraints can be written in a convex form, the cost function may remain nonconvex because efficiency depends on temperature. In thermal-network applications, Wirtz et al. [57] proposed a mixed-integer linear program (MILP) for short term optimization of the network temperature in fifth-generation district heating and cooling systems, while Quaggiotto et al. [58] formulated district-heating operation as an MILP-based MPC problem solved in a rolling-horizon scheme. Jansen et al. [59] further showed that when nonlinear network physics and discrete equipment decisions must both be preserved, the predictive control problem naturally becomes a mixed-integer nonlinear program (MINLP). These studies are not CO_2TN studies, but they are useful to position the supervisory complexity that can arise in shared-source and networked thermal systems when discrete equipment states, staging decisions, and nonlinear thermodynamics must be handled simultaneously. Alongside model-based methods, the transcritical CO_2 literature also contains a substantial stream of online model-free optimal control, most commonly through extremum seeking control (ESC). In these approaches, the controller does not rely on a calibrated plant model; instead, it uses measured performance to adapt a supervisory input toward the operating point that optimizes a chosen index. Hu et al. [60] introduced ESC for an air-source transcritical CO_2 heat pump water heater to maximize COP in real time by regulating the discharge-pressure setpoint. Their study used a dynamic Modelica model to evaluate the controller under fixed and varying operating conditions and showed that the method can search for and track the optimum without requiring an explicit system model. Cui et al. [61] later provided an experimental investigation of ESC on a transcritical CO_2 heat pump water heater. Their results demonstrated repeatable convergence of the controller under both fixed and varying inlet-water conditions and confirmed experimentally that the discharge pressures identified by the ESC correspond to the optimal operating points of the system. Rampazzo et al. [62] broadened the scope by investigating ESC experimentally on both refrigeration and heat pump CO_2 units operating in transcritical and subcritical conditions. They also compared ESC with a conventional optimal-pressure correlation, showing the value of measurement-based adaptation when the optimum varies with system configuration and operating conditions.

More recent work extends online model-free optimization from single-variable discharge-pressure tuning to more complex transcritical CO_2 architectures. Cui et al. [63] considered a dedicated-mechanical-subcooling transcritical CO_2 heat pump water heater and proposed a multi-input single-output ESC strategy developed from a validated Dymola model. Their results showed better performance than standard solutions based on physical correlations, under both fixed and variable ambient conditions. These studies show that model-free online optimization remains attractive for transcritical CO_2 systems as complexity increases, but they also make its limitations more visible. In particular, the convergence speed, the need for excitation and filtering, and the growing difficulty of tuning multi-variable ESC schemes become more problematic as the number of manipulated variables increases and as feasibility constraints become tighter.

Overall, the online optimal-control literature for transcritical CO_2 systems spans online model-based optimization of the current operating point, predictive dynamic optimization through MPC, and model-free optimization through ESC. Model-based methods offer a clearer framework for handling multiple actuators and explicit constraints, but they depend on the availability of reliable control-oriented models. Model-free methods avoid this modeling burden and can adapt directly to changing operating conditions, but they face practical challenges in convergence, tuning, and constraint handling, especially in multi-variable systems.

2.3.2 Offline optimal control

Offline optimal control refers to supervisory approaches in which the main optimization effort is carried out before system operation and the resulting decision rule is evaluated online without solving a new optimization problem at each control step. The offline rule may be derived from a physical model, from experimental or simulated data, or from a combination of both. In vapor compression and transcritical CO_2 systems, this strategy is attractive because it keeps online supervision simple, and fast while still embedding information from optimization studies performed over the expected operating range.

In the literature, offline-executed supervisory rules usually appear in three main forms. The first form is a fitted analytical map, such as an empirical correlation, polynomial regression, or response-surface model, in which the desired setpoint is expressed as a function of a small number of measured variables. The second form is a tabulated map, in which the operating space is sampled offline and the best feasible setpoint is stored at each grid point for later look up or interpolation. The third form is an explicit control law, in which the optimization problem is solved offline over a prescribed operating region so that online implementation reduces to evaluating a precomputed rule. Although these forms differ in how the rule is represented, they share the same principle: the computationally expensive part of the supervisory decision is shifted offline, and the online controller only evaluates the resulting map.

A large portion of the transcritical CO_2 control literature uses fitted maps to generate the high side pressure setpoint from boundary conditions. Early studies relied mainly on thermodynamic cycle simulations to identify the pressure that maximizes COP and then expressed the optimum as a simple correlation. Kauf [64] used a simulation model to determine the optimal high pressure as a function of gas cooler outlet temperature and reported that the resulting control function keeps COP within 5.8% of the maximum over the tested conditions. Liao et al. [65] similarly developed a cycle simulation model, showed that COP varies nonmonotonically with heat rejection pressure, and derived a correlation for the optimal pressure in terms of gas cooler outlet temperature, evaporation temperature, and compressor performance. These studies established the basic offline-map idea for transcritical CO_2 control: the supervisor does not solve an optimization problem online, but instead evaluates a precomputed relation to generate the pressure setpoint.

Later work extended this approach from simulation-based correlations to experimentally supported setpoint rules. Qi et al. [66] experimentally investigated the optimal heat rejection pressure of a transcritical CO_2 heat pump water heater and proposed a correlation intended for direct use in control. Li et al. [67] also examined the optimal compressor discharge pressure experimentally for an air-source transcritical CO_2 heat pump, developed a fitted correlation over a broader temperature range, and proposed a superheat-corrected control strategy for practical implementation. These studies show that offline fitted maps are not limited to purely theoretical cycle analyses, but can also be calibrated or corrected from measured plant behavior.

A recurring issue in fitted high pressure correlations is robustness under changing boundary conditions, especially near the critical region. Cecchinato et al. [68] evaluated several literature approximations for optimal heat rejection pressure and showed that their performance depends strongly on the application and regulation structure. In particular, approximations that remain acceptable in commercial refrigeration can become much less reliable in heat pump water heater operation when the assumed relation between secondary side conditions and gas cooler outlet temperature no longer holds. Shao et al. [69] addressed this issue by developing constrained optimal pressure equations in which the high pressure is reduced subject to an allowed COP loss. Taken together, these studies show that offline fitted maps are useful only when their validity range is consistent with the intended control structure and operating envelope, and that explicit constraint handling may be needed when feasible operating regions are narrow.

Offline fitted maps have also been extended from low-dimensional correlations to higher-dimensional surrogate models. Liang et al. [70] used response-surface methodology to analyze the factors governing the optimal high pressure in transcritical CO_2 refrigeration and heat pump water-heater applications. Their results showed that gas-cooler outlet temperature is the dominant factor in refrigeration applications, whereas multiple variables contribute in heat pump water heater operation. They also reported that adding variables to the fitted map substantially reduced prediction error. This illustrates a common trade-off in offline map design: a richer map can reduce bias, but it also increases data requirements and makes the supervisory rule more sensitive to coverage of the offline dataset.

Beyond analytical correlations and response surfaces, the literature also includes data-driven fitted maps trained on offline datasets of optimal operating points. In these approaches, the online controller still evaluates a precomputed map, but the functional relation is learned from data rather than prescribed in advance. Yin et al. [71] generated a dataset of operating conditions and corresponding optimal discharge pressures and then used group method of data handling (GMDH) for variable selection together with a PSO–BP neural network to predict the optimal discharge pressure. In the companion experimental study, Song et al. [72] implemented the learned mapping as a real-time setpoint generator on a subcooler-based transcritical CO_2 heat pump prototype and reported improved performance relative to a baseline strategy. In this sense, data-driven maps are not a separate online-execution category from model-based maps; rather, they are another way of constructing a fitted offline map. The practical distinction is whether the final rule is obtained directly from a physical optimization model or learned from a dataset of optimal operating points.

The same offline philosophy also appears in predictive-control theory through explicit MPC. In explicit MPC, the constrained predictive-control problem is solved offline over a prescribed operating region, and the resulting optimal control law is stored in a form that can be evaluated directly online. Bemporad et al. [73] showed that, for MPC problems that can be expressed in this framework, the explicit solution can be written in region-based form so that online implementation reduces to simple function evaluation. Alessio and Bemporad [74] further emphasized that explicit MPC is particularly attractive when online solvers are too expensive or difficult to certify, although the number of operating regions and the memory requirement can increase rapidly with model dimension, horizon length, and the number of constraints. This line of work is more general than the transcritical CO_2 high pressure literature, but it provides the clearest theoretical example of offline optimal control in which the optimization result itself, rather than a fitted approximation of it, is stored for online use.

Overall, the main advantage of offline optimal control is that it shifts most of the computational burden to an offline stage, so that online supervision reduces to direct evaluation of a precomputed rule. This feature underlies classical fitted optimal-pressure correlations [64,65], experimentally calibrated setpoint maps [66, 67], learned surrogate predictors [71, 72], and explicit predictive-control laws [73, 74]. The main limitation is coverage: the offline rule is reliable only within the range of operating conditions represented by the offline model, dataset, or operating-region partition. In fitted maps, insufficient coverage or oversimplified variable selection can increase prediction bias, as reflected by the strong dependence of optimal-pressure correlations on application and boundary-condition representation [68] and by the error reduction obtained when additional variables were included in response-surface models [70]. Learned surrogate maps are subject to the same requirement for representative training data [71]. Explicit MPC faces an analogous limitation in that the number of regions and the associated memory requirement can grow rapidly with problem size and constraints [74]. Reported remedies therefore include higher-dimensional surrogate maps [70], constrained-map formulations [69], and hybrid implementations in which an offline pressure map is corrected online using additional measured information such as superheat [67]. For multi-terminal systems such as CO_2 thermal networks, the same issue is expected to become more pronounced because the supervisory input space must also reflect changing terminal-activation combinations in addition to external boundary conditions.

2.3.3 Summary

The supervisory literature reviewed above can be organized into two broad routes: online optimal control and offline optimal control. Within online optimal control, the literature includes both model-based approaches, such as current-operating-point optimization and MPC, and model-free approaches, most commonly ESC. Within offline optimal control, the literature includes fitted analytical maps, tabulated lookup maps, and explicit control laws derived from offline optimization. Across these routes, the main trade-off is between online adaptability and explicit constraint handling on the one hand, and computational simplicity on the other.

For transcritical CO_2 systems, online strategies are attractive because they can adapt set-points to changing operating conditions and can, in principle, coordinate several manipulated variables under constraints. However, the reviewed studies also show that these methods usually require either a reliable control-oriented model or carefully tuned adaptation logic, and their computational or implementation burden increases as the number of decision variables, constraints, and operating modes grows. These difficulties become more pronounced in shared-source and networked systems, where supervisory decisions must remain feasible across changing terminal combinations and coupled thermodynamic interactions.

2.4 Summary and research gaps

The literature reviewed in this chapter shows that CO_2-based thermal networks are a promising direction for multi-zone building applications because they can combine low-GWP operation, heat recovery between zones, and reduced temperature drift when CO_2 is distributed near saturation. District-scale studies have demonstrated the thermodynamic and techno-economic potential of refrigerant-based distribution, while early building-scale studies and the pilot-scale prototype have established the basic feasibility of the single-pipe CO_2TN concept. The modeling literature also provides a broad set of methods for representing compressors and heat exchangers in transcritical CO_2 systems, and the control literature shows that both online and offline optimization strategies can improve the operation of stand-alone transcritical CO_2 heat pumps.

At the same time, the review reveals several gaps that are directly relevant to CO_2TN development:

- Existing CO_2TN studies remain limited in number and scope. Early building-scale assessments established feasibility and climate sensitivity, and the prototype study demonstrated physical implementation, but the literature still lacks a comprehensive, experimentally validated modeling framework that represents the coupled network and terminal behavior across the full range of relevant operating modes.
- Integration between detailed CO_2TN models and dynamic building simulations remains limited, so that annual performance under realistic boundary conditions is not quantified.
- Most prior control strategies for CO_2TN focus on enforcing strictly two phase operation at fixed loop pressure and do not fully exploit the potential of coordinated control of compressor configuration, compressor speed, discharge and suction pressures, and loop pressure.

These gaps motivate the main developments of this thesis: the construction of an experimentally validated CO_2TN model, its coupling to building-level performance assessment, and the development of offline supervisory strategies that remain feasible, computationally tractable, and suitable for annual simulation as well as real-time implementation. The next chapter formulates the research objectives and presents the overall structure of the thesis.

CHAPTER 3 OBJECTIVES AND THESIS STRUCTURE

3.1 Research objectives

The general objective of this thesis is to develop an experimentally validated, numerical model of a single-pipe CO_2 thermal network (CO_2TN) coupled with local heat pumps, and to use this model to design and assess supervisory control strategies for multi-zone building applications. This objective is pursued through the following specific objectives:

1. Develop a component- and system-level numerical model of the CO_2TN, including the circulation unit, local heat pumps, and the main heat-exchange interfaces (gas cooler and evaporator/condenser), with the required supporting components (e.g., internal heat exchanger, desuperheater, and geothermal coupling).

2. Validate the component- and system-level performance of the CO_2TN model using measured data gathered from experiments conducted on the CO_2TN prototype.

3. Formulate supervisory control strategies for the CO_2TN to reduce overall electricity consumption while respecting operational constraints.

4. Evaluate and compare the proposed supervisory strategies under representative annual multi-zone building operation using the validated model.

3.2 Thesis structure

This paper-based thesis consists of six chapters. Chapter 1 presents the context and motivation, introduces CO_2-based thermal networks and the CO_2TN concept, and states the research problem. Chapter 2 reviews relevant system architectures, modeling approaches, and supervisory control methods for heat pumps and thermal networks, thereby establishing the background for Objectives 1–4. Chapter 3 states the research objectives and explains how the preliminary studies carried out during the Ph.D. led to the two journal articles that form the core contributions of the thesis.

Chapter 4 reproduces Article 1 and focuses on model development and experimental validation of the CO_2TN, thereby addressing Objectives 1 and 2. Chapter 5 reproduces Article 2 and builds on the validated model to formulate and compare supervisory strategies and to assess their performance under annual building operation, thereby addressing Objectives 3 and 4. Finally, Chapter 6 synthesizes the main findings of Articles 1 and 2, discusses the main implications and limitations, and proposes directions for future work.

3.2.1 Research path leading to the thesis articles

Before the two journal articles were completed, several conference papers were produced during the Ph.D. They are presented here because they document the progression of the research and show how the main questions of the thesis evolved.

The first preliminary study was reported in 15th IIR-Gustav Lorentzen conference on natural refrigerants in 2022 [75]. That paper presented a simplified heating-season analysis of the CO_2TN and introduced the first control strategy, referred to as the minimum-mass-flow method. In that study, the auxiliary heater and cooler used in the earlier feasibility work of Bastani and Eslami-Nejad [23] were removed, and the operating point of the circulation unit was determined from the imposed loop condition and the combination of active local heat pumps. For a prescribed loop pressure, the method selected the loop inlet condition and the minimum CO_2 mass flow rate required to keep the loop within the two phase region while satisfying the imposed loads. The paper also included an initial seasonal comparison with a conventional water-loop heat pump system for the same building under simplified assumptions. This study established the first closed operating-point calculation for the CO_2TN, but it remained limited to heating-season operation and simplified, non-validated models.

A subsequent conference paper presented at eSim 2024 [76] marked an important intermediate step in the development of this thesis. The study was the first to formulate a detailed semi-transient TRNSYS model of the CO_2TN for office-building heating and cooling, with dedicated sub-models for the circulation system, outdoor unit, and local heat pump units. It reports the first preliminary experimental validation of key component models and demonstrated the applicability of the modeling framework through a multi-zone building case study. In this sense, the eSim paper established the first integrated framework combining detailed system representation, control implementation, and initial experimental corroboration. The later journal article in Chapter 4 built directly on that foundation by extending the model formulation and providing a more comprehensive experimental validation at both the component and system levels.

The next step was reported in 16th IIR-Gustav Lorentzen conference on natural refrigerants in 2024 [77], which shifted the focus toward supervisory control in transcritical cooling operation. Through a parametric study of compressor discharge pressure, loop pressure, and CO_2 mass flow rate, that paper showed that the minimum-mass-flow assumption is not always performance-optimal. In particular, it showed that allowing a limited departure from strictly two phase loop operation can improve overall system performance under some cooling conditions. This result marked an important point in the control development of the thesis and directly motivated the later formulation of the temperature-bounded supervisory strategy presented in Article 2. The parametric cooling results reported in that conference paper therefore serve as the preliminary basis for the control developments consolidated in Chapter 5.

In parallel with the model development work, an additional study was carried out on the local heat pumps and was later published in the conference paper included in the Appendix A. That study showed that conventional local heat pumps are not the most suitable option for the CO_2TN and that low-lift heat pumps are better aligned with the CO_2TN concept. This finding influenced the configuration adopted in Article 2, where low-lift local heat pumps were used to better explore the performance potential of the system. The detailed results of that local-heat-pump study are kept in the appendix because they support the thesis storyline but do not constitute one of its two main journal contributions.

CHAPTER 4 ARTICLE 1: Modeling and experimental validation of a single-pipe CO_2 thermal network connected to local heat pumps

Authors: Sepehr Gholamrezaie, Massimo Cimmino, Parham Eslami-Nejad

Journal: Applied Thermal Engineering

Date: Available online 22 September 2025

4.1 Abstract

This study develops a modular numerical model for a CO_2 thermal network (CO_2TN) that connects local heat pumps (HPs) via a two-phase CO_2-loop, for building heating and cooling and thermal energy recovery. Implemented in TRNSYS with newly developed TYPES, the model is designed for flexibility, allowing the study of various system configurations and integration into broader simulations with detailed building models. The model is experimentally validated at both the component and system levels using a prototype setup. For component-level validation, key components—including the CO_2 circulation compressor and heat exchangers—are compared against experimental data, demonstrating a maximum deviation of ±15% across all components. System-level validation is conducted by assembling the component models into a system resembling the experimental prototype and comparing the system coefficient of performance (COP) across different operating modes, with a maximum deviation of 16%.

4.2 Introduction

A thermal network refers to a system used to distribute a heat carrier fluid (HCF), such as water or a refrigerant, through a network of pipes to deliver heating or cooling to various spaces or processes. These networks can be employed in district heating and cooling systems or on a smaller scale, such as within buildings [78]. Thermal networks enable the integration of renewable energy sources, such as geothermal or solar thermal energy, and the recovery of waste heat from one user to deliver it as useful heat to another [79]. However, controlling these networks and managing piping complexity are significant challenges in their implementation. The are two classes of approaches for implementing thermal networks: the secondary loop method (indirect method) and the direct method. In the secondary loop method, end users are connected to a low-temperature thermal network, and local heat pumps (HPs) deliver the required thermal energy to each user. Conversely, in the direct method, the HCF directly provides the required thermal energy to end users, simplifying the system but potentially limiting its flexibility.

One of the most widely used secondary loop building thermal network system is the water loop heat pump (WLHP) system. In WLHP systems, a central loop circulates water within a specific temperature range as the primary heat transfer medium. Local HPs throughout the building provide zone-level heating and cooling by either absorbing or rejecting heat to the central water loop. The design of WLHP systems can vary, as explored by Gagné-Boisvert and Bernier [80], with two typical configurations being the single-pipe and two-pipe systems. In single-pipe configurations, HP performance is affected by uneven fluid temperature distribution across the thermal network, leading to variations in performance between HPs. To maintain system efficiency, water temperatures should ideally remain between 16°C and 32°C [81]. In contrast, two-pipe configurations mitigate temperature fluctuations with separate supply and return lines, though this increases piping costs. Pietsch [82] and Yuan and Garbon [83] analyzed the effect of the water loop temperature on energy consumption, proposing that there is an optimal water temperature range for the water loop system that minimizes overall energy consumption depending on the scale and building layout. Lian [84] demonstrated that optimizing the water temperature range could reduce HP electricity consumption by up to 13%.

A widely used direct thermal network system is the variable refrigerant flow (VRF) system. VRF systems provide direct space heating, cooling, or simultaneous heating and cooling through the circulation of refrigerant. Mechanically, they achieve this by reversing the refrigerant flow via a four-way valve for heating or cooling modes and by incorporating a heat recovery unit (HRU) to enable simultaneous heating and cooling. In VRF systems with an HRU, 3-pipe or 4-pipe configurations are used to distribute refrigerant throughout the building in different states. High-pressure vapor refrigerant is supplied to indoor units operating in heating mode, while low-pressure liquid refrigerant is directed to indoor units requiring cooling. VRF systems adjust the mass flow rate and pressure to each indoor unit through electronic expansion valves and variable-speed compressors. This system can offer up to 30% energy savings compared to conventional HVAC systems like constant air volume systems [85]. However, VRF systems come with several challenges, particularly in control and piping complexity [86]. Heat-recovery VRF systems, while improving efficiency, add further complexity with intricate piping networks and heat recovery units, raising the risk of refrigerant leaks [87]. Proper refrigerant charge management is crucial, as both undercharging and overcharging can result in efficiency losses—up to 20% performance degradation with improper charge levels [88].

To achieve environmentally friendly space heating and cooling while leveraging the benefits of thermal networks, natural refrigerants like CO_2—featuring a global warming potential of 1 and zero ozone depletion potential [16]—are promising for use in these systems. Henchoz et al. [8], Weber and Favrat [9], and Henchoz [10] investigated CO_2-based district heating and cooling networks, showing that CO_2 outperforms conventional water loop systems by reducing exergy losses and requiring smaller pipe diameters. For instance, Weber and Favrat [9] found that using CO_2 reduces pipe diameter by up to 30% and achieves better exergy efficiency, while Henchoz [10] reported an 84.4% reduction in energy consumption when transitioning from conventional heating oil boilers and air-cooled compression chillers to a CO_2 district network in Geneva, Switzerland. More recently, Ungar et al. [11] showed that converting a real district heating network in Italy from water to low-temperature CO_2 increased electricity production by 39% compared to a conventional water loop system, due not only to lower condenser temperatures in the Organic Rankine cycle, but also to reduced pumping requirements and smaller pipe diameters.

As highlighted in the WLHP system, a single-pipe configuration simplifies the thermal network but introduces challenges, such as temperature fluctuations at local HPs, which degrade performance along the piping. In contrast, VRF systems, which use the direct flow of refrigerant for heating and cooling, do not face the issue of temperature fluctuations as in WLHP systems. However, they encounter challenges related to more complex control strategies and intricate piping networks. To overcome these issues and streamline refrigerant-based thermal networks, Eslami-Nejad et al. [12] proposed a novel thermal management approach called the CO_2 thermal network (CO_2TN), a secondary loop thermal network system that uses CO_2 as the HCF. In this design, a central loop circulates two-phase CO_2 at near-ambient temperature, acting as both a heat source and sink for local HPs that handle space heating and cooling. The two-phase nature of the CO_2-loop ensures a stable source temperature, which in turn maintains consistent efficiency and capacity for the local HPs. The single-pipe design of the CO_2TN also simplifies the piping network, offering a more compact solution for thermal energy management in building applications. It also incorporates high thermal energy density benefits of refrigerant HCFs offered by VRF systems. Bastani and Gholamrezaie [24] presented a prototype of the single-pipe CO_2TN and conducted experiments to evaluate its performance in transcritical operation. Their results demonstrated the existence of optimal control points for such a system, highlighting the need for a numerical model to further analyze system efficiency under different conditions and scales.

To evaluate the efficiency and optimize the operation of complex thermal networks such as CO_2TN, component-by-component modeling is highly beneficial. It enables a detailed understanding of the system's performance under various conditions (e.g., different building layouts, weather zones) and allows for assessing the impact of each component on the overall system performance. Moreover, this approach facilitates the development of effective control strategies to ensure the optimal operation of the system. Eslami-Nejad and Bastani [13] presented a preliminary investigation demonstrating the potential of a CO_2TN to enhance building energy performance. Their approach was based on a simplified energy balance method, with assumptions such as constant performance of the CO_2 circulation system. Building on this, Bastani and Eslami-Nejad [23] developed a numerical model in Matlab to simulate the system's application in office buildings, using a quasi-steady-state approach with hourly thermal load profiles and weather data. Heat exchanger models are overly simplified, treating the gas cooler as a single node, despite the system operating near the critical point, where rapid changes in CO_2 properties can lead to substantial calculation errors. Additionally, the study neglects the possibility of subcritical operation, leaving this area open for further investigation to develop a more realistic and accurate model for such systems. To further simplify the calculations, they fixed the pressure of the outdoor unit meaning the effect of outdoor temperature was not considered. Their work also lacks experimental validation, undermining its reliability.

Due to the unique characteristics of the CO_2 thermodynamic cycle and its properties, modeling CO_2-based systems presents significant challenges. Rapid variations in thermophysical properties, particularly near the pseudocritical line, necessitate the use of detailed models to accurately capture system behavior during transitions between transcritical and subcritical operations [89, 90]. Among the system components, compressors and heat exchangers are particularly challenging to model due to their complex interactions and sensitivity to changing operating conditions.

Compressors can be modeled at various levels of detail: black-box, gray-box, and white-box models [27]. Black-box models represent only numerical relationships between inputs and outputs without addressing physical phenomena. Gray-box models combine statistical relations with some fundamental equations to capture key physical processes. White-box models rely solely on fundamental equations to comprehensively describe all processes. Gabel and Bradshaw [91] evaluate the predictive accuracy of various compressor models under conditions including extrapolation, modulation (variable speed), and variable superheat. They assess the AHRI 540 standard, the most widely recognized black-box model with a 10-coefficient map [28], and several gray-box models. These gray-box models are more computationally efficient than white-box models, making them suitable for system simulations while offering greater fidelity than black-box models. The gray-box models used for comparison include those by Shao et al. [92], Popovic and Shapiro [93], and Winandy et al. [94]. Using detailed experimental data from four compressor types and multiple refrigerants, each model was trained on a baseline dataset and tested across subsets under different conditions. The gray-box models, particularly the Winandy et al. model, generally outperformed the AHRI model in extrapolation, achieving error rates below 5% for scroll and spool compressors. The AHRI model, while performing well within trained data, showed significant inaccuracies in extrapolation, with errors reaching 6.78%. This study highlights the limitations of purely empirical models like AHRI for dynamic conditions, suggesting that polynomial-based models trained on robust datasets are well-suited for stable conditions with lower computational costs, while gray-box models provide better accuracy in transient scenarios. Viviescas and Bernier [95] applied the AHRI model with a third-order polynomial and ten coefficients to model their compressor, achieving validation results with deviations below 9% from experimental data. In a follow-up study, they extended the AHRI 540 standard to variable-speed compressors, incorporating manufacturer-specific data in a third-order polynomial with three variables and 30 coefficients [33]. Their results indicated that adapting the AHRI model with more coefficients results in higher accuracy.

Heat exchanger models can vary depending on the thermodynamic region and the process in which they operate. A heat exchanger may operate above the critical point and function as a gas cooler, which cools down a single-phase, supercritical refrigerant. Alternatively, it can operate below the critical point, where cooling the refrigerant involves three thermodynamic regions: the superheated region, the two-phase region, and the sub-cooled region, all under the condenser model. When the system needs to absorb energy, the heat exchanger operates as an evaporator. The gas cooler model presents significant challenges as it operates in the supercritical region, often near the critical point, where small changes in refrigerant exit temperature can cause large enthalpy shifts [19]. Yin et al. [96] utilized a 1-D finite element method to model a transcritical CO_2 gas cooler, achieving a prediction accuracy for gas cooler capacity within $\pm 2\%$ and pressure drop within the experimental error range. The finite element method was selected specifically to manage the rapid variations in thermophysical properties near the critical point, allowing precise optimization across multi-pass and multi-slab configurations. Similarly, Sánchez et al. [97] developed and validated a 1-D finite element model for a water-to-CO_2 coaxial gas cooler, examining the effects of various parameters on its thermal effectiveness. Their findings revealed that the $\epsilon - NTU$ method consistently over-predicted thermal effectiveness, reinforcing the value of more detailed modeling approaches. Cecchinato et al. [68] also adopted a finite volume model to determine optimal heat rejection pressure in CO_2 systems. Their results highlighted the sensitivity of refrigerant outlet temperature to secondary fluid properties and heat exchanger geometry, emphasizing that discretized models better capture these dependencies than simplified methods. The modeling of condensers and evaporators can be broadly categorized into three types, as described in the literature [98, 99]: lumped parameter models, moving boundary models, and segment-by-segment (distributed parameter) models. Among these, the lumped parameter model is the simplest, employing a single-node approach, and is not suitable for modeling phase change transitions. The moving boundary method is computationally efficient and fast, making it suitable for modeling phase transitions in different heat exchangers [41, 100, 101]. In this approach, the heat exchanger is divided into a minimum number of zones (typically up to three), representing regions where the refrigerant exists as superheated vapor, saturated mixture, and subcooled liquid. Each zone is solved using the lumped parameter approach, combining computational simplicity with the capability to model phase transitions. Experimental studies on chevron plate heat exchangers using CO_2 as the refrigerant have shown that dividing the heat exchanger into three zones results in less than 10% error in heat transfer predictions compared to experimental data [39]. The segment-by-segment method, on the other hand, divides the heat exchanger into multiple nodes and can achieve higher accuracy, but at the cost of significantly higher computational effort [43].

This study extends our previous preliminary work, which began with the development of a numerical model using hourly thermal load profiles and weather data. The initial model incorporated the thermal capacitance of building zones and was tailored for heating-dominant operation modes with simplified component representations [75]. Building on that, we developed a more comprehensive model capable of handling both heating and cooling modes with more detailed component modeling [76]. The aim of the present study is to introduce a comprehensive quasi-transient numerical model that operates across all modes (heating-dominant, cooling-dominant, and balanced), with detailed models for each component and experimental validation at both the component and system levels. This model supports hourly simulations to evaluate system performance and is adaptable to various building configurations, outdoor unit designs, and component sizes, enabling analysis across diverse conditions.

4.3 System Description

The CO_2 thermal network consists of a circulation system, a desuperheater (DSPHTR), an outdoor unit (OU), and local units equipped with heat pumps (HPs), as illustrated in Figure 4.1. The CO_2 circulation system operates as a reversible vapor compression cycle (RVCC) and incorporates a variable-speed compressor, an internal heat exchanger (IHE), electronic expansion valves (EEVs), pressure regulating valves (PRVs), and reversing valves (RVs). The system's primary role is to supply CO_2 with the appropriate mass flow rate and vapor quality based on the building's thermal demand. The DSPHTR and the OU exchange heat with thermal energy sources to balance the thermal system. The DSPHTR specifically reduces the temperature of the hot gas while preheating domestic water. The OU adapts its function based on system requirements to thermally balance the cycle, operating as a gas cooler, condenser, or evaporator. Two-phase CO_2 is then transported via a single pipe (green line in Figure 4.1), known as the "CO_2-loop", to the source side of local heat pumps (HPs) located in each building zone. These local HPs maintain comfort in their respective zones by either rejecting or absorbing heat as required. The two-phase CO_2 remains at a nearly constant temperature (around 20°C), ensuring a stable source temperature for all local HPs.

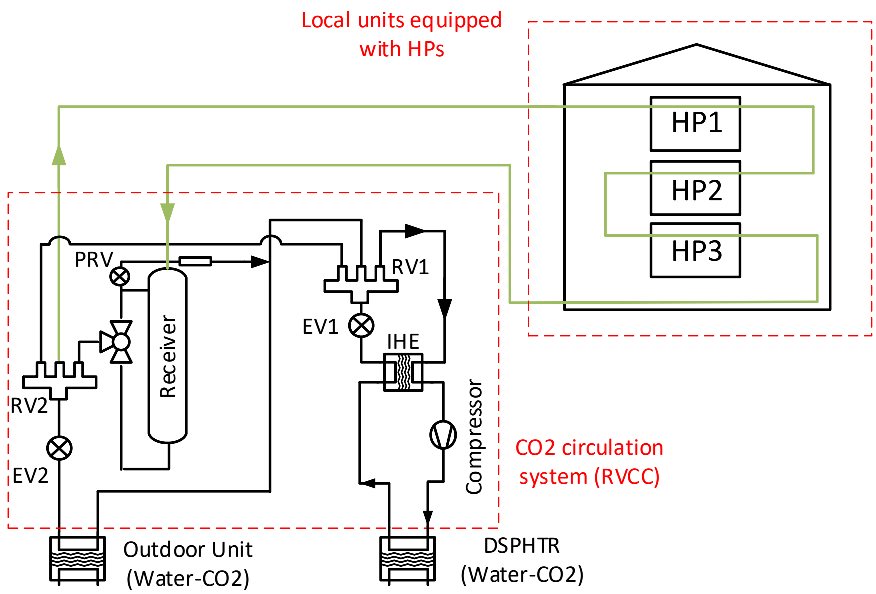

Figure 4.1 Process flow diagram

The system can operate in three modes: heating mode (subdivided into heating-only and heating-dominant modes), cooling mode (including cooling-only and cooling-dominant modes), and balanced mode. These modes are defined by the net heat exchange within the CO_2-loop via the local HPs. A net heat rejection into the CO_2-loop indicates cooling mode, while net heat absorption indicates heating mode. When heat rejection and absorption are balanced, the system operates in balanced mode.

4.3.1 Cooling mode

In cooling mode, the system operates with two pressure levels, functioning either in a transcritical or subcritical cycle. Figure 4.2 illustrates the pressure-enthalpy diagram for the system when operating in the transcritical cycle. Starting at point 1, the compressor raises the CO_2 pressure to a high level suitable for heat exchange on the high-pressure side (point

2). Between points 2 and 3, the DSPHTR cools the CO_2 while preheating water for domestic use. Next, the IHE (points 3 to 4) transfers heat to ensure sufficient superheat at the compressor suction (points 7 to 1). From points 4 to 5, the OU further reduces the CO_2 temperature before expansion to the CO_2-loop (points 5 to 6). The vapor quality at point 6 is adjusted by controlling the outlet state at point 5 to ensure that CO_2 remains in a two-phase state after passing through each local HP. From Point 6, if the local HP is operating in heating mode, the CO_2 undergoes condensation. Conversely, if the local HP is in cooling mode, which is the primary scenario, the CO_2 evaporates before reaching Point 7. Note that the horizontal dashed line indicates that if some local HPs are operating in heating mode, they absorb heat from the CO_2-loop, leading to CO_2 condensation. As a result, the CO_2 may cool further, potentially reaching a state below point 6 and continuing to the saturated liquid phase. However, since the system operates in a cooling-dominant mode, the remaining HPs reject heat to the CO_2-loop, causing the CO_2 to evaporate until it reaches point 7, where it exits the loop.

4.3.2 Heating mode

In heating-dominant mode, the system operates at three pressure levels, functioning either in a transcritical or subcritical cycle. Figure 4.3 illustrates the pressure-enthalpy diagram for the system when operating in the transcritical cycle. The process begins at point 1, where the compressor raises the CO_2 pressure to a high level suitable for heat exchange on the high-pressure side (point 2). Between points 2 and 3, the DSPHTR cools the CO_2 while preheating water for domestic use. Next, the IHE (points 3 to 4) transfers heat to ensure sufficient superheat at the compressor suction (points 10 to 1). From point 4 to point 5, the CO_2 undergoes expansion before entering the CO_2-loop at point 5. The horizontal dashed line in the figure indicates that if a local HP operates in cooling mode, it causes the CO_2 to evaporate, potentially leading to enthalpies even higher than at point 5. Since this is a heating-dominant mode, most local HPs absorb heat from the CO_2-loop, causing the CO_2 to condense. Then, a receiver separates the liquid phase (point 6_l) from any remaining vapor (point 6_v). The liquid then expands to the OU (from point 6_l to point 7), while the vapor in the receiver is flashed and directed to the suction line. The OU, functioning as an evaporator in this scenario, absorbs heat (from point 7 to point 8), converting the CO_2 into saturated vapor. Finally, this saturated vapor mixes with the flashed vapor from the receiver at point 10, where the combined flow enters the IHE to absorb the required heat, achieving the specified superheat at the compressor suction (point 1).

It is worth noting that this setup also supports operation at two pressure levels: the high-

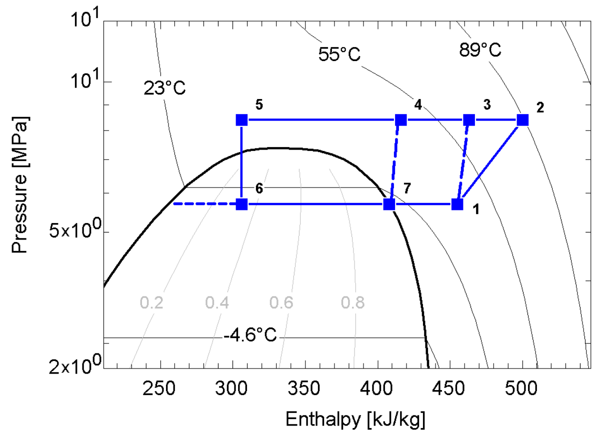

Figure 4.2 Pressure-enthalpy diagram: cooling-dominant mode

pressure side corresponds to the CO_2-loop, and the low-pressure side corresponds to the OU (evaporator). This occurs when the enthalpy at point 5 is set to saturated vapor, and the DSPHTR can exchange heat at the loop pressure.

4.4 Model

A modular approach is used to model the system, including the local heat pumps (HPs), the circulation compressor, and heat exchangers. A water-to-CO_2 heat exchanger model is developed for the desuperheater (DSPHTR), gas cooler (GC), condenser (COND), and evaporator (EVAP), and a CO_2-to-CO_2 heat exchanger model is developed for the internal heat exchanger (IHE).

4.4.1 Local heat pumps (HPs)

A linear regression is applied to capture the HP capacity and power consumption as functions of the source-side CO_2 temperature, derived from experimental data on modified CO_2-to-air HPs. These data, specifically from studies by Gholamrezaie et al. [77] and experiments conducted at CanmetENERGY (Varennes), Canada, provide the basis for the linear regressions. For the heating mode, six independent tests were conducted on the laboratory test bench with the loop temperature varied between 10 °C and 30 °C. The resulting linear fits for both heating capacity and COP showed good agreement, with coefficients of determination of $R^2 = 99.69\%$ and $R^2 = 99.90\%$, respectively. For the cooling mode, the experimental dataset covers loop temperatures from 5 °C to 25 °C, yielding $R^2 = 98.69\%$ for the capacity

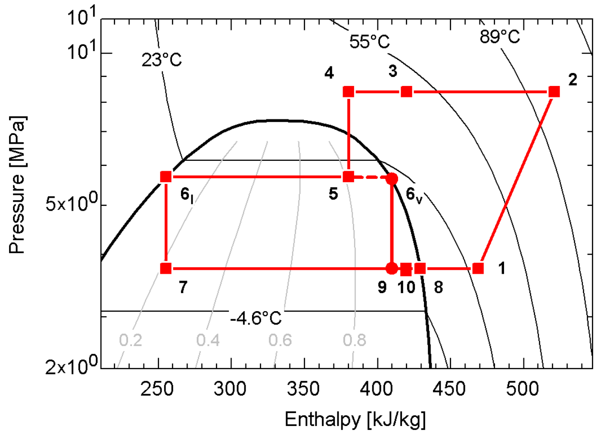

Figure 4.3 Pressure-enthalpy diagram: heating-dominant mode

regression and $R^2 = 99.68\%$ for the COP regression. The local HP correlations are expressed as:

$$\begin{cases} \dot{Q}_{\text{HP,C}} = -23.22 \cdot T_{CO_2} + 3304.48 \\ \dot{Q}_{\text{HP,H}} = 84.79 \cdot T_{CO_2} + 2055.32 \end{cases} \tag{4.1}$$

$$\begin{cases} \text{COP}_{\text{HP,C}} = -0.08 \cdot T_{CO_2} + 5.04 \\ \text{COP}_{\text{HP,H}} = 0.050 \cdot T_{CO_2} + 2.77 \end{cases} \tag{4.2}$$

$$\dot{W}_{\text{HP}} = \frac{\dot{Q}_{\text{HP}}}{\text{COP}_{\text{HP}}} \tag{4.3}$$

where T_{CO_2} is the source-side CO_2 temperature (°C), constant along the CO_2-loop. $\dot{Q}_{\text{HP}}$, COP_{HP}, and $\dot{W}_{\text{HP}}$ represent the HP capacity (W), coefficient of performance, and power consumption (W), respectively. The subscripts H and C denote the parameters related to the HP operating in heating and cooling modes, respectively. An energy balance on the HP enables the evaluation of the outlet enthalpy of CO_2.

In heating mode:

$$\dot{Q}_{\text{HP,H,i}} - \dot{W}_{\text{HP,i}} = \dot{m}_{CO_2} \cdot (h_{HP,in,i} - h_{HP,out,i}) \tag{4.4}$$

where $h_{HP,in,i}$ and $h_{\text{HP,out},i}$ represent the inlet and outlet enthalpies of CO_2 for the i-th heat pump, respectively.

In cooling mode:

$$\dot{Q}_{\text{HP,C,i}} + \dot{W}_{\text{HP,i}} = \dot{m}_{CO_2} \cdot (h_{HP,out,i} - h_{HP,in,i}) \tag{4.5}$$

Note that the thermodynamic relationships between CO_2 pressure, temperature, quality, and enthalpy are calculated using COOLPROP [102], which employs the Span-Wagner equation of state [103].

For implementation, the model is adapted from TRNSYS Type 919, which was originally developed for water-to-air HPs, to accommodate two-phase CO_2 as the heat transfer fluid. This modified Type receives user-provided catalog data files containing normalized capacity and power values for the HPs, derived from the polynomial expressions in Eqs. 4.1 to 4.3. In this modified version, source-side inputs—CO_2 mass flow rate, enthalpy, and pressure—are provided, while output values are calculated using energy balance equations outlined in Eqs. 5.10 and 5.11.

4.4.2 Compressor

The compressor model utilized in this study is an enhanced version of the model introduced by Gholamrezaie et al. [76]. It is based on a third-order polynomial fitted to the manufacturer's data for a semi-hermetic reciprocating compressor with R744 refrigerant. The model uses suction pressure (P_{suc}) in MPa, discharge pressure (P_{dis}) in MPa, and compressor speed (S) in Hertz as inputs to calculate the compressor's power input ($\dot{W}_{comp}$) in kW and the CO_2 mass flow rate ($\dot{m}_{CO_2}$) in kg/hr. To develop the model, a total of 100 data points were used, all within the compressor's operating envelope, covering compressor speeds from 30 to 75 Hz, discharge pressures (P_{dis}) from 6 to 12 MPa, and suction pressures (P_{suc}) from 2 to 5.8 MPa. For $\dot{W}_{comp}$, the root mean square (RMS) error is 0.137 kW, and the coefficient of determination (R^2) is 99.42%; for $\dot{m}_{CO_2}$, the RMS error is 4.57 kg/hr, and R^2 is 99.94%. The equation governing the compressor model is as follows:

$$
\begin{aligned}
X = {} & a_1 + a_2 \cdot S + a_3 \cdot S^2 + a_4 \cdot S^3 + a_5 \cdot P_{dis} + a_6 \cdot P_{dis}^2 + a_7 \cdot P_{dis}^3 \\
& + a_8 \cdot P_{suc} + a_9 \cdot P_{suc}^2 + a_{10} \cdot P_{suc}^3 + a_{11} \cdot S \cdot P_{dis} + a_{12} \cdot S \cdot P_{dis}^2 \\
& + a_{13} \cdot S \cdot P_{suc} + a_{14} \cdot S \cdot P_{suc}^2 + a_{15} \cdot S^2 \cdot P_{dis} + a_{16} \cdot S^2 \cdot P_{dis}^2 \\
& + a_{17} \cdot S^2 \cdot P_{suc} + a_{18} \cdot S^2 \cdot P_{suc}^2 + a_{19} \cdot P_{dis} \cdot P_{suc} + a_{20} \cdot P_{dis} \cdot P_{suc}^2 \\
& + a_{21} \cdot P_{dis}^2 \cdot P_{suc} + a_{22} \cdot P_{dis}^2 \cdot P_{suc}^2
\end{aligned} \tag{4.6}
$$

where X can be the power input or the mass flow rate based on the constants defined in Table 4.1.

To calculate the state of CO_2 at discharge of the compressor, the work and the mass flow rate of CO_2 from the compressor are determined using Eq. 4.6 and then substituted into the

Table 4.1 Compressor model coefficients

Coefficient	Value (Power input)	Value (Mass flow rate)
a_1	2.39E+01	3.43E+02
a_2	7.30E-02	7.36E+00
a_3	-8.74E-04	-7.70E-02
a_4	-1.99E-06	2.37E-04
a_5	-5.91E-03	-1.11E-01
a_6	2.93E-07	7.35E-06
a_7	6.68E-13	-6.93E-11
a_8	-1.03E-02	-1.84E-01
a_9	1.01E-06	2.79E-05
a_{10}	4.82E-13	-6.32E-10
a_{11}	3.05E-05	1.70E-04
a_{12}	-1.51E-09	-3.16E-08
a_{13}	-8.50E-05	-1.30E-03
a_{14}	9.62E-09	3.81E-07
a_{15}	-1.76E-07	-3.76E-06
a_{16}	1.28E-11	3.07E-10
a_{17}	9.25E-07	2.43E-05
a_{18}	-1.07E-10	-2.40E-09
a_{19}	2.73E-06	4.41E-05
a_{20}	-2.91E-10	-5.51E-09
a_{21}	-1.41E-10	-2.31E-09
a_{22}	1.57E-14	2.76E-13

following equation.

$$\dot{W}_{comp} = \dot{m}_{CO_2} \cdot (h_{dis} - h_{suc}) \tag{4.7}$$

where h_{dis}, and h_{suc} are the discharge and suction enthalpy respectively.

4.4.3 Water-to-CO_2 heat exchanger

The water-to-CO_2 plate heat exchanger is used for the outdoor unit (OU) (serving as gas cooler (GC), condenser (COND), and evaporator (EVAP)) as well as for the desuperheater (DSPHTR). The heat carrier fluid in the heat exchangers is water mixed with 30% glycol, which flows in a counter-flow configuration to exchange heat with CO_2 within the plate heat exchangers. Depending on the thermodynamic region where CO_2 operates, different models are used to simulate the heat exchanger. Three models are applied based on the heat exchanger's working pressure: one for the supercritical and superheated regions (covering the GC and the DSPHTR) and two for the subcritical region (COND and EVAP models). The heat exchangers are considered adiabatic and pressure drop is neglected. To implement the model, CO_2 pressure, inlet enthalpy, and mass flow rate, as well as the inlet water temperature and mass flow rate, are used as inputs, while the model outputs the CO_2 enthalpy and pressure at the heat exchanger outlet and the water outlet temperature.

Supercritical or superheated regions

In the supercritical and superheated regions, the thermophysical properties of CO_2 change rapidly, making it essential to discretize the heat exchanger for modeling, as recommended in the literature. As illustrated in Figure 4.4, the heat exchanger is divided into n cells. At each cell, the water-glycol properties are assumed constant and equal to the properties at the downstream node of the cell, while the CO_2 properties are calculated using COOLPROP [102] with the Span-Wagner equation of state [103].

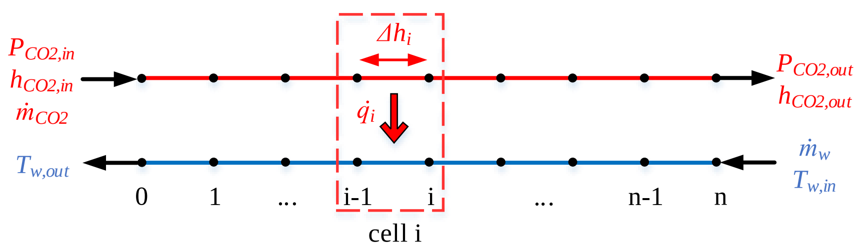

Figure 4.4 Discretized heat exchanger model

The model is governed by energy balance equations for both CO_2 and water-glycol, with the heat transfer rate $\dot{q}_i$ at each cell (from $i = 1$ to $i = n$) described by three equations: the CO_2 energy balance, the water energy balance, and the heat transfer equation between CO_2 and water-glycol:

$$\dot{q}_i = \dot{m}_{CO_2} \cdot (h_{CO_2,i-1} - h_{CO_2,i}) \tag{4.8}$$

$$\dot{q}_i = \dot{m}_w \cdot c_{p,w} \cdot (T_{w,i} - T_{w,i-1}) \tag{4.9}$$

$$\dot{q}_i = U_i \cdot \frac{A}{n} \cdot (T_{CO_2,i} - T_{w,i-1}) \tag{4.10}$$

where $\dot{m}_{CO_2}$ is the mass flow rate of CO_2, and $h_{CO_2,i}$ is the specific enthalpy at node i, $\dot{m}_w$ is the mass flow rate of water, $c_{p,w}$ is the specific heat capacity, $T_{w,i}$ is water temperatures at node i, U_i is the heat transfer coefficient of the heat exchanger at cell i, and A is the overall heat transfer area.

The total heat transfer rate across the heat exchanger is the sum of heat transferred across all cells:

$$\dot{Q} = \sum_{i=1}^{n} \dot{q}_i \tag{4.11}$$

where $\dot{Q}$ is the total heat transfer in the heat exchanger. To complete the system of equations, the model uses the following boundary conditions: $h_{CO_2,0} = h_{CO_2,in}$ and $T_{w,n} = T_{w,in}$, where $h_{CO_2,in}$ and $T_{w,in}$ are the inlet CO_2 enthalpy and water temperature to the heat exchanger, respectively.

Based on the experimental study conducted by Kim and Park [104], the correlation proposed by Wanniarachchi et al. [105] for chevron-type plate heat exchangers is chosen to calculate the CO_2 heat transfer coefficient ($\alpha_{CO_2,i}$) at each cell i:

$$m = 0.646 + 0.0011 \cdot (90 - \beta) \tag{4.12}$$

$$Nu_{t,i} = 12.6 \cdot \phi^{(1-m)} \cdot Re_i^m \cdot (90 - \beta)^{-1.14} \tag{4.13}$$

$$Nu_{l,i} = 3.65 \cdot \phi^{0.66} \cdot Re_i^{0.33} \cdot (90 - \beta)^{-0.45} \tag{4.14}$$

$$Nu_i = \left(Nu_{t,i}^3 + Nu_{l,i}^3\right)^{\frac{1}{3}} \cdot Pr_i^{\frac{1}{3}} \tag{4.15}$$

$$\alpha_{CO_2,i} = \frac{Nu_i \cdot k_{CO_2,i}}{D_h} \tag{4.16}$$

where Nu_i is the local Nusselt number in cell i, $k_{CO_2,i}$ is the thermal conductivity of CO_2, β is the chevron angle of the plate heat exchanger, and ϕ is the enlargement factor.
The hydraulic diameter D_h [48], Reynolds number Re_i and Prandtl number Pr_i are defined as follows:

$$D_h = \frac{2b}{\phi} \tag{4.17}$$

$$Re_i = \frac{\dot{m}_{CO_2} \cdot D_h}{\mu_{CO_2,i} \cdot b \cdot W \cdot NC} \tag{4.18}$$

$$Pr_i = \frac{c_{p,CO_2,i} \cdot \mu_{CO_2,i}}{k_{CO_2,i}} \tag{4.19}$$

where $c_{p,CO_2,i}$ is the specific heat capacity of CO_2 in cell i (evaluated using the properties at node i), $\mu_{CO_2,i}$ is the dynamic viscosity of CO_2, b is the corrugation depth, W is the width of the plate heat exchanger, and NC is the number of channels.

The water heat transfer coefficient, α_w, is given by [106]:

$$Nu = \frac{\alpha_w D_h}{k_w} = 0.6701 \cdot {Re_w}^{0.5195} \cdot {Pr_w}^{\frac{1}{3}} \tag{4.20}$$

where Re_w and Pr_w are the Reynolds number and the Prandtl number on the water side, respectively.

The overall heat transfer coefficient at each cell is given by:

$$U_i = \frac{1}{\alpha_{CO_2,i}} + \frac{1}{\alpha_w} + \frac{t}{k_{PHX}} \tag{4.21}$$

where t and k_{PHX} are the thickness and thermal conductivity of the heat exchanger, respectively.

To solve the system of equations governing the heat exchanger, an explicit finite difference method was employed. The heat exchanger was discretized into n cells along the CO_2 flow direction, enabling the calculation of CO_2 and water temperatures at each node. At each iteration (k), the enthalpy of CO_2 ($h_{CO_2,i}$) and its corresponding temperature ($T_{CO_2,i}$) were updated using an explicit energy balance:

$$h^{(k)}_{CO_2,i} = h^{(k)}_{CO_2,i-1} - \frac{U_i^{(k-1)} \cdot \frac{A}{n} \cdot \left(T^{(k-1)}_{CO_2,i} - T^{(k-1)}_{w,i-1}\right)}{\dot{m}_{CO_2}} \tag{4.22}$$

The water-side temperature ($T_{w,i-1}$) was similarly updated at each iteration:

$$T^{(k)}_{w,i-1} = T^{(k)}_{w,i} + \frac{U_i^{(k-1)} \cdot \frac{A}{n} \cdot \left(T^{(k)}_{CO_2,i} - T^{(k-1)}_{w,i-1}\right)}{\dot{m}_w \cdot c_{p,w}} \tag{4.23}$$

Convergence was determined using two criteria. The first assessed the stability of the CO_2 temperature profile by evaluating the maximum difference between temperatures in successive iterations to ensure that the temperature distribution had reached a consistent state:

$$\max_k |T^{(k)}_{\mathrm{CO_2}} - T^{(k-1)}_{\mathrm{CO_2}}| < \text{tolerance(T)} \tag{4.24}$$

The second criterion verified the energy balance between the heat released or absorbed by CO_2 and the heat exchanged by the water-glycol mixture:

$$\max_i |\frac{(\dot{m}_{CO_2} \cdot (h_{CO_2,i-1} - h_{CO_2,i})) - (\dot{m}_w \cdot c_{p,w} \cdot (T_{w,i} - T_{w,i-1}))}{\dot{m}_{CO_2} \cdot (h_{CO_2,i-1} - h_{CO_2,i})}| < \text{tolerance}(\dot{q}) \tag{4.25}$$

Iterations continued until both criteria met their respective tolerance limits, defined in this study as tolerance(T) $= 0.1$°C and tolerance($\dot{q}$) $= 0.01$.

Subcritical region

Two models are introduced for the subcritical region: a condenser model and an evaporator model. The condenser model uses the moving boundary method, as described by Hayes et al. [39], to capture the heat transfer process in a plate heat exchanger when the discharge pressure is below the critical pressure. This method divides the condenser into three regions—superheated, two-phase, and subcooled—based on the CO_2 inlet enthalpy relative to its saturation states shown on Figure 4.5.

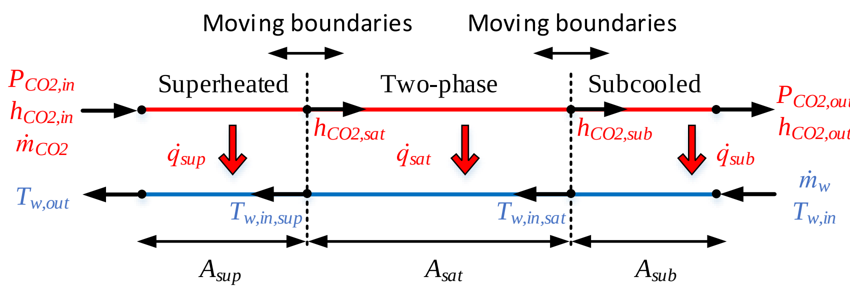

Figure 4.5 Moving boundary heat exchanger model

In the steady-state condenser model, the refrigerant transitions through three regions: superheated vapor, two-phase condensation, and subcooled liquid. The boundaries between these regions are fixed for a given operating condition, determined by the refrigerant's thermodynamic properties and heat transfer conditions. The heat removed in each region is calculated using an energy balance and the effectiveness-NTU (ϵ-NTU) method. For the superheated region, the heat removed is:

$$\dot{q}_{sup} = \dot{m}_{CO_2} \cdot (h_{CO_2,in} - h_{CO_2,sat}) \tag{4.26}$$

$$\dot{q}_{sup} = \epsilon_{sup} \cdot C_{\min,sup} \cdot (T_{CO_2,in} - T_{w,in,sup}) \tag{4.27}$$

where:

$$\mathrm{NTU}_{sup} = \frac{U_{sup} \cdot A_{sup}}{C_{min,sup}}, \quad \epsilon_{sup} = \frac{1 - \exp[-\mathrm{NTU}_{sup}(1 - C_r)]}{1 - C_r \exp[-\mathrm{NTU}_{sup}(1 - C_r)]} \quad C_r = \frac{C_{min,sup}}{C_{max,sup}} \tag{4.28}$$

where $h_{CO_2,in}$ and $h_{CO_2,sat}$ are the CO_2 inlet enthalpy and CO_2 saturated vapor enthalpy, respectively. ϵ_{sup}, NTU_{sup}, and C_r are the effectiveness, number of transfer units, and heat capacity rate ratio, respectively. U_{sup} is the heat transfer coefficient for superheated CO_2 in the plate heat exchanger and is calculated using Eqs. 4.12 to 4.21, using constant thermodynamic properties for CO_2 equal to the inlet properties. C_{min}, and C_{max} are the minimum and maximum amount between ($\dot{m}_{CO_2} \cdot c_{p,CO_2}$) and ($\dot{m}_w \cdot c_{p,w}$). $T_{CO_2,in}$ and $T_{w,in,sup}$ are the inlet temperature to the superheated section of the heat exchanger.

In the two-phase region, the heat transfer required for complete CO_2 condensation from saturated vapor to saturated liquid is calculated as follows:

$$\dot{q}_{sat} = \dot{m}_{CO_2} \cdot (h_{CO_2,sat} - h_{CO_2,sub}) \tag{4.29}$$

where $h_{CO_2,sub}$ is the CO_2 saturated liquid enthalpy at the discharge pressure. The calculated $\dot{q}_{sat}$ from Equation 4.29 is then substituted into the following equation to calculate the required area for full condensation:

$$\dot{q}_{sat} = \epsilon_{sat} \cdot C_{\min,sat} \cdot (T_{CO_2,sat} - T_{w,in,sat}) \tag{4.30}$$

where

$$\mathrm{NTU}_{sat} = \frac{U_{sat} \cdot A_{sat}}{C_{min,sat}}, \quad \epsilon_{sat} = 1 - \exp(-\mathrm{NTU}_{sat}) \tag{4.31}$$

where U_{sat} is the heat transfer coefficient for saturated CO_2 in the plate heat exchanger and is considered constant and $T_{CO_2,sat}$ and $T_{w,in,sat}$ are the CO_2 saturation temperature and the inlet water temperature to the saturated section, respectively. Note that U_{sat} is determined by applying the heat transfer coefficient correlations from Yan et al. [107] to Equation 4.21:

$$\overline{Nu} = \frac{\overline{\alpha}_{CO_2} D_h}{k_{CO_2,l}} = 4.118 \cdot Re^{0.4} \cdot Pr_l^{\frac{1}{3}} \tag{4.32}$$

where $\overline{\alpha}_{CO_2}$ is the average heat transfer coefficient for CO_2, and Re and Pr_l represent the Reynolds and Prandtl numbers as follows:

$$Re = \frac{G_{eq} D_h}{\mu_l}, \quad G_{eq} = G\left[1 - x_m + x_m \left(\frac{\rho_l}{\rho_v}\right)^{1/2}\right], \quad G = \frac{\dot{m}_{\mathrm{CO_2}}}{b \cdot W \cdot NC} \tag{4.33}$$

where G is the mass flux, x_m is the arithmetic mean of the inlet and outlet CO_2 quality, and the subscripts v and l refer to saturated vapor and liquid properties, respectively.

$$Pr_l = \frac{c_{p,CO_2,l} \cdot \mu_{CO_2,l}}{k_{CO_2,l}} \tag{4.34}$$

After calculating the required area for complete condensation (A_{sat}), this value is compared with the available area ($A - A_{sup}$). If the available area in the two-phase region is sufficient for complete condensation to saturated liquid, the remaining heat exchanger area ($A - A_{sup} - A_{sat}$)

is used for subcooling. However, if the area required for complete condensation exceeds the available area after the desuperheating section, the CO_2 outlet state is determined by substituting $A_{sat} = A - A_{sup}$ into Equation 4.30.

In the subcooled region (if $A - A_{sup} - A_{sat} > 0$), the heat removed is:

$$\dot{q}_{sub} = \dot{m}_{CO_2} \cdot (h_{CO_2,sub} - h_{CO_2,out}) \tag{4.35}$$

$$\dot{q}_{sub} = \epsilon_{sub} \cdot C_{min,sub} \cdot (T_{CO_2,sub} - T_{w,in,sub}) \tag{4.36}$$

where:

$$\mathrm{NTU}_{sub} = \frac{U_{sub} \cdot A_{sub}}{C_{\min,sub}}, \quad \epsilon_{sub} = \frac{1 - \exp[-\mathrm{NTU}_{sub}(1 - C_r)]}{1 - C_r \exp[-\mathrm{NTU}_{sub}(1 - C_r)]}, \quad C_r = \frac{C_{min,sub}}{C_{max,sub}} \tag{4.37}$$

where U_{sub} is the heat transfer coefficient for single-phase subcooled CO_2 in the plate heat exchanger and is calculated using Eqs. 4.12 to 4.21, using constant thermodynamic properties for CO_2 equal to the inlet properties to the subcooled region.

The total heat exchanger area is the sum of the areas for the superheated, two-phase, and subcooled regions:

$$A = A_{sup} + A_{sat} + A_{sub} \tag{4.38}$$

For the evaporator, the heat transfer rate is calculated using the $\epsilon - NTU$ method:

$$\dot{q} = \epsilon \cdot C_{min} \cdot (T_{w,in} - T_{CO_2,in}) \tag{4.39}$$

$$\dot{q} = \dot{m}_{CO_2} \cdot (h_{CO_2,out} - h_{CO_2,in}) \tag{4.40}$$

$$\dot{q} = \dot{m}_w \cdot c_{p,w} \cdot (T_{w,in} - T_{w,out}) \tag{4.41}$$

where

$$\epsilon = 1 - \exp\left(-\mathrm{NTU}\right), \quad \mathrm{NTU} = \frac{U_{evap} \cdot A}{C_{min}} \tag{4.42}$$

The overall heat transfer coefficient U_{evap} is calculated using empirical correlations for CO_2 evaporation. The heat transfer coefficient for CO_2 in plate heat exchangers is determined using the following correlation [108]:

$$\overline{Nu} = \frac{\overline{\alpha}_{\mathrm{CO_2}} D_h}{k_{\mathrm{CO_2}}} = 98.7 \cdot \left(\left(\frac{Re_v}{Re_l} \right)^{-0.0848} \right) \cdot \left(Bo^{-0.0597} \right) \cdot \left(X_{tt}^{0.0973} \right) \tag{4.43}$$

where X_{tt} is the Martinelli parameter:

$$X_{tt} = \left(\frac{1 - x_m}{x_m}\right)^{0.87} \cdot \left(\frac{\rho_v}{\rho_l}\right)^{0.5} \cdot \left(\frac{\mu_l}{\mu_v}\right)^{0.12} \tag{4.44}$$

where Reynolds number (Re) and Boiling number (Bo) are defined as follows:

$$Re = \frac{G \cdot D_h}{\mu}, \quad Bo = \frac{\dot{q}}{A \cdot G \cdot h_{\mathrm{fg}}} \tag{4.45}$$

4.4.4 $\mathbf{CO_2}$-$\mathbf{CO_2}$ heat exchanger

The CO_2-to-CO_2 heat exchanger considered in this study is the internal heat exchanger (IHE). Its primary function is to provide sufficient superheat at the compressor suction by absorbing heat from the high pressure side (discharge of the compressor). This heat exchanger is not modeled in detail since both the suction and discharge sides involve single-phase CO_2 vapor. For simplicity, it is assumed that the IHE extracts the necessary heat from the compressor discharge to maintain a specific superheat at the compressor suction. The suction-side heat transfer relation is expressed as:

$$\dot{Q}_{IHE,suc} = \dot{m}_{CO_2} \cdot (h_{IHE,out,suc} - h_{IHE,in,suc}) \tag{4.46}$$

where $h_{IHE,in,suc}$ and $h_{IHE,out,suc}$ represent the enthalpy at the inlet and outlet of the IHE suction side, respectively The discharge-side heat transfer relation is:

$$\dot{Q}_{IHE,dis} = \dot{m}_{CO_2} \cdot (h_{IHE,in,dis} - h_{IHE,out,dis}) \tag{4.47}$$

where $h_{IHE,in,dis}$ and $h_{IHE,out,dis}$ represent the enthalpy at the inlet and outlet of the IHE discharge side, respectively. The energy balance across the internal heat exchanger is given by:

$$\dot{Q}_{IHE,dis} = \dot{Q}_{IHE,suc} \tag{4.48}$$

This balance ensures that the heat absorbed on the suction side is equal to the heat released on the discharge side, conserving energy across the internal heat exchanger.

4.5 Model Assembly

4.5.1 Mathematical Assembly

To mathematically assemble CO_2TN, the system is divided into two main sections: RVCC and components exchanging heat with the external environment. The RVCC is responsible for the circulation of CO_2 and includes the compressor, internal heat exchanger (IHE), reversing valves (RV), pressure regulating valves (flash gas bypass valve - PRV), expansion valves (EV), and the CO_2 receiver. External components include local HPs, the desuperheater (DSPHTR), and the outdoor unit (OU). This division enables a modular approach, where the system's operation is captured through its pressure, enthalpy, and mass flow at the inlet and outlet of each component.

Figure 4.6 and Figure 4.7 illustrate the process flow diagrams for the cooling-dominant mode and the heating-dominant mode, respectively. The CO_2 flow begins in the RVCC, where the compressor initiates circulation from point 1 to point 2. The CO_2 is then directed to the DSPHTR. At the DSPHTR, CO_2 transfers heat to the water side, with inlet properties ($P_{CO_2,in} = P_2 = P_{dis}$, $h_{CO_2,in} = h_2 = h_{dis}$) and water-side boundary conditions ($T_{w,in} = T_{w,in,DSPHTR}$, $\dot{m}_w = \dot{m}_{w,DSPHTR}$). After heat exchange, the CO_2 returns to the RVCC for further distribution based on the system's operational mode.

In the cooling-dominant mode, CO_2 flows from the DSPHTR back to the RVCC at point 3, where it enters the IHE to supply the required heat at the compressor suction ($P_3 = P_2$, $h_3 = h_{IHE,in,dis} = h_{DSPHTR,out}$). At point 4, the CO_2 is directed to the OU, where it undergoes additional heat rejection ($P_4 = P_3$, $h_4 = h_{IHE,out,dis} = h_{OU,in}$). Depending on the CO_2 pressure at the OU inlet, the gas cooler model is applied if $P_4 > 7.4\,\text{MPa}$, whereas the condenser model is used for lower pressures. The water-side boundary conditions at the OU ($T_{w,in} = T_{w,in,OU}$, $\dot{m}_w = \dot{m}_{w,OU}$) dictate the heat transfer process. After leaving the OU at point 5 ($P_5 = P_4$, $h_5 = h_{OU,out}$), the CO_2 flows back to the RVCC. Inside the RVCC, the CO_2 passes through EV2, where it expands to the loop pressure ($P_6 = P_{CO_2-loop}$) in an isenthalpic process ($h_5 = h_6$) before being distributed to the local HPs. At point 6, the CO_2 exits the RVCC and enters the first HP (HP1), with inlet properties ($P_{HP,in,1} = P_6$, $h_{HP,in,1} = h_6$). The outlet of HP1 becomes the inlet for the next heat pump, and this sequence continues through all the local HPs ($P_{HP,in,i} = P_{HP,out,i-1} = P_6$, $h_{HP,in,i} = h_{HP,out,i-1}$). After passing through the final HP, the CO_2 returns to the RVCC at point 7 ($P_7 = P_6$, $h_7 = h_{HP,out,N}$). Within the RVCC, CO_2 flows to the IHE at point 8 ($P_8 = P_7$, $h_8 = h_{IHE,in,suc} = h_7$) where it is heated to achieve the superheated temperature required for compressor suction at point 1 ($P_1 = P_8 = P_{suc}$, $h_1 = h_{IHE,out,suc} = h_{suc}$), completing the cooling cycle.

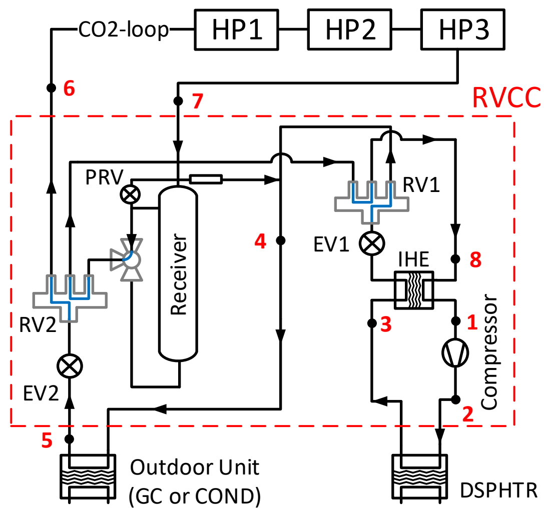

Figure 4.6 Process flow diagram in cooling-dominant mode

In the heating-dominant mode, after leaving the DSPHTR and the IHE at point 4, CO_2 undergoes an isenthalpic expansion to the loop pressure at point 5 ($P_5 = P_{CO_2-loop}$, $h_5 = h_4 = h_{IHE,out,dis}$) and flows to the local HPs. HP1 receives CO_2 from the RVCC ($P_{HP,in,1} = P_5$, $h_{HP,in,1} = h_5$), and the outlet of each HP serves as the inlet for the next ($P_{HP,in,i} = P_{HP,out,i-1} = P_5$, $h_{HP,in,i} = h_{HP,out,i-1}$). After passing through the final HP, the CO_2 returns to the RVCC at point 6 ($P_6 = P_5$, $h_6 = h_{HP,out,N}$) with specific vapor quality (x). Within the RVCC, the CO_2 flows to the receiver, where any gaseous CO_2 at point 6_v is injected directly into the suction line at point 9 in an isenthalpic process ($P_9 = P_1 = P_{suc}$, $h_9 = h_{6_v}$) and with a CO_2 mass flow rate of $\dot{m}_{CO_2,v} = \dot{m}_{CO_2} \cdot x$. The liquid CO_2 at point 6_l, which constitutes the majority of the CO_2, expands to the pressure of the OU in an isenthalpic process ($P_7 = P_{OU,in}$, $h_7 = h_{OU,in} = h_{6_l}$) and is directed to the OU, which operates as an evaporator in this mode with a liquid CO_2 mass flow rate of $\dot{m}_{CO_2,l} = \dot{m}_{CO_2} \cdot (1-x)$. At the OU, the CO_2 absorbs heat, governed by water-side boundary conditions ($T_{w,in} = T_{w,in,OU}$, $\dot{m}_w = \dot{m}_{w,OU}$). The CO_2 then returns to the RVCC at point 8 ($P_8 = P_7$, $h_8 = h_{OU,out}$), mixing with the flashed gas at point 9 in an adiabatic mixing process resulting in point 10 ($P_{10} = P_9 = P_8$, $h_{10} = \frac{(\dot{m}_{CO_2,l} \cdot h_8) + (\dot{m}_{CO_2,v} \cdot h_9)}{\dot{m}_{CO_2}} = h_{IHE,in,suc}$), which flows to the IHE to achieve the appropriate superheated temperature and is delivered to the suction of the compressor ($P_1 = P_{suc} = P_{10}$, $h_1 = h_{suc} = h_{IHE,out,suc}$), completing the heating cycle.

The CO_2 flow between components is defined by its mass flow, pressure, and enthalpy, which serve as key inputs and outputs for each component. Independent variables in the system

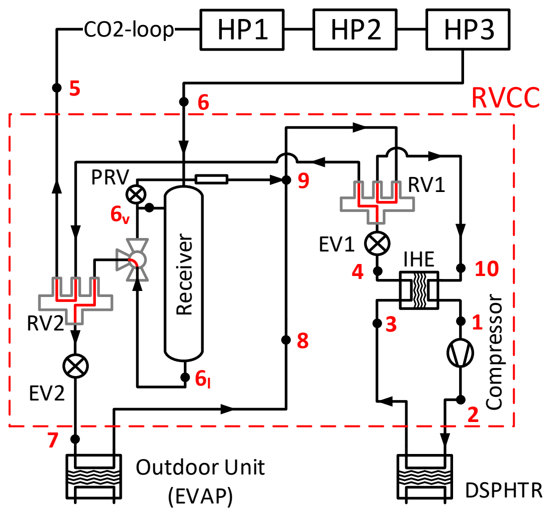

Figure 4.7 Process flow diagram in heating-dominant mode

include the compressor speed (S), the operation mode (cooling or heating), and the water-side boundary conditions for the DSPHTR and OU. Furthermore, the suction (P_{suc}) and discharge pressures (P_{dis}), are determined iteratively within the RVCC. The control of the CO_2-loop inlet quality and the OU (EVAP) outlet enthalpy results in unique discharge and suction pressures. In cooling mode, the CO_2-loop inlet enthalpy is controlled by setting a setpoint on the outlet enthalpy of the OU ($h_{5,setpoint}$) which corresponds to the CO_2-loop inlet enthalpy. Conversely, in heating mode, the CO_2-loop inlet enthalpy is controlled by setting a setpoint on the outlet enthalpy of the IHE ($h_{4,setpoint}$) which defines the CO_2-loop inlet enthalpy. On the suction side, the setpoint for the suction pressure ensures that the outlet of the OU (EVAP) reaches the saturated vapor enthalpy at the suction pressure, such that: $h_{8,setpoint} = h_{sat,v}(P_{suc})$.

4.5.2 TRNSYS Assembly

To simulate CO_2TN operation over a specified time period, TRNSYS Studio was selected for dynamic assembly and simulation. The system model is organized into two main layers: a physical model layer and a simulation logic layer.

The physical layer integrates sub-models for each major component, including the RVCC, DSPHTR, outdoor unit, and local heat pumps, as described in Section 4.4. Each component is implemented as a custom TRNSYS TYPE, enabling interactions within the TRNSYS environment to simulate system performance (Figure 4.8).

Standard TRNSYS libraries were insufficient for simulating the CO_2-based thermal system, so custom TYPES were developed to model a CO_2-based thermal network and to facilitate tailored interactions between the components. Each TYPE in the model contains three core elements: PARAMETERS, INPUTS, and OUTPUTS. PARAMETERS are fixed values set before the simulation, defining each component's specific characteristics, such as geometric dimensions and thermal properties. INPUTS are variable quantities fed into components during the simulation, which change over time based on conditions or outputs from other components. OUTPUTS represent the performance metrics or results generated by each component after processing the inputs and parameters.

As outlined in the mathematical assembly section, determining the suction and discharge pressures is essential to solving the system of equations. In cooling-dominant mode, the system operates with two pressure levels. The suction pressure is set equal to the CO_2-loop pressure ($P_{suc} = P_{CO_2-loop}$), while the discharge pressure must be calculated. The discharge pressure is determined by ensuring that the enthalpy at the CO_2-loop inlet meets its setpoint, which corresponds to the enthalpy at the outlet of the OU $h_{5,setpoint} = h_6$. To achieve this, the system must exchange a sufficient amount of heat on the discharge side, defined as $\dot{Q}_{setpoint,dis} = \dot{m}_{CO_2} \cdot (h_2 - h_{5,setpoint})$. In heating-dominant mode, both suction and discharge pressures must be calculated, each with their own setpoint. The discharge pressure setpoint is defined by the CO_2-loop inlet enthalpy, which is equal to the enthalpy at the IHE outlet ($h_{4,setpoint} = h_5$). The suction pressure setpoint is determined by requiring that the outlet of the OU contains saturated vapor at the corresponding pressure ($h_{8,setpoint} = h_{sat,v}(P_{suc})$). To meet these setpoints, the system must exchange sufficient heat on both the discharge side $\dot{Q}_{setpoint,dis} = \dot{m}_{CO_2} \cdot (h_2 - h_{4,setpoint})$ and the suction side $\dot{Q}_{setpoint,suc} = \dot{m}_{CO_2} \cdot (h_{8,setpoint} - h_7)$.

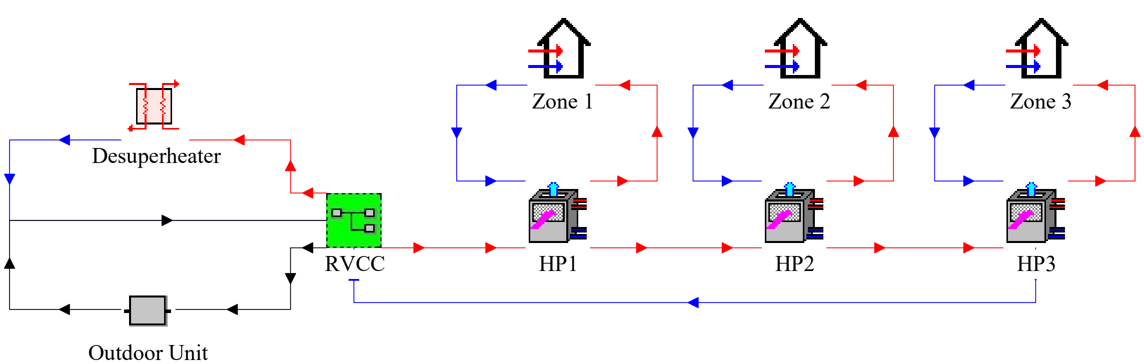

Figure 4.8 TRNSYS Studio - Physical layer

A simulation logic layer was developed in TRNSYS to solve this system of equations and perform two key tasks: (1) switching between operational modes based on the cycles described in the previous section, and (2) determining the appropriate suction and discharge pressures. This simulation logic layer comprises four main components, as shown in Figure 4.9: The RVCC, a switch, and two iterative feedback controllers (TRNSYS TYPE 22) responsible for calculating the suction and discharge pressures. The layer inputs are the system's operation mode, CO_2-loop inlet enthalpy setpoint, and outputs from the OU, IHE, and DSPHTR. Based on the operational mode, the switch processes the heat transfer values from these components and directs the appropriate values to the TYPE 22 controllers. In cooling mode, the heat transfer on the discharge side is calculated as $\dot{Q}_{HX,dis} = \dot{Q}_{DSPHTR} + \dot{Q}_{OU} + \dot{Q}_{IHE}$, while on the suction side, $\dot{Q}_{HX,suc} = 0$. This configuration effectively deactivates the suction-side controller (TYPE 22) and sets the suction pressure equal to the loop pressure ($P_{suc} = P_{CO_2-loop}$). Conversely, in heating mode, the heat transfer on the discharge side is $\dot{Q}_{HX,dis} = \dot{Q}_{DSPHTR} + \dot{Q}_{IHE}$, and on the suction side, $\dot{Q}_{HX,suc} = \dot{Q}_{OU}$. TYPE 22 functions as an iterative feedback controller, adjusting the control signals (pressures) to ensure that the controlled variables ($\dot{Q}_{HX,dis}$ and $\dot{Q}_{HX,suc}$) match their respective setpoints provided by the RVCC. The iterative process within TRNSYS enables accurate tracking of these setpoints.

4.6 Experimentation

4.6.1 Experimental setup

CanmetENERGY designed and operated a prototype of the CO_2TN in their research laboratory in Varennes, Canada, as presented in the study by Bastani and Gholamrezaie [24]. CanmetENERGY provided the experimental data used in this study. Figure 4.10(a) illustrates the local HPs section, which includes three commercial heat pumps: one air-to-water heat pump (HP1) and two water-to-air heat pumps (HP2 and HP3). These heat pumps were modified to use CO_2 on their source side. Figure 4.10(b) shows the RVCC, DSPHTR, and OU. A 10 kW constant-temperature bath is used to supply water to both the DSPHTR and the OU. The setup follows the model assembly principle.

4.6.2 Uncertainty calculation

The CO_2TN prototype is equipped with instruments to measure the temperature, pressure, and mass flow rates of both CO_2 and water throughout the system, as well as the electrical power consumption of the compressor and local HPs. The data collected are subject to two types of uncertainties: fixed uncertainties provided by the instrument manufacturers,

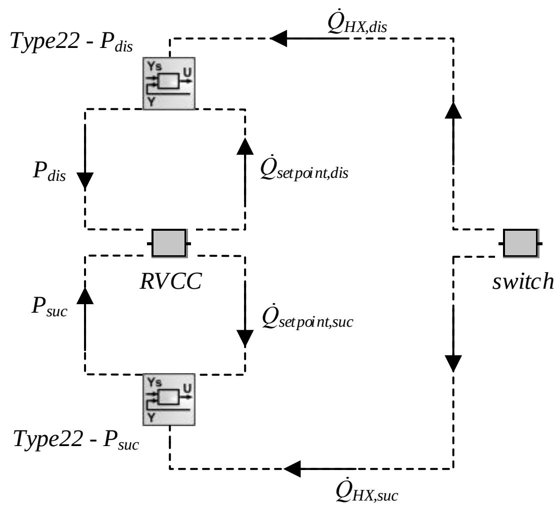

Figure 4.9 TRNSYS Studio - Simulation logic layer

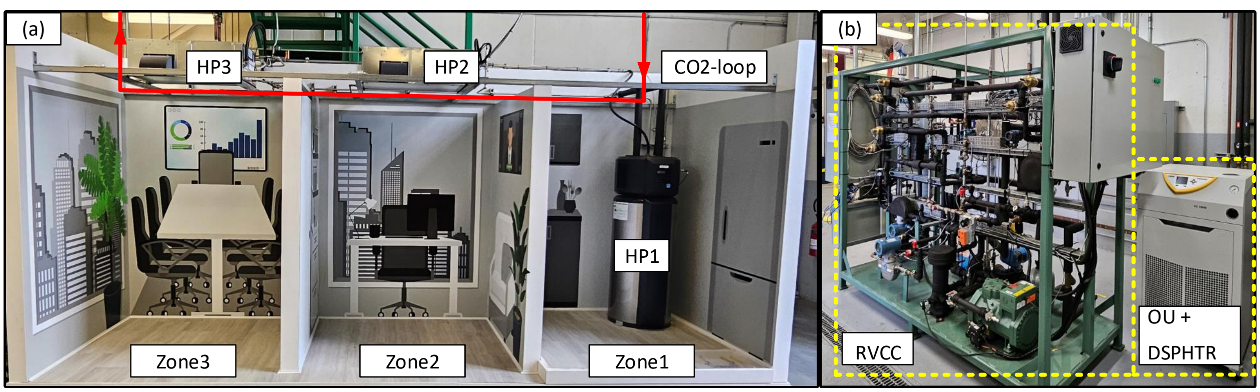

Figure 4.10 Experimental setup [24]: (a) Local HPs (b) The RVCC, OU, DSPHTR

summarized in Table 4.2, and operational uncertainties primarily arising from mass flow rate oscillations. The total uncertainty, u_{total}, is calculated as the root-sum-square of the systematic uncertainty from the instruments, u_{sys}, and the operational uncertainties arise from system oscillations, u_{op}, using the equation:

$$u_{\text{total}} = \sqrt{u_{\text{sys}}^2 + (z \cdot u_{\text{op}})^2} \tag{4.49}$$

where u_{sys} represents the fixed uncertainties of the instruments (reported at a 95% confidence level), and u_{op} is the standard deviation of the measurements over the period of experiment, scaled to match a 95% confidence level using the factor $z = 1.96$. To evaluate the systematic uncertainty, u_{sys}, the individual uncertainties of the measured variables X_i are propagated to the calculated quantity Y using the method described in NIST Technical Note 1297 [109]. For a quantity Y expressed as a function of directly measured variables X_i, i.e., $Y = f(X_1, X_2, \dots)$, the systematic uncertainty is determined by:

$$u_{sys} = \sqrt{\sum_i \left(\frac{\partial Y}{\partial X_i}\right)^2 u_{X_i}^2} \tag{4.50}$$

Here, u_{X_i} represents the uncertainty of the individual measured variables, and $\frac{\partial Y}{\partial X_i}$ is the partial derivative of Y with respect to X_i.

Table 4.2 Systematic uncertainty of the measurement instruments used in the CO_2TN prototype.

Instrument	**Uncertainty**
RTD temperature sensor	±0.10 °C
Pressure meter	±0.08%
CO_2 mass flow meter	±0.75%
Water mass flow meter	±0.10%
Wattmeter	±0.40%

Note that the uncertainty calculation is performed for both the experiments and the model. Since the model contains iterations to reach the final solution, it is not possible to evaluate the partial derivatives required to calculate the model uncertainties. The uncertainties are instead calculated using an equivalent model implemented in the Engineering Equation Solver (EES), which offers a more convenient way of evaluating the partial derivatives and propagating the uncertainties. The EES implementation of the model was validated against TRNSYS results to ensure that the uncertainties showed in this section are representative of that of the TRNSYS model.

To collect data and minimize operational errors during both component-level and system-level validation, the system was first allowed to stabilize at the setpoints. Data was then recorded for 20 minutes, and the average results over this timeframe were compared for validation purposes.

4.7 Validation

For validation, each component of the system, including the compressor and heat exchangers, was individually assessed. The complete system model was then validated by comparing its predicted performance with experimental results.

4.7.1 Component-Level Validation

Compressor

The experimental setup features a variable-speed reciprocating compressor. To validate the compressor model, tests were conducted at five distinct compressor speeds: 30 Hz, 36 Hz, 42 Hz, 48 Hz, and 60 Hz. These speeds correspond to varying mass flow rates while maintaining a constant pressure ratio, enabling an investigation of the relationship between compressor speed and mass flow rate. Each compressor speed was tested at six different pressure ratios. The suction pressure was fixed at 5.7 MPa, while the discharge pressure was varied from 7.8 MPa to 8.8 MPa in increments of 0.2 MPa. In total, 30 experimental test runs were performed.

Figure 4.11 and Figure 4.12 present a comparison between the experimental data and the model predictions for CO_2 mass flow production and compressor power input, respectively. Each dataset includes vertical error bars representing the experimental uncertainty. The modeling error was assessed using statistical metrics, including the Mean Absolute Percentage Error (MAPE) and the maximum percentage deviation of the model from the experimental results. MAPE is defined as:

$$\mathrm{MAPE} = \frac{1}{n}\sum_{i=1}^{n}\left|\frac{y_i^{\mathrm{exp}} - y_i^{\mathrm{model}}}{y_i^{\mathrm{exp}}}\right| \times 100 \tag{4.51}$$

For CO_2 mass flow rate, the MAPE was 7.24%, with a maximum deviation of 14%. For compressor power input, the model showed good agreement with the experimental data, achieving a MAPE of 0.96% and a maximum deviation of 2%.

Water-to-CO_2 heat exchanger

The experimental setup includes three CO_2-to-water heat exchangers designated for desuperheating (DSPHTR), gas cooling and condensation (GC/COND), and evaporation (EVAP). The physical specifications of the heat exchanger, provided in Table 4.3, are divided into two sections. The upper section lists the specifications provided by the manufacturer, while the lower section presents physical parameters not included in the manufacturer's documentation. These parameters were determined using a calibration method based on 10 sets of experimental data solely drawn for this purpose, and the calibrated model was subsequently used to validate the experimental results. To ensure realistic parameters for the heat exchanger, realistic boundaries from the literature [110–113], were set during the process of determining the values.

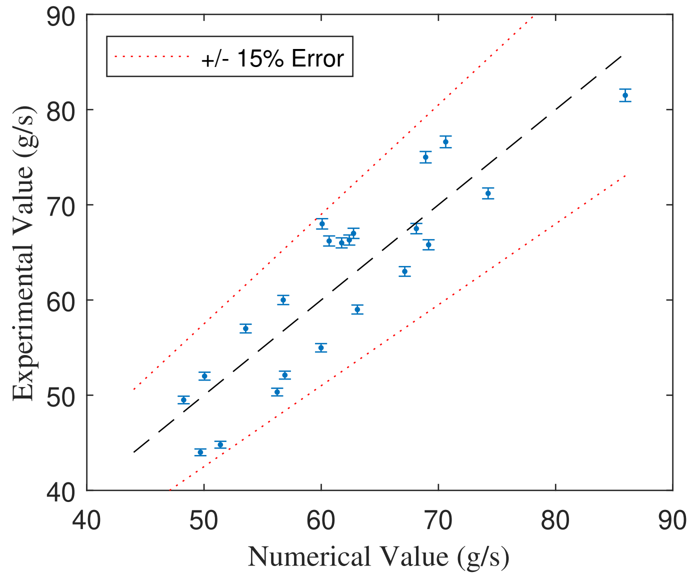

Figure 4.11 Compressor model validation (mass flow rate) — the black dashed line represents 0% error between numerical and experimental values, the red dotted lines indicate ±15% prediction error margins

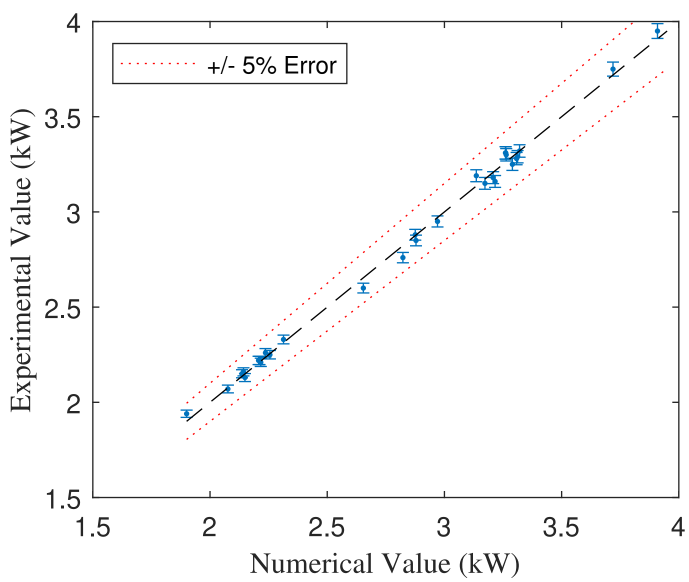

Figure 4.12 Compressor model validation (power input) — the black dashed line represents 0% error between numerical and experimental values, the red dotted lines indicate ±5% prediction error margins

As described in Section 4.4, the water-to-CO_2 heat exchanger models are primarily divided into two sections: the supercritical or superheated regions (Section 4.4.3) and the subcritical

Table 4.3 Specifications of heat exchangers

Specifications	**DSPHTR**	**GC/COND**	**EVAP**
Length (mm)	314	314	314
Width (mm)	76	76	76
Height (mm)	61	65	73
Number of channels (CO_2-side)	11	12	9
Heat transfer area (m^2)	0.425	0.468	0.540
Plate material	SUS 316	SUS 316	SUS 316
Plate thickness (mm)	0.6	0.6	0.6
Corrugation depth (mm)	4.74	4.74	4.74
Area enlargement factor (ϕ)	1.32	1.30	1.26
Chevron angle (β)	65	65	65

region (Section 4.4.3). The validation is conducted using heat exchangers operating under identical conditions on the test bench. The validation compares the heat transfer rate predicted by the model to the actual heat transfer rate, calculated from experimental data. This was achieved by measuring the inlet and outlet water temperatures of the heat exchanger and applying the energy equation on the water side using the measured data. Figure 4.13 presents the comparison of the experimental and model-predicted heat transfer rates for the DSPHTR and the GC. Note that the input parameters and the corresponding results are tabulated in the appendices section (4.9). Statistical metrics were calculated to evaluate the model performance. For the GC, the model showed good agreement with the experimental data, achieving a MAPE of 1.37% and a maximum deviation of 3%. For the DSPHTR, the MAPE was 8.36% and the maximum deviation was 9%.

To validate the subcritical heat exchanger model, the same approach was applied. Two subcritical models, introduced in Section 4.4.3, are used to represent the heat exchangers operating in either condensation or evaporation modes. Figure 4.14 illustrates the validation results for the condenser (COND) and evaporator (EVAP) models. Note that the input parameters and the corresponding results are tabulated in the appendices section (4.9). For the EVAP, the model demonstrated a good predictions, with a MAPE of 8.10%, and a maximum deviation of 12%. For the COND, the model showed a MAPE of 4.05%, and a maximum error of 5.5%. It is worth noting that the experimental setup, originally built to validate the models, was not designed to include a condenser. However, the system was adjusted to acquire two datasets specifically for validating the condenser model.

It is important to mention that Figures 4.13 and 4.14 include horizontal error bars to represent model uncertainties and vertical error bars to account for experimental uncertainties. The model uncertainties arise from the measured variables used as inputs to the model. For the

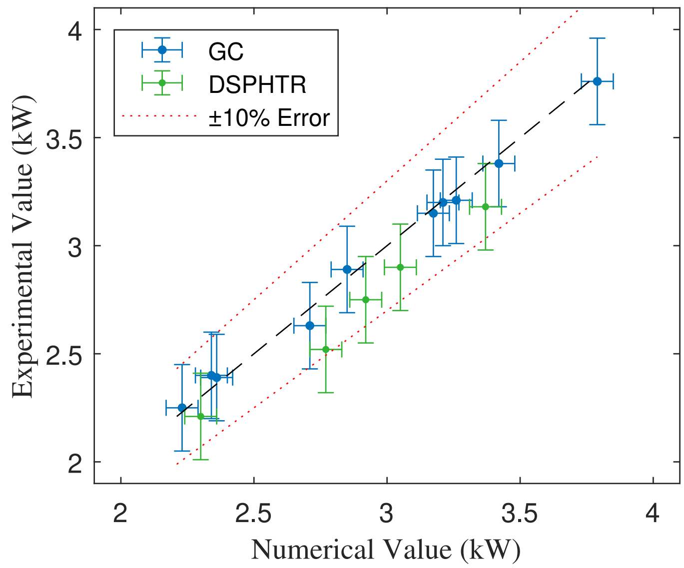

Figure 4.13 Superheated and supercritical heat exchanger model validation (heat transfer rate) — the black dashed line represents 0% error between numerical and experimental values, the red dotted lines indicate ±10% prediction error margins

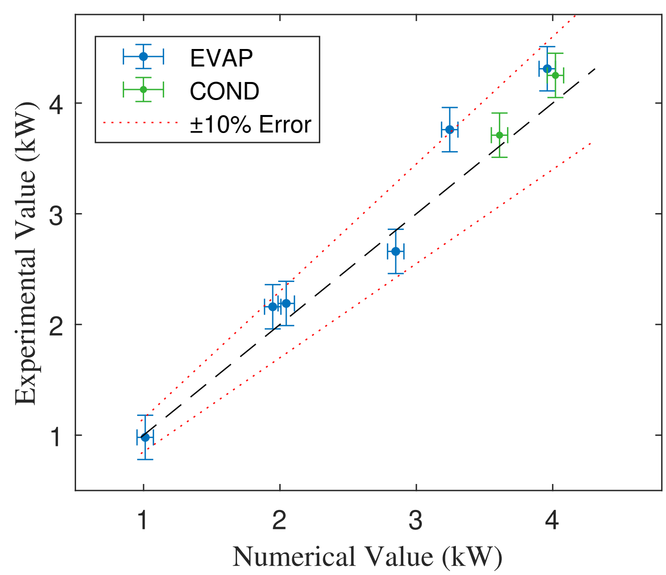

Figure 4.14 Subcritical heat exchanger model validation (heat transfer rate) — the black dashed line represents 0% error between numerical and experimental values, the red dotted lines indicate ±10% prediction error margins

water-to-CO_2 heat exchangers, the input variables are the CO_2 mass flow rate ($\dot{m}_{CO_2}$), CO_2 inlet pressure ($P_{CO_2,in}$), CO_2 inlet temperature ($T_{CO_2,in}$), water mass flow rate ($\dot{m}_w$), and the water inlet temperature to the heat exchanger ($T_{w,in}$). The model uncertainty is obtained using Equation 4.49. The operational uncertainties (u_{op}) represent the standard deviation of the measured input oscillations. The systematic uncertainty u_{sys}, which is determined using Equation 4.50 as follows:

$$\begin{aligned} u_{\text{sys}} =& \sqrt{\left(\frac{\partial \dot{q}}{\partial \dot{m}_w}\right)^2 u_{\dot{m}_w}^2 + \left(\frac{\partial \dot{q}}{\partial T_{w,in}}\right)^2 u_T^2 + \left(\frac{\partial \dot{q}}{\partial \dot{m}_{CO_2}}\right)^2 u_{\dot{m}_{CO_2}}^2} \\ & \overline{+ \left(\frac{\partial \dot{q}}{\partial P_{CO_2,in}}\right)^2 u_P^2 + \left(\frac{\partial \dot{q}}{\partial T_{CO_2,in}}\right)^2 u_T^2} \end{aligned} \tag{4.52}$$

On the other hand, the experimental uncertainties arise from the combination of operational uncertainties and systematic uncertainties (Equation 4.49). The operational uncertainties (u_{op}) represent the standard deviation of the experimental oscillations, which, in this case, are obtained from the variations in q during the experiment. The systematic uncertainty u_{sys} is calculated as:

$$u_{\text{sys}} = \sqrt{\left(\frac{\partial \dot{q}}{\partial \dot{m}_w}\right)^2 u_{\dot{m}_w}^2 + \left(\frac{\partial \dot{q}}{\partial T_{w,\text{in}}}\right)^2 u_T^2 + \left(\frac{\partial \dot{q}}{\partial T_{w,\text{out}}}\right)^2 u_T^2} \tag{4.53}$$

where q is the heat transfer rate, and $u_{\dot{m}_w}$ and u_T are the measurement uncertainties associated with the water flow meter and temperature sensors, respectively, as listed in Table 4.2.

CO_2-to-CO_2 heat exchanger

To validate the method introduced for modeling the internal heat exchanger (IHE) which is the only CO_2-to-CO_2 heat exchanger, two factors were investigated: the 10 °C superheat requirement at the compressor suction and the assumption of negligible heat loss. The IHE model simplifies the process by assuming that the heat required on suction-side is equal to the heat extracted from the discharge-side. Regarding the capability to provide the required superheat, experimental data from 20 test bench datasets under different conditions showed consistent achievement of the target 10 ± 0.1 °C superheat in all cases. As for the assumption of negligible heat loss and the ability of the IHE to transfer the required heat from the discharge to the suction, Figure 4.15 illustrates the relationship between the heat exchanged on the suction-side and the heat extracted from the discharge-side for the IHE. The heat transfer on the suction side and discharge side are calculated as follows:

$$\dot{q}_{\text{suction-side}} = \dot{m}_{CO_2} \cdot (h_{IHE,out,suc} - h_{IHE,in,suc}) \tag{4.54}$$

$$\dot{q}_{\text{discharge-side}} = \dot{m}_{CO_2} \cdot (h_{IHE,in,dis} - h_{IHE,out,dis}) \tag{4.55}$$

where $\dot{m}_{CO_2}$ is measured using the CO_2 mass flow meter, and the inlet and outlet enthalpies of the IHE are calculated using the Span-Wagner equation of state [103], based on pressure readings and temperature measurements taken at the inlet and outlet of the IHE. The statistical evaluation of the data shows a MAPE of 9.45%, and a maximum error of 11%.

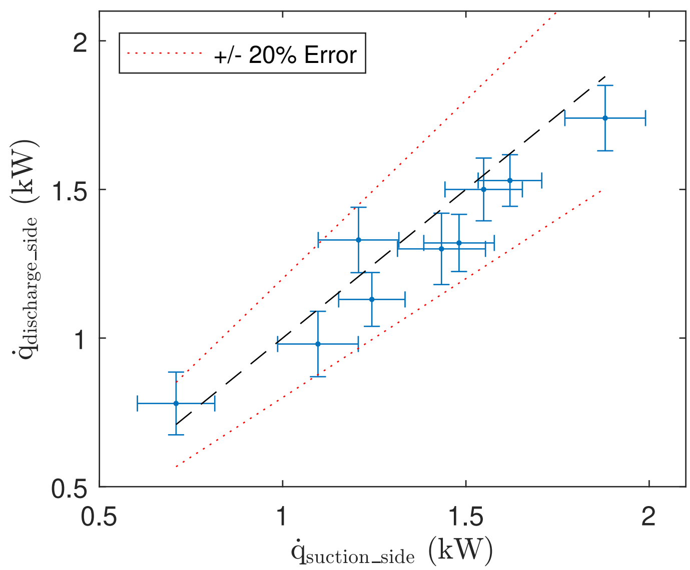

Figure 4.15 Heat exchanged on the suction side vs. heat extracted from the discharge side — the black dashed line represents 0% error between numerical and experimental values, the red dotted lines indicate ±20% prediction error margins

4.7.2 System-Level Validation

After validating each component individually, the entire thermal network model was assembled in TRNSYS using the same parameters and specifications as the experimental setup at CanmetENERGY (Varennes). To validate the system, three different HP configurations were considered, representing the possible system operating conditions. These configurations are summarized in Table 4.4.

These cases encompass the system's operation under both subcritical and transcritical conditions. During the tests, the compressor speed (S) was fixed at 30 Hz, and the CO_2-loop

Table 4.4 System validation cases and fixed parameters

Case	**Operating Mode**	**HP1**	**HP2**	**HP3**
1	Cooling-dominant	OFF	Cooling	OFF
2	Heating-dominant	OFF	Heating	OFF
3	Balance	OFF	Heating	Cooling

pressure (P_{CO_2-loop}) on the source side of the local HPs was maintained at 5.7 MPa. Additionally, during the experiment, significant pressure drops were observed due to the design and sizing of the first prototype. These pressure drops were directly incorporated into the model. Notably, the major pressure drops occurred on the discharge side of the IHE and at the receiver outlet through the PRV, which directs the CO_2 to the compressor suction. In the cooling-dominant mode configuration, the pressure drop on the discharge side is incorporated from P_3 to P_4, and on the suction side, it is applied from P_7 to P_8. In the heating-dominant mode configuration, the pressure drop occurs only on the discharge side and is incorporated from P_4 to P_5.

A comparison of system COP between the experimental data and the model, as well as the total power input and heat pump capacities, is presented in Table 4.5. The model demonstrates good agreement with experimental data, particularly in power consumption ($\dot{W}$), where relative errors range from 1.45% to 7.89%. Heating/cooling capacity ($\dot{Q}_{HP}$) is slightly overestimated across all cases, with errors between 4.48% and 7.80%. For the COP, the statistical analysis shows a maximum deviation of 16.9% in case 2. These test points are solely chosen for validation purposes and do not reflect the optimized performance of the system. Discrepancies between model predictions and experimental measurements arise from both experimental and modeling sources. Experimental errors are primarily attributed to instrument uncertainties (Table 4.2) and case-specific operational variability. For instance, in case 2, the standard deviation of the water mass flow rate is 6 g/s; the standard deviation of the water inlet temperature to the EVAP is 0.20 °C, while that of the outlet temperature is 0.14 °C. The DSPHTR inlet and outlet temperatures have standard deviations of 0.15 °C and 0.34 °C, respectively. The standard deviation of the power input is 0.01 kW for both the circulation compressor and the heat pump. Ultimately, the operational uncertainty (u_{op}) used to calculate the COP for this case is 0.06.

On the modeling side, there are three main sources of errors and uncertainties: (i) operational and instrumental uncertainties in the input parameters obtained from the experiment, which are included in the uncertainty propagation analysis; (ii) direct pressure-drop values taken from the experiment and plugged into the model, which introduce additional operational uncertainties; and (iii) the use of referenced correlations—such as heat transfer correlations applied in the heat exchangers—which introduce further uncertainty. On the refrigerant side of the GC and DSPHTR, literature-reported Nusselt correlations can exhibit errors of up to approximately 8% [104], while the evaporator's refrigerant-side correlation can have errors of up to approximately 10% [108]. These correlation errors were not considered in the uncertainty propagation analysis, potentially leading to additional modeling inaccuracies. In summary, error sources beyond the scope of the uncertainty propagation analysis include: (i) underestimation of the operational variability, which can influence both the experimental measurements and the modeled results, and (ii) correlation inaccuracies, which not only introduce modeling errors but also contribute to underestimating the model's overall uncertainty.

To assess the system's performance, the COP is calculated as follows:

$$\mathrm{COP}_{sys} = \frac{\dot{Q}_{\mathrm{HP}}}{\dot{W}} \tag{4.56}$$

$$\dot{Q}_{\mathrm{HP}} = \sum_{i=1}^{n} \dot{Q}_{\mathrm{HP},i} \tag{4.57}$$

$$\dot{W} = \dot{W}_{comp} + \sum_{i=1}^{n} \dot{W}_{\mathrm{HP},i} \tag{4.58}$$

where n is the number of heat pumps (HPs), $\dot{W}$ represents the total power consumption [kW], which includes the power consumed by the CO_2 circulation compressor ($\dot{W}_{comp}$) and the local HPs ($\dot{W}_{\mathrm{HP,i}}$). $\dot{Q}_{\mathrm{HP}}$ refers to the total heating, and cooling capacity of the activated HPs. To calculate the system COP from the model ($\mathrm{COP}_{sys,mod}$) $\dot{Q}_{\mathrm{HP},i}$, $\dot{W}_{\mathrm{HP,i}}$, and $\dot{W}_{comp}$ are determined using Equations 4.1, 4.3, and 4.6, respectively. Furthermore, for the COP calculation, the input variables are the speed of compressor (S), CO_2-loop pressure (P_{CO_2-loop}), water mass flow rate ($\dot{m}_w$), and the water inlet temperature ($T_{w,in}$) to DSPHTR and OU. The model uncertainty is obtained using Equation 4.49.

For the experimental COP ($\mathrm{COP}_{sys,exp}$), the power consumptions are measured using wattmeter installed on the test bench and the capacities of the local HPs are calculated using the following relations [24]:

$$\dot{Q}_{\mathrm{HP,H,exp}} = \dot{Q}_{w,\mathrm{EVAP}} - \dot{Q}_{w,\mathrm{DSPHTR}} + \dot{W}_{\mathrm{comp}} + \dot{W}_{\mathrm{HP}} \tag{4.59}$$

$$\dot{Q}_{\mathrm{HP,C,exp}} = \dot{Q}_{w,\mathrm{DSPHTR}} + \dot{Q}_{w,\mathrm{GC}} - \dot{W}_{\mathrm{comp}} - \dot{W}_{\mathrm{HP}} \tag{4.60}$$

where $\dot{Q}_{w,\mathrm{DSPHTR}}$, $\dot{Q}_{w,\mathrm{GC}}$, and $\dot{Q}_{w,\mathrm{EVAP}}$ are calculated using an energy balance equation on the water side of the heat exchangers, based on the measured inlet and outlet water temperatures obtained from RTD temperature sensors and the water mass flow rate measured by flow meters installed on the test bench.

Table 4.5 System validation

Case	$\dot{W}_{mod}$ (kW)	$\dot{W}_{exp}$ (kW)	$\dot{Q}_{mod}$ (kW)	$\dot{Q}_{exp}$ (kW)	$\mathbf{COP}_{sys,mod}$ $(-)$	$\mathbf{COP}_{sys,exp}$ $(-)$
1	3.18	3.32	2.80	2.68	0.87 ± 0.04	0.80 ± 0.09
2	2.45	2.66	3.73	3.46	1.52 ± 0.05	1.30 ± 0.12
3	4.08	4.14	6.56	6.14	1.61 ± 0.04	1.48 ± 0.11

To further investigate the sources of deviation between model predictions and experimental results, a local sensitivity and uncertainty propagation analysis was performed for each system-level validation case. This analysis quantifies the relative contribution of each uncertain input parameter—CO_2 loop pressure (P_{CO_2-loop}), compressor speed (S), water mass flow rate ($\dot{m}_w$), and water inlet temperature ($T_{w,in}$) to the GC, DSPHTR, and EVAP—to the propagated uncertainty in system performance (COP$_{sys,mod}$), total heating/cooling capacity ($\dot{Q}_{mod}$), and total power input ($\dot{W}_{mod}$). In this analysis, it was assumed that the compressor speed had no associated measurement uncertainty; therefore, its contribution to the propagated uncertainty is zero for all cases. Table 4.6 presents the percentage contributions for the three validation cases, based on the instrument uncertainties listed in Table 4.2.

Table 4.6 shows that the propagated uncertainty of $\dot{Q}_{mod}$ is entirely dependent on P_{CO_2-loop}. This is because, in the local HP correlations used, the capacity of the HPs are expressed solely as a function of the loop temperature, which in the model is computed from the saturation temperature corresponding to the input P_{CO_2-loop}. Furthermore, $\dot{W}_{mod}$ represents the sum of the circulation compressor work ($\dot{W}_{comp}$) and the local HP work ($\dot{W}_{HP}$). $\dot{W}_{comp}$ depends on the compressor speed, discharge pressure, and suction pressure. In cooling mode, the discharge pressure is determined from the GC, and DSPHTR water inlet temperature and mass flow rate. In heating mode, a similar dependence exists on the evaporator side to determine the suction pressure. For the local HPs, $\dot{W}_{HP}$ depends solely on the loop temperature derived from the P_{CO_2-loop} saturation temperature. Consequently, the total work is influenced by all input parameters.

As mentioned, the experimental setup inherently includes pressure drops. To highlight the importance of system design in minimizing these losses, the model was also run with all pressure drops set to zero and compared to the current results with pressure drops. Table 4.7 summarizes the total input power ($\dot{W}$), heating/cooling capacity ($\dot{Q}$), and system COP for each case, both with (wp) and without (np) pressure drop. Results show that eliminating

Table 4.6 Percentage contribution of each input parameter to the propagated uncertainty for $COP_{sys,mod}$, $\dot{Q}_{mod}$, and $\dot{W}_{mod}$ in the three validation cases

Case	**Input**	$\mathbf{COP}_{sys,mod}$ (%)	$\dot{Q}_{mod}$ (%)	$\dot{W}_{mod}$ (%)
1	P_{CO_2-loop}	0.50	100.00	0.23
	$\dot{m}_{w,DSPHTR}$	0.16	0.00	0.16
	$T_{w,in,DSPHTR}$	4.48	0.00	4.47
	$\dot{m}_{w,GC}$	3.12	0.00	3.57
	$T_{w,in,GC}$	91.74	0.00	91.57
2	P_{CO_2-loop}	15.60	100.00	13.66
	$\dot{m}_{w,DSPHTR}$	0.10	0.00	0.10
	$T_{w,in,DSPHTR}$	2.52	0.00	2.50
	$\dot{m}_{w,EVAP}$	0.35	0.00	0.29
	$T_{w,in,EVAP}$	81.43	0.00	83.45
3	P_{CO_2-loop}	34.27	100.00	25.32
	$\dot{m}_{w,DSPHTR}$	0.62	0.00	0.70
	$T_{w,in,DSPHTR}$	16.97	0.00	19.28
	$\dot{m}_{w,GC}$	1.61	0.00	1.83
	$T_{w,in,GC}$	46.53	0.00	52.87

pressure losses increases COP by 21% in cooling mode, 7% in heating mode, and 20% in balance mode. This underscores the need to minimize pressure drop in future prototype iterations to maximize system efficiency.

Table 4.7 System performance with (wp) and without (np) pressure drop

Case	$\dot{W}_{np}$ (kW)	$\dot{W}_{wp}$ (kW)	$\dot{Q}_{np}$ (kW)	$\dot{Q}_{wp}$ (kW)	COP_{np}	COP_{wp}
1	2.56	3.18	2.80	2.80	1.10	0.87
2	2.25	2.45	3.73	3.73	1.66	1.52
3	3.35	4.08	6.56	6.56	1.96	1.61

Figures 4.16, 4.17, and 4.18 illustrate the pressure-enthalpy diagrams for cases 1 to 3, respectively, demonstrating the validation of the model against experimental data for transcritical and subcritical operations.

As shown in Figure 4.16, the model predictions align well with the experimental results. The significant pressure drops observed in the experiment were incorporated into the model at specific points, including point 3, which represents the IHE inlet on the discharge-side, and point 7, corresponding to the flash gas outlet of the RVCC receiver. It is important to note that all experimental points, except points 6, 7, and 8, are directly measured. Points 6 and 8 were estimated based on an isenthalpic pressure change assumption. For point 7, since it was not possible to measure the quality at the last HP, the tests were conducted to ensure that point 7 was close to saturated vapor conditions.

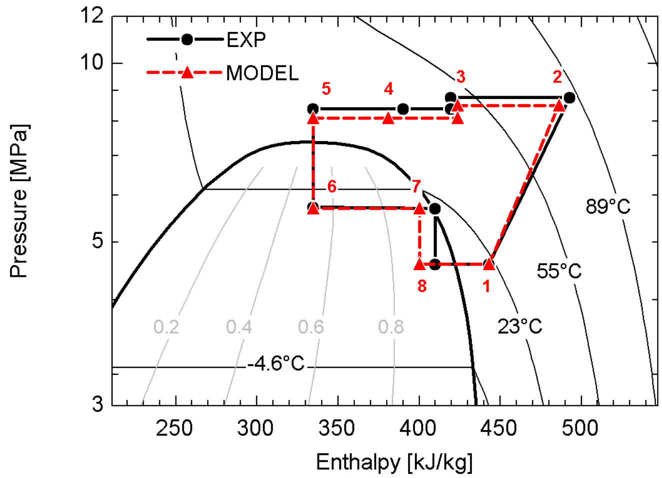

Figure 4.16 Comparison of model predictions and experimental data on a P-h diagram for Case 1 (Cooling-dominant)

Figure 4.17 illustrates the comparison between the model predictions and experimental results for a heating mode case, demonstrating the model's accuracy for subcritical operation. The observed pressure drop in heating mode was identified after the IHE, coinciding with the location of the expansion valve (EV1). Therefore, the pressure drop between points 4 and 5 results from both the natural pressure losses in the system and the controlled pressure drop across the expansion valve. In this experiment, all points were measured except for point 7 and 9, which was estimated based on the assumption of an isenthalpic expansion process from point 6_l, and 6_v respectively. Note that, since in this experiment all the CO_2 turned to liquid after passing through the local HPs, there was no mixing between points 8 and 9. Therefore, point 10 is equal to point 8.

Figure 4.18 presents the comparison for a balance scenario where the first HP operates in heating mode while the second operates in cooling mode. Although referred to as a balance mode, the system uses the same configuration as in the cooling mode, operating in the transcritical regime. The results show good agreement between the model predictions and experimental data. A key point to note in this diagram is the behavior of CO_2 as it enters the loop at point 6 ($h_6 = 377, \mathrm{kJ/kg}$). Since the first HP is operating in heating mode, the CO_2 is condensed to a specified enthalpy of $h_{\mathrm{CO_2,out,HP1}} = h_{6'} = 331, \mathrm{kJ/kg}$, a value determined by the model but not measurable in the experimental setup. The CO_2 then flows to the second

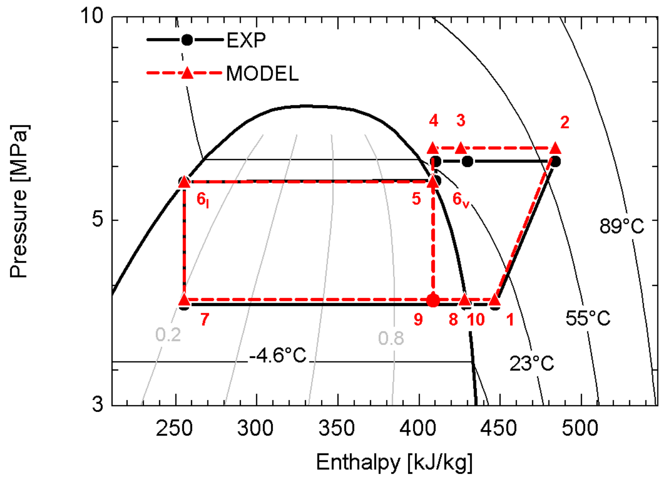

Figure 4.17 Comparison of model predictions and experimental data on a P-h diagram for Case 2 (Heating-dominant)

HP, which operates in cooling mode, evaporating the CO_2 to point 7 ($h_7 = 400,\mathrm{kJ/kg}$). This value, too, cannot be measured experimentally due to the lack of instrumentation at this point.

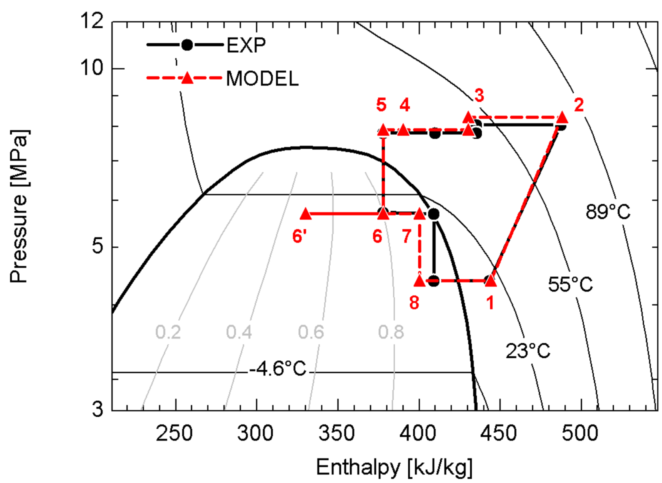

Figure 4.18 Comparison of model predictions and experimental data on a P-h diagram for Case 3 (Balance)

4.8 Conclusion

This study presents a comprehensive modeling framework for a compression-based, low-temperature CO_2 thermal network (CO_2TN), with a focus on the detailed development of component models and their integration into a complete system. Models were developed for key components, including the local HPs, the CO_2 circulation compressor, water-to-CO_2 heat exchangers, and CO_2-to-CO_2 heat exchangers, specifically designed to capture the unique thermophysical behavior of CO_2 in both transcritical and subcritical regimes. These models were implemented in TRNSYS using newly developed TYPES, allowing for a flexible and scalable approach to simulating the CO_2TN across various operational modes. The system was assembled by dividing the CO_2TN into two primary sections: the reversible vapor compression cycle (RVCC) and the components exchanging heat with the external environment, namely the local HPs and the water-to-CO_2 heat exchangers. A systematic methodology for integrating these components was developed, incorporating pressure-enthalpy relationships to ensure energy and mass balance throughout the system. Validation was performed at both the component and system levels using experimental data from a prototype system. The component models demonstrated good accuracy, with deviations within ±15% for heat transfer rates, mass flow, and energy consumption predictions. At the system level, the model reliably predicted key performance metrics, including the coefficient of performance (COP), heat capacities, and power consumption across various operating scenarios, with COP predictions within 16% of the experimental results. This work establishes a robust framework for modeling, assembling, and validating CO_2-based thermal networks, providing a foundation for accurate system performance prediction. Future efforts will focus on optimizing control strategies and expanding the framework to accommodate larger-scale systems.

Acknowledgment

The authors wish to express their gratitude to CanmetENERGY in Varennes, Canada, for providing the experimental data used for validation in this study. The authors acknowledge the Natural Sciences and Engineering Research Council of Canada (NSERC) for funding the Ph.D. student contributing to this work through discovery grant, [funding application number: RGPIN-2020-06556].

Declaration of generative AI and AI-assisted technologies in the writing process

During the preparation of this work the authors used ChatGPT in order to improve the readability and language of the manuscript. After using this tool/service, the authors reviewed and edited the content as needed and take full responsibility for the content of the published article.

4.9 Appendix: Heat exchanger validation data

The input parameters and the corresponding results for the validation of CO_2-to-water heat exchangers, including the DSPHTR, GC, EVAP, and COND, are presented in Tables 4.8 and 4.9.

Table 4.8 Gas cooler and desuperheater validation data

$\dot{m}_{CO_2}$ (kg/hr)	$P_{CO_2,in}$ (MPa)	$T_{CO_2,in}$ (°C)	$\dot{m}_w$ (kg/hr)	$T_{w,in}$ (°C)	$\dot{q}_{mod}$ (kW)	$\dot{q}_{exp}$ (kW)
DSPHTR						
156.17	7.88	99.60	25.20	15.00	2.30	2.21
175.32	8.06	95.80	28.80	15.00	2.77	2.52
182.52	8.28	95.74	33.84	15.00	2.92	2.75
254.88	8.98	72.35	54.00	20.00	3.05	2.90
241.13	9.10	75.33	57.60	20.00	3.37	3.18
GC						
205.56	7.60	35.18	176.40	14.54	3.79	3.76
223.20	7.60	35.68	136.80	13.85	3.17	3.15
172.80	7.80	35.43	144.00	14.28	3.26	3.21
230.40	7.80	38.17	136.80	14.35	3.42	3.38
187.20	8.00	36.75	133.20	14.31	3.21	3.20
241.20	8.00	38.77	86.40	13.70	2.34	2.40
219.60	8.20	40.46	100.80	14.11	2.85	2.89
255.60	8.20	41.34	97.20	18.78	2.36	2.39
240.84	8.40	40.89	93.60	18.40	2.23	2.25
178.20	8.40	40.61	118.80	18.94	2.71	2.63

Table 4.9 Evaporator and condenser validation data

$\dot{m}_{CO_2}$ (kg/hr)	$P_{CO_2,in}$ (MPa)	$T_{CO_2,in}$ (°C)	$\dot{m}_w$ (kg/hr)	$T_{w,in}$ (°C)	$\dot{q}_{mod}$ (kW)	$\dot{q}_{exp}$ (kW)
EVAP						
120.42	3.52	Sat. Temp.	338.40	6.10	3.24	3.76
132.84	3.77	Sat. Temp.	849.60	9.78	3.96	4.31
66.60	4.69	Sat. Temp.	882.00	15.80	2.04	2.19
99.86	4.72	Sat. Temp.	882.00	15.69	1.94	2.16
116.35	4.95	Sat. Temp.	943.20	15.63	1.01	0.98
56.23	4.47	Sat. Temp.	867.60	15.80	2.84	2.66
COND						
194.22	6.40	54.83	126.00	13.13	3.61	3.71
147.60	6.60	61.20	151.20	12.10	4.02	4.25

4.10 Appendix: Mesh-independence of the gas cooler model discretization[1]

A mesh-independence analysis is performed to determine the number of cells used in the discretized gas cooler (GC) model. Since the thermophysical properties of CO_2 vary strongly in the supercritical region, the required discretization may depend on the inlet pressure, inlet temperature, and mass flow rates. Therefore, the analysis is not limited to a single operating point. Instead, it is repeated for the GC validation operating points listed in Table 4.8, which cover the representative operating range of the experimental data.

For each operating point, the number of cells is increased progressively and the solution is compared with a fine-grid reference solution using 400 cells. The comparison is based on the heat transfer rate, the CO_2 outlet temperature, and the water-glycol outlet temperature. The relative deviation of the heat transfer rate and the absolute deviations of the outlet temperatures are calculated as follows:

$$\delta_{\dot{Q},j}(n) = \left| \frac{\dot{Q}_{n,j} - \dot{Q}_{ref,j}}{\dot{Q}_{ref,j}} \right| \times 100 \tag{4.61}$$

$$\delta_{T,CO_2,j}(n) = |T_{CO_2,out,n,j} - T_{CO_2,out,ref,j}| \tag{4.62}$$

$$\delta_{T,w,j}(n) = |T_{w,out,n,j} - T_{w,out,ref,j}| \tag{4.63}$$

[1]This appendix section was not included in the journal paper and was added only for the thesis.

$$\delta_{\dot{Q},max}(n) = \max_{j}\left(\delta_{\dot{Q},j}(n)\right) \tag{4.64}$$

$$\delta_{T,CO_2,max}(n) = \max_{j}\left(\delta_{T,CO_2,j}(n)\right), \qquad \delta_{T,w,max}(n) = \max_{j}\left(\delta_{T,w,j}(n)\right) \tag{4.65}$$

where n is the number of cells, j is the GC operating point, and the subscript ref denotes the fine-grid reference solution. The final discretization is selected based on the maximum deviation among all tested operating points, so that the selected mesh remains valid for the most demanding GC condition.

The acceptance criteria are set to 0.5% for the heat transfer rate and 0.1 $°C$ for the outlet temperatures. The temperature tolerance is selected to remain consistent with the temperature measurement uncertainty; using a numerical tolerance smaller than the experimental uncertainty would not provide a physically meaningful improvement in the validation context.

Figure 4.19 shows the maximum relative difference in the predicted heat transfer rate as a function of the number of cells. The error decreases rapidly as the mesh is refined and becomes lower than the selected 0.5% tolerance at $n = 50$. Figure 4.20 shows the corresponding maximum absolute differences in the CO_2 and water-glycol outlet temperatures. At $n = 50$, both temperature deviations are below the 0.1 $°C$ tolerance.

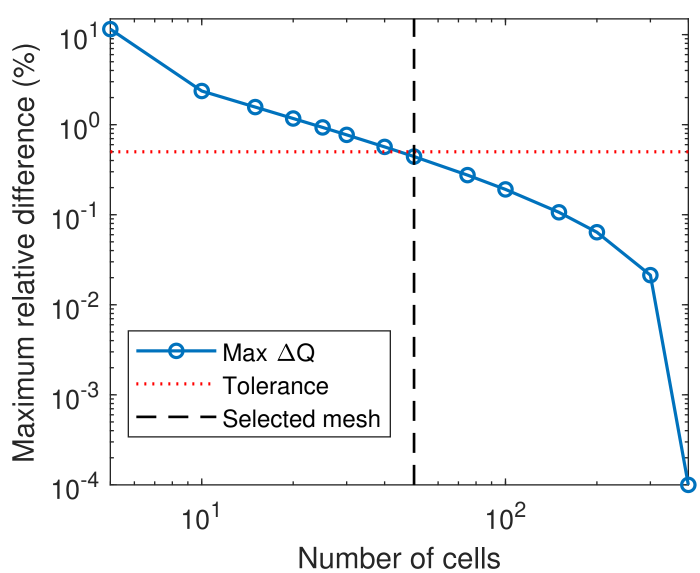

Figure 4.19 Mesh-independence analysis of the GC model based on the maximum relative difference in heat transfer rate

Based on this analysis, $n = 50$ cells is selected for the GC model. At this discretization, the

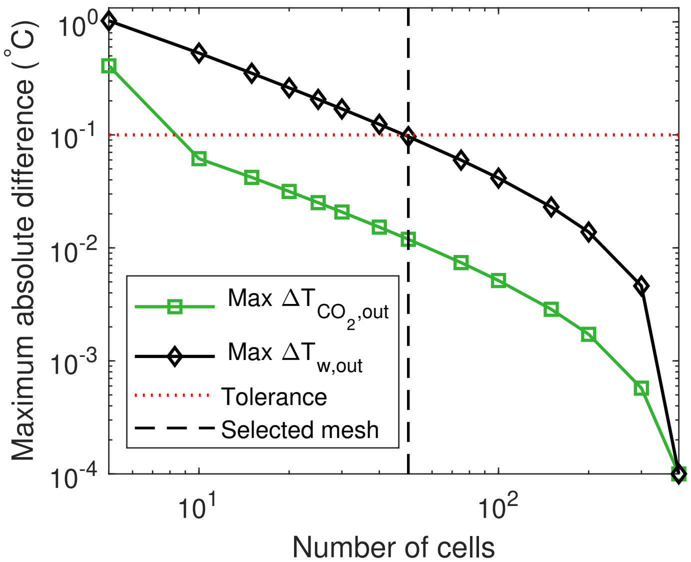

Figure 4.20 Mesh-independence analysis of the GC model based on the maximum absolute difference in CO_2 and water-glycol outlet temperatures

maximum deviation over all tested GC operating points is 0.4% for the heat transfer rate, 0.01 $°C$ for the CO_2 outlet temperature, and 0.09 $°C$ for the water-glycol outlet temperature. Therefore, further refinement of the GC mesh is not expected to affect the validation results significantly, while the selected mesh avoided unnecessary computational cost.

CHAPTER 5 ARTICLE 2: Map-based supervisory control strategies of a single-pipe CO_2 thermal network connected to local heat pumps

Authors: Sepehr Gholamrezaie, Massimo Cimmino, Parham Eslami-Nejad

Journal: Energy and Buildings

Date: Submitted 19 February 2026

5.1 Abstract

This paper investigates supervisory control for a single-pipe CO_2 thermal network (CO_2TN) that supplies the source side of multiple local heat pumps (LHPs) in a multi-zone building. The network comprises a reversible CO_2 vapor compression circulation unit coupled to a ground loop heat exchanger, with all LHPs connected in series on a single CO_2 loop. Two supervisory strategies are formulated and compared. The minimum-mass-flow strategy enforces two phase operation along the loop and selects the smallest CO_2 mass flow that satisfies the aggregate zone demand. The temperature-bounded strategy constrains loop temperatures within a narrow band around saturation, permitting limited single-phase operation to shift the cycle toward thermodynamically favorable states. Both strategies are implemented using an offline map, and executed online via lookup of the optimized decision variables. Annual co-simulation (TRNSYS + MATLAB tables) for a five-zone office building in Montréal shows that the temperature-bounded strategy improves performance relative to minimum mass flow: the mean time-step COP_{sys} increases from 3.08 to 3.75 (+22.1%), the median from 2.95 to 4.27 (+44.7%), and $SPF_{sys,ann}$ from 2.98 to 3.65 (+22.3%).

5.2 Introduction

In multi-zone buildings, heating and cooling demands differ from zone to zone, so heat pumps are an attractive choice. The present study examines a networked architecture in which local heat pumps (LHPs) draw from a common source whose operating conditions are actively controlled. The system is a closed, single-pipe loop that circulates two phase CO_2 (R-744) to the source side of multiple packaged LHPs, a concept introduced as the CO_2 Thermal Network (CO_2TN) by Eslami-Nejad et al. [12].

Figure 5.1 illustrates the CO_2TN, which functions similarly to a cascade heat-pump system built around a single, two phase CO_2 loop shared by multiple LHPs. The CO_2 loop is maintained at an intermediate pressure P_{loop}; this pressure sets the saturation temperature of the circulating two phase CO_2 and therefore the effective source/sink temperature that supplies all LHPs. CO_2 enters the loop (Point 4 in the heating-mode cycle and Point 5 in the cooling-mode cycle) and then flows in series past the LHP units (LHP-1 to LHP-4). At each interface, the corresponding LHP exchanges heat with the loop before the working fluid continues downstream to the next unit. As heat is absorbed from, or rejected to, the loop, the CO_2 quality x and enthalpy change from one LHP to the next, while the loop temperature remains largely governed by P_{loop} because the fluid stays close to saturation. Depending on whether the overall operation is heating-dominant or cooling-dominant, the CO_2 loop can be on the low-pressure side (heating) or on the high-pressure side (cooling), with the LHPs operating on the opposite side when they act against the dominant mode. This single-pipe, series arrangement enables direct heat recovery among zones, because heat added to the loop by one LHP can be carried downstream and used by another.

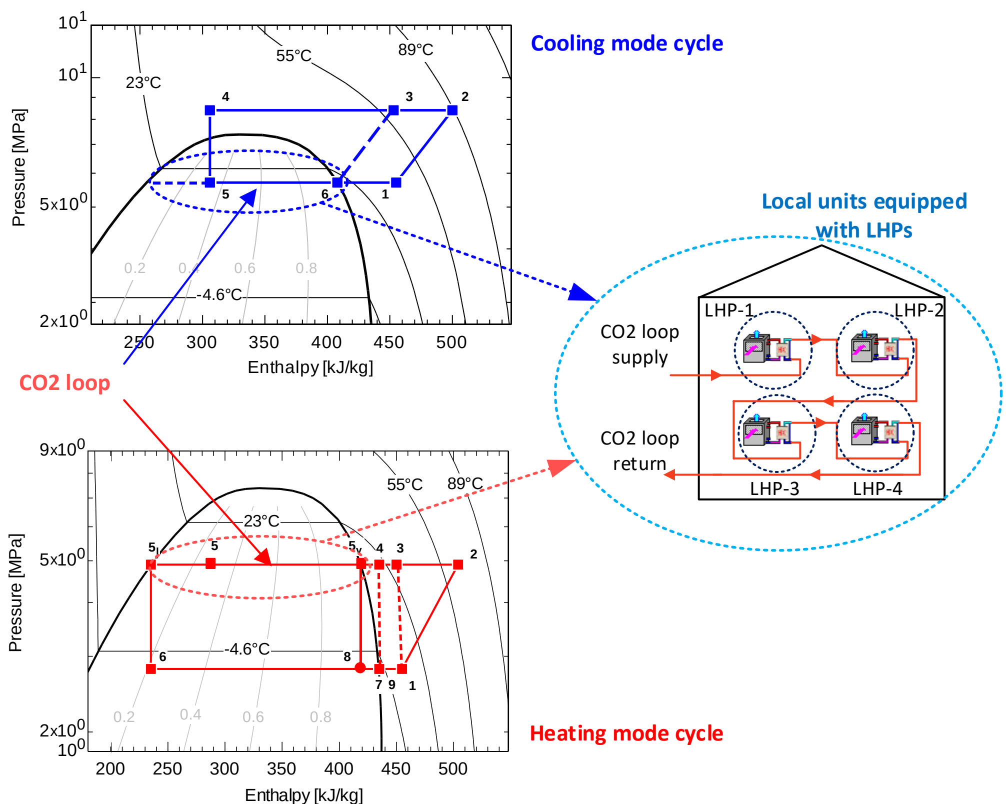

Figure 5.1 CO_2 thermal network (CO_2TN) connected to local heat pumps (LHP)

This architecture offers several advantages relative to conventional hydronic loops: use of a natural refrigerant (GWP = 1, ODP = 0), reduced pipe diameters due to latent-heat transport and favorable CO_2 properties, source temperatures close to ambient with modest axial variation (which eases LHP control and reduces insulation needs), and straightforward interzone heat recovery at approximately constant source temperature. The centralized outdoor unit can also be coupled to renewable or low-grade sources (e.g. geothermal).

Peer-reviewed CO_2TN studies are converging on three themes: control design, experimental feasibility, and model validation. On the control side, Gholamrezaie et al. [75] introduced a heating-mode framework with a minimum-mass-flow supervisory rule that calculates loop vapor quality and selects the lowest circulation rate that preserves two phase conditions across the loop over seasonal operation. A key limitation, however, is that the loop pressure remained fixed and was not a control variable, even though pressure directly governs system performance. Extending to transcritical cooling, a follow-up parametric study quantified the sensitivity of network performance to compressor speed, discharge pressure (gas-cooler setpoint), and loop pressure, and identified near-optimal combinations for given gas-cooler conditions [77]. The study showed that, in some cases, the system achieves its best performance when the CO_2 partially enters the single-phase region along the CO_2 loop. Experimentally, Bastani and Gholamrezaie [24] demonstrated a first prototype with three packaged LHPs (a CO_2-to-water and two CO_2-to-air LHP) supplied by a single-pipe, two phase CO_2 loop, confirming the concept and showing that circulation-unit setpoints—especially discharge pressure and gas-cooler control—strongly influence efficiency and stability. Building on these data, Gholamrezaie et al. [14] assembled a modular CO_2TN model and validated it at component and system levels for both cooling and heating operation modes.

Although the topology is novel, the control problem of CO_2TN involves essentially the same decision variables as a stand-alone transcritical CO_2 heat pump. Device-level studies consistently show that discharge (high-side) pressure, gas-cooler water-side conditions (inlet temperature and flow rate), compressor speed/frequency, and expansion-side control (Electronic expansion Valve opening, i.e. suction superheat) are the dominant levers for COP and capacity.

The central theme is that the COP-optimal discharge pressure is not a constant value. It shifts with boundary conditions—especially with gas-cooler outlet temperature—so model-based supervision outperforms fixed rules under varying weather and loads [17]. Zhang et al. [114] combined theory and experiments to show a clear COP maximum versus high-side pressure, arising from the trade-off between increased heat rejection and rising compression work. They found that the optimal discharge pressure depends mainly on the gas-cooler outlet temperature, with evaporating temperature and compressor characteristics that affect compression work (e.g. isentropic efficiency and its variation with pressure ratio) playing secondary roles, and they demonstrated that controlling evaporator-outlet superheat (via throttling architecture) stabilizes the suction condition needed to realize the high-side pressure.

Compressor speed strongly interacts with the discharge-pressure selection. Qin et al. [115] varied inverter-compressor frequency and showed that speed primarily modulates refrigerant mass flow and mechanical efficiency. COP displays a peak versus discharge pressure at each condition, and they provided a dimensionless correlation for the optimal pressure with small error. They also reported hot-water outlet temperatures exceeding 80°C at favorable points without sacrificing COP—evidence that compressor speed should be coordinated with the high-side pressure to meet temperature and capacity targets efficiently. Complementing this, Wei et al. [116] optimized frequency-conversion control on an experimental platform and quantified gains of up to 6.35% in COP and 3.11% shorter heating time relative to a baseline strategy.

Expansion valve control matters because it regulates the compressor-inlet superheat and therefore stabilizes the suction state under which the target high-side pressure is achievable. In Zhang et al. [114], the two-stage throttling arrangement decouples high-side pressure regulation from compressor-inlet superheat regulation, showing that maintaining a stable suction condition enables high-side optimization rather than competing with it.

Water-side conditions (i.e. the gas-cooler inlet temperature and the circulating mass flow) govern the gas-cooler outlet temperature, which in turn strongly influences the discharge-pressure optimum. In practice, the outlet temperature is bounded below by the approach to the inlet-water temperature and varies with water mass flow. Sensitivity and parametric studies consistently show that raising the inlet temperature or reducing the flow shifts the optimal pressure and lowers COP, whereas higher flow at a given inlet temperature sustains a lower refrigerant outlet temperature and increases the enthalpy drop across the gas cooler [17,117]. Taken together, these studies indicate that the discharge-pressure setpoint is most effectively controlled as a function of the measured gas-cooler outlet temperature—hence indirectly of the water inlet temperature and mass flow—while compressor speed is coordinated with the pressure set point to meet load with minimal impact on COP, and expansion valve adjustments maintain a suction-superheat band. Reported gains include several-percent increases in COP and faster attainment of water-side targets.

Supervisory coordination strategies for vapor compression systems can be organized along two main dimensions. The first dimension is the setpoint generation mechanism, setpoints are either computed online through an optimization or adaptation routine, or precomputed offline and executed online through a map or lookup table. The second dimension is the information basis, the supervisor is either model-based (an explicit plant or surrogate model predicts performance and constraints) or model-free (setpoints are adapted primarily from measurements) [118]. These two dimensions define four common families: online model-based optimization, online model-free optimization, offline model-based map execution, and offline data-driven map execution.

Online model-based approaches generate supervisory setpoints by solving a constrained optimization problem at each control update using an explicit model of the plant. In building HVAC, the dominant realization of this idea is model predictive control (MPC), in which a reduced-order physics model or an identified state-space model is used to predict zone and equipment dynamics over a prediction horizon; the controller then selects the control moves that minimize a cost function that typically balances comfort-tracking errors and energy (or demand) penalties while respecting actuator, rate, and comfort constraints, and applies the first move in a receding-horizon manner [119,120]. Because HVAC and heat pump plants combine nonlinear thermodynamics with discrete operating logic, reported MPC implementations span linear MPC and nonlinear MPC, and also include mixed-integer MPC formulations that explicitly represent on/off decisions, staging, or mode switching [119,121]. In vapor compression cycles, MPC has also been formulated directly at cycle level as a multivariable controller that coordinates coupled manipulated variables through a constrained optimization on a reduced-order cycle model [122]. For transcritical CO_2 heat pumps, this framework is particularly relevant because efficiency hinges on coordinated manipulation of the heat-rejection pressure and other actuators [52, 53]; for example, Wang et al. [51] implemented MPC for a transcritical CO_2 air-source heat-pump water heater, where the controller predicts future operation and computes optimal inputs (including water-side mass flow and expansion-valve openings) to maximize COP subject to system constraints, providing a model-based alternative to conventional PI (proportional–integral) loops paired with correlation-based optimal-pressure references. At larger supervisory layers (multi-equipment plants or district/community energy), online optimization-based dispatch is frequently posed as mixed-integer linear programming (MILP), which can encode equipment availability, technology choices, and operating logic while remaining computationally tractable for real-time scheduling [57,123–125].

Online model-free approaches pursue the same objective of self-optimization but adapt setpoints directly from measurements, for example by extremum-seeking strategies that iteratively adjust pressure setpoints to improve COP without an explicit plant model [126,127]. These methods can be attractive when models are uncertain; however, convergence speed and robustness can degrade when the optimum moves quickly with boundary conditions, or when the feasible region is tight and strongly constraint-limited, as is common in transcritical operation and envelope-bounded compressors.

Offline map-based supervision precomputes a feasible operating envelope indexed by the dominant variables (e.g. high- and low-side pressures, compressor speed, and source/sink temperatures). Online execution then reduces to fast selection or interpolation on this envelope rather than solving an online optimization. This family includes classic optimal-pressure correlations for transcritical CO_2 operation [65] as well as model- or data-generated performance maps used as surrogates. Recent digital-twin frameworks often fit into a hybrid form: maps are identified or updated offline (or periodically), while an online planning optimizer (often MILP) uses those maps to choose operating targets [128]. In that sense, digital twins are best viewed as online optimization enabled by offline-built surrogates.

The CO_2TN supervisory problem considered here is constraint-driven and contains both discrete and continuous decisions: the multi-zone thermostat command vector is discrete (OFF/HEAT/COOL per zone), whereas pressures, compressor speed, and staging are continuous or hybrid. In addition, feasibility is governed by hard operating limits (compressor envelope, phase/temperature bounds along a series loop, and heat-exchanger capability under imposed secondary-side conditions). Under these characteristics, offline model-based map execution is a practical and robust choice: it allows feasibility screening and constraint enforcement to be performed offline with a validated model, while online control remains deterministic and computationally light for implementation on a PLC.

In this classification, the supervisory controllers studied here belong to the offline model-based, map-executed family: a validated steady-state model is used to enumerate feasible operating points over the dominant levers and to select near-optimal setpoints subject to compressor-envelope and system constraints. Specifically, the present study (i) reconstructs and extends the baseline minimum-mass-flow method from previous work [77] to year-round operation (heating and cooling) and completes it by considering all performance-critical variables—most notably including loop pressure, together with the discharge/suction-pressure setpoint and compressor speed—so that operation remains within the feasible envelope with near-optimal efficiency. Building on this enhanced baseline, we then (ii) introduce a temperature-bounded supervisory controller that searches the same feasible map while allowing bounded departures from strictly two phase operation to enlarge the feasible set, and (iii) evaluate year-round efficiency in transient simulations to compare the two methods.

5.3 System Description

5.3.1 System Overview

Figure 5.2 illustrates the CO_2TN and its connection to the LHPs. The diagram shows both the physical components of the system and the associated control signals. Conceptually, the network can be regarded as a heat pump connected to other heat pumps. Each building zone is equipped with a thermostat and a dedicated LHP to condition the space. On the source side, all LHPs are connected in series to a single-pipe, two phase CO_2 loop. This configuration facilitates heat recovery between zones: when an LHP operates in heating mode, it absorbs heat from the CO_2 loop; when in cooling mode, it rejects heat to the loop. To maintain system balance, the CO_2 loop is coupled to a reversible vapor compression cycle (RVCC), which functions similarly to a stand-alone CO_2 heat pump. The RVCC ensures that the total energy absorbed or rejected by the LHPs is compensated. This section includes a variable-speed and a fixed-speed compressor, an internal heat exchanger (IHE) that transfers heat from the discharge to the suction line to maintain superheat, a pressure-regulating valve (PRV), electronic valves (EVs), and a CO_2 receiver. Additional components exchange heat with the environment to stabilize loop operation. In particular, the desuperheater (DSPHTR) and the outdoor unit provide heat rejection or absorption when system experiences a net surplus or deficit. The outdoor unit consists of a CO_2-to-secondary-fluid heat exchanger (OU-HX) connected to a secondary loop that exchanges heat with the ground. Overall, the CO_2TN integrates the circulation loop, the RVCC, and the LHPs to enable simultaneous heating and cooling while promoting heat recovery between zones.

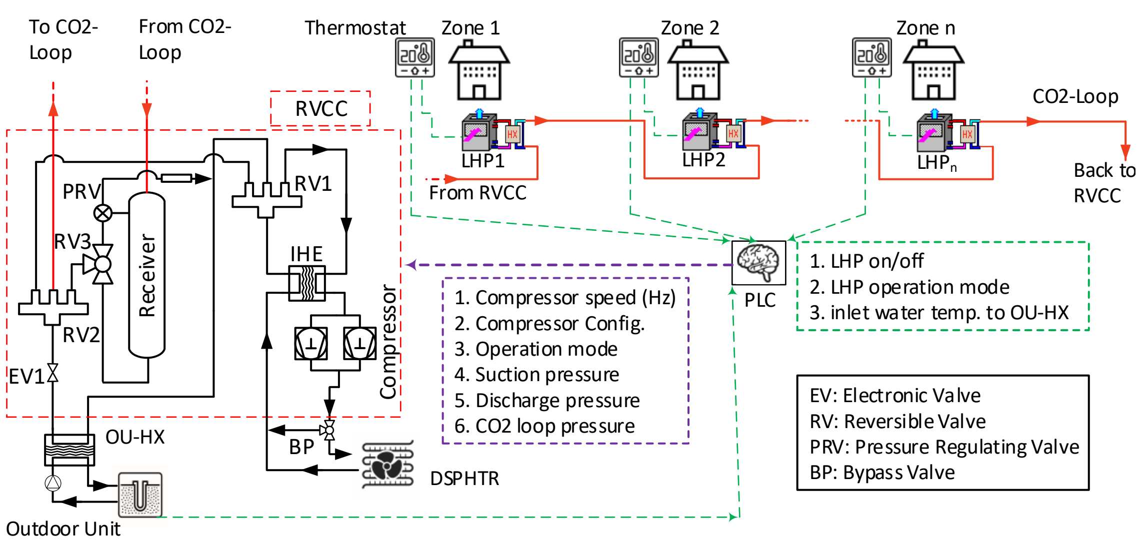

Figure 5.2 System schematic and control signals of the CO_2TN

5.3.2 Operational Modes

The system operates with two main thermodynamic configurations, determined by the net heat exchange with the CO_2 loop: heating-dominant (net heat extraction from the loop) and cooling-dominant (net heat rejection to the loop). In the heating-dominant mode, the LHPs collectively extract net heat from the CO_2 loop. Figure 5.3 presents both the process flow diagram and the corresponding pressure–enthalpy diagram of this configuration. In this mode, the cycle operates under subcritical conditions, since additional pressure is not required for heat rejection. Consequently, the CO_2-loop pressure is equal to the system discharge pressure. The cycle begins at point 1, where the compressor raises the CO_2 to the discharge/loop pressure (point 2). Between points 2 and 3, the DSPHTR cools the refrigerant. From points 3 to 4, the internal heat exchanger (IHE) transfers heat from the discharge line to the suction side, ensuring adequate superheat at the compressor inlet (points 9 to 1). After the IHE, at point 4, the CO_2 enters the single-pipe loop. The flow then returns to the receiver at point 5, where liquid (point 5_l) is separated from the remaining vapor (point 5_v). The liquid expands through an expansion device (EV1) toward the OU-HX (from 5_l to point 6), while the flashed vapor from the receiver is directed to the suction line (point 8). The OU, acting as an evaporator in this configuration, absorbs heat from the secondary fluid, converting the CO_2 from point 6 to saturated vapor at point 7. At point 9, this vapor mixes with the flashed vapor from the receiver (point 8). The combined stream then passes through the IHE, where it absorbs additional heat, reaching the required superheat before returning to the compressor suction at point 1.

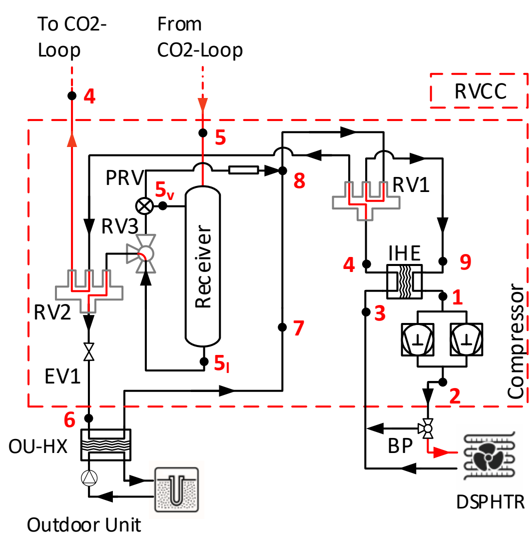

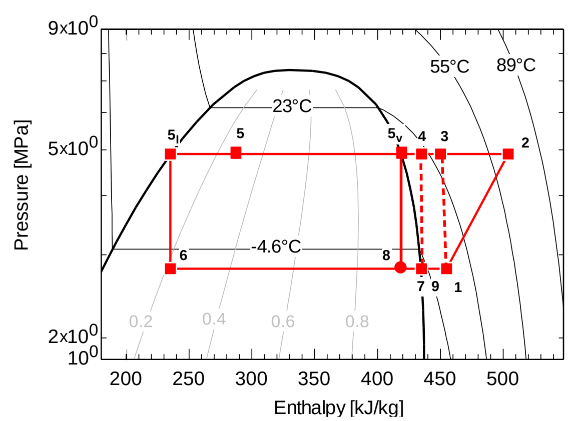

Figure 5.3 Heating-dominant mode: process flow diagram (left) and pressure-enthalpy (P-h) diagram (right)

In the cooling-dominant mode, the LHPs collectively reject net heat to the CO_2 loop. Figure 5.4 presents the process flow diagram and the corresponding pressure–enthalpy diagram for this configuration. In this mode, the cycle operates under transcritical conditions, with the discharge pressure adjusted to achieve effective heat rejection. Consequently, the CO_2-loop pressure is equal to the system suction pressure. The cycle begins at point 1, where the compressor raises the CO_2 pressure to the transcritical discharge level (point 2). From points 2 to 3, the refrigerant bypasses the DSPHTR and passes directly through the IHE. Here, heat is transferred from the high-pressure discharge line to the suction side, ensuring sufficient superheat at the compressor inlet (points 6 to 1). After the IHE, at point 3, the CO_2 flows to the OU-HX, where it rejects heat to the ground through a secondary water-glycol loop. The refrigerant then expands from point 4 to point 5 through the electronic expansion valve (EV1), reducing its pressure to the loop level. At point 5, the CO_2 enters the single-pipe CO_2 loop, where heat exchange occurs with the LHPs. In cooling-dominant operation, most LHPs reject heat to the loop, causing the CO_2 to evaporate. The dashed line in the P-h diagram indicates the possibility that some LHPs may operate in heating mode, potentially condensing the CO_2 locally. However, the dominant effect remains evaporation due to the majority of LHPs operating in cooling mode. Finally, at point 6, the refrigerant returns from the CO_2 loop to the receiver. Any remaining liquid is assumed to be vaporized in the IHE (from points 6 to 1), where it absorbs heat from the discharge stream. This process ensures that the flow entering the compressor suction is superheated, thereby completing the cycle.

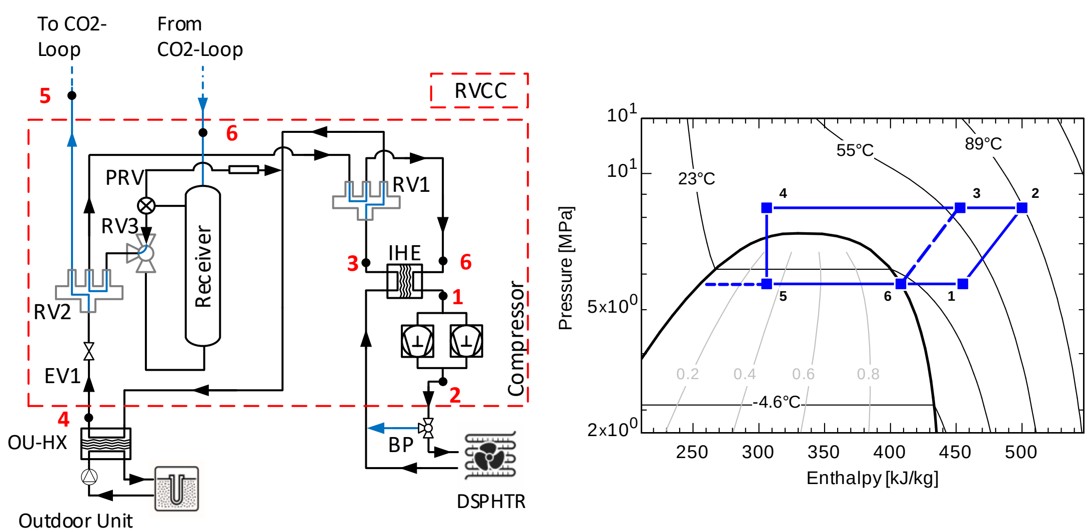

Figure 5.4 Cooling-dominant mode: process flow diagram (left) and pressure-enthalpy (P-h) diagram (right)

5.3.3 Control Parameters

To ensure sustainable and optimal operation of the CO_2TN, a programmable logic controller (PLC) regulates the system by processing input signals and generating appropriate control actions. As shown in Figure 5.2, the input signals originate from the thermostats installed in each zone, which indicate the status of the LHPs (on/off) and their operating mode (heating or cooling), as well as from a temperature sensor at the outlet of the geothermal loop that measures the inlet water temperature to the OU-HX. Combined with the rated capacity of the LHPs, this information enables the PLC to determine the configuration of the compressors, including whether one or both units are operating and the speed of the variable-speed compressor. The PLC also selects the system's operation mode by modulating the valves to configure the RVCC accordingly, regulates the suction and discharge pressures by adjusting the electronic expansion valves, controls the DSPHTR fan speed to reject specified amount of heat, and sets the water mass flow rate ($\dot{m}_w$) in the secondary loop of the OU by adjusting the pump speed.

5.4 Model

This study evaluates supervisory control strategies for a CO_2TN by combining a validated component and system model with dynamic building simulation. The CO_2TN model builds upon a modular framework previously validated against an experimental setup [14]. Here, we restate only the elements required to reproduce the control study and to generate supervisory operating maps. In the presented models, CO_2 thermophysical properties are computed with CoolProp [102] using the Span–Wagner equation of state [103]. The system consists of an RVCC connected to a single-pipe, two phase CO_2 loop that serves the source side of packaged LHPs. Major components include building zones, LHPs, circulation compressor, heat exchangers, and the geothermal unit.

5.4.1 Building zones

Each thermal zone is represented with a lumped-capacitance model implemented in TRNSYS Type 690. While the component can convert prescribed sensible and latent loads into air temperature and humidity ratio, the present study considers sensible effects only and reports temperature dynamics. Latent handling remains available in Type 690 but is not considered here. The component advances a single first-order energy balance for the zone air temperature T_z. With user-specified thermal capacitance C_z [kJ/K] and a ventilation stream characterized by mass flow $\dot{m}_{vent}$, supply temperature T_{vent}, and air specific heat $c_{p,air}$, the governing equation is

$$C_z \frac{dT_z}{dt} = \dot{m}_{vent}\, c_{p,air} \Big(T_{vent} - T_z\Big) \;+\; \dot{Q}_{sens} \tag{5.1}$$

where $\dot{Q}_{sens}$ is the prescribed net sensible heat gain of the zone, excluding the conditioning provided by the LHPs. The model outputs the trajectory $T_z(t)$, which is provided to the rest of the simulation.

The model assumes a single, well-mixed air node with no stratification. Envelope losses, infiltration, internal radiative/convective splits, and occupant/equipment gains are not computed explicitly; their effects are embedded in the externally supplied load. Thermal capacitance and air properties are treated as constant over each time step. Ventilation is modeled as a controlled external stream acting on the lump; other mass exchanges are ignored.

For implementation, externally generated time series of $\dot{Q}_{sens}$ are provided to Type 690 along with zone-specific capacity (C_z). For ventilation, the air mass flow rate $\dot{m}_{vent}$ and the temperature T_{vent} are specified in the following section, where the LHP modeling is described (Eq. (5.12)). Finally, Type 690 numerically integrates Eq. (5.1) to produce $T_z(t)$.

5.4.2 Local heat pumps (LHPs)

Each LHP is modeled as a steady-state, low-lift vapor compression heat pump exchanging heat with the zone (load side) and the CO_2 loop (source side). Low-lift operation is selected because the CO_2 loop delivers a relatively warm and stable source temperature—typically 10–25°C—so minimizing temperature lift yields higher COP. This choice also aligns with the experimental low-lift R290 reciprocating unit reported by Gasser et al. [129], which is taken here as a representative technology. LHP performance is approximated as a fixed fraction of the corresponding Carnot COP, using prescribed approach (pinch) temperatures on both heat exchangers and enforcing a minimum temperature lift to avoid unrealistically small lifts.

In heating mode, the LHP delivers heat to the zone and extracts heat from the CO_2 loop. The heating COP is written as follows:

$$\mathrm{COP}_H(T_{loop,i}) \;=\; \eta_H \, \frac{T^K_{cond,H}(T_{loop,i})}{T^K_{cond,H}(T_{loop,i}) - T^K_{evap,H}(T_{loop,i})} \qquad \eta_H = 0.55 \;\; [129] \tag{5.2}$$

where $\mathrm{COP}_H(T_{loop,i})$ is the coefficient of performance of LHP i in heating mode, $T_{loop,i}$ is the CO_2 loop temperature at that LHP, and η_H is the adopted Carnot-efficiency factor (fraction of the ideal Carnot COP). $T^K_{evap,H}$ and $T^K_{cond,H}$ are the LHP evaporation and condensation temperatures in heating mode (in K), respectively.

To relate the CO_2 loop temperature to the refrigerant-side evaporation temperature, we assume that the source-side heat exchanger operates with a fixed pinch, so the evaporation temperature is approximated as the loop temperature minus the pinch. To avoid extrapolating the adopted low-lift performance assumptions, the loop temperature is clipped to a stated validity range:

$$T^{\circ C}_{evap,H}(T_{loop,i}) = \mathrm{clip}(T_{loop,i}; 10, 27) - \Delta T_{pp,HP} \tag{5.3}$$
$$T^{\circ C}_{cond,H}(T_{loop,i}) = \max\Big(T_{s,H} + \Delta T_{pp,HP},\ T^{\circ C}_{evap,H}(T_{loop,i}) + \Delta T_{\min,H}\Big) \tag{5.4}$$

where $\Delta T_{pp,HP}$ is the assumed approach temperature (pinch) on each heat exchanger, $T_{s,H}$ is the hot-air supply temperature setpoint in heating mode, and $\Delta T_{\min,H}$ is the enforced minimum heating lift. The $\max(\cdot)$ operator sets the condensing temperature to the larger of (i) the value required to deliver the supply setpoint with the prescribed pinch on the load side, $T_{s,H}+\Delta T_{pp,HP}$, and (ii) the value required to satisfy the minimum lift, $T^{\circ C}_{evap,H}+\Delta T_{\min,H}$. The clip operator is defined as $\mathrm{clip}(x; a, b) = \min\{\max(x, a),\, b\}$. In this study, $T_{s,H} = 32\,^{\circ}\mathrm{C}$, $\Delta T_{pp,HP} = 3\,\mathrm{K}$, and $\Delta T_{\min,H} = 15\,\mathrm{K}$.

In cooling mode, the LHP removes heat from the zone and rejects it to the CO_2 loop. The cooling COP is written as

$$\mathrm{COP}_C(T_{loop,i}) \;=\; \eta_C \,\frac{T^{K}_{evap,C}(T_{loop,i})}{T^{K}_{cond,C}(T_{loop,i}) - T^{K}_{evap,C}(T_{loop,i})}, \qquad \eta_C = 0.55 \;\; [129] \tag{5.5}$$

where $\mathrm{COP}_C(T_{loop,i})$ is the COP of LHP i in cooling mode, η_C is the Carnot-efficiency factor in cooling, and $T^{K}_{evap,C}$ and $T^{K}_{cond,C}$ are the evaporation and condensation temperatures in cooling mode (in K). On the load side, the evaporating temperature is set by the chilled-air supply setpoint with the prescribed pinch. On the source side, the condensing temperature is approximated as the loop temperature plus the pinch, with the same clipping and a minimum lift constraint:

$$T^{\circ C}_{evap,C}(T_{loop,i}) = T_{s,C} - \Delta T_{pp,HP} \tag{5.6}$$
$$T^{\circ C}_{cond,C}(T_{loop,i}) = \max\Big(\mathrm{clip}(T_{loop,i}; 10, 27) + \Delta T_{pp,HP},\ T^{\circ C}_{evap,C}(T_{loop,i}) + \Delta T_{\min,C}\Big) \tag{5.7}$$

where $T_{s,C}$ is the chilled-air supply setpoint in cooling mode and $\Delta T_{\min,C}$ is the enforced minimum cooling lift. In this study, $T_{s,C} = 12\,^{\circ}\mathrm{C}$, $\Delta T_{pp,HP} = 3\,\mathrm{K}$, and $\Delta T_{\min,C} = 10\,\mathrm{K}$.

The model assumes negligible pressure drop within the LHP; and stepwise steady-state behavior within each simulation time step. Start-up transients, and small auxiliaries are not represented explicitly and are embedded in the Carnot efficiency factors η_H, η_C.

At design stage, a nominal CO_2 loop temperature $T_{nom} = 15°C$ is specified, and each LHP is sized so that—at $T_{loop,i} = T_{nom}$ and at the load-side setpoint—the nameplate capacity matches the zone's peak requirement. During simulation, the instantaneous electrical input is obtained from the COP:

$$\dot{W}_{HP,i} = \begin{cases} \dfrac{\dot{Q}_{HP,H,i}}{\mathrm{COP}_H(T_{loop,i})} & \text{heating mode,} \\ \dfrac{\dot{Q}_{HP,C,i}}{\mathrm{COP}_C(T_{loop,i})} & \text{cooling mode,} \end{cases} \tag{5.8}$$

where $\dot{W}_{HP,i}$ is the electrical power input to the i-th LHP, and $\dot{Q}_{HP,H,i}$ and $\dot{Q}_{HP,C,i}$ are its heating and cooling capacities, respectively.

The signed heat exchange between the i-th LHP and the CO_2 loop is then obtained by combining the load-side capacity with the corresponding COP. With the sign convention that $\dot{Q}_{loop,i} > 0$ denotes heat rejected to the loop and $\dot{Q}_{loop,i} < 0$ denotes heat extracted from the loop, the exchange is

$$\dot{Q}_{loop,i} = \begin{cases} -\dot{Q}_{HP,H,i}\left(1 - \dfrac{1}{\mathrm{COP}_H(T_{loop,i})}\right) & \text{heating mode,} \\ +\dot{Q}_{HP,C,i}\left(1 + \dfrac{1}{\mathrm{COP}_C(T_{loop,i})}\right) & \text{cooling mode,} \\ 0 & \text{off,} \end{cases} \tag{5.9}$$

In this study, $\dot{Q}_{HP,H,i}$ and $\dot{Q}_{HP,C,i}$ are taken as the peak sensible heating and cooling loads of zone i, i.e. the nominal capacities required to meet the design peaks at the nominal loop temperature.

An energy balance on the LHP enables the evaluation of the outlet enthalpy of CO_2. In heating mode,

$$\dot{Q}_{HP,H,i} - \dot{W}_{HP,i} = \dot{m}_{CO_2}\Big(h_{HP,in,i} - h_{HP,out,i}\Big) \tag{5.10}$$

and in cooling mode,

$$\dot{Q}_{HP,C,i} + \dot{W}_{HP,i} = \dot{m}_{CO_2}\Big(h_{HP,out,i} - h_{HP,in,i}\Big) \tag{5.11}$$

where $h_{HP,in,i}$ and $h_{HP,out,i}$ are the inlet and outlet CO_2 enthalpies on the source side (CO_2 loop) of the i-th LHP, respectively.

To calculate the LHP supply-air temperature, the ventilation air mass flow rate $\dot{m}_{vent}$ is assumed constant because the LHP fans operate at a fixed speed. Therefore, the LHP supply-air temperature is computed as follows:

$$T_{vent,i} = \begin{cases} T_{z,i} + \dfrac{\dot{Q}_{HP,H,i}}{\dot{m}_{vent} c_{p,air}} & \text{heating mode,} \\ T_{z,i} - \dfrac{\dot{Q}_{HP,C,i}}{\dot{m}_{vent} c_{p,air}} & \text{cooling mode,} \end{cases} \tag{5.12}$$

For implementation, the structure of TRNSYS Type 919 (originally for water-to-air HPs) is adapted to accept a two phase CO_2 source. At each time step, inputs are $\dot{m}_{CO_2}$, $h_{HP,in,i}$, and P_{loop} on the source side together with load-side setpoints ($T_{s,H}$ or $T_{s,C}$). The model returns $\dot{Q}_{HP,\cdot,i}$ and $\dot{W}_{HP,i}$ consistent with the current lift; then Eqs. (5.10) or (5.11) is applied to compute $h_{HP,out,i}$.

5.4.3 Compressor

We adopt the polynomial compressor maps introduced in [14], fitted to manufacturer data for a semi-hermetic R744 reciprocating unit. The maps calculate power input $\dot{W}_{comp}$ and mass flow $\dot{m}_{CO_2}$ as functions of suction pressure P_{suc}, discharge pressure P_{dis}, and compressor speed S (Hz):

$$\begin{aligned} X = {} & a_1 + a_2 \cdot S + a_3 \cdot S^2 + a_4 \cdot S^3 + a_5 \cdot P_{dis} + a_6 \cdot P_{dis}^2 + a_7 \cdot P_{dis}^3 \\ & + a_8 \cdot P_{suc} + a_9 \cdot P_{suc}^2 + a_{10} \cdot P_{suc}^3 + a_{11} \cdot S \cdot P_{dis} + a_{12} \cdot S \cdot P_{dis}^2 \\ & + a_{13} \cdot S \cdot P_{suc} + a_{14} \cdot S \cdot P_{suc}^2 + a_{15} \cdot S^2 \cdot P_{dis} + a_{16} \cdot S^2 \cdot P_{dis}^2 \\ & + a_{17} \cdot S^2 \cdot P_{suc} + a_{18} \cdot S^2 \cdot P_{suc}^2 + a_{19} \cdot P_{dis} \cdot P_{suc} + a_{20} \cdot P_{dis} \cdot P_{suc}^2 \\ & + a_{21} \cdot P_{dis}^2 \cdot P_{suc} + a_{22} \cdot P_{dis}^2 \cdot P_{suc}^2 \end{aligned} \tag{5.13}$$

where X is either $\dot{W}_{comp}$ (kW) or $\dot{m}_{CO_2}$ (kg/h) depending on the coefficient set.

In this study, we use two compressors that are geometrically similar to the mapped unit but have exactly half the displacement (one fixed-speed at $S = 60\,\text{Hz}$ and one variable-speed over $S \in [30, 75]\,\text{Hz}$). Under geometric similarity for positive-displacement machines, volumetric flow and indicated power scale linearly with displacement at fixed (P_{suc}, P_{dis}, S). Table 5.1 lists the scaled coefficients used in Eq. (5.13).

5.4.4 Heat exchangers

Heat exchanger geometries, correlations, and solution procedures follow Gholamrezaie et al. [14]. The model includes a water–CO_2 plate heat exchanger (OU-HX), an air–CO_2 heat

Table 5.1 Compressor model coefficients for half-displacement unit (values are baseline coefficients from [14] divided by two).

Coefficient	Power input	Mass flow rate
a_1	1.19E+1	1.72E+2
a_2	3.65E-2	3.68E+0
a_3	-4.37E-4	-3.85E-2
a_4	-9.95E-7	1.19E-4
a_5	-2.96E-3	-9.20E-2
a_6	1.46E-7	3.68E-6
a_7	3.34E-13	-3.46E-11
a_8	-5.15E-3	-9.20E-2
a_9	5.05E-7	1.40E-5
a_{10}	2.41E-13	-3.16E-10
a_{11}	1.52E-5	8.50E-5
a_{12}	-7.55E-10	-1.58E-8
a_{13}	-4.25E-5	-6.50E-4
a_{14}	4.81E-9	1.90E-7
a_{15}	-8.80E-8	-1.88E-6
a_{16}	6.40E-12	1.54E-10
a_{17}	4.63E-7	1.22E-5
a_{18}	-5.35E-11	-1.20E-9
a_{19}	1.37E-6	2.21E-5
a_{20}	-1.46E-10	-2.76E-9
a_{21}	-7.05E-11	-1.16E-9
a_{22}	7.85E-15	1.38E-13

exchanger (DSPHTR), and a CO_2–CO_2 plate heat exchanger (IHE). Note that a 30% glycol–water mixture flows in counterflow with CO_2 in the OU-HX. All heat exchangers are treated as adiabatic with negligible pressure drop, and the local overall conductance is evaluated using the cited, regime-dependent correlations.

In supercritical or superheated operation (gas cooler (GC)), the exchanger is discretized into n counterflow identical cells and three coupled relations are solved in each cell:

$$\dot{q}_i = \dot{m}_{CO_2} \Big(h_{i-1} - h_i\Big) \tag{5.14}$$

where $\dot{q}_i$ is the heat transferred in cell i (positive from CO_2 to water), $\dot{m}_{CO_2}$ is the CO_2 mass flow rate, and h_{i-1} and h_i are the CO_2 specific enthalpies at the cell inlet and outlet, respectively. The water-side energy balance is written as

$$\dot{q}_i = \dot{m}_w \, c_{p,w} \Big(T_{w,i} - T_{w,i-1}\Big) \tag{5.15}$$

where $\dot{m}_w$ is the water mass flow rate, $c_{p,w}$ is the local (assumed constant) water specific heat, and $T_{w,i}$ and $T_{w,i-1}$ are the water temperatures at the cell inlet and outlet. The cellwise heat-transfer relation closes the system,

$$\dot{q}_i = U_i \frac{A}{n} \left(T_{CO_2,i} - T_{w,i-1} \right) \tag{5.16}$$

where U_i is the local overall heat-transfer coefficient, A is the total exchanger area, n is the number of cells, $T_{CO_2,i}$ is the CO_2 outlet temperature from cell i, and $T_{w,i-1}$ is the counter-flow water temperature at the opposing node. The total heat-transfer rate is then

$$\dot{Q} = \sum_{i=1}^{n} \dot{q}_i \tag{5.17}$$

where $\dot{Q}$ denotes the exchanger heat-transfer rate. Boundary conditions are imposed as $h_0 = h_{in}$ on the CO_2 side and $T_{w,n} = T_{w,in}$ on the water side.

When the OU-HX operates as a subcritical condenser, a moving-boundary formulation partitions the exchanger into superheated, two phase, and subcooled regions whose areas satisfy

$$A = A_{\text{sup}} + A_{\text{sat}} + A_{\text{sub}} \tag{5.18}$$

where A is the total area and A_{sup}, A_{sat}, and A_{sub} are the areas assigned to the superheated, saturated, and subcooled regions. For each region, the heat rate is evaluated using an effectiveness–NTU relation,

$$\dot{q}_{reg} = \varepsilon_{reg}\, C_{\min,reg} \left(T_{h,in} - T_{c,in} \right) \tag{5.19}$$

where $\dot{q}_{reg}$ is the regional heat-transfer rate and ε_{reg} is the effectiveness. For each thermodynamic region, a specific ε_{reg} relation is used, as introduced in [14]. Moreover, $C_{\min,reg} = \min(C_h, C_c)$ with $C_{h/c} = \dot{m}_{h/c} c_{p,h/c}$ the hot/cold heat-capacity rates, and $T_{h,in}$ and $T_{c,in}$ are the regional inlet temperatures of the hot and cold streams. The effectiveness follows the counter-flow formula written in terms of

$$\text{NTU}_{reg} = \frac{U_{reg} A_{reg}}{C_{\min,reg}}, \qquad C_{r,reg} = \frac{C_{\min,reg}}{C_{\max,reg}} \tag{5.20}$$

where U_{reg} and A_{reg} are the overall coefficient and area of the region. The total heat transfer rate of the heat exchanger is the sum of the regional heat rates as follows:

$$\dot{Q} = \sum_{reg \in \{\mathrm{sup}, \mathrm{sat}, \mathrm{sub}\}} \dot{q}_{reg} \tag{5.21}$$

When the OU-HX operates as an evaporator, the heat-transfer rate is computed with an effectiveness–NTU model and enforced consistency with the stream balances,

$$\dot{Q} = \varepsilon \, C_{\min} \Big(T_{w,in} - T_{CO_2,in} \Big), \qquad \varepsilon = 1 - \exp(-\mathrm{NTU}), \qquad \mathrm{NTU} = \frac{UA}{C_{\min}} \tag{5.22}$$

$$\dot{Q} = \dot{m}_{CO_2} \left(h_{out} - h_{in} \right) = \dot{m}_w \, c_{p,w} \left(T_{w,in} - T_{w,out} \right) \tag{5.23}$$

where $\dot{Q}$ is the exchanger heat rate, ε is the effectiveness, $C_{\min} = \min(C_h, C_c)$ is the minimum heat-capacity rate, $T_{w,in}$ and $T_{CO_2,in}$ are the inlet temperatures of water and CO_2, NTU is the number of transfer units, U is the overall coefficient, A is the area, h_{in} and h_{out} are the CO_2 inlet and outlet enthalpies, and $T_{w,out}$ is the water outlet temperature.

The DSPHTR is an air-CO_2 heat exchanger for which a detailed model is not developed in the present study. Instead, it is assumed that the DSPHTR is appropriately sized to reject the required heat rate to reach the specified outlet CO_2 enthalpy setpoint. This simplification is motivated by two considerations. First, the DSPHTR is only used in heating-dominant operation, i.e. under low outdoor-air temperatures, for which the CO_2 stream to be cooled is at a substantially higher temperature than the ambient air; under these conditions, adequate heat rejection can be achieved through a practical design, and the rejected heat rate can be modulated by adjusting the DSPHTR fan speed. Second, the scope of this work focuses on the CO_2-side thermodynamic behavior and supervisory control; fan power and air-side details are not modeled. As a result, a detailed DSPHTR design would not affect the predicted CO_2-side energy consumption or the supervisory-control conclusions.

The IHE is modeled as an adiabatic CO_2–CO_2 counter-flow heat exchanger, such that all heat rejected by the discharge stream is absorbed by the suction stream. Therefore, the two sides satisfy equal and opposite heat rates, which are used to enforce the target suction superheat.

$$\dot{Q}_{IHE,dis} = \dot{Q}_{IHE,suc} \tag{5.24}$$

$$\dot{Q}_{IHE,suc} = \dot{m}_{CO_2} \Big(h_{suc,out} - h_{suc,in} \Big) \tag{5.25}$$

$$\dot{Q}_{IHE,dis} = \dot{m}_{CO_2} \Big(h_{dis,in} - h_{dis,out} \Big) \tag{5.26}$$

where $\dot{Q}_{IHE,suc}$ and $\dot{Q}_{IHE,dis}$ are the suction- and discharge-side heat rates and $h_{suc,in/out}$ and $h_{dis,in/out}$ are the suction and discharge inlet/outlet enthalpies, respectively.

For implementation, the inputs are the CO_2 pressure, inlet enthalpy, and mass flow together with the water inlet temperature and mass flow; the solvers return the CO_2 outlet enthalpy and pressure and the water outlet temperature. Convergence is verified on maximum temperature change between iterations and on a heat-balance residual, consistent with [14].

5.4.5 Ground heat exchanger and borefield sizing

The CO_2TN exchanges heat with the ground through a water–glycol secondary loop coupled to vertical GHX modeled with TRNSYS Type 557a. The component represents U-tube or concentric-tube exchangers installed in vertical boreholes. Convection inside the pipes is coupled to radial conduction in the surrounding ground, which is treated as a cylindrical storage volume. The ground temperature response is obtained by superposition of a global term, a local term (both advanced in time with an explicit finite-difference scheme), and a steady-flux analytical term. Given inlet fluid temperature and mass flow from the plant, the model returns outlet temperature and heat rate each time step. Inputs include undisturbed ground temperature T_g, ground conductivity k_g and heat capacity, bore radius and depth, bore spacing, grout and pipe properties (including shank spacing), and fluid properties. These parameters are taken from the sizing described below and from literature data.

The borefield is sized with the Alternative ASHRAE method [130,131]. Three design ground-load pulses are considered: a long-term pulse (year-scale), an intermediate pulse (month-scale), and a short-term pulse (hour-scale). The corresponding pulse durations are denoted by Δt_y, Δt_m, and Δt_h. The cumulative end-times of these pulses are then defined as follows:

$$t_1 = \Delta t_y, \qquad t_2 = \Delta t_y + \Delta t_m, \qquad t_3 = \Delta t_y + \Delta t_m + \Delta t_h$$

With these definitions the effective ground resistances based on g-functions are

$$R_y = \frac{g(t_3) - g(t_3 - t_1)}{2\pi k_g}, \qquad R_m = \frac{g(t_3 - t_1) - g(t_3 - t_2)}{2\pi k_g}, \qquad R_h = \frac{g(t_3 - t_2)}{2\pi k_g}$$

The required total borefield length is

$$L = \frac{q_y\, R_y + q_m\, R_m + q_h\, R_h + q_h R_b}{\dfrac{T_{w,in} + T_{w,out}}{2} - T_g} \tag{5.27}$$

where q_y, q_m, and q_h are the yearly, monthly, and hourly design ground loads; R_b is the borehole thermal resistance; and $T_{w,in}$ and $T_{w,out}$ are the design inlet and outlet temperatures of the secondary fluid at the OU-HX, respectively. Because g-functions already embed thermal interaction among boreholes, no separate temperature-penalty term is needed in Eq. (5.27).

Loads can be supplied directly or derived from plant loads and COPs. The $g(\cdot)$ values depend on non-dimensional time and geometry. We evaluate g at t/t_s with $t_s = H^2/(9\alpha_s)$, where H is bore depth and α_s is the soil thermal diffusivity; geometry enters through ratios such as s/H where s is the center-to-center borehole spacing, and r_b/H and through the field layout. The borehole thermal resistance R_b is calculated using the first-order expression of the multipole equation (Eq. (13) in Ref. [132]). Equation (5.27) is solved iteratively because $g(\cdot)$ depends on H through t_s and the geometry ratios. In practice, the borefield layout and spacing are first fixed from site constraints, which define the admissible range for the number of boreholes N_b and the allowable borehole depth H. For a chosen value of N_b within this range, we (i) select an initial depth H (so that $L = N_b H$), (ii) evaluate the required g-functions for that layout at t_3, $t_3 - t_2$, and $t_3 - t_1$, (iii) compute R_y, R_m, R_h, and R_b, (iv) recalculate L from Eq. (5.27), and (v) update $H = L/N_b$. Steps (ii)–(v) are repeated until L (equivalently H) changes by less than a prescribed tolerance. If the converged depth H does not satisfy drilling or site constraints (for example, if it exceeds the maximum drillable depth), a new value of N_b is selected and the procedure is repeated. The final design provides N_b, per-bore depth H, spacing, R_b, and material properties, which are then passed to Type 557a_v2a for use in the dynamic system simulation.

5.5 Control strategies

The system comprises two layers: (i) packaged LHPs, each with its own refrigerant circuit and embedded controller, and (ii) a centralized CO_2TN that supplies the source side of all LHPs through a single-pipe loop. Each zone thermostat issues a discrete command (OFF/HEAT/COOL). In this work, the embedded LHP controllers are assumed to successfully track these local commands. The supervisory controller developed here governs the CO_2 network. Its objective is to operate near system-level optima for the prevailing loads and outdoor conditions. Controller inputs are the vector of zone commands and the inlet water temperature to the OU-HX. Controller outputs coordinate the circulation unit: compressor configuration and speed S, network operating mode, loop pressure P_{loop} (and P_{suc}, P_{dis} as applicable), DSPHTR fan command, and OU water mass flow rate.

A model-based supervisory approach with offline map generation and online lookup is adopted so that the circulation-unit setpoints can be selected in real time without solving an optimization problem. Offline, a validated CO_2TN model and equipment envelopes are used to enumerate representative operating requests, defined by the LHP command vector U_{HP} together with the boundary condition $T_{w,OU,in}$. For each pair $(U_{HP}, T_{w,OU,in})$, feasible circulation-unit setpoints $\mathbf{\Theta}$ are computed subject to compressor-envelope and system constraints, and the corresponding performance is evaluated. The resulting best feasible setpoint is stored in a supervisory lookup table that maps $(U_{HP}, T_{w,OU,in})$ to the control outputs of the CO_2TN. Online, the supervisory controller reads the current $(U_{HP}, T_{w,OU,in})$ at each control interval, retrieves the associated table entry, and applies the stored setpoints to the plant.

Two supervisory methods are proposed in this study to generate the offline lookup table of circulation-unit setpoints. The first method, referred to as the minimum mass flow (MM) method, searches for the loop pressure P_{loop} that yields the best system performance while enforcing a strictly two phase CO_2 loop. Among feasible candidates, the MM method selects the operating point that satisfies the two phase constraint with the minimum CO_2 mass flow rate. The second method, referred to as the temperature-bounded (TB) method, relaxes the strict two phase requirement and instead constrains the loop temperatures to remain within ± 10 K of saturation.

5.5.1 System-level objective and coefficient of performance

Both control strategies select circulation-unit setpoints that maximize the system coefficient of performance, COP_{sys}, subject to the equipment envelopes and feasibility constraints. At a generic operating point, the circulation compressor consumes $\dot{W}_{comp}$ and the i-th LHP consumes $\dot{W}_{HP,i}$ (Section 5.4.2). On the load side, the same i-th LHP delivers either heating or cooling to its zone. We denote the delivered heating and cooling rates by $\dot{Q}_{HP,H,i}$ and $\dot{Q}_{HP,C,i}$, respectively, with the convention that at most one of these two quantities is non-zero at a given operating point and both are zero when the unit is OFF. With this convention, the total useful thermal rate delivered by the LHP array is defined as follows:

$$\dot{Q}_{HP} = \sum_{i=1}^{n_{HP}} \left(\dot{Q}_{HP,H,i} + \dot{Q}_{HP,C,i} \right) \tag{5.28}$$

The total electrical input to the CO_2TN is

$$\dot{W}_{tot} = \dot{W}_{comp} + \sum_{i=1}^{n_{HP}} \dot{W}_{HP,i} \tag{5.29}$$

The system coefficient of performance is then defined as

$$\mathrm{COP}_{sys} = \frac{\dot{Q}_{HP}}{\dot{W}_{tot}} \tag{5.30}$$

5.5.2 Water-side mass flow at the OU

The OU water mass flow rate, $\dot{m}_{w,OU}$, sets the water-side boundary condition of the OU-HX and affects the compressor suction and discharge pressures through the achievable heat transfer. To evaluate the OU-HX consistently during offline map generation and annual simulations, a water-side operating condition must be specified. In this work, $\dot{m}_{w,OU}$ is computed using simple correlations. The objective of these correlations is not to optimize pumping energy, but to maintain feasible operation with respect to the compressor envelope over a wide range of distributed load conditions.

A key difficulty in distributed systems is that a single constant water mass flow cannot be suitable for all LHP activation patterns. If $\dot{m}_{w,OU}$ is too low, the OU-HX may not be able to reject (or absorb) the required heat at the specified water inlet temperature, and the controller may be forced to increase (or decrease) the compressor pressure ratio, which can push the operating point outside the envelope. Conversely, if $\dot{m}_{w,OU}$ is too high when only a small number of LHPs are active, the OU-HX can remove more heat than needed, which can overcool the CO_2 relative to the target condition and may drive the corresponding discharge pressure toward the lower envelope bound. For this reason, the correlations explicitly depend on the number of active LHPs on the dominant mode, n_{HP}, so that the water flow decreases when fewer LHPs are operating. The correlations are constructed from a bound on the OU heat-transfer rate. For a given number of active LHPs, the required OU heat-transfer rate is estimated as follows:

$$\dot{Q}_{OU} = n_{HP}\, \dot{Q}_{LHP,ref} \tag{5.31}$$

where $\dot{Q}_{LHP,ref}$ is a reference capacity chosen as an upper bound on any individual LHP capacity (taken as the largest LHP in the case study). This assumption provides a conservative estimate for each value of n_{HP}.

The OU water mass flow rate is computed in both operating modes from the water-side energy balance,

$$\dot{m}_{w,OU} = \frac{\dot{Q}_{OU}}{c_{p,w}\left(T_{w,OU,out} - T_{w,OU,in}\right)} \tag{5.32}$$

where $c_{p,w}$ is the water specific heat, $T_{w,OU,in}$ is provided by the secondary loop, and the OU heat rate is conservatively estimated from Eq. (5.31). For the extreme combinations of $(T_{w,OU,in}, n_{HP})$ considered in this study, the only unknown in Eq. (5.32) is therefore the outlet water temperature $T_{w,OU,out}$. In this work, $T_{w,OU,out}$ is determined through a one-dimensional search using the OU-HX model evaluated at limiting conditions (i.e. edges of the feasible operating domain), such that the resulting $\dot{m}_{w,OU}$ remains feasible over the full range of operating points encountered during annual simulations. Once this search is completed, a conservative value of $T_{w,OU,out}$ is selected and fixed for each operating mode.

In cooling-dominant operation, the OU-HX acts as a gas cooler. The search for $T_{w,OU,out}$ is conducted under cooling-limit conditions representative of the loop-pressure bounds and compressor-envelope edges, while enforcing numerical convergence of the GC model and a CO_2 outlet condition consistent with the supervisory temperature bounds. A conservative value of $T_{w,OU,out}$ is then selected and fixed for cooling mode, and the corresponding $\dot{m}_{w,OU}$ follows from Eq. (5.32) during map construction and annual simulations.

In heating-dominant operation, the OU-HX acts as an evaporator. The search for $T_{w,OU,out}$ is conducted under heating-limit conditions, including the most restrictive suction-side operating point on the compressor envelope, while enforcing numerical convergence of the evaporator model and the evaporator outlet requirement (fully evaporated CO_2 at the prescribed suction condition). A conservative value of $T_{w,OU,out}$ is then selected and fixed for heating mode, and the corresponding $\dot{m}_{w,OU}$ is computed from Eq. (5.32).

The resulting water-flow curves used in the case study are reported in Section 5.6.1. It is worth noting that beyond feasibility, $\dot{m}_{w,OU}$ also directly influences the compressor operating pressures because it sets the OU-HX water-side approach temperature and therefore the attainable CO_2 outlet condition. In cooling-dominant operation, increasing $\dot{m}_{w,OU}$ generally improves the gas-cooler heat rejection for a fixed $T_{w,OU,in}$, which can reduce the discharge pressure required to satisfy the supervisory CO_2 outlet constraint. In heating-dominant operation, increasing $\dot{m}_{w,OU}$ improves the evaporator heat absorption, which can relax the suction-side requirement by enabling the target evaporator outlet state to be achieved at a higher suction pressure (i.e. less restrictive low-pressure operation) for the same $T_{w,OU,in}$. These benefits, however, come at the expense of higher secondary-loop pumping power, which would reduce the overall system COP when included. Because this study focuses on CO_2-side operation and the secondary-loop pump was not modeled, $\dot{m}_{w,OU}$ is not optimized with respect to pumping energy; instead, it is selected conservatively to ensure feasibility across the operating domain. A systematic optimization that trades off compressor electricity and secondary-loop pumping power is therefore left for future work.

5.5.3 Dual-compressor coordination (circulation unit)

Circulation of CO_2 is provided by two compressors: a variable-speed (VS) unit driven by an inverter, with speed $S \in [30, 75]$ Hz, and a fixed-speed (FS) unit operating nominally at 60 Hz. The variable $U_{FS} \in \{0, 1\}$ denotes the on/off command of the fixed-speed compressor, with $U_{FS} = 1$ when the FS compressor is enabled and $U_{FS} = 0$ when it is disabled.

The coordination between the two follows a staged logic. Operation starts with the FS unit off ($U_{FS} = 0$) and the VS compressor running at its minimum speed ($S = 30$ Hz). As the required CO_2 mass flow increases, the VS speed is ramped up towards 75 Hz. If the maximum VS speed is reached and additional flow is still required, the FS compressor is switched on ($U_{FS} = 1$), the VS speed is reset to 30 Hz to avoid an excessive overshoot in mass flow, and then the VS speed is increased again as needed. When the required mass flow decreases from a two-compressor operating point, the reverse sequence is applied. The VS speed is first reduced down to its minimum value of 30 Hz while keeping the FS compressor on. If a further reduction in mass flow is needed, the FS compressor is switched off ($U_{FS} = 0$) and the VS compressor is temporarily set to 75 Hz to compensate for the lost displacement, after which the VS speed is ramped down as required to meet the lower flow demand. In this way, low and medium flow demands are covered by the VS machine alone, while the FS unit is engaged only for high-flow operation. The step changes in CO_2 mass flow associated with enabling or disabling the FS compressor are accepted in this study as a practical compromise.

The CO_2 mass flow rate, and the corresponding compressor work is expressed as follows:

$$\dot{m}_{CO_2}(S, P_{suc}, P_{dis}, U_{FS}) = X(S, P_{suc}, P_{dis}) + U_{FS}\, X(60 \text{ Hz}, P_{suc}, P_{dis}) \tag{5.33}$$

$$\dot{W}_{comp}(S, P_{suc}, P_{dis}, U_{FS}) = X(S, P_{suc}, P_{dis}) + U_{FS}\, X(60 \text{ Hz}, P_{suc}, P_{dis}) \tag{5.34}$$

where $X(S, P_{suc}, P_{dis})$ is the compressor map defined in Eq. (5.13).

5.5.4 Minimum-mass-flow method (MM)

Control problem

For a given LHP command vector $\boldsymbol{U_{HP}} \in \{-1, 0, +1\}^n$ (HEAT/OFF/COOL) and OU-HX inlet water temperature $T_{w,OU,in}$, the MM method treats the loop pressure P_{loop} as the decision variable and selects the operating point that maximizes the system efficiency. For each candidate value of P_{loop}, the loop inlet state is closed by enforcing strictly two phase operation and by computing the corresponding minimum CO_2 mass flow rate $\dot{m}^*_{CO_2}$ required to accommodate the aggregate heat exchange along the CO_2 loop. This minimum mass flow is therefore enforced through the model closure (i.e. as an equality constraint) while COP_{sys} remains the objective used to select the best feasible P_{loop}. The decision vector is expressed as follows:

$$\boldsymbol{\Theta} \; = \; \{P_{loop}, P_{suc}, P_{dis}, S, U_{FS}, Mode\} \tag{5.35}$$

where $\boldsymbol{\Theta}$ is the decision vector. The corresponding optimization problem is as follows:

$$
\begin{aligned}
\max_{\boldsymbol{P_{loop}}} \quad & \mathrm{COP}_{sys}(\boldsymbol{\Theta}, \boldsymbol{U_{HP}}, T_{w,OU,in}) \\
\text{s.t.} \quad & h^*_{in,loop} = f_1(P_{loop}, \boldsymbol{U_{HP}}) \\
& \dot{m}^*_{CO_2} = f_2(P_{loop}, \boldsymbol{U_{HP}}) \\
& (P_{suc}, P_{dis}) \in \mathcal{E}_{\mathrm{comp}} \\
& S \in [30, 75] \text{ Hz} \\
& U_{FS} \in \{0, 1\}
\end{aligned}
\tag{5.36}
$$

where $h^*_{in,loop}$ is the target loop inlet enthalpy, $\dot{m}^*_{CO_2}$ is the corresponding minimum loop mass flow rate, and $\mathcal{E}_{\mathrm{comp}}$ is the compressor envelope. Note that, in this problem, the only free variable in Eq. (5.35) that is optimized is P_{loop}; f_1 and f_2 are equality constraints evaluated using Eqs. (5.39)-(5.42).

Offline map construction

For a candidate loop pressure P_{loop}, the saturation temperature $T_{sat}(P_{loop})$ sets the effective source temperature seen by all LHPs. For each zone i, the LHP model (Sec. 5.4.2) provides the signed heat exchange with the CO_2 loop, $\dot{Q}_{loop,i}$, as defined in Eq. (5.9). Traversing the zones in their physical single–pipe order yields the cumulative net heat exchange as follows:

$$
\dot{Q}_{net,i} = \sum_{j=1}^{i} \dot{Q}_{loop,j} \tag{5.37}
$$

We define

$$
H = |\min_i(\dot{Q}_{net,i})|, \qquad C = |\max_i(\dot{Q}_{net,i})| \tag{5.38}
$$

as the maximum absolute net cumulative heat extracted from the loop (heating branch) and injected into the loop (cooling branch), respectively. Let $h_f(P_{loop})$ and $h_g(P_{loop})$ denote the saturated–liquid and saturated–vapor enthalpies at P_{loop}. The inlet enthalpy that minimizes the loop mass flow while keeping the loop two–phase is the weighted average

$$
h^*_{in,loop} = \frac{h_g(P_{loop})\, H + h_f(P_{loop})\, C}{H + C} \tag{5.39}
$$

with inlet quality as follows:

$$
x_{in,loop} = \frac{h^*_{in,loop} - h_f(P_{loop})}{h_g(P_{loop}) - h_f(P_{loop})} \in (0, 1) \tag{5.40}
$$

and targeted minimum CO_2 mass flow as follows:

$$\dot{m}^*_{CO_2} = \frac{H}{h^*_{in,loop} - h_f(P_{loop})} = \frac{C}{h_g(P_{loop}) - h^*_{in,loop}} \tag{5.41}$$

In the limiting cases of all–cooling ($H \to 0$) or all–heating ($C \to 0$) the mass flow is defined as follows:

$$\dot{m}^*_{CO_2} = \begin{cases} \dfrac{C}{h_g(P_{loop}) - h_f(P_{loop})}, & H \to 0 \quad \text{(all-cooling)} \\ \dfrac{H}{h_g(P_{loop}) - h_f(P_{loop})}, & C \to 0 \quad \text{(all-heating)} \end{cases} \tag{5.42}$$

The pressure pair (P_{suc}, P_{dis}) is computed from the candidate loop pressure P_{loop} and the target loop inlet enthalpy $h^*_{in,loop}$. Because the circulation configuration differs between cooling-dominant and heating-dominant operation, the corresponding pressure-closure relations are defined on a mode-specific basis. The operating mode is selected according to the criteria introduced in Section 5.3.2.

In cooling-dominant operation, the CO_2 loop is on the low-pressure side; therefore, the compressor suction pressure equals the loop pressure,

$$P_{suc} = P_{loop} \tag{5.43}$$

The loop inlet state corresponds to the GC outlet, and the expansion to P_{loop} is assumed isenthalpic. Hence, the loop inlet enthalpy is related to the discharge pressure as

$$h^*_{in,loop} = h_{out,GC}(P_{dis}) \tag{5.44}$$

where $h_{out,GC}$ is the CO_2 enthalpy at the GC outlet computed by the heat-exchanger model for the current water-side conditions. The discharge pressure P_{dis} is obtained by solving (5.44) for P_{dis} using a one-dimensional root-finding method, with the admissible search interval restricted to the compressor envelope $(P_{suc}, P_{dis}) \in \mathcal{E}_{comp}$ (with P_{suc} fixed by Eq. (5.43)).

In heating-dominant operation, the cycle is subcritical and the discharge pressure equals the loop pressure,

$$P_{dis} = P_{loop} \tag{5.45}$$

The receiver at the loop outlet separates the return flow into saturated vapor and saturated liquid. Therefore, the liquid stream leaving the receiver is saturated at P_{loop}; thus, the evaporator (OU-HX) inlet enthalpy is

$$h_{in,evap} = h_f(P_{loop}) \tag{5.46}$$

and the expansion to P_{suc} is isenthalpic. The suction pressure is obtained by enforcing saturated vapor at the evaporator (OU-HX) outlet. Accordingly, P_{suc} is defined by

$$h_{out,evap}(P_{suc}) = h_g(P_{suc}) \tag{5.47}$$

where $h_{out,evap}(P_{suc})$ is the evaporator outlet enthalpy calculated by the OU-HX evaporator model for the given inlet state and water-side conditions, and $h_g(P_{suc})$ is the saturated-vapor enthalpy at P_{suc}. Therefore, P_{suc} is calculated using a root-finding method, with the admissible search interval restricted to the compressor envelope.

Finally, in heating-dominant operation the loop inlet enthalpy $h^*_{in,loop}$ is the state downstream of the discharge-side heat exchangers (DSPHTR followed by IHE). The IHE extracts the amount of heat required to ensure suction superheat at the compressor inlet ($\dot{Q}_{IHE}$). Because the DSPHTR precedes the IHE on the discharge line, the DSPHTR rejects the remaining discharge-side heat required to match the target loop inlet enthalpy $h^*_{in,loop}$, which yields as:

$$\dot{Q}_{DSPHTR} = (\dot{m}_{CO_2} \cdot (h_{dis} - h^*_{in,loop})) - \dot{Q}_{IHE} \tag{5.48}$$

Here, $\dot{Q}_{DSPHTR}$ is modulated by regulating the DSPHTR fan speed on the air side.

Once $h^*_{in,loop}$ and $\dot{m}^*_{CO_2}$ have been determined for a given P_{loop}, the pressure closure relations specified above provide the corresponding pressure pair (P_{suc}, P_{dis}). The remaining task is then to select the compressor staging and speed commands (S, U_{FS}) that deliver a CO_2 mass flow rate as close as possible to the target $\dot{m}^*_{CO_2}$ while respecting the compressor limits. First, the fixed-speed (FS) compressor command is determined for the known pressure pair (P_{suc}, P_{dis}) and the target $\dot{m}^*_{CO_2}$ as follows:

$$U_{FS} = \begin{cases} 0 & \dot{m}^*_{CO_2} \leq X(75 \text{ Hz}, P_{suc}, P_{dis}) \\ 1 & \text{otherwise} \end{cases} \tag{5.49}$$

where $X(S, P_{suc}, P_{dis})$ is the compressor mass flow map (Eq. (5.13)). In the second step, the VS compressor speed S is chosen so that the total delivered mass flow matches the target $\dot{m}^*_{CO_2}$ as closely as possible while respecting the admissible speed range. Let $X^{-1}(\cdot, P_{suc}, P_{dis})$ denote the inverse of X with respect to S at fixed (P_{suc}, P_{dis}), i.e. it returns the speed required for the VS compressor to deliver a specified mass flow. The VS speed command is therefore computed by subtracting the FS contribution from the target and inverting the VS map:

$$S = \mathrm{clip}\Big(X^{-1}\Big(\dot{m}^*_{CO_2} - (U_{FS} \cdot X(60\ \mathrm{Hz}, P_{suc}, P_{dis})), P_{suc}, P_{dis}\Big)\,; 30, 75\Big) \tag{5.50}$$

The realized loop mass flow rate $\dot{m}_{CO_2}$ can differ from the target value $\dot{m}^*_{CO_2}$ because compressor staging is discrete and the VS speed is bounded. This mismatch occurs in particular around the transition between one-compressor and two-compressor operation. The staged logic enables the FS compressor only after the VS compressor reaches 75 Hz, and the logic resets the VS speed to 30 Hz when the FS compressor is enabled. As a result, the minimum attainable two-compressor mass flow equals $X(60\ \mathrm{Hz}, P_{suc}, P_{dis}) + X(30\ \mathrm{Hz}, P_{suc}, P_{dis})$, whereas the maximum attainable one-compressor mass flow equals $X(75\ \mathrm{Hz}, P_{suc}, P_{dis})$. Any target in the interval cannot be matched exactly by the staged actuation, and the implemented mass flow becomes larger than the target.

The optimization problem (5.36) is solved offline by treating P_{loop} as the main decision variable. For each input pair $(\boldsymbol{U_{HP}}, T_{w,OU,in})$, a discrete set of loop pressures, $P_{loop} \in [4.7, 6.7]$ MPa in 0.2 MPa increments is scanned. At every candidate P_{loop}, the quantities $h^*_{in,loop}$, $x_{in,loop}$, and $\dot{m}^*_{CO_2}$ are computed from Eqs. (5.39)–(5.42). The rest of the corresponding decision vector $\boldsymbol{\Theta}$, $(P_{suc}, P_{dis}, S, U_{FS})$ is obtained by solving the heating or cooling pressure closure (Eqs. (5.44), (5.47)); and the resulting COP_{sys} is evaluated using Eq. (5.30)

Once (5.36) is solved for a given pair $(\boldsymbol{U_{HP}}, T_{w,OU,in})$, the corresponding decision vector $\boldsymbol{\Theta^*}$ along with COP_{sys} are stored as the minimum–mass–flow operating point for that condition. Repeating this procedure over all combinations of the LHP command vector $\boldsymbol{U_{HP}}$ and the OU-HX inlet water temperature $T_{w,OU,in}$, with $T_{w,OU,in}$ varied from 5 to 25,°C, produces the lookup table used by the supervisory controller. The resulting lookup table is defined as follows:

$$\mathcal{T}_{\mathrm{MM}} = \Big\{\boldsymbol{U_{HP}}, T_{w,OU,in}, \boldsymbol{\Theta}^*, \mathrm{COP}^*_{sys}\Big\} \tag{5.51}$$

Online lookup

During system operation, the controller reads the current zone-command vector $\boldsymbol{U_{HP}}$ and the measured OU-HX inlet water temperature $T_{w,OU,in}$, retrieves the corresponding entry in $\mathcal{T}_{\mathrm{MM}}$, and applies the stored setpoints $\boldsymbol{\Theta}^*$ to the circulation unit. The integration of $\mathcal{T}_{\mathrm{MM}}$ into the annual TRNSYS simulations is described in Section 5.6.2.

5.5.5 Temperature-bounded method (TB)

Control problem

The temperature-bounded (TB) method relaxes the strict two phase requirement of the MM strategy while maintaining the operation by constraining the loop temperature to remain in a narrow band around saturation. The decision vector is the same as for the MM method (Eq. (5.35)). For a given LHP command vector $\boldsymbol{U_{HP}}$ and outdoor unit inlet water temperature $T_{w,OU,in}$, the supervisory problem is defined as follows:

$$
\begin{aligned}
\max_{\boldsymbol{\Theta}} \quad & \mathrm{COP}_{sys}(\boldsymbol{\Theta}, \boldsymbol{U_{HP}}, T_{w,OU,in}) \\
\text{s.t.} \quad & T_{HP,i,out}(\boldsymbol{\Theta}) \ \geq \ T_{sat,f}(P_{loop}) - \Delta T \\
& T_{HP,i,out}(\boldsymbol{\Theta}) \ \leq \ T_{sat,g}(P_{loop}) + \Delta T \\
& (P_{suc}, P_{dis}) \in \mathcal{E}_{\mathrm{comp}} \\
& S \in [30, 75] \text{ Hz} \\
& U_{FS} \in \{0, 1\}
\end{aligned}
\tag{5.52}
$$

where $T_{HP,i,out}$ is the CO_2 outlet temperature of LHP i, $T_{sat,f}$ and $T_{sat,g}$ are the saturated liquid and saturated vapor temperatures at P_{loop}, and $\Delta T = 10$ K defines the temperature bounds. The choice $\Delta T = 10$ K is motivated by the circulation compressor recommendation adopted in this study, which targets approximately 10 K of suction superheat for stable operation. This superheat can be provided partly by the IHE and partly by the loop itself when the loop exits the LHP array in a mildly superheated state, in which case the required IHE contribution is reduced. The TB method therefore imposes symmetric bounds of ± 10 K around saturation so that the upper bound permits up to 10 K of superheat, while the lower bound allows an equivalent margin on the subcooled side. In words, the TB method seeks the most efficient operating point whose minimum and maximum loop temperatures remain within $\pm\Delta T$ of saturation.

Solving Eq. (5.52) directly in real time would require exploring many combinations of P_{loop}, P_{suc}, P_{dis}, S and U_{FS} and repeatedly calling the detailed component models. To make the problem tractable, the procedure is decomposed into two stages. First, a base table is constructed that maps a representation of the loop heat exchange and a candidate compressor operating point to the corresponding system COP, while enforcing the compressor envelope. This base table acts as a discretized surrogate model of the circulation unit: it is generated once, without reference to any particular LHP array or OU-HX inlet temperature, and depends only on an aggregated six–component heat exchange vector $\dot{\mathbf{Q}}$ and the compressor settings. As a result, it can be built at relatively low computational cost and reused for any building configuration. Second, this base table is combined with the full system model to solve Eq. (5.52) for all relevant combinations of $(\boldsymbol{U_{HP}}, T_{w,OU,in})$, yielding a final supervisory table that has the same structure as the MM lookup table and is the only object queried at the online stage.

Surrogate model

The base table implements the mapping described as follows:

$$(\dot{\mathbf{Q}}, \boldsymbol{\Theta}) \longrightarrow \Big(\mathrm{COP}_{sys},\ T_{\min},\ T_{\max}\Big) \tag{5.53}$$

where $\boldsymbol{\Theta} = \{P_{loop}, P_{suc}, P_{dis}, S, U_{FS}, Mode\}$ is the decision vector, and the vector of $\dot{\mathbf{Q}}$ is defined as follows:

$$\dot{\mathbf{Q}} = \Big[\dot{Q}_{C,\mathrm{sub}},\ \dot{Q}_{C,2\phi},\ \dot{Q}_{C,\mathrm{sup}},\ \dot{Q}_{H,\mathrm{sub}},\ \dot{Q}_{H,2\phi},\ \dot{Q}_{H,\mathrm{sup}}\Big] \tag{5.54}$$

where $\dot{Q}_{C,\mathrm{sub}}$, $\dot{Q}_{C,2\phi}$, and $\dot{Q}_{C,\mathrm{sup}}$ denote the net heat rejected to the CO_2 loop by all zones operating in cooling while the loop state lies in the subcooled, two phase, and superheated regions respectively. Likewise, $\dot{Q}_{H,\mathrm{sub}}$, $\dot{Q}_{H,2\phi}$, and $\dot{Q}_{H,\mathrm{sup}}$ denote the net heat extracted from the loop by all zones operating in heating in the same three regions. By convention, $\dot{Q}_{C,r} \geq 0$ and $\dot{Q}_{H,r} \leq 0$ for $r \in \{\mathrm{sub}, 2\phi, \mathrm{sup}\}$. This six component preserves the information required by the surrogate model: it determines the extreme enthalpies (and therefore $T_{\min}$ and $T_{\max}$) used to enforce the temperature bounds, and it provides region-wise representative loop temperatures used by the LHP performance model.

For a given pair $(\dot{\mathbf{Q}}, \boldsymbol{\Theta})$, the system COP is evaluated using Eq. (5.30), but with an explicit decomposition of the LHP electrical power by thermodynamic region. The dual–compressor maps provide the circulation power and the CO_2 mass flow rate from Eqs. (5.33), (5.34). Representative loop temperatures are assigned to each region as follows:

$$T_{2\phi} = T_{\mathrm{sat}}(P_{loop}) \tag{5.55}$$

$$T_{\mathrm{sub}} = \tfrac{1}{2}\Big[T\Big(P_{loop}, h_{\min}\Big) + T\Big(P_{loop}, h_f\Big)\Big] \tag{5.56}$$

$$T_{\mathrm{sup}} = \tfrac{1}{2}\Big[T\Big(P_{loop}, h_g\Big) + T\Big(P_{loop}, h_{\max}\Big)\Big] \tag{5.57}$$

where $T_{2\phi}$, T_{sub}, and T_{sup} are region-wise CO_2 loop temperatures for the two phase, subcooled, and superheated regions, respectively. $T_{\mathrm{sat}}(P_{loop})$ is the saturation temperature at the loop pressure P_{loop}, and $T(P,h)$ denotes the CO_2 temperature obtained from the equation of state at pressure P and specific enthalpy h. The extrema $h_{\min}$ and $h_{\max}$ denote the minimum and maximum specific enthalpies reached along the loop for the considered operating point (defined below), so that T_{sub} averages the temperatures associated with $h_{\min}$ and h_f, and T_{sup} averages those associated with h_g and $h_{\max}$.

These temperatures represent the arithmetic average of the enthalpy endpoints in each single phase region, and the saturation temperature in the two phase region. The corresponding heating and cooling COPs for each region are obtained from Eqs. (5.2) and (5.5). Using the notation in Eq. (5.54), the region wise electrical inputs are written as

$$\dot{W}_{HP,C,r} = \frac{\dot{Q}_{C,r}}{\text{COP}_C(T_r)+1}, \qquad \dot{W}_{HP,H,r} = -\frac{\dot{Q}_{H,r}}{\text{COP}_H(T_r)-1} \tag{5.58}$$

The total LHP electrical power ($\dot{W}_{HP}$) is then calculated as follows:

$$\dot{W}_{HP} = \sum_{r\in\{\text{sub},2\phi,\text{sup}\}} \Big(\dot{W}_{HP,C,r} + \dot{W}_{HP,H,r}\Big) \tag{5.59}$$

The overall performance metric used in the table is calculated from Eq. (5.30).

To build the base table, the variables $\dot{\mathbf{Q}}$ and $\boldsymbol{\Theta}$ are swept over discrete grids while enforcing compressor constraints, together with a cap on the total exchanged heat. Under the assumption that the loop inlet always lies in the two–phase region, the most subcooled and most superheated enthalpy levels reached anywhere along the loop can be written directly in terms of $\dot{\mathbf{Q}}$ as

$$h_{\min} = h_f + \frac{\dot{Q}_{H,\text{sub}}}{\dot{m}_{CO_2}}, \qquad h_{\max} = h_g + \frac{\dot{Q}_{C,\text{sup}}}{\dot{m}_{CO_2}} \tag{5.60}$$

where $h_f(P_{loop})$ and $h_g(P_{loop})$ are the saturated–liquid and saturated–vapor enthalpies at P_{loop}. The corresponding extreme loop temperatures,

$$T_{\min} = T\Big(P_{loop}, h_{\min}\Big), \qquad T_{\max} = T\Big(P_{loop}, h_{\max}\Big) \tag{5.61}$$

approximate the minimum and maximum CO_2 temperatures seen at the LHP outlets. The first stage therefore constructs a base table as follows:

$$\mathcal{T}_{\text{base}} = \Big\{\dot{\mathbf{Q}}, \boldsymbol{\Theta}, \text{COP}_{sys}, T_{\min}, T_{\max}\Big\} \tag{5.62}$$

which stores the discrete mapping $(\dot{\mathbf{Q}}, \boldsymbol{\Theta}) \mapsto (\text{COP}_{sys}, T_{\min}, T_{\max})$. This table is built on a Cartesian grid of candidate compressor settings: $P_{loop} \in [4.7, 6.7]$ MPa in 0.2 MPa steps,

$S \in \{30{:}7.5{:}75\}$ Hz with different compressor configurations, and, depending on the mode, $P_{dis} \in [7.5, 13.5]$ MPa for cooling or $P_{suc} \in [2.2, 4.9]$ MPa for heating. At each grid point, the dual–compressor maps provide $\dot{m}_{CO_2}$ and $\dot{W}_{comp}$, and all combinations of $\dot{\mathbf{Q}}$ are enumerated on a quantization grid $\Delta q = 1$ kW while limiting the total magnitude of the net heat exchange to $Q_C + |Q_H| \leq 25$ kW. For each candidate $\dot{\mathbf{Q}}$ the enthalpy levels $h_{\min}$ and $h_{\max}$ are evaluated using Eq. (5.60), the temperatures $T_{\min}$ and $T_{\max}$ follow from Eq. (5.61), and the envelope $(P_{suc}, P_{dis}) \in \mathcal{E}_{\text{comp}}$ are checked. When all constraints are satisfied, COP_{sys} is computed from Eq. (5.30), and the corresponding row is stored in $\mathcal{T}_{\text{base}}$. This yields a dense surrogate mapping $(\dot{\mathbf{Q}}, \boldsymbol{\Theta}) \mapsto \text{COP}_{sys}$ that already respects compressor constraints and remains independent of the particular building and LHP configuration.

Offline map construction

In the second stage, the base table is combined with the full system model to solve the optimization problem stated in Eq. (5.52) for all relevant combinations of inputs $(\boldsymbol{U_{HP}}, T_{w,OU,in})$. The objective is to obtain a final table as follows:

$$\mathcal{T}_{\text{TB}} = \left\{ \boldsymbol{U_{HP}}, T_{w,OU,in}, \boldsymbol{\Theta}^*, \text{COP}^*_{sys} \right\} \tag{5.63}$$

which has the same structure as the MM lookup table.

For any candidate decision vector $\boldsymbol{\Theta}$, the full circulation and loop models are evaluated for the respective input $(\boldsymbol{U_{HP}}, T_{w,OU,in})$. This evaluation returns the CO_2 mass flow rate $\dot{m}_{CO_2}$ and, for each active LHP i, the inlet and outlet CO_2 enthalpies along the loop, $(h_{HP,in,i}, h_{HP,out,i})$, at $(P_{loop}, \dot{m}_{CO_2})$. The resulting enthalpy evolution is then recast into the six-segment heat-exchange representation used by the base table. At fixed P_{loop}, the saturated-liquid and saturated-vapor enthalpies are denoted by h_f and h_g, which define the subcooled ($h < h_f$), two phase ($h_f \leq h \leq h_g$), and superheated ($h > h_g$) regions. The segment-wise loop heat exchanges for each active LHP i are defined as follows:

$$\dot{Q}_{\text{sub},i} = \dot{m}_{CO_2} \Big[\min\Big(h_f, h_{HP,out,i}\Big) - \min\Big(h_f, h_{HP,in,i}\Big) \Big] \tag{5.64}$$

$$\dot{Q}_{2\phi,i} = \dot{m}_{CO_2} \Big[\text{clip}(h_{HP,out,i}; h_f, h_g) - \text{clip}(h_{HP,in,i}; h_f, h_g) \Big] \tag{5.65}$$

$$\dot{Q}_{\text{sup},i} = \dot{m}_{CO_2} \Big[\max\Big(h_g, h_{HP,out,i}\Big) - \max\Big(h_g, h_{HP,in,i}\Big) \Big] \tag{5.66}$$

so that

$$\dot{Q}_{\text{sub},i} + \dot{Q}_{2\phi,i} + \dot{Q}_{\text{sup},i} = \dot{m}_{CO_2}(h_{HP,out,i} - h_{HP,in,i})$$

When zone i operates in cooling mode ($U_{HP,i} = +1$), the enthalpy rise satisfies $h_{HP,out,i} \geq h_{HP,in,i}$ and the three components in Eqs. (5.64)-(5.66) are positive, representing heat rejected to the loop. In heating mode ($U_{HP,i} = -1$), $h_{HP,out,i} \leq h_{HP,in,i}$ and the same expressions yield negative values, representing heat extracted from the loop. To match the full model with the base table, we form the model computed (continuous) exchange vector $\dot{\mathbf{Q}}_m$, which has the same ordering and physical meaning as $\dot{\mathbf{Q}}$ in Eq. (5.54). The resulting six component vector associated with $(\boldsymbol{\Theta}, \boldsymbol{U_{HP}}, T_{w,OU,in})$ is then obtained as follows:

$$\dot{\mathbf{Q}}_m(\boldsymbol{\Theta}, \boldsymbol{U_{HP}}, T_{w,OU,in}) = \Big[\dot{Q}_{C,\mathrm{sub}},\, \dot{Q}_{C,2\phi},\, \dot{Q}_{C,\mathrm{sup}},\, \dot{Q}_{H,\mathrm{sub}},\, \dot{Q}_{H,2\phi},\, \dot{Q}_{H,\mathrm{sup}}\Big] \tag{5.67}$$

This definition is consistent with the representation used in the base–table stage and provides the continuous vector $\dot{\mathbf{Q}}_m$ for the given inputs.

To populate $\mathcal{T}_{\mathrm{TB}}$ for each input pair $(\boldsymbol{U_{HP}}, T_{w,OU,in})$, the algorithm in Fig. 5.5 proceeds as follows. An initial decision vector $\boldsymbol{\Theta}^{(0,0)}$ is first computed using Eqs. (5.37)-(5.50), in which a nominal loop pressure $P_{loop}^{(0,0)} = 5.2$ MPa is assumed to close the initialization. The full system models are then evaluated at $\boldsymbol{\Theta}^{(0,0)}$ to obtain $\dot{m}_{CO_2}^{(0,0)}$ and the enthalpy pairs $(h_{HP,in,i}^{(0,0)}, h_{HP,out,i}^{(0,0)})$, from which the continuous exchange vector $\dot{\mathbf{Q}}_m^{(0,0)}$ is computed using Eq. (5.67). Each component of $\dot{\mathbf{Q}}_m^{(0,0)}$ is projected onto the discrete Δq grid to define the initial target vector $\dot{\mathbf{Q}}_p^{(0)}$. We denote this quantization (projection) operator as follows:

$$\Pi_{\Delta q}(\mathbf{x}) := \Delta q\, \mathrm{round}(\mathbf{x}/\Delta q) \tag{5.68}$$

so that $\dot{\mathbf{Q}}_p^{(0)} = \Pi_{\Delta q}\Big(\dot{\mathbf{Q}}_m^{(0,0)}\Big)$. As shown in Fig. 5.5, the algorithm uses two nested iterations. The outer index n counts successive updates of the discrete target vector $\dot{\mathbf{Q}}_p$ used to subsample $\mathcal{T}_{\mathrm{base}}$, whereas the inner index k enumerates the ranked candidate settings $\boldsymbol{\Theta}^{(n,k)}$ retrieved for a fixed target. For the first outer iteration, we set $n = 1$ and use $\dot{\mathbf{Q}}_p^{(0)}$ as the initial target, i.e. $\dot{\mathbf{Q}}_p^{(n-1)} = \dot{\mathbf{Q}}_p^{(0)}$. A subset of rows in $\mathcal{T}_{\mathrm{base}}$ satisfying $\dot{\mathbf{Q}} = \dot{\mathbf{Q}}_p^{(n-1)}$ is first selected (subsampled) and then ordered by decreasing stored COP_{sys}, yielding an ordered list of candidate compressor settings $\{\boldsymbol{\Theta}^{(n,k)}\}$.

The candidates are then tested sequentially, starting from the first ranked row ($k = 1$). For each candidate $\boldsymbol{\Theta^{(n,k)}}$, the full loop model is re-evaluated under the current $(\boldsymbol{U_{HP}}, T_{w,OU,in})$ while using the corresponding OU water mass flow rate $\dot{m}_{w,OU}$ calculated as described in Section 5.5.2. The simulation returns $\dot{m}_{CO_2}^{(n,k)}$, the updated enthalpy pairs $(h_{HP,in,i}^{(n,k)}, h_{HP,out,i}^{(n,k)})$, and the associated continuous exchange vector $\dot{\mathbf{Q}}_m^{(n,k)}$ computed again from Eqs. (5.64)-(5.67). It also provides $\mathrm{COP}_{sys}^{(n,k)}$ and the loop extrema temperatures $T_{\min}$ and $T_{\max}$.

For each candidate $\boldsymbol{\Theta^{(n,k)}}$, feasibility also requires numerical convergence of the heat exchanger models under the imposed water-side boundary conditions. In cooling-dominant operation, specifying $\boldsymbol{\Theta}^{(\boldsymbol{n},\boldsymbol{k})}$ fixes $P_{dis}^{(n,k)}$; the GC model must then converge with respect to the water-side boundary condition such that the resulting CO_2 outlet state from the GC is consistent with the CO_2 loop constraints. In heating-dominant operation, specifying $\boldsymbol{\Theta}^{(\boldsymbol{n},\boldsymbol{k})}$ fixes $P_{suc}^{(n,k)}$; the EVAP model must converge with respect to the water-side boundary condition such that the CO_2 stream fully evaporates and reaches the saturated-vapor condition at the evaporator outlet at $P_{suc}^{(n,k)}$. If any of these feasibility checks fails (e.g. no convergence or violation of bounds), the candidate is rejected and the search proceeds to the next ranked row ($k \leftarrow k+1$).

Once a candidate $\boldsymbol{\Theta}^{(n,k)}$ satisfies (i) heat-exchanger model convergence under the imposed water-side boundary condition, (ii) the temperature bounds in Eq. (5.52), we then project the resulting continuous exchange vector onto the Δq grid to obtain $\dot{\mathbf{Q}}_p^{(n)} = \Pi_{\Delta q}\Big(\dot{\mathbf{Q}}_m^{(n,k)}\Big)$, and compare it to the target used to subsample $\mathcal{T}_{\text{base}}$ in the current outer iteration, i.e. $\dot{\mathbf{Q}}_p^{(n-1)}$. If $\dot{\mathbf{Q}}_p^{(n)} = \dot{\mathbf{Q}}_p^{(n-1)}$, the candidate is accepted and taken as the solution of Eq. (5.52) for that $(\boldsymbol{U_{HP}}, T_{w,OU,in})$, and its decision vector $\boldsymbol{\Theta}^*$ together with COP_{sys}^* are stored in $\mathcal{T}_{TB}$.

Otherwise, if $\dot{\mathbf{Q}}_p^{(n)} \neq \dot{\mathbf{Q}}_p^{(n-1)}$, we update the target by setting $\dot{\mathbf{Q}}_p^{(n-1)} \leftarrow \dot{\mathbf{Q}}_p^{(n)}$, increment the outer iteration ($n \leftarrow n+1$), subsample $\mathcal{T}_{\text{base}}$ again using the updated target $\dot{\mathbf{Q}}_p^{(n-1)}$, and restart the ranked search from the first row ($k \leftarrow 1$). This outer-loop update is repeated until the projected target remains unchanged between successive outer iterations.

Online lookup

Once $\mathcal{T}_{\text{TB}}$ has been constructed, at each timestep, the controller reads the current inputs, $(\boldsymbol{U_{HP}}, T_{w,OU,in})$ and selects the corresponding decision vector in $\mathcal{T}_{\text{TB}}$.

5.6 Results and Discussion

5.6.1 Case study

The proposed supervisory control is evaluated on a small office building located in Montréal, Canada. This section summarizes the case-study configuration, including the building layout, zone thermal capacities and annual loads, LHP sizing, the OU water-side flow used in the simulations, and the sizing of the ground heat exchanger.

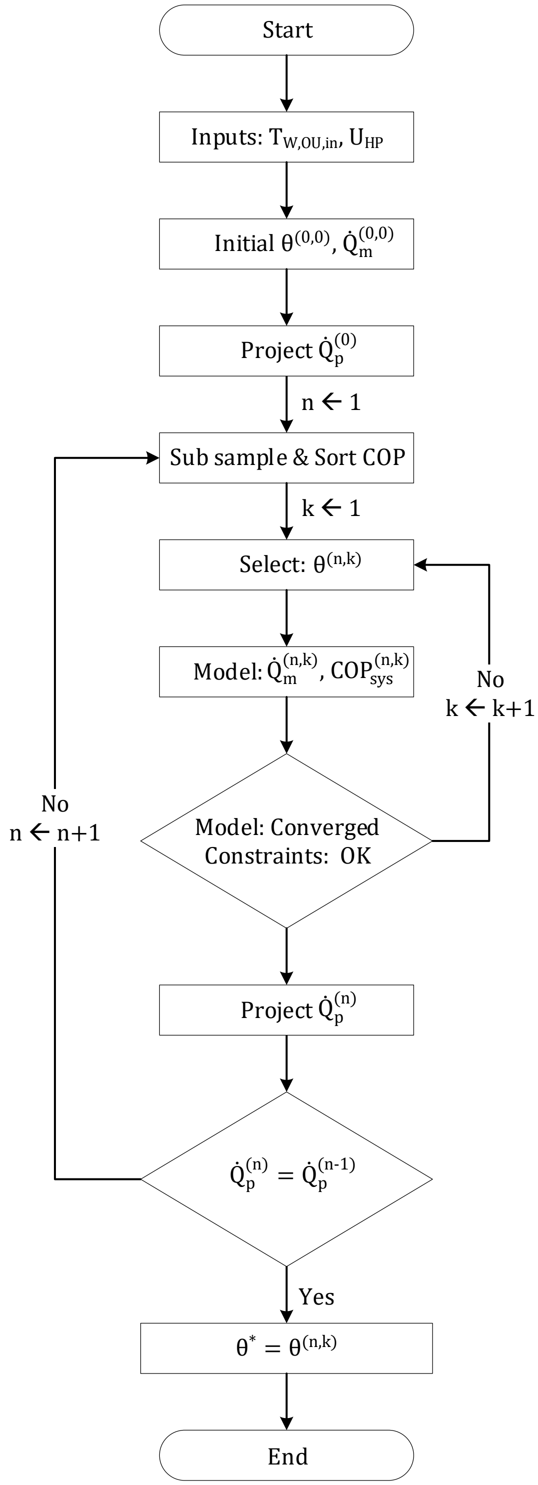

Figure 5.5 TB method flowchart

Building layout and zone loads

The floor plan comprises five thermal zones: four perimeter zones (West, South, East, North) surrounding a Core zone (see floor plan in Fig. 5.6). Zone floor areas (A) and thermal capacities C_z are given in Fig. 5.6. A single-pipe distribution loop supplies the zones in series and then returns to the RVCC. Annual zone loads follow Tamasauskas et al. [133] and are summarized in Table 5.2, where H and C denote heating and cooling, respectively.

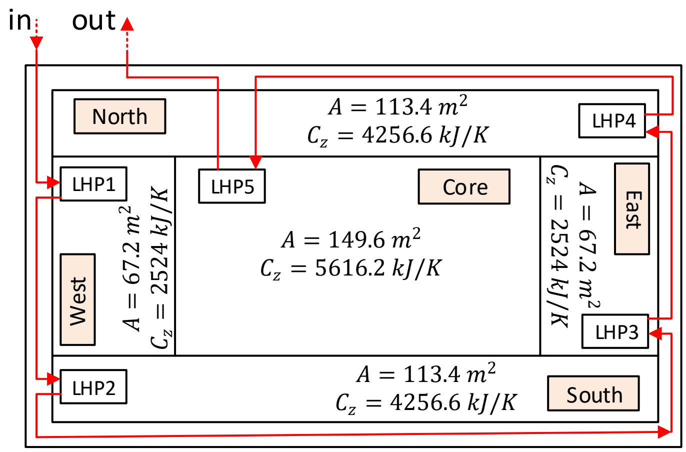

Figure 5.6 Floor plan of the office building

Table 5.2 Load characteristics (adapted from Tamasauskas et al. [133]) H: heating; C: cooling

	West		South		East		North		Core	
Metric	H	C	H	C	H	C	H	C	H	C
Total demand (kWh)	2050	2813	2198	5122	1849	2773	3020	3732	1014	6070
Peak load (kW)	3.3	4.2	5.1	4.4	3.3	3.8	5.3	3.4	4.2	3.7
Total demand duration (h)	3692	2482	2263	4074	3352	2816	2585	3722	1267	4885

Each thermal zone is served by a LHP. To guarantee that the zone peak loads in Table 5.2 are met, the LHP capacities were sized so that, at their rated source temperatures ($T_{loop,rated} = 15$ °C), each LHP can supply the corresponding peak load (see Sec. 5.4.2 for the map formulation).

Outdoor-unit water mass flow for the case study

To run annual TRNSYS simulations for the five-zone case study, the OU secondary-loop mass flow rate $\dot{m}_{w,OU}$ is prescribed as a set of conservative setpoints parameterized by the OU-HX inlet water temperature $T_{w,OU,in}$ and by the instantaneous activation level of the LHPs. In the present implementation, the activation level is represented by the number of active LHPs in the dominant mode, denoted by n_{cool} in cooling-dominant operation (OU-HX acting as a gas cooler) and n_{heat} in heating-dominant operation (OU-HX acting as an evaporator).

The setpoints were constructed offline using the detailed component models to ensure that, over the expected range of $T_{w,OU,in}$ and activation patterns encountered in the case study, the circulation unit can be operated within the compressor envelope with stable OU-HX convergence. It is worth mentioning that the water mass flows are not optimized. They are therefore used only to provide a conservative secondary-loop boundary condition for comparing the MM and TB supervisory strategies under identical assumptions.

Figures 5.7 and 5.8 report the water mass flows used in the annual simulations. In cooling-dominant operation (gas-cooler side), the required $\dot{m}_{w,OU}$ increases with n_{cool} and depends on $T_{w,OU,in}$ through the available water-side temperature driving force. In heating-dominant operation (evaporator side), $\dot{m}_{w,OU}$ increases with n_{heat} and shows the corresponding sensitivity to $T_{w,OU,in}$. A systematic optimization of these setpoints that explicitly accounts for the trade-off between reduced compressor work and increased secondary-loop pumping energy is left for future work.

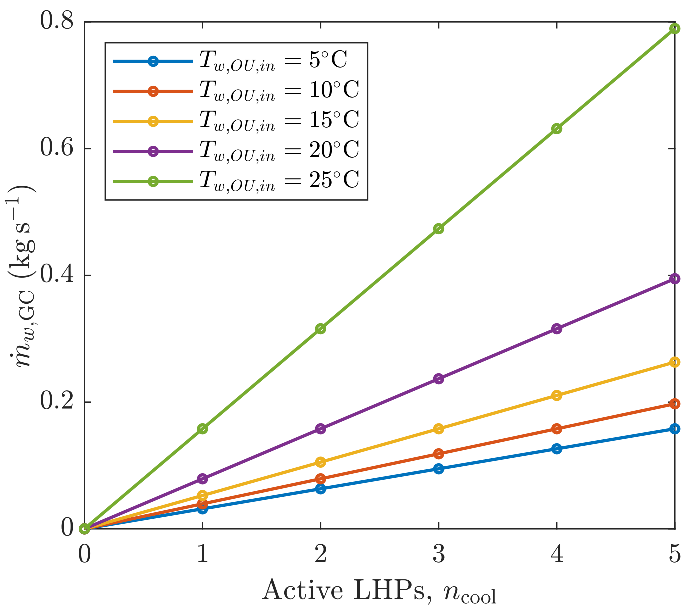

Figure 5.7 Cooling-dominant (GC side): gas-cooler source-side water mass flow rate as a function of the number of active LHPs in cooling mode for different supply temperatures

Ground heat exchanger sizing

The OU is a water–glycol loop coupled to a vertical GHX. It is sized to maintain the borehole outlet temperature within 5–25 °C while supplying the total load of the CO_2TN used in this study, with an undisturbed ground temperature of $T_g = 10.5$ °C in Montréal, Canada [134]. Sizing of the GHX follows the Alternative ASHRAE method (Sec. 5.4.5) and the resulting

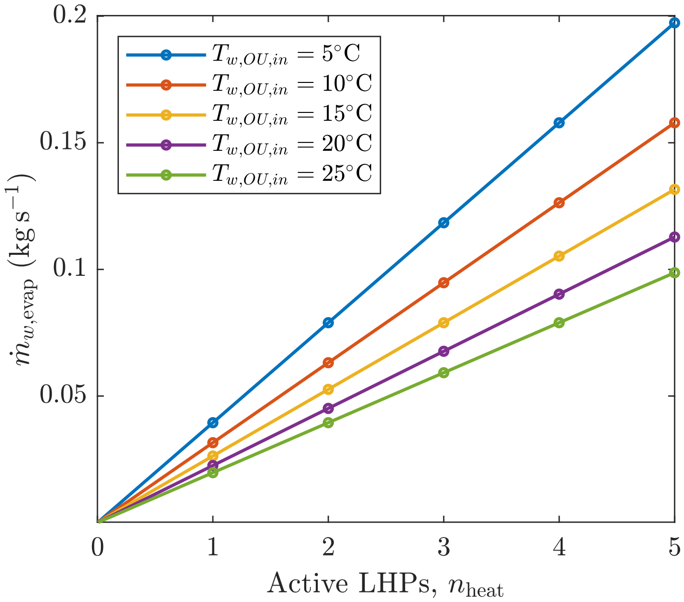

Figure 5.8 Heating-dominant (EVAP side): evaporator source-side water mass flow rate as a function of the number of active LHPs in heating mode for different supply temperatures

geometry and properties are passed to Type557a_v2a for the dynamic simulation. Table 5.3 summarizes the design inputs (soil, fluid, borehole, and field layout).

5.6.2 Implementation framework

The MATLAB tables are embedded in TRNSYS through a dedicated component ("RVCC & Control"), as illustrated in Fig. 5.9. At each simulation time step, this component receives the thermostat commands from the five zones (U_{HP}) and the current water temperature provided by the secondary borehole model (Type 557a). To ensure a consistent match to the discrete operating-map grid, the borehole-side temperature used for the query is rounded to the nearest 0.1 °C. Using (U_{HP}, T_w) as the lookup key, the component retrieves the corresponding row of the control table.

In addition to the supervisory decision vector $\mathbf{\Theta}$, each table row stores the associated precomputed CO_2 operating states which required by the TRNSYS plant components. In particular, the retrieved row provides the CO_2 loop mass flow rate $\dot{m}_{CO_2}$ and circulation-compressor power $\dot{W}_{comp}$, as well as the loop inlet enthalpy $h_{in,loop}$. The same row also provides the OU-HX water-side setpoints/outputs (e.g. $T_{w,OU,out}$ and $\dot{m}_w$) consistent with that operating point. These precalculated quantities are then passed directly as inputs to the remaining TRNSYS components representing the CO_2 loop and the LHP array. With this structure, TRNSYS resolves the building and borehole dynamics over the full year while the circulation-

Table 5.3 Borefield parameters (Alternative ASHRAE method)

Quantity (symbol)	Value	Unit
Ground properties		
Ground conductivity k_g	2.65	$\mathrm{W\,m^{-1}K^{-1}}$
Ground diffusivity α	0.08	$\mathrm{m^2/day}$
Undisturbed ground temperature T_g	10.5	°C
Fluid & LHP bounds		
Thermal conductivity k_f	0.43	$\mathrm{W\,m^{-1}K^{-1}}$
Dynamic viscosity μ_f	0.01	$\mathrm{kg\,m^{-1}s^{-1}}$
Heat capacity $c_{p,f}$	3800	$\mathrm{J\,kg^{-1}K^{-1}}$
Density ρ_f	1030	$\mathrm{kg\,m^{-3}}$
LHP inlet range $T_{in,HP}$	5–25	°C
Borehole & grout		
Bore radius r_b	0.08	m
Buried header depth D_b	2.0	m
U-tubes per bore N_U	2	–
Pipe inner radius $r_{p,in}$	0.028	m
Pipe outer radius $r_{p,out}$	0.030	m
Shank spacing L_U	0.10	m
Grout conductivity k_{gr}	1.50	$\mathrm{W\,m^{-1}K^{-1}}$
Borefield layout		
Layout $N_{bx} \times N_{by}$	5×1	–
Bore spacing s	7.5	m
Per-bore depth H	127.3	m
Total length L_{tot}	636.5	m

unit operating point is enforced through the lookup-based supervisory layer.

5.6.3 Performance metrics

The system is simulated over a finite time horizon of duration N using a fixed time step Δt. Discrete times are defined as $t_k = k\,\Delta t$ for $k = 1, \ldots, N_{step}$, where $N_{step} = N/\Delta t$. At each step k, heat rates and electrical powers are evaluated at t_k in kW, and time-integrated energies are reported in kWh.

Zones are indexed by $i = 1, \ldots, n_z$ where each zone is served by one LHP. For each zone i, the delivered heating and cooling rates are denoted by $\dot{Q}_{HP,H,i}(t_k)$ and $\dot{Q}_{HP,C,i}(t_k)$, respectively, with the convention that at most one of these two quantities is non-zero at a given time step (and both are zero when the LHP is OFF). The corresponding LHP electrical power is

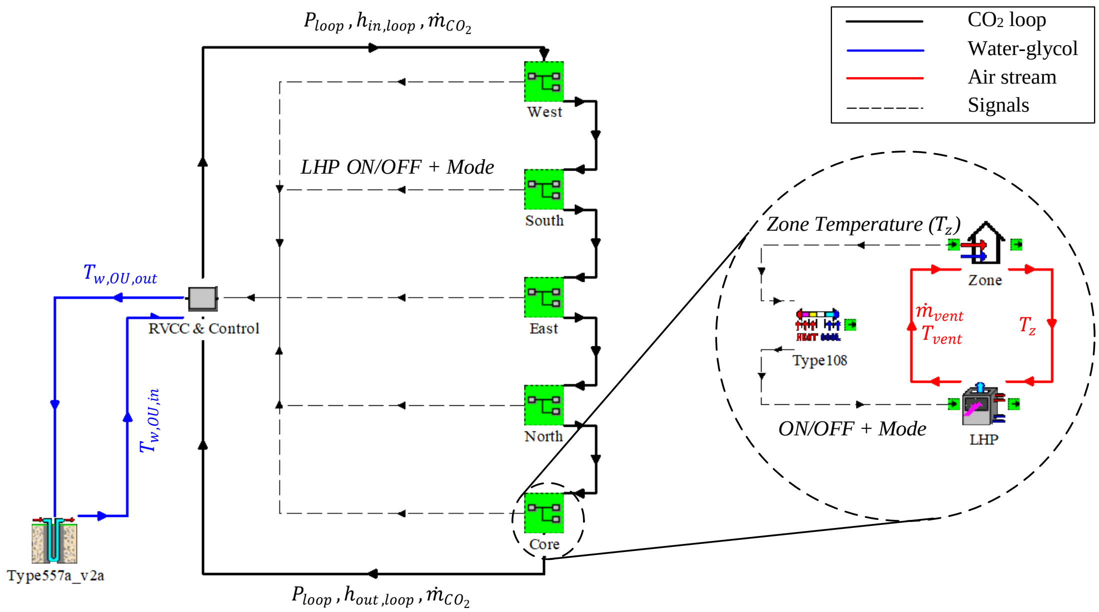

Figure 5.9 TRNSYS Simulation Studio

$\dot{W}_{HP,i}(t_k)$, and the circulation-compressor power is $\dot{W}_{comp}(t_k)$.

Time-step COP

At each time step, the total useful thermal rate delivered by the LHP array is

$$\dot{Q}_{HP}(t_k) = \sum_{i=1}^{n_{HP}} \left(\dot{Q}_{HP,H,i}(t_k) + \dot{Q}_{HP,C,i}(t_k) \right) \tag{5.69}$$

and the total electrical input is

$$\dot{W}_{tot}(t_k) = \dot{W}_{comp}(t_k) + \sum_{i=1}^{n_{HP}} \dot{W}_{HP,i}(t_k) \tag{5.70}$$

The system coefficient of performance is therefore

$$COP_{sys}(t_k) = \begin{cases} \dfrac{\dot{Q}_{HP}(t_k)}{\dot{W}_{tot}(t_k)}, & \dot{W}_{tot}(t_k) > 0 \\ 0, & \dot{W}_{tot}(t_k) = 0 \end{cases} \tag{5.71}$$

which is consistent with the system-level definition in Eq. (5.30).

Annual overall Seasonal Performance Factor (SPF)

The annual (heating and cooling) system Seasonal Performance Factor is defined as

$$SPF_{sys,ann} = \frac{Q_H + Q_C}{W_{comp} + W_{LHP}} \tag{5.72}$$

where Q_H and Q_C are the annual delivered heating and cooling energies, and W_{comp} and W_{LHP} are the corresponding annual electrical energies. These quantities are obtained by time-summing the instantaneous rates:

$$Q_H = \sum_{k=1}^{N_{step}} \sum_{i=1}^{n_{HP}} \dot{Q}_{HP,H,i}(t_k)\,\Delta t \tag{5.73}$$

$$Q_C = \sum_{k=1}^{N_{step}} \sum_{i=1}^{n_{HP}} \dot{Q}_{HP,C,i}(t_k)\,\Delta t \tag{5.74}$$

$$W_{comp} = \sum_{k=1}^{N_{step}} \dot{W}_{comp}(t_k)\,\Delta t \tag{5.75}$$

$$W_{LHP} = \sum_{k=1}^{N_{step}} \sum_{i=1}^{n_{HP}} \dot{W}_{HP,i}(t_k)\,\Delta t \tag{5.76}$$

5.6.4 Time-based analysis in TRNSYS

We simulate the CO_2TN for one full year with a fixed half-hour time step ($\Delta t = 0.5$ h) to resolve transient operation under mixed heating and cooling demands for the office building described in Section 5.6.1. At each step t_k, the system coefficient of performance COP_{sys} is computed from Eq. (5.71). Seasonal performance is obtained by time-integration of the thermal and electrical rates in Eqs. (5.73)–(5.76), yielding the annual overall $\mathrm{SPF}_{\mathrm{sys,ann}}$. We compare two supervisory strategies: a minimum–mass-flow (MM) controller that seeks to reduce CO_2 circulation while meeting constraints, and a temperature-bounded (TB) controller that constrains the loop temperature to a narrow band around the saturation temperature at the selected loop pressure.

Figure 5.10 compares the COP_{sys} distributions for the two supervisory strategies. The violin shapes visualize how frequently each COP level occurs over the year, showing that the TB strategy shifts the distribution toward higher COP and places more operating time in the high-efficiency region, while still retaining a smaller low-COP cluster under constrained conditions. The internal markers denote the first quartile (Q_1), median, and third quartile (Q_3); the interquartile range (IQR) equals $Q_3 - Q_1$ and measures the width of the middle 50% of the distribution.

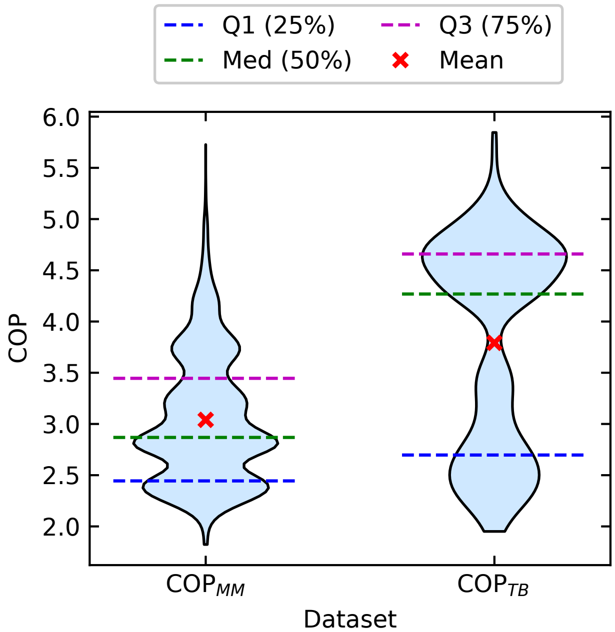

Figure 5.10 System COP distributions for the two supervisory strategies

Table 5.4 reports the corresponding descriptive statistics and shows a systematic upward shift of the COP distribution with the TB method. The mean COP rises from 3.075 to 3.754 (22.1%), reflecting broad improvement across operating conditions. The median increases from 2.950 to 4.268 (44.7%), showing that the typical operating point moves into a more favorable thermodynamic regime. The upper quartile moves from 3.582 to 4.650; accordingly, the fraction of COP time steps with $COP_{sys} > 4$ increases from 8% under the MM method to 55% under the TB method. At the same time, the IQR enlarges from 1.135 to 1.953; because both quartiles shift upward, this wider IQR indicates a broader central band of high-efficiency operation rather than dispersion driven by outliers. These instantaneous gains accumulate over the year. Aggregation with Eqs. (5.73)–(5.76) yields $SPF_{sys,ann} = 2.98$ for the MM method and $SPF_{sys,ann} = 3.65$ for the TB method (22.3% improvement).

Table 5.4 Descriptive statistics of COP over time steps

Dataset	n	Mean	Median	Q1 (25%)	Q3 (75%)	IQR	Min–Max
COP_{MM}	6,887	3.075	2.950	2.447	3.582	1.135	1.823-5.909
COP_{TB}	6,884	3.754	4.268	2.697	4.650	1.953	1.951-5.845

To compare the control methods, Fig. 5.11 reports the monthly seasonal performance factor. Both methods follow the expected seasonal pattern, with the highest efficiency occurring in the shoulder months when heat recovery is more frequent. Over the full year, the TB method consistently outperforms the MM method. In March, the SPF increases from 2.96 (MM) to 3.29 (TB), corresponding to an improvement of 11.3%. The gap widens through the warm season: from May to September, the TB method maintains an SPF of 4.49-4.55 while the MM method remains between 3.10 and 3.37, yielding an improvement of 34.8%-44.8% (with the maximum occurring in July). The difference then narrows in late fall and winter; for example, the SPF is 3.27 (TB) versus 2.96 (MM) in November (10.5%), and 2.57 (TB) versus 2.53 (MM) in December (1.6%).

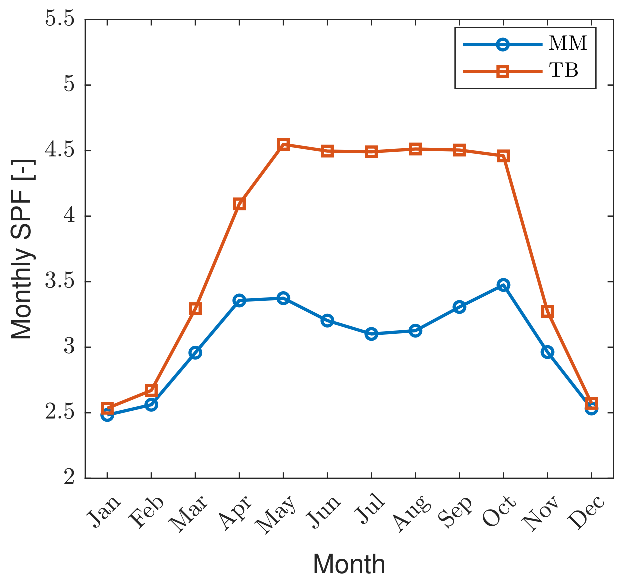

Figure 5.11 Monthly seasonal performance factor for both supervisory methods

Figure 5.12 complements this result by aggregating the monthly electrical energy consumption, $E_m = \sum_{t \in m} \dot{W}_{tot}(t_k)\, \Delta t$, reported in kWh with $\Delta t = 0.5$ h. The control choice matters most from May to September, where the TB method lowers E_m by roughly 20%-30% compared with the MM method. Furthermore in winter season the gap between the two methods are typically less than 10%.

The maximum difference between the two methods occurs in the week of *11–17 August*. The gap stems primarily from the circulation system power—i.e. the compressor input ($\dot{W}_{comp}$). Under the MM method, $\dot{W}_{comp}$ rises by roughly +65% relative to the TB method, whereas the LHP power consumption ($\dot{W}_{LHP}$) changes only modestly (15%). Consequently, the weekly total under MM is about +50% higher, with the increase dominated by the circulation compressor power rather than by local loads.

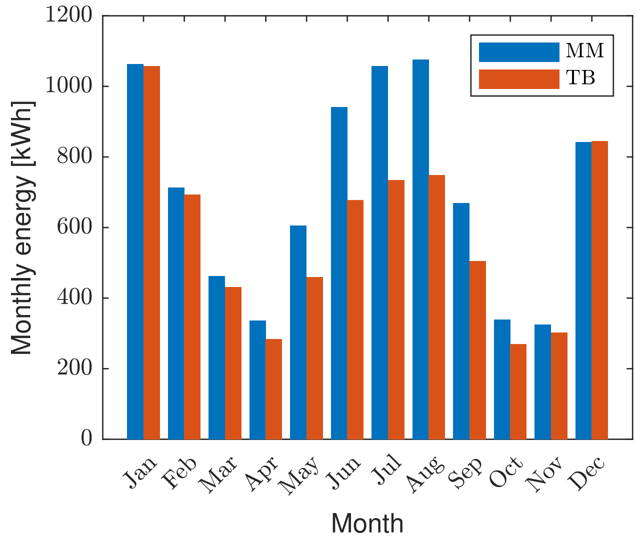

Figure 5.12 Monthly electrical energy consumption, comparing MM and TB methods

The time-series in Fig. 5.13 (Aug. 15-16, cooling and transcritical operation) and Fig. 5.14 (Feb. 15-16, heating and subcritical operation) help explain why the SPF gap is larger in summer. As shown in Fig. 5.13, the MM strategy sustains both a higher CO_2 mass flow rate $\dot{m}_{CO_2}$ and a larger pressure ratio (P_{dis}/P_{suc}) than the TB strategy, which results in higher compressor-power plateaus. In transcritical operation, compressor work is highly sensitive to both $\dot{m}_{CO_2}$ and pressure ratio; therefore, this combination amplifies $\dot{W}_{comp}$ under the MM strategy. By contrast, Fig. 5.14 shows that on Feb. 15-16 the required $\dot{m}_{CO_2}$ and the pressure ratio are lower and more similar across strategies, leading to a smaller weekly and seasonal difference. Overall, the larger SPF advantage of the TB strategy in cooling is primarily associated with its reductions in $\dot{m}_{CO_2}$ and pressure ratio during transcritical operation, which directly reduces compressor energy.

The comparison between the two supervisory strategies showed that the TB method consistently outperforms the MM method for the present case study. To further examine the shape and variability of the COP distribution under TB operation, we partitioned the annual simulation timesteps into four operating compositions based on the zone thermostat calls: (i) Only heating (all active LHPs in heating mode), (ii) Only cooling (all active LHPs in cooling mode), (iii) Mixed (cooling-dominant) (simultaneous heating and cooling with more zones requesting cooling than heating), and (iv) Mixed (heating-dominant) (simultaneous heating and cooling with more zones requesting heating than cooling). Figure 5.15 shows the resulting COP distributions. The results indicate that the operation is dominated by

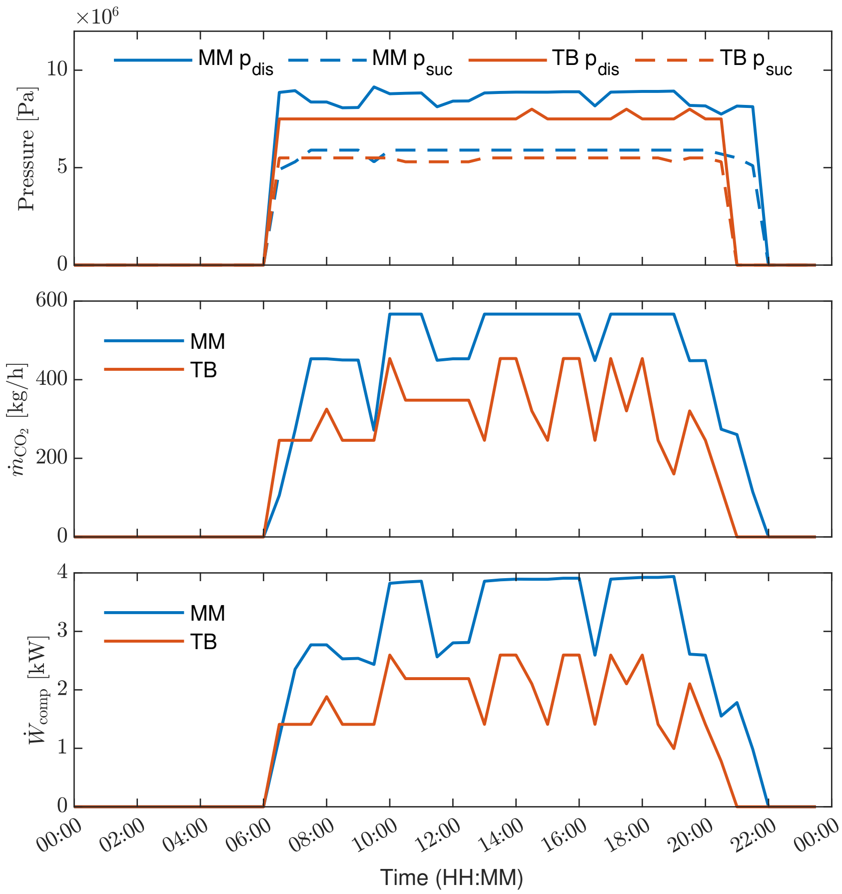

Figure 5.13 Aug. 15–16: top: discharge/suction pressures, middle: CO_2 mass flow, and bottom: compressor power for MM and, TB methods

single-mode periods (only heating: $n = 2425$; only cooling: $n = 4419$), whereas mixed-mode operation is rare (mix more cooling: $n = 34$; mix more heating: $n = 6$). The only-cooling cluster exhibits a higher central tendency (median of 3.324, mean of 3.391) than only-heating operation (median of 2.439, mean of 2.486). Mixed-mode clusters show wider spreads and higher upper quartiles, but the small sample size limits the statistical significance of these mixed-mode observations.

Since most timesteps fall into heating only or cooling only operation, we further refined the analysis by clustering these single-mode periods according to the number of activated LHPs for the TB method. Figures 5.16 and 5.17 show the COP distributions for pure heating and pure cooling, respectively, as a function of the number of active units. In both modes, the highest average COP occurs when two LHPs are active. This behavior is explained by the RVCC staging logic: for one to two active LHPs, the variable-speed circulation compressor alone can typically supply the required CO_2 mass flow and pressure lift, whereas higher ag-

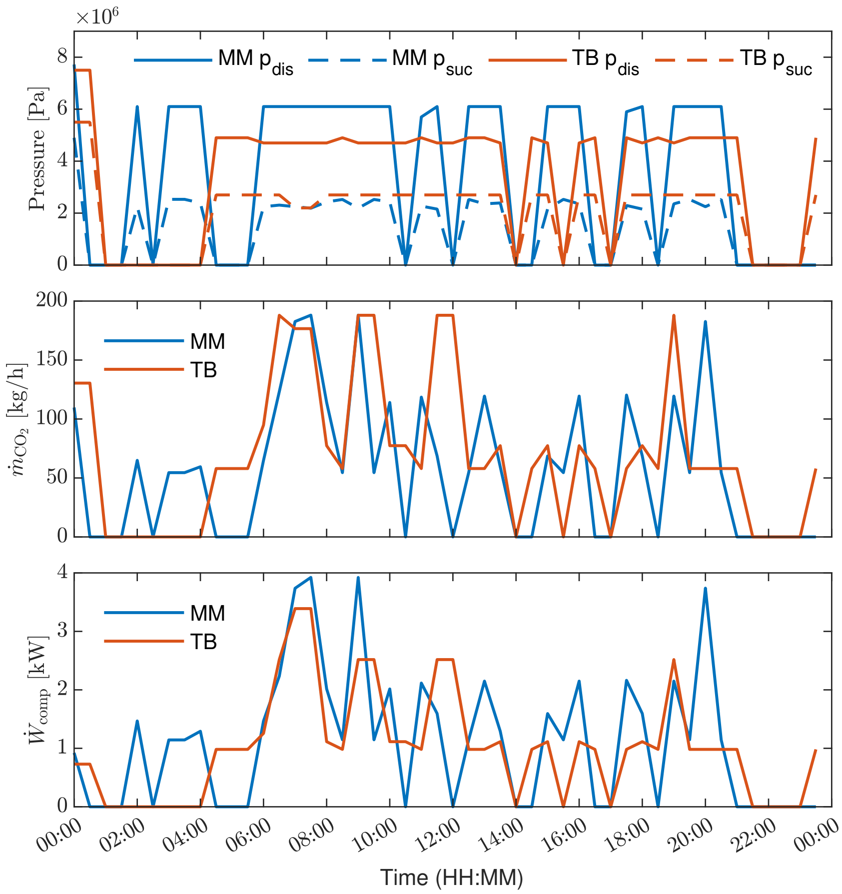

Figure 5.14 Feb. 15–16: top: discharge/suction pressures, middle: CO_2 mass flow, and bottom: compressor power for MM and, TB methods

gregate loads require engaging the fixed-speed compressor. The additional electrical input associated with fixed-speed operation reduces the overall COP despite the larger delivered capacity. These results highlight the importance of compressor staging and sizing in the system design: the part-load operating region around one to two active LHPs largely governs the achieved performance; therefore, when flexibility exists within comfort constraints, a supervisory scheduling or dispatch logic that promotes operating conditions with two simultaneously active LHPs (and limits periods with three or more active units that trigger fixed-speed operation) is expected to increase the overall system COP.

5.7 Conclusions

This work investigated supervisory control of a single-pipe CO_2 thermal network (CO_2TN) that supplies the source side of multiple packaged local heat pumps (LHPs) in a multi-zone

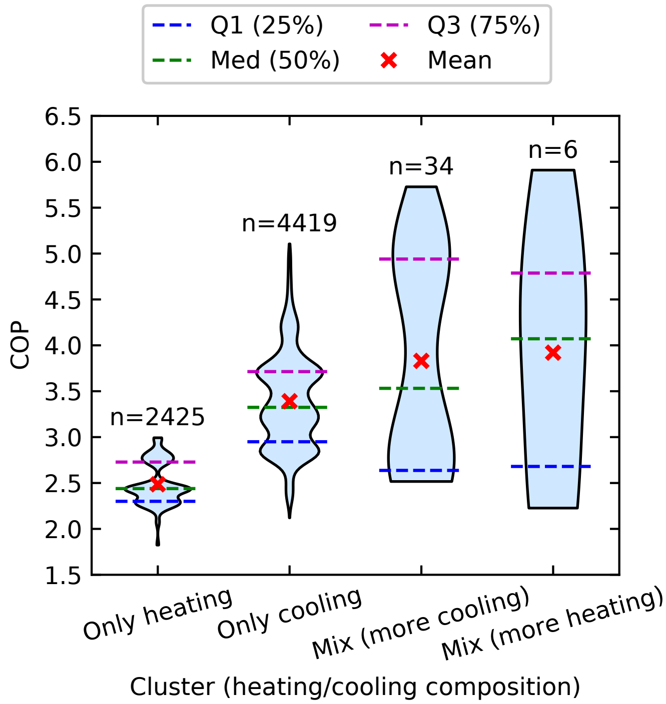

Figure 5.15 Distribution of system COP grouped by operating modes for TB method

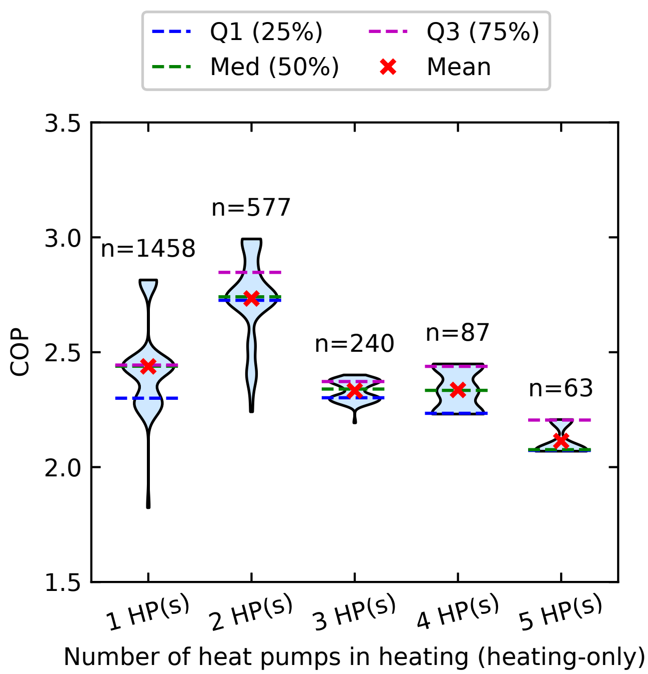

Figure 5.16 Distribution of system COP grouped by the number of active LHPs operating in heating mode for the TB method

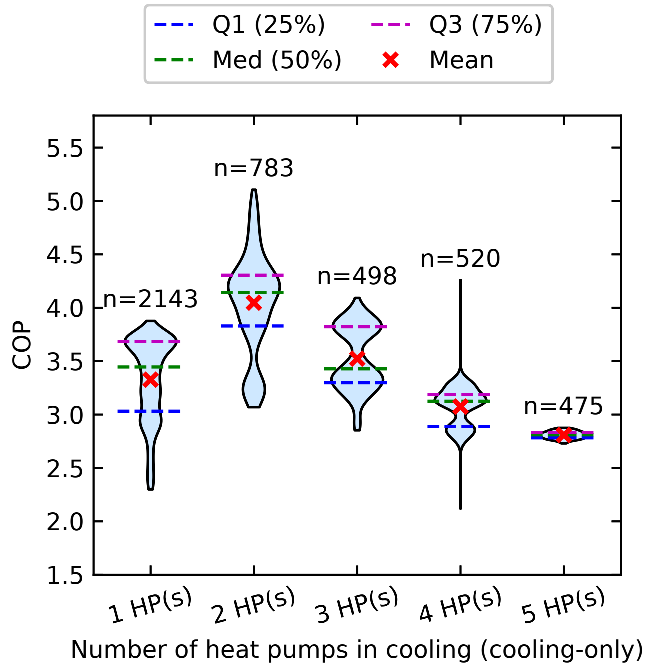

Figure 5.17 Distribution of system COP grouped by the number of active LHPs operating in cooling mode for the TB method

building. Two supervisory strategies were formulated and implemented within a common workflow: feasible operating points are enumerated offline using a validated steady-state CO_2TN model and equipment envelopes, and the supervisory decision is executed online via lookup. The minimum-mass-flow (MM) strategy enforces a strictly two phase CO_2 loop and uses the minimum loop mass flow as a model-closure constraint for each candidate loop pressure. The temperature-bounded (TB) strategy relaxes the strict two phase requirement and instead constrains loop temperatures within a ±10 K band around saturation, permitting bounded single-phase excursions while preserving a tight temperature band for the LHP source.

Annual co-simulation for a five-zone office building in Montréal showed that the TB method consistently improved performance relative to the MM method. The mean COP_{sys} increased from 3.08 to 3.75 (+22.1%) and the median increased from 2.95 to 4.27 (+44.7%). These time-step improvements accumulated over the year: $SPF_{sys,ann}$ increased from 2.98 to 3.65 (+22.3%). The COP distribution shifted upward under the TB method; in particular, the fraction of time steps with $COP_{sys} > 4$ increased from 8% under the MM method to 55% under the TB method.

The time-series and clustering analyses clarify the physical drivers of this gain and highlight actionable design/control implications. The TB strategy reduces circulation-compressor energy primarily in cooling-dominant operation by operating at lower CO_2 mass flow rates and lower compressor pressure ratios than MM, which directly reduces $\dot{W}_{comp}$ and explains the larger seasonal gap in summer. Moreover, the highest COP values in both heating-only and cooling-only periods occur when two LHPs are active, reflecting the staged circulation-compressor logic: one-to-two active LHPs are often met with the variable-speed compressor alone, whereas larger aggregate demands more frequently require engaging the fixed-speed compressor, which shifts operation to lower overall COP. This result suggests that CO_2TN performance is strongly shaped by part-load operation and compressor staging thresholds, and that the supervisor's ability to select favorable thermodynamic states (via loop pressure and bounded temperature constraints) is most valuable when the system operates near these part-load regions.

The present conclusions are subject to two main limitations. First, results are based on a single five-zone case study with fixed-capacity LHPs and a specific staged dual-compressor configuration; the quantitative gains will depend on equipment sizing, staging thresholds, and the distribution of zone loads. Second, the OU water-side mass flow correlations were chosen to ensure feasibility over a wide range of operating requests and were not optimized for auxiliary energy; incorporating secondary-loop pumping power could change the net benefit of more aggressive water-side operation.

Future work that follows directly from the observed trends includes: (i) adding a supervisory coordination layer for the LHP array to preferentially consolidate operation into high-efficiency regimes (e.g. encouraging synchronized operation of two LHPs when thermal comfort and zone constraints allow); (ii) evaluating variable-capacity, low-lift LHPs (or multi-stage/variable-speed packaged units) to smooth the net heat exchange on the CO_2 loop and reduce the frequency of large step changes in circulation demand; and (iii) extending the supervisory optimization to include water-side mass flow setpoints as decision variables and to penalize the associated pumping power, so that the supervisor maximizes global system performance (including auxiliary hydraulic energy). Finally, (iv) improving the supervisory representation beyond the current table-based operating map. In this study, lookup tables provided a practical first implementation for execution; however, they are not a definitive surrogate choice. Alternative surrogate choices to explore include: (a) smooth interpolation/regression surrogates (e.g. splines or radial-basis interpolation) to remove rounding effects and produce continuous setpoints; (b) Gaussian-process/Kriging surrogates to obtain both a prediction and a confidence level, enabling targeted offline sampling where the surrogate is uncertain; and (c) compact neural-network surrogates trained on the offline-optimal solutions to scale to higher-dimensional inputs and additional decision variables.

Acknowledgment

The authors acknowledge the Natural Sciences and Engineering Research Council of Canada (NSERC) for funding the Ph.D. student contributing to this work through discovery grant, [funding application number: RGPIN-2020-06556].

Declaration of generative AI and AI-assisted technologies in the writing process

During the preparation of this work the authors used ChatGPT in order to improve the readability and language of the manuscript. After using this tool/service, the authors reviewed and edited the content as needed and take full responsibility for the content of the published article.

5.8 Appendix: Time-step check of the TRNSYS annual simulation[1]

The annual TRNSYS simulation was performed using a simulation time step of 0.5 h. This value was selected as a practical compromise between the temporal resolution of the imposed building loads, the representation of thermostat-based control actions, and the computational cost of the annual simulations.

The thermal loads applied to the building zones were available at an hourly resolution. Therefore, using a very small simulation time step would not introduce additional information into the imposed load profiles. However, the zone thermostats and the activation signals sent to the local heat pumps were evaluated during the simulation. A 0.5 h time step was therefore used to allow the control logic to be updated twice within each hourly load interval, instead of limiting the zone-level response to one update per hour.

To verify that this choice did not significantly affect the annual performance results, an a posteriori time-step check was performed. The annual simulation was repeated using time steps of 1 h, 0.5 h, 0.25 h, and 0.125 h, while keeping all other inputs and control settings unchanged. The finest case, 0.125 h, was used as the reference solution. The relative error in the annual system SPF is calculated as follows:

$$\varepsilon_{SPF}(\Delta t) = \left| \frac{SPF_{sys}(\Delta t) - SPF_{sys,ref}}{SPF_{sys,ref}} \right| \times 100 \tag{5.77}$$

where Δt is the simulation time step and $SPF_{sys,ref}$ is the annual system SPF obtained with the finest time step. The results are summarized in Table 5.5.

[1]This appendix section was not included in the journal paper and was added only for the thesis.

Table 5.5 TRNSYS time-step comparison based on the annual system SPF

Δt (h)	SPF_{sys}	ε_{SPF} (%)
1	3.80	0.36
0.5	3.81	0.15
0.25	3.81	0.23
0.125	3.82	0.00

The annual SPF_{sys} obtained with the selected 0.5 h time step differed from the reference case by only 0.15%. Even the coarsest time step of 1 h resulted in a relative SPF error of only 0.36%. These small differences show that the main annual performance indicator is practically insensitive to further time-step refinement.

The number of ON/OFF occurrences was also checked because it is directly related to thermostat-based switching. As expected, this quantity was more sensitive to the time step than the annual energy-based performance indicators, since it depends on discrete switching events. However, this sensitivity did not lead to a meaningful change in SPF_{sys}, as shown in Table 5.5. Therefore, the 0.5 h time step was retained as a suitable compromise for the annual simulations. It provides sufficient resolution for the thermostat and local heat pump control logic while avoiding unnecessary computational cost.

CHAPTER 6 CONCLUSION AND RECOMMENDATIONS FOR FUTURE WORK

6.1 Thesis synthesis and main findings

This thesis addressed the need for a validated model and supervisory control methods for a single-pipe CO_2 thermal network (CO_2TN) connected to local heat pumps (LHPs) in multi-zone buildings. The work was organized around four objectives: model development, experimental validation, supervisory-control development, and annual performance evaluation.

The main contributions of the thesis are as follows:

1. Development of a CO_2TN model and its implementation in TRNSYS and Matlab, with dedicated component TYPES for the circulation unit, the main heat exchangers, and the coupling with local heat pumps.
2. Experimental validation of the model at both component and system levels using data from a CO_2TN prototype.
3. Formulation of two control strategies for the CO_2TN, namely the minimum-mass-flow (MM) method and the temperature-bounded (TB) method, both intended for implementation through offline map generation and online lookup.
4. Annual comparison of these supervisory strategies for a representative five-zone office building in Montréal using TRNSYS–MATLAB co-simulation.

6.1.1 Model development and validation

Chapter 4 established a modular CO_2TN model implemented in TRNSYS using dedicated component TYPES for the circulation unit, heat exchangers, and LHP coupling interfaces and validated it against experimental measurements from the prototype.

At the component level, the compressor model predicted the CO_2 mass flow rate with a MAPE of 7.24% and compressor power with a MAPE of 0.96%. For the water-to-CO_2 heat exchangers, the gas cooler model gave a MAPE of 1.37%, the desuperheater model 8.36%, the evaporator model 8.10%, and the condenser model 4.05%. The internal heat exchanger validation gave a MAPE of 9.45%.

At the system level, the model predicted total power with relative errors between 1.45% and 7.89%, and heating and cooling capacity with errors between 4.48% and 7.80%. The maximum COP deviation among the validation cases was 16.9%.

The study also showed that pressure drop in the prototype has an important effect on performance. When the measured pressure losses were removed from the model, the system COP increased by 21% in cooling mode, 7% in heating mode, and 20% in balanced mode.

6.1.2 Supervisory control and annual performance

Chapter 5 used the validated model to develop and compare two supervisory strategies.

The MM method keeps the loop strictly in two phase operation and selects the minimum CO_2 mass flow rate that satisfies feasibility for a given loop pressure. The TB strategy relaxes this requirement and instead keeps the loop temperatures within a ± 10 K band around saturation.

For the annual simulation of a five-zone office building in Montréal, the TB strategy performed better than the MM strategy. The mean system COP increased from 3.075 to 3.754, and the median COP increased from 2.950 to 4.268. The fraction of time steps with $COP_{sys} > 4$ increased from 8% to 55%. Over the full year, the seasonal performance factor increased from $SPF_{sys,ann} = 2.98$ for the MM method to $SPF_{sys,ann} = 3.65$ for the TB method.

The improvement was most significant during cooling dominant operation. In these periods, the TB strategy reduced the required CO_2 mass flow rate and also reduced the pressure ratio of the circulation compressor. As a result, circulation compressor electricity consumption was lower.

The annual results also showed that seasonal performance is affected not only by the supervisory method, but also by part-load operation and compressor staging in the circulation unit. Better performance was obtained when the load could be met mainly by the variable-speed compressor, with less frequent use of the fixed-speed staging compressor.

6.1.3 Overall conclusions

Based on the results of this thesis, the following conclusions can be drawn:

1. A dynamic validated model for the CO_2TN is developed that can represent the system with acceptable accuracy at both component and system levels and can be used for annual simulation and supervisory-control studies.

2. The TB supervisory strategy performs better than the MM strategy for the studied building and equipment configuration.

3. The main reason for the better performance of the TB strategy is that it allows more efficient operating points, especially in cooling-dominant transcritical conditions, by reducing both CO_2 circulation rate and circulation-compressor pressure ratio.

4. The annual performance of the CO_2TN depends on both control and design. In particular, pressure drop, compressor sizing, and staging logic have a direct effect on the benefit that can be obtained from improved supervision.

6.2 Limitations

The main limitations of this thesis are summarized below.

1. **Simplified representation of the CO_2 loop.** The current model does not include an explicit pipe model for the CO_2 loop, and pressure drops in several components are either neglected or imposed from prototype measurements rather than predicted from geometry and operating conditions. This is an important limitation because the validation showed that pressure drop has a strong effect on system performance.

2. **Simplified representation of some heat exchangers.** The main water-to-CO_2 heat exchangers were modeled and validated in detail, but the same level of detail was not used for all components. In particular, the desuperheater was not modeled in detail on the air side, and the internal heat exchanger was represented using simplifying assumptions. Although the internal heat exchanger model remained in acceptable agreement with experiments, this part of the model can still be improved.

3. **Supervisory control focused on the CO_2 side.** The supervisory strategies developed in this thesis optimize CO_2-side variables. On the source side, the outdoor-unit water mass flow rate was selected conservatively to ensure feasibility over the operating range, but it was not optimized with respect to pumping power. Similarly, on the desuperheater side, fan power and air-side effects were not included in the supervisory objective.

6.3 Recommendations for future work and system improvement

1. **Pressure-drop modeling.** A first priority is to develop predictive pressure drop models for the CO_2 loop, including the piping network and the main components. This

would allow pressure losses to be calculated from geometry and operating conditions rather than imposed from prototype data. Such an extension is necessary for design studies, for more predictive annual simulations, and for evaluating supervisory strategies.

2. **Improved models for the internal heat exchanger and desuperheater.** Future work should improve the representation of components that are still modeled in a simplified way. For the internal heat exchanger, a more detailed model could better capture the coupled heat transfer on the suction and discharge sides. For the desuperheater, a dedicated air-side model should be developed so that the effect of air flow rate, fan operation, and heat-exchanger sizing can be represented.

3. **Integrated supervision of CO_2-side and secondary-side variables.** The supervisory problem should be extended beyond the CO_2 side of the system. In particular, the outdoor-unit water mass flow rate should be treated as a decision variable and optimized together with the CO_2-side operating conditions while accounting for secondary-loop pumping power. Likewise, desuperheater fan power should be included in the system objective so that the supervisor minimizes total electricity use rather than compressor electricity alone.

4. **More advanced supervisory-control methods.** The offline-map framework proposed in this thesis is a first step, but future work should investigate more general supervisory methods. Candidate approaches include smooth surrogate-based optimization, hybrid offline–online refinement, and model predictive control. These methods could reduce lookup-table discretization effects, improve adaptability to off-design conditions, and better handle a larger number of decision variables and constraints.

5. **Broader validation of the control conclusions.** The supervisory strategies should be tested for additional building types, climates, and equipment configurations. In particular, future studies should examine the sensitivity of the MM and TB strategies to LHP sizing, variable-capacity LHP operation, circulation-compressor staging logic, and different zone-load distributions. This would clarify which conclusions are general and which are specific to the present case study.

6. **Optimal design and co-design of the CO_2TN.** A final and important step is to move from performance assessment to optimal design. Future work should optimize the hardware and the supervision together, including pipe sizing, pressure-drop reduction, circulation-unit sizing, compressor staging thresholds, and outdoor heat-exchanger design.

In summary, the next stage of research should move from a validated and controlled prototype-oriented framework toward a more predictive and more general design framework. This requires adding detail to some component models, expanding the supervisory decision variables to include auxiliary energy use, adopting more flexible control methods than static look up maps, and pursuing joint optimization of hardware design and supervisory control.

REFERENCES

[1] T. Li, M. A. Shapiro, M. Heidarinejad, and B. Stephens, "Ten questions concerning building electrification," *Building and Environment*, vol. 261, p. 111653, 2024. [Online]. Available: https://www.sciencedirect.com/science/article/pii/S0360132324004955

[2] M. González-Torres, L. Pérez-Lombard, J. F. Coronel, I. R. Maestre, and D. Yan, "A review on buildings energy information: Trends, end-uses, fuels and drivers," *Energy Reports*, vol. 8, pp. 626–637, 2022. [Online]. Available: https://www.sciencedirect.com/science/article/pii/S235248472101427X

[3] M. Ghajarkhosravi, Y. Huang, A. S. Fung, R. Kumar, and V. Straka, "Energy benchmarking analysis of multi-unit residential buildings (MURBs) in Toronto, canada," *Journal of Building Engineering*, vol. 27, p. 100981, 2020. [Online]. Available: https://www.sciencedirect.com/science/article/pii/S2352710219311787

[4] S. Buffa, M. Cozzini, M. D'Antoni, M. Baratieri, and R. Fedrizzi, "5th generation district heating and cooling systems: A review of existing cases in Europe," *Renewable and Sustainable Energy Reviews*, vol. 104, pp. 504–522, 2019. [Online]. Available: https://www.sciencedirect.com/science/article/pii/S1364032118308608

[5] F. Bünning, M. Wetter, M. Fuchs, and D. Müller, "Bidirectional low temperature district energy systems with agent-based control: Performance comparison and operation optimization," *Applied Energy*, vol. 209, pp. 502–515, 2018. [Online]. Available: https://www.sciencedirect.com/science/article/pii/S0306261917314940

[6] United Nations, *Montreal Protocol on Substances that Deplete the Ozone Layer*. Montreal: United Nations Treaty Series, 1987, vol. 1522. [Online]. Available: https://treaties.un.org/doc/Publication/UNTS/Volume%201522/volume-1522-I-26369-English.pdf

[7] ——, "Kigali amendment to the Montreal Protocol on Substances that Deplete the Ozone Layer," 2016, adopted on October 15, 2016, in Kigali, Rwanda. Entered into force on January 1, 2019. [Online]. Available: https://treaties.un.org/Pages/ViewDetails.aspx?src=IND&mtdsg_no=XXVII-2-f&chapter=27&clang=_en

[8] S. Henchoz, "On a multi-service, CO2 based, district energy system for a better energy efficiency of urban areas," in *WEC 2011*, 2011.

[9] C. Weber and D. Favrat, “Conventional and advanced CO2 based district energy systems,” *Energy*, vol. 35, no. 12, pp. 5070–5081, 2010. [Online]. Available: https://www.sciencedirect.com/science/article/pii/S0360544210004354

[10] S. Henchoz, C. Weber, F. Maréchal, and D. Favrat, “Performance and profitability perspectives of a CO2 based district energy network in Geneva’s city centre,” *Energy*, vol. 85, pp. 221–235, 2015.

[11] P. Ungar, L. Milli, G. Manfrida, D. Fiaschi, and L. Talluri, “Re-designing district heating networks through innovative CO2 solutions,” in *Journal of physics: Conference series*, vol. 2385, no. 1. IOP Publishing, 2022, p. 012125.

[12] P. Eslami-Nejad, A. Bastani, and D. Giguere, “Single-pipe thermal energy system,” 2023, united States Patent, His Majesty The King In Right of Canada, as represented by the Minister of Natural Resources.

[13] P. Eslami-Nejad and A. Bastani, “Two-phase CO2 loop for thermal energy management in buildings: Concept and building energy performance improvement,” in *14th Gustav Lorentzen Conference on Natural Refrigerants*, Kyoto, Japan, 2020.

[14] S. Gholamrezaie, M. Cimmino, and P. Eslami-Nejad, “Modeling and experimental validation of a single-pipe CO2 thermal network connected to local heat pumps,” *Applied Thermal Engineering*, vol. 280, p. 128363, 2025. [Online]. Available: https://www.sciencedirect.com/science/article/pii/S1359431125029552

[15] C. Perry, T. Nickson, C. Starr, T. Grabiel, S. Geoghegan, B. Porter, A. Mahapatra, and F. Walravens, “More to offer from the montreal protocol: how the ozone treaty can secure further significant greenhouse gas emission reductions in the future,” *Journal of Integrative Environmental Sciences*, vol. 21, no. 1, p. 2362124, 2024.

[16] S. Dilshad, A. R. Kalair, and N. Khan, “Review of carbon dioxide (CO2) based heating and cooling technologies: Past, present, and future outlook,” *International Journal of Energy Research*, vol. 44, no. 3, pp. 1408–1463, 2020.

[17] R. U. Rony, H. Yang, S. Krishnan, and J. Song, “Recent advances in transcritical CO2 (R744) heat pump system: A review,” *Energies*, vol. 12, no. 3, p. 457, 2019.

[18] G. Lorentzen, “Revival of carbon dioxide as a refrigerant,” *International Journal of Refrigeration*, vol. 17, no. 5, pp. 292–301, 1994. [Online]. Available: https://www.sciencedirect.com/science/article/pii/0140700794900590

[19] M.-H. Kim, J. Pettersen, and C. W. Bullard, "Fundamental process and system design issues in CO2 vapor compression systems," *Progress in Energy and Combustion Science*, vol. 30, no. 2, pp. 119–174, 2004. [Online]. Available: https://www.sciencedirect.com/science/article/pii/S0360128503000765

[20] H. Lund, S. Werner, R. Wiltshire, S. Svendsen, J. E. Thorsen, F. Hvelplund, and B. V. Mathiesen, "4th generation district heating (4GDH): Integrating smart thermal grids into future sustainable energy systems," *Energy*, vol. 68, pp. 1–11, 2014. [Online]. Available: https://www.sciencedirect.com/science/article/pii/S0360544214002369

[21] S. Werner, "International review of district heating and cooling," *Energy*, vol. 137, pp. 617–631, 2017. [Online]. Available: https://www.sciencedirect.com/science/article/pii/S036054421730614X

[22] D. Fiaschi, P. Ungar, F. Gigliotti, and A. Meana-Fernández, "Thermo-economic analysis of a geothermal-driven district heating network: Comparison between a water-based and a CO2-based grid," *Applied Thermal Engineering*, vol. 281, p. 128794, 2025. [Online]. Available: https://www.sciencedirect.com/science/article/pii/S1359431125033861

[23] A. Bastani and P. Eslami-Nejad, "CO2 network for thermal management in buildings," in *Proceedings of eSim 2020: 11th Conference of IBPSA-Canada*, ser. eSim, vol. 11. Vancouver, Canada: IBPSA-Canada, June 2020. [Online]. Available: https://publications.ibpsa.org/conference/paper/?id=esim2020_1124

[24] A. Bastani and S. Gholamrezaie, "CO2 thermal network prototype: Identifying control parameters for optimal operation in transcritical mode," *Energy Conversion and Management*, vol. 322, p. 119170, 2024. [Online]. Available: https://www.sciencedirect.com/science/article/pii/S0196890424011117

[25] T. El Samad, A. Żabnieńska Góra, H. Jouhara, and A. I. Sayma, "A review of compressors for high temperature heat pumps," *Thermal Science and Engineering Progress*, vol. 51, p. 102603, 2024. [Online]. Available: https://www.sciencedirect.com/science/article/pii/S245190492400221X

[26] J. Wang, M. Belusko, M. Liu, H. Semsarilar, R. Liddle, A. Alemu, M. Evans, C. Zhao, J. Hudson, and F. Bruno, "A comprehensive study on a novel transcritical CO2 heat pump for simultaneous space heating and cooling – concepts and initial performance," *Energy Conversion and Management*, vol. 243, p. 114397, 2021. [Online]. Available: https://www.sciencedirect.com/science/article/pii/S0196890421005732

[27] B. D. Rasmussen and A. Jakobsen, "Review of compressor models and performance characterizing variables," in *Fifteenth International Compressor Engineering Conference at Purdue University*, West lafayette, USA, 2000.

[28] Air-Conditioning, Heating, and Refrigeration Institute (AHRI), "AHRI 540 – Standard for Performance Rating of Positive Displacement Refrigerant Compressors and Compressor Units," 2020.

[29] A. L. Hjortland and R. R. Crawford, "A comparative analysis of a new semi-empirical model and the AHRI polynomial model for positive displacement compressors," *International Journal of Refrigeration*, vol. 159, pp. 254–263, 2024. [Online]. Available: https://www.sciencedirect.com/science/article/pii/S0140700723004656

[30] V. Aute and C. Martin, "A comprehensive evaluation of regression uncertainty and the effect of sample size on the AHRI-540 method of compressor performance representation," 2016.

[31] Y. Guo, G. Li, H. Chen, Y. Hu, L. Shen, H. Li, M. Hu, and J. Li, "Development of a virtual variable-speed compressor power sensor for variable refrigerant flow air conditioning system," *International Journal of Refrigeration*, vol. 74, pp. 73–85, 2017. [Online]. Available: https://www.sciencedirect.com/science/article/pii/S014070071630322X

[32] A. Dabiri and C. K. Rice, "A compressor simulation model with corrections for the level of suction gas superheat," *ASHRAE Transactions*, vol. 87, no. Part 2, pp. 771–782, 1981.

[33] G. Viviescas and M. Bernier, "A variable speed water-to-water heat pump model used for ground-source applications," *Science and Technology for the Built Environment*, vol. 30, no. 3, pp. 266–279, 2024.

[34] D. Sánchez, R. Larrondo-Sancho, F. Vidan-Falomir, and R. Cabello, "Empirical modelling of a semihermetic reciprocating compressor for different CO2-based mixtures," *Applied Thermal Engineering*, vol. 250, p. 123536, 2024. [Online]. Available: https://www.sciencedirect.com/science/article/pii/S1359431124012043

[35] W. Wu, H. M. Skye, and J. J. Dyreby, "Modeling and experiments for a CO2 ground-source heat pump with subcritical and transcritical operation," *Energy Conversion and Management*, vol. 243, p. 114420, 2021. [Online]. Available: https://www.sciencedirect.com/science/article/pii/S0196890421005963

[36] Y. Yang, X. Peng, G. Wang, X. Liu, and D. Wang, “Energetic and exergetic analysis of a transcritical CO2 air-source heat pump water heating system in the cold region,” *Energy and Buildings*, vol. 298, p. 113558, 2023. [Online]. Available: https://www.sciencedirect.com/science/article/pii/S0378778823007880

[37] C. Vering, M. Engelpracht, S. Göbel, S. Hoseinpoori, F. Wüllhorst, C. Schwenzer, M. Rademacher, S. Hinrichs, F. Chandra, P. Mehrfeld *et al.*, “Open-source vapor compression library (vclib): Heat pump modeling for education and research,” *Computer Applications in Engineering Education*, vol. 30, no. 5, pp. 1498–1509, 2022.

[38] S. Martínez-Ballester, J.-M. Corberán, J. Gonzálvez-Maciá, and P. A. Domanski, “Impact of classical assumptions in modelling a microchannel gas cooler,” *International Journal of Refrigeration*, vol. 34, no. 8, pp. 1898–1910, 2011. [Online]. Available: https://www.sciencedirect.com/science/article/pii/S0140700711001782

[39] N. Hayes, A. Jokar, and Z. H. Ayub, “Study of carbon dioxide condensation in chevron plate exchangers; heat transfer analysis,” *International Journal of Heat and Mass Transfer*, vol. 54, no. 5-6, pp. 1121–1131, 2011.

[40] A. Desideri, B. Dechesne, J. Wronski, M. Van den Broek, S. Gusev, V. Lemort, and S. Quoilin, “Comparison of moving boundary and finite-volume heat exchanger models in the modelica language,” *Energies*, vol. 9, no. 5, p. 339, 2016.

[41] I. H. Bell, S. Quoilin, E. Georges, J. E. Braun, E. A. Groll, W. T. Horton, and V. Lemort, “A generalized moving-boundary algorithm to predict the heat transfer rate of counterflow heat exchangers for any phase configuration,” *Applied Thermal Engineering*, vol. 79, pp. 192–201, 2015.

[42] A. M. Bahman, D. Ziviani, and E. A. Groll, “A generalized moving-boundary algorithm to predict the heat transfer rate of transcritical CO2 gas coolers,” *International Journal of Refrigeration*, vol. 118, pp. 491–503, 2020. [Online]. Available: https://www.sciencedirect.com/science/article/pii/S0140700720302449

[43] Y.-G. Chen and Q.-Y. Yang, “A new moving-boundary algorithm to predict heat transfer rate of counter-flow water-cooled transcritical CO2 gas cooler,” *International Journal of Refrigeration*, vol. 146, pp. 357–365, 2023.

[44] B. M. Fronk and S. Garimella, “Water-coupled carbon dioxide microchannel gas cooler for heat pump water heaters: Part ii – model development and validation,”

International Journal of Refrigeration, vol. 34, no. 1, pp. 17–28, 2011. [Online]. Available: https://www.sciencedirect.com/science/article/pii/S014070071000109X

[45] F. Bruno, M. Belusko, and E. Halawa, "CO2 refrigeration and heat pump systems—a comprehensive review," *Energies*, vol. 12, no. 15, p. 2959, 2019.

[46] H. Qiao, V. Aute, H. Lee, K. Saleh, and R. Radermacher, "A new model for plate heat exchangers with generalized flow configurations and phase change," *International Journal of Refrigeration*, vol. 36, no. 2, pp. 622–632, 2013, sI: New Developments in Boiling and Condensation. [Online]. Available: https://www.sciencedirect.com/science/article/pii/S0140700712003283

[47] Z. H. Ayub, "Plate heat exchanger literature survey and new heat transfer and pressure drop correlations for refrigerant evaporators," *Heat transfer engineering*, vol. 24, no. 5, pp. 3–16, 2003.

[48] A. Zendehboudi, Z. Ye, A. Hafner, T. Andresen, and G. Skaugen, "Heat transfer and pressure drop of supercritical CO2 in brazed plate heat exchangers of the tri-partite gas cooler," *International Journal of Heat and Mass Transfer*, vol. 178, p. 121641, 2021. [Online]. Available: https://www.sciencedirect.com/science/article/pii/S0017931021007444

[49] L. Cecchinato, M. Corradi, G. Cosi, S. Minetto, and M. Rampazzo, "A real-time algorithm for the determination of R744 systems optimal high pressure," *International Journal of Refrigeration*, vol. 35, no. 4, pp. 817–826, 2012. [Online]. Available: https://www.sciencedirect.com/science/article/pii/S0140700712000060

[50] Y. Li, N. Nord, H. Yin, G. Pan, C. Wang, T. Wu, and I. H. Rekstad, "A study of optimal control approaches of water-to-water co2 heat pump for domestic hot water use," *Case Studies in Thermal Engineering*, vol. 65, p. 105615, 2025. [Online]. Available: https://www.sciencedirect.com/science/article/pii/S2214157X24016460

[51] W. Wang, Z. Zhao, Q. Zhou, Y. Qiao, and F. Cao, "Model predictive control for the operation of a transcritical CO2 air source heat pump water heater," *Applied Energy*, vol. 300, p. 117339, 2021. [Online]. Available: https://www.sciencedirect.com/science/article/pii/S0306261921007479

[52] T. Zhang, F. Cao, Y. Song, J. Ren, G. Bai, X. Pang, and Y. He, "The model predictive control strategy of the transcritical CO2 air conditioning system used in

railway vehicles," *Applied Thermal Engineering*, vol. 218, p. 119376, 2023. [Online]. Available: https://www.sciencedirect.com/science/article/pii/S1359431122013060

[53] H. Wang, W. Wang, Y. Song, X. Yang, P. Valdiserri, E. Rossi di Schio, G. Yu, and F. Cao, "Data-driven model predictive control of transcritical CO2 systems for cabin thermal management in cooling mode," *Applied Thermal Engineering*, vol. 235, p. 121337, 2023. [Online]. Available: https://www.sciencedirect.com/science/article/pii/S1359431123013662

[54] C. Cui, H. Xing, Y. Song, M. Rampazzo, W. Wang, X. Yin, and F. Cao, "Real-time multi-variable optimization of the interstage subcooling vapor-injection based transcritical CO2 hpwh: An integrated model predictive control approach," *International Journal of Refrigeration*, vol. 159, pp. 218–229, 2024. [Online]. Available: https://www.sciencedirect.com/science/article/pii/S0140700723004851

[55] T. G. Hovgaard, S. Boyd, L. F. Larsen, and J. B. Jørgensen, "Nonconvex model predictive control for commercial refrigeration," *International Journal of Control*, vol. 86, no. 8, pp. 1349–1366, 2013.

[56] T. G. Hovgard, L. F. Larsen, J. B. Jørgensen, and S. Boyd, "Fast nonconvex model predictive control for commercial refrigeration," *IFAC Proceedings Volumes*, vol. 45, no. 17, pp. 514–521, 2012, 4th IFAC Conference on Nonlinear Model Predictive Control. [Online]. Available: https://www.sciencedirect.com/science/article/pii/S147466701631494X

[57] M. Wirtz, L. Neumaier, P. Remmen, and D. Müller, "Temperature control in 5th generation district heating and cooling networks: An MILP-based operation optimization," *Applied Energy*, vol. 288, p. 116608, 2021. [Online]. Available: https://www.sciencedirect.com/science/article/pii/S0306261921001422

[58] D. Quaggiotto, J. Vivian, and A. Zarrella, "Management of a district heating network using model predictive control with and without thermal storage," *Optimization and Engineering*, vol. 22, no. 3, pp. 1897–1919, 2021.

[59] J. Jansen, F. Jorissen, and L. Helsen, "Mixed-integer non-linear model predictive control of district heating networks," *Applied Energy*, vol. 361, p. 122874, 2024. [Online]. Available: https://www.sciencedirect.com/science/article/pii/S0306261924002575

[60] B. Hu, Y. Li, F. Cao, and Z. Xing, "Extremum seeking control of cop optimization for air-source transcritical CO2 heat pump water heater system,"

Applied Energy, vol. 147, pp. 361–372, 2015. [Online]. Available: https://www.sciencedirect.com/science/article/pii/S0306261915002949

[61] C. Cui, S. Zong, Y. Song, X. Yin, and F. Cao, "Experimental investigation of the extreme seeking control on a transcritical CO2 heat pump water heater," *International Journal of Refrigeration*, vol. 133, pp. 111–122, 2022. [Online]. Available: https://www.sciencedirect.com/science/article/pii/S0140700721003856

[62] M. Rampazzo, A. Cervato, C. Corazzol, L. Mattiello, A. Beghi, L. Cecchinato, and A. Virzi, "Energy-efficient operation of transcritical and subcritical co2 inverse cycles via extremum seeking control," *Journal of Process Control*, vol. 81, pp. 87–97, 2019. [Online]. Available: https://www.sciencedirect.com/science/article/pii/S0959152419304226

[63] C. Cui, J. Ren, M. Rampazzo, Y. Song, X. Yin, and F. Cao, "Real-time energy-efficient operation of a dedicated mechanical subcooling based transcritical co2 heat pump water heater via multi-input single-output extreme seeking control," *International Journal of Refrigeration*, vol. 144, pp. 76–89, 2022. [Online]. Available: https://www.sciencedirect.com/science/article/pii/S0140700722002511

[64] F. Kauf, "Determination of the optimum high pressure for transcritical CO2-refrigeration cycles," *International Journal of Thermal Sciences*, vol. 38, no. 4, pp. 325–330, 1999. [Online]. Available: https://www.sciencedirect.com/science/article/pii/S1290072999800982

[65] S. Liao, T. Zhao, and A. Jakobsen, "A correlation of optimal heat rejection pressures in transcritical carbon dioxide cycles," *Applied Thermal Engineering*, vol. 20, no. 9, pp. 831–841, 2000. [Online]. Available: https://www.sciencedirect.com/science/article/pii/S1359431199000708

[66] P.-C. Qi, Y.-L. He, X.-L. Wang, and X.-Z. Meng, "Experimental investigation of the optimal heat rejection pressure for a transcritical CO2 heat pump water heater," *Applied Thermal Engineering*, vol. 56, no. 1, pp. 120–125, 2013. [Online]. Available: https://www.sciencedirect.com/science/article/pii/S1359431113002238

[67] C. Li, P. Jiang, and Y. Zhu, "Optimal compressor discharge pressure and performance characteristics of transcritical CO2 heat pump for crude oil heating," *International Journal of Refrigeration*, vol. 144, pp. 99–107, 2022. [Online]. Available: https://www.sciencedirect.com/science/article/pii/S0140700722002602

[68] L. Cecchinato, M. Corradi, and S. Minetto, “A critical approach to the determination of optimal heat rejection pressure in transcritical systems,” *Applied Thermal Engineering*, vol. 30, no. 13, pp. 1812–1823, 2010. [Online]. Available: https://www.sciencedirect.com/science/article/pii/S135943111000178X

[69] L.-L. Shao, Z.-Y. Zhang, and C.-L. Zhang, “Constrained optimal high pressure equation of CO2 transcritical cycle,” *Applied Thermal Engineering*, vol. 128, pp. 173–178, 2018. [Online]. Available: https://www.sciencedirect.com/science/article/pii/S1359431116322451

[70] X.-Y. Liang, Y.-J. He, J.-H. Cheng, L.-L. Shao, and C.-L. Zhang, “Difference analysis on optimal high pressure of transcritical CO2 cycle in different applications,” *International Journal of Refrigeration*, vol. 106, pp. 384–391, 2019. [Online]. Available: https://www.sciencedirect.com/science/article/pii/S0140700719302841

[71] X. Yin, F. Cao, J. Wang, M. Li, and X. Wang, “Investigations on optimal discharge pressure in CO2 heat pumps using the gmdh and pso-bp type neural network—part a: Theoretical modeling,” *International Journal of Refrigeration*, vol. 106, pp. 549–557, 2019. [Online]. Available: https://www.sciencedirect.com/science/article/pii/S0140700719301835

[72] Y. Song, D. Yang, M. Li, and F. Cao, “Investigations on optimal discharge pressure in CO2 heat pumps using the gmdh and pso-bp type neural network—part b: Experimental study,” *International Journal of Refrigeration*, vol. 106, pp. 248–257, 2019. [Online]. Available: https://www.sciencedirect.com/science/article/pii/S0140700719302506

[73] A. Bemporad, F. Borrelli, M. Morari *et al.*, “Model predictive control based on linear programming˜ the explicit solution,” *IEEE transactions on automatic control*, vol. 47, no. 12, pp. 1974–1985, 2002.

[74] A. Alessio and A. Bemporad, “A survey on explicit model predictive control,” in *Nonlinear model predictive control: towards new challenging applications*. Springer, 2009, pp. 345–369.

[75] S. Gholamrezaie, M. Cimmino, and P. Eslami-Nejad, “Simulation and control strategy of a CO2 loop for building thermal management in heating mode,” in *15th IIR-Gustav Lorentzen Conference on Natural Refrigerants*, Trondheim, Norway, 2022.

[76] ——, “Heating and cooling of an office building using distributed heat pumps connected to a two-phase CO2 thermal management system: Detailed simulation,” in *Proceedings of the eSim 2024 Conference, 13th Conference of IBPSA-Canada.* IBPSA-Canada, 2024.

[77] ——, “Investigating control parameters of a CO2-based thermal network connecting decentralized heat pumps,” in *16th IIR-Gustav Lorentzen Conference on Natural Refrigerants.* International Institute of Refrigeration (Maryland, USA), 2024.

[78] T. Sommer, M. Sulzer, M. Wetter, A. Sotnikov, S. Mennel, and C. Stettler, “The reservoir network: A new network topology for district heating and cooling,” *Energy*, vol. 199, p. 117418, 2020.

[79] K. Gjoka, B. Rismanchi, and R. H. Crawford, “Fifth-generation district heating and cooling systems: A review of recent advancements and implementation barriers,” *Renewable and Sustainable Energy Reviews*, vol. 171, p. 112997, 2023.

[80] L. Gagné-Boisvert and M. Bernier, “Integrated model for comparison of one-and two-pipe ground-coupled heat pump network configurations,” *Science and Technology for the Built Environment*, vol. 24, no. 7, pp. 726–742, 2018.

[81] ASHRAE, *HVAC systems and equipment handbook.* American Society of Heating, Refrigerating and Air-Conditioning Engineers, 2020.

[82] J. Pietsch, “Water-loop heat pump systems: Assessment study update,” Electric Power Research Inst., Palo Alto, CA (United States), Tech. Rep., 1991.

[83] S. Yuan and M. Grabon, “Optimizing energy consumption of a water-loop variable-speed heat pump system,” *Applied Thermal Engineering*, vol. 31, no. 5, pp. 894–901, 2011.

[84] X. Lian, “Optimized control strategies for a typical water loop heat pump system,” PhD Thesis, University of Nebraska - Lincoln, 2011.

[85] W. Goetzler, “Variable refrigerant flow systems,” *ASHRAE Journal*, vol. 49, no. 4, pp. 24–31, 2007.

[86] X. Lin, H. Lee, Y. Hwang, and R. Radermacher, “A review of recent development in variable refrigerant flow systems,” *Science and Technology for the Built Environment*, vol. 21, no. 7, pp. 917–933, 2015.

[87] J. Wang, X. Lu, V. Adetola, and E. Louie, "Modeling variable refrigerant flow (VRF) systems in building applications: A comprehensive review," *Energy and Buildings*, p. 114128, 2024.

[88] G. Li, Y. Hu, H. Chen, L. Shen, H. Li, J. Li, and W. Hu, "Extending the virtual refrigerant charge sensor (VRC) for variable refrigerant flow (VRF) air conditioning system using data-based analysis methods," *Applied Thermal Engineering*, vol. 93, pp. 908–919, 2016.

[89] L.-L. Shao and C.-L. Zhang, "Thermodynamic transition from subcritical to transcritical CO2 cycle," *International Journal of Refrigeration*, vol. 64, pp. 123–129, 2016.

[90] A. Afram and F. Janabi-Sharifi, "Review of modeling methods for HVAC systems," *Applied thermal engineering*, vol. 67, no. 1-2, pp. 507–519, 2014.

[91] K. S. Gabel and C. R. Bradshaw, "Evaluation and quantification of compressor model predictive capabilities under modulation and extrapolation scenarios," *International Journal of Refrigeration*, vol. 149, pp. 1–10, 2023. [Online]. Available: https://www.sciencedirect.com/science/article/pii/S0140700722004418

[92] S. Shao, W. Shi, X. Li, and H. Chen, "Performance representation of variable-speed compressor for inverter air conditioners based on experimental data," *International journal of refrigeration*, vol. 27, no. 8, pp. 805–815, 2004.

[93] P. Popovic and H. N. Shapiro, "A semi-empirical method for modeling a reciprocating compressor in refrigeration systems," American Society of Heating, Refrigerating and Air-Conditioning Engineers, Tech. Rep., 1995.

[94] E. Winandy, C. Saavedra, and J. Lebrun, "Experimental analysis and simplified modelling of a hermetic scroll refrigeration compressor," *Applied thermal engineering*, vol. 22, no. 2, pp. 107–120, 2002.

[95] G. Viviescas and M. Bernier, "A water-to-water heat pump model with experimental validation," *Energies*, vol. 17, no. 8, p. 1858, 2024.

[96] J. M. Yin, C. W. Bullard, and P. S. Hrnjak, "R-744 gas cooler model development and validation," *International Journal of Refrigeration*, vol. 24, no. 7, pp. 692–701, 2001.

[97] D. Sánchez, R. Cabello, R. Llopis, and E. Torrella, "Development and validation of a finite element model for water–CO2 coaxial gas-coolers," *Applied energy*, vol. 93, pp. 637–647, 2012.

[98] O. Sarfraz, C. K. Bach, and C. Bradshaw, "A literature review of numerical modeling techniques for vapor compression systems with focus on heat exchanger modeling," in *INTERNATIONAL REFRIGERATION AND AIR CONDITIONING CONFERENCE*, Purdue, USA, 2018.

[99] G.-l. Ding, "Recent developments in simulation techniques for vapour-compression refrigeration systems," *International Journal of refrigeration*, vol. 30, no. 7, pp. 1119–1133, 2007.

[100] M. M. Costa and J. Parise, "A three-zone simulation model for a air-cooled condensers," *Heat Recovery Systems and CHP*, vol. 13, no. 2, pp. 97–113, 1993.

[101] C. Le, P. Bansal, and J. Tedford, "Three-zone system simulation model of a multiple-chiller plant," *Applied thermal engineering*, vol. 24, no. 14-15, pp. 1995–2015, 2004.

[102] I. H. Bell, J. Wronski, S. Quoilin, and V. Lemort, "Pure and pseudo-pure fluid thermophysical property evaluation and the open-source thermophysical property library coolprop," *Industrial & Engineering Chemistry Research*, vol. 53, no. 6, pp. 2498–2508, 2014. [Online]. Available: http://pubs.acs.org/doi/abs/10.1021/ie4033999

[103] R. Span and W. Wagner, "A new equation of state for carbon dioxide covering the fluid region from the triple-point temperature to 1100 k at pressures up to 800 mpa," *Journal of physical and chemical reference data*, vol. 25, no. 6, pp. 1509–1596, 1996.

[104] M. B. Kim and C. Y. Park, "An experimental study on single phase convection heat transfer and pressure drop in two brazed plate heat exchangers with different chevron shapes and hydraulic diameters," *Journal of Mechanical Science and Technology*, vol. 31, pp. 2559–2571, 2017.

[105] A. Wanniarachchi, U. Ratnam, B. Tilton, and K. Dutta-Roy, "Approximate correlations for chevron-type plate heat exchangers," in *30th National Heat Transfer Conference*. American Society of Mechanical Engineers, New York, NY (United States), 1995.

[106] K. Nilpueng, L. G. Asirvatham, A. S. Dalkılıç, O. Mahian, H. S. Ahn, and S. Wongwises, "Heat transfer and fluid flow characteristics in a plate heat exchanger filled with copper foam," *Heat and Mass Transfer*, vol. 56, pp. 3261–3271, 2020.

[107] Y.-Y. Yan, H.-C. Lio, and T.-F. Lin, "Condensation heat transfer and pressure drop of refrigerant r-134a in a plate heat exchanger," *International Journal of Heat and Mass Transfer*, vol. 42, no. 6, pp. 993–1006, 1999.

[108] E. Lee, H. Kang, and Y. Kim, “Flow boiling heat transfer and pressure drop of water in a plate heat exchanger with corrugated channels at low mass flux conditions,” *International journal of heat and mass transfer*, vol. 77, pp. 37–45, 2014.

[109] B. N. Taylor, C. E. Kuyatt *et al.*, *Guidelines for evaluating and expressing the uncertainty of NIST measurement results.* US Department of Commerce, Technology Administration, National Institute of . . . , 1994, vol. 1297.

[110] A. Kanaris, A. Mouza, and S. Paras, “Optimal design of a plate heat exchanger with undulated surfaces,” *International Journal of Thermal Sciences*, vol. 48, no. 6, pp. 1184–1195, 2009.

[111] F. A. Mota, M. A. Ravagnani, and E. Carvalho, “Optimal design of plate heat exchangers,” *Applied Thermal Engineering*, vol. 63, no. 1, pp. 33–39, 2014.

[112] L. Wang and B. Sunden, “Optimal design of plate heat exchangers with and without pressure drop specifications,” *Applied Thermal Engineering*, vol. 23, no. 3, pp. 295–311, 2003.

[113] J. Zhang, X. Zhu, M. E. Mondejar, and F. Haglind, “A review of heat transfer enhancement techniques in plate heat exchangers,” *Renewable and Sustainable Energy Reviews*, vol. 101, pp. 305–328, 2019.

[114] X. Zhang, X. Fan, F. Wang, and H. Shen, “Theoretical and experimental studies on optimum heat rejection pressure for a CO2 heat pump system,” *Applied Thermal Engineering*, vol. 30, no. 16, pp. 2537–2544, 2010, selected Papers from the 12th Conference on Process Integration, Modelling and Optimisation for Energy Saving and Pollution Reduction. [Online]. Available: https://www.sciencedirect.com/science/article/pii/S1359431110002784

[115] X. Qin, H. Liu, X. Meng, X. Wei, L. Zhao, and L. Yang, “A study on the compressor frequency and optimal discharge pressure of the transcritical CO2 heat pump system,” *International Journal of Refrigeration*, vol. 99, pp. 101–113, 2019. [Online]. Available: https://www.sciencedirect.com/science/article/pii/S0140700718305279

[116] C. Wei, Y. Guo, Y. Li, Y. Wang, Y. Liu, C. Du, and L. Zhang, “Research on optimization of compressor frequency conversion control in transcritical heat pump system,” *Energy*, vol. 313, p. 133928, 2024. [Online]. Available: https://www.sciencedirect.com/science/article/pii/S036054422403706X

[117] L. Jiang, Y. Chu, Y. Song, and F. Cao, "Study on working condition adaptability of transcritical CO2 heat pump based on intermediate temperature heating," *Applied Thermal Engineering*, vol. 277, p. 127038, 2025. [Online]. Available: https://www.sciencedirect.com/science/article/pii/S1359431125016308

[118] A. Goyal, M. A. Staedter, and S. Garimella, "A review of control methodologies for vapor compression and absorption heat pumps," *International Journal of Refrigeration*, vol. 97, pp. 1–20, 2019. [Online]. Available: https://www.sciencedirect.com/science/article/pii/S0140700718303220

[119] A. Afram and F. Janabi-Sharifi, "Theory and applications of HVAC control systems – a review of model predictive control (MPC)," *Building and Environment*, vol. 72, pp. 343–355, 2014. [Online]. Available: https://www.sciencedirect.com/science/article/pii/S0360132313003363

[120] M. Schwenzer, M. Ay, T. Bergs, and D. Abel, "Review on model predictive control: An engineering perspective," *The International Journal of Advanced Manufacturing Technology*, vol. 117, no. 5, pp. 1327–1349, 2021.

[121] Z. Lee, K. Gupta, K. J. Kircher, and K. M. Zhang, "Mixed-integer model predictive control of variable-speed heat pumps," *Energy and Buildings*, vol. 198, pp. 75–83, 2019. [Online]. Available: https://www.sciencedirect.com/science/article/pii/S0378778819302609

[122] X.-H. Yin and S.-Y. Li, "Model predictive control for vapor compression cycle of refrigeration process," *International Journal of Automation and Computing*, vol. 15, no. 6, pp. 707–715, 2018.

[123] M. Swanson, B. Barnes, R. J. Liesen, M. Case, and A. Zhivov, "Community-scale energy supply and distribution optimization using mixed-integer linear programming." *ASHRAE Transactions*, vol. 120, no. 1, 2014.

[124] H. Krützfeldt, C. Vering, P. Mehrfeld, and D. Müller, "MILP design optimization of heat pump systems in German residential buildings," *Energy and Buildings*, vol. 249, p. 111204, 2021. [Online]. Available: https://www.sciencedirect.com/science/article/pii/S0378778821004886

[125] L. Maier, M. Schönegge, S. Henn, D. Hering, and D. Müller, "Assessing mixed-integer-based heat pump modeling approaches for model predictive control

applications in buildings," *Applied Energy*, vol. 326, p. 119894, 2022. [Online]. Available: https://www.sciencedirect.com/science/article/pii/S0306261922011576

[126] F. Liu, W. Zhu, and J. Zhao, "Model-based dynamic optimal control of a CO2 heat pump coupled with hot and cold thermal storages," *Applied Thermal Engineering*, vol. 128, pp. 1116–1125, 2018. [Online]. Available: https://www.sciencedirect.com/science/article/pii/S1359431117332520

[127] H. Ji, J. Pei, J. Niu, C. Ding, F. Guo, and Y. Wang, "Hybrid offline and online strategy for optimal high pressure seeking of the transcritical CO2 heat pump system in an electric vehicle," *Applied Thermal Engineering*, vol. 228, p. 120514, 2023. [Online]. Available: https://www.sciencedirect.com/science/article/pii/S1359431123005434

[128] J. J. Aguilera, R. Padullés, W. Meesenburg, W. B. Markussen, B. Zühlsdorf, and B. Elmegaard, "Operation optimization in large-scale heat pump systems: A scheduling framework integrating digital twin modelling, demand forecasting, and MILP," *Applied Energy*, vol. 376, p. 124259, 2024. [Online]. Available: https://www.sciencedirect.com/science/article/pii/S0306261924016428

[129] L. Gasser, S. Flück, M. Kleingries, C. Meier, M. Bätschmann, and B. Wellig, "High efficiency heat pumps for low temperature lift applications," in *Proceedings of the 12th IEA Heat Pump Conference*, 2017.

[130] M. Ahmadfard and M. Bernier, "A review of vertical ground heat exchanger sizing tools including an inter-model comparison," *Renewable and Sustainable Energy Reviews*, vol. 110, pp. 247–265, 2019.

[131] ——, "An alternative to ASHRAE's design length equation for sizing borehole heat exchangers." *ASHRAE Transactions*, vol. 120, no. 2, pp. NA–NA, 2014.

[132] S. Javed and J. Spitler, "Accuracy of borehole thermal resistance calculation methods for grouted single u-tube ground heat exchangers," *Applied Energy*, vol. 187, pp. 790–806, 2017. [Online]. Available: https://www.sciencedirect.com/science/article/pii/S0306261916317111

[133] J. Tamasauskas, M. Kegel, and J. Blake, "The potential of heat pump technologies for the replacement of rooftop units in small commercial buildings," in *Proceedings of the eSim 2018 Conference*. IBPSA-Canada, 2018.

[134] M. Cimmino and P. Eslami-Nejad, "A simulation model for solar assisted shallow ground heat exchangers in series arrangement," *Energy and Buildings*, vol. 157, pp.

227–246, 2017. [Online]. Available: https://www.sciencedirect.com/science/article/pii/S0378778816301566

[135] M. Badache, P. Eslami-Nejad, M. Ouzzane, Z. Aidoun, and L. Lamarche, "A new modeling approach for improved ground temperature profile determination," *Renewable Energy*, vol. 85, pp. 436–444, 2016. [Online]. Available: https://www.sciencedirect.com/science/article/pii/S0960148115300434

APPENDIX A IEA CONFERENCE PAPER: IMPACT OF LOCAL HEAT PUMP CHARACTERISTICS ON THE PERFORMANCE OF A CO_2-BASED THERMAL NETWORK

Authors: Sepehr Gholamrezaie, Massimo Cimmino, Parham Eslami-Nejad

Conference: 15th IEA Heat Pump Conference

Date: Accepted for oral presentation on 20 February 2026

Abstract

CO_2-based thermal networks (CO_2TN) connected to local heat pumps (LHPs) offer a promising approach for thermal energy distribution in buildings. These systems circulate two-phase CO_2 at near-indoor (room) temperature through a single pipe (the CO_2 loop), which serves as the source side for LHPs connected in series. This configuration enables heat recovery between zones and as it operates at an almost constant temperature near indoor temperature, it reduces both heat losses through pipes and insulation requirements. Previous studies have shown that LHP's performance has a significant impact on the overall system performance. Standard heat pumps, typically designed for higher temperature difference between source and sink (temperature lift), operate quite well for conventional outdoor temperature ranges. However, they may not operate optimally when the source side is near room temperature and the required temperature lift is relatively small. This study evaluates how local heat pump performance characteristics influence the system-wide efficiency of a representative CO_2TN. The network includes a CO_2 circulation system, LHPs, and an outdoor unit that exchanges heat between the CO_2TN and the environment. A detailed simulation model is developed, incorporating all major system components: the circulation compressor, internal heat exchanger, outdoor-side heat exchangers (gas cooler, condenser, and evaporator), and local heat pumps. The base case is modeled using a commercially available LHP unit that has been modified at CanmetENERGY (Varennes, Canada) to integrate with the CO_2 loop. To explore potential system improvements, additional simulations are conducted using idealized performance curves that approximate thermodynamically optimized cycles. Based on the presented simulation results, avenues to improve the efficiency of the system by better selection of the heat pump units are identified.

Introduction

CO_2 Thermal Network (CO_2TN) is a building-scale cascade system proposed by Eslami-

Nejad et al. [12]. It arranges a central reversible vapor-compression cycle using CO_2 (R744) to circulate a two-phase CO_2 stream at near-room-temperature through a single-pipe loop that serves multiple packaged local heat pumps (LHPs). We refer to the central plant as the RVCC (reversible vapor-compression cycle) and to the circulating line at the source of the LHPs as the "CO_2-loop." The loop intentionally operates close to room temperature so that the source side experienced by all LHPs is nearly isothermal; the loop fluid carries heat primarily through phase change, so relatively small mass flow rates and compact pipe diameters are sufficient. LHPs are connected in series along the single pipe. Each LHP has its own sealed refrigerant circuit sized for the zone it serves. When a LHP runs in cooling, it rejects heat into the two-phase CO_2 stream and increases the CO_2 quality (vapor mass fraction); when a LHP runs in heating, it absorbs heat from the loop and decreases the CO_2 quality. This counter-balancing behavior enables internal heat recovery: heat rejected upstream can be re-used downstream without changing the loop temperature. Figure A.1 illustrates the system on a pressure-enthalpy (p-h) diagram. The cycle shows the RVCC preparing CO_2 to enter the CO_2-loop at point 5, after which it flows through the series of LHPs.

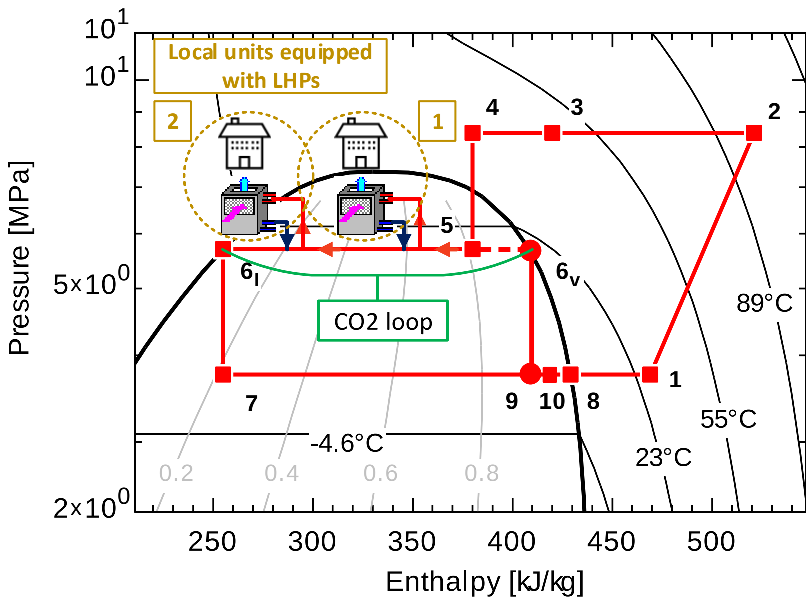

Figure A.1 CO_2TN overview

The concept has been demonstrated experimentally with a pilot-scale prototype built at CanmetENERGY–Varennes and presented by Bastani and Gholamrezaie [24]. In brief, the prototype comprises a CO_2 RVCC (compressor, gas cooler, internal heat exchangers, receiver/accumulator, expansion/control valve set) feeding a stainless-steel single-pipe loop and instrumented with pressure, temperature and mass-flow sensors. Three packaged LHPs are used that can be set in all-cooling or all-heating and mixed arrangements to emulate diverse multi-zone demands and simultaneous operation. This prototype established feasibility, provided high-resolution datasets for model validation, and established the reference architecture used in the present work.

Using the prototype data as ground truth, we developed and validated a detailed model of the CO_2TN [14], including component-level representations (compressor maps, gas cooler and CO_2-CO_2/CO_2-water heat exchangers, internal heat exchangers) and a building-side representation of LHPs and zone loads. Validation was performed both at component level and system level against the prototype. The model reproduces the loop thermodynamics (pressure, enthalpy evolution, and quality path) and the RVCC operating envelope across the heating and cooling modes used in the experiments.

On supervisory control, our 2022 study [75] introduced a minimum-mass-flow strategy tailored to the single-pipe, two-phase CO_2 loop. Based on cumulative heat exchange along the loop (evaluated at the outlet of each heat pump), a loop entry enthalpy can be evaluated to allow the smallest possible CO_2 mass flow that still maintains the loop within two-phase from start to end. The plant setpoints are selected to deliver that target within equipment limits. As our next study in 2024 revealed [77], we found that operating strictly at minimum mass flow with a saturated loop outlet can impair performance compared to the optimum operation. In practice, the overall efficiency varies with both the loop circulation and the chosen pressures: the maximum system efficiency often occurs away from the minimum-flow point, and allowing a small amount of superheat or sub-cool along the loop and at its outlet can further reduce circulation and compression work with only a slight performance penalty at LHPs. This motivates a relaxed-constraint supervisory approach that treats circulation and pressures as free decision variables rather than simply aiming for minimum CO_2 mass flow in the loop.

For the system to perform optimally, energy consumption of both the RVCC and the LHPs are equally important and they must operate efficiently. In our study, the key linkage between the RVCC and the LHPs is the source-side temperature seen by the LHPs, which the RVCC indirectly controls through the CO_2 loop pressure and mass flow it generates. The RVCC can provide this source temperature only within a workable range, bounded by equipment limits and operation stability. This raises a research question: how does LHP performance impact the overall efficiency of the system?

The efficiency of each LHP depends strongly on its source temperature. For a given building demand, a higher source temperature lowers the internal temperature lift—the difference between the evaporation and condensation temperatures within the heat pump—and thereby increases the coefficient of performance (COP). In practice, conventional commercial units are optimized for temperature lifts of 30 to 60 K, which limits their potential for efficiency improvement when operating at lower temperature lift conditions such as those provided by the CO_2 thermal network. In contrast, low-temperature-lift heat pumps, designed specifically for small lifts of 10 to 30 K, can achieve substantially higher performance. Gasser et al. [129] developed and experimentally tested two such prototypes: one using a reciprocating compressor and the other employing a small-scale, oil-free turbo compressor. The study demonstrated that at a lift of 20 K, the reciprocating unit achieved a heating COP above 9, while the turbo-compressor variant reached COP values of up to 14 for lifts below 15 K, corresponding to a nearly constant Carnot efficiency of about 60%. These results confirm the significant potential of low-lift systems when the temperature difference between the source and the sink is minimized.

Consistent with our previous prototype [24] and modeling work [14], the baseline LHPs are modified commercial units integrated into the CO_2TN. To explore the impact of different LHPs, we extend that baseline with two low-lift concepts from the literature: (1) a reciprocating-compressor heat pump optimized for small lifts and (2) an oil-free, small-scale turbo-compressor heat pump designed to maintain a high, relatively constant fraction of Carnot efficiency across 10 to 30 K lifts. Because the overall system performance depends on both the RVCC and the LHPs, it is not evident a priori how an increase in LHP COP will translate into system-level COP. In particular, the COPs of the LHPs depend on their source-side temperature, which is set by the CO_2 loop and therefore controlled by the RVCC; any change in LHP performance can thus modify the optimal loop pressure, mass flow rate, and operating regime of the circulation compressor. This study implements those two LHP models alongside the commercial baseline within the validated CO_2TN framework and compares the overall COP of the system for a five-zone case under identical RVCC and control settings.

System overview

The system comprises three main sections. First, a reversible vapor-compression cycle (RVCC) circulates CO_2, exchanges heat at the outdoor unit (absorbing or rejecting as needed), and supplies the CO_2 loop at the required pressure and temperature. Second, the outdoor unit is, in this study, a secondary hydronic loop coupled to geothermal boreholes. Third, packaged local heat pumps (LHPs) connect in series to the CO_2 loop and condition the individual zones. Figure A.2 shows the process flow diagram of the system.

Figure A.3 presents the CO_2 thermal network (CO_2TN) on a pressure-enthalpy chart and an-

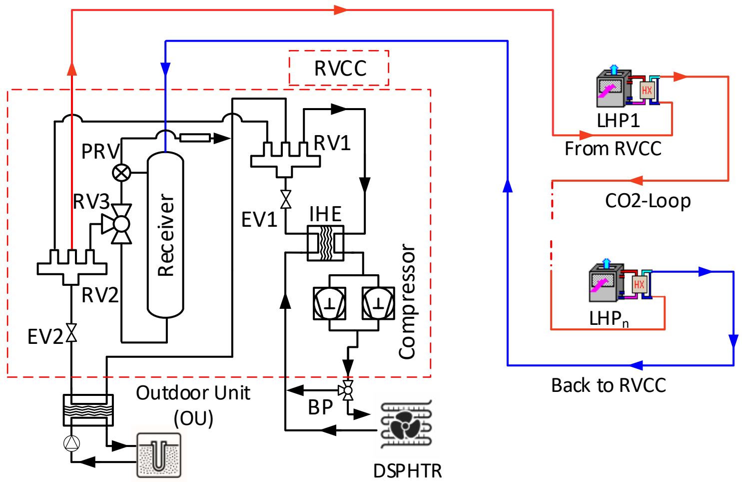

Figure A.2 System process flow diagram

chors the description of both operating regimes. The RVCC is a reversible vapor-compression circulation unit comprising two compressors (one variable-speed and one fixed-speed), a desuperheater, an outdoor heat exchanger whose role switches with the mode, an internal heat exchanger, a receiver, and expansion/pressure-regulation valves. A single-pipe CO_2 loop carries a near-room temperature, two-phase CO_2 that serves the source side of packaged local heat pumps (LHPs) connected in series. Each LHP conditions its zone and exchanges heat with the loop: in cooling, it rejects heat to the loop; in heating, it extracts heat from it.

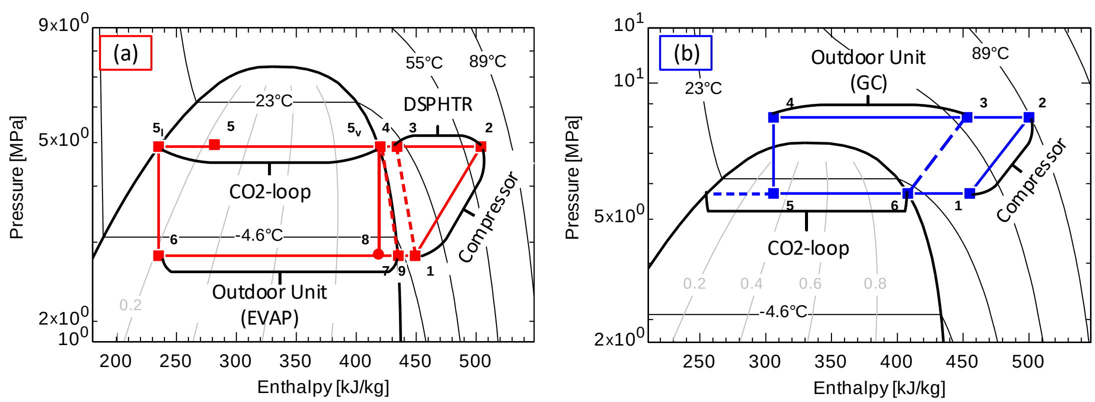

Figure A.3 (a) Heating-dominant mode; (b) Cooling-dominant mode

In heating-dominant operation (Figure A.3 a, red), the cycle begins at the compressor inlet (point 1) and proceeds to the discharge state (point 2). The discharge then passes through the desuperheater, where sensible heat is removed (points 2 to 3). Next, the internal heat exchanger transfers heat from the high-pressure side (points 3 to 4) to the suction side (points 9 to 1), ensuring a superheat of +10 °C at the compressor inlet. At point 4, the CO_2 enters the CO_2 loop and circulates through the source side of the LHPs. As the fluid flows through the series of LHPs (points 4 to 5), zones requiring heating extract heat from the loop, while any cooling zones reject heat. This combined effect alters the vapor fraction along the pipe until the stream exits the building loop at point 5. The returning flow accumulates in the receiver, where vapor (point 5v) and liquid (point 5l) phases separate. The liquid portion expands in an isenthalpic process from point 5 to 6 down to a pressure suitable to exchange heat with the outdoor unit. From point 6 to 7, the CO_2 passes through the outdoor unit, which operates as an evaporator (EVAP) absorbing heat from the external geothermal source. Finally, the vapor stream passes through the suction side of the internal heat exchanger (point 9), where the desired +10 °C superheat is maintained before returning to the compressor inlet (point 1), thus completing the heating-dominant cycle.

In cooling-dominant operation (Figure A.3 b, blue), the compressor again raises the CO_2 pressure and temperature from suction (point 1) to discharge (point 2). Between points 2 and 3, the internal heat exchanger provides heat to the suction side, ensuring sufficient superheat at the compressor inlet. From points 3 to 4, the outdoor unit now rejects heat to the environment, acting as a gas cooler (GC) in transcritical operation or as a condenser (COND) in subcritical conditions. At the gas cooler outlet (point 4), the CO_2 expands through the expansion valve to the inlet of the CO_2 loop, where it then flows on the source side of the LHPs (point 5). As the fluid progresses through the LHPs (points 5 to 6), zones operating in cooling reject heat to the loop and increase its vapor fraction, while any heating zones absorb heat from the stream. The return flow then passes through the internal heat exchanger (point 6) and suction line before reaching the compressor inlet (point 1), completing the cooling-dominant cycle. The same hardware supports both operating regimes; the distinction lies in the aggregate building demand and the role of the outdoor unit. When the combined effect of the active LHPs adds heat to the loop, the plant operates in cooling-dominant mode with the outdoor unit rejecting heat. When the net effect removes heat from the loop, the plant operates in heating-dominant mode with the outdoor unit absorbing heat. Either regime can operate in subcritical or transcritical conditions depending on the selected pressures and the external environment.

Case study: 5-zone building

We implemented the CO_2TN on a small office building in Montreal, Canada to evaluate its performance. The floor plan comprises five thermal zones—four perimeter zones (West, South, East, North) surrounding a Core zone. Annual zone loads follow Tamasauskas et al. [133] and are summarized in Table A.1. H and C denote heating and cooling, respectively. With respect to this case study, we sized and implemented the system.

Table A.1 Load characteristics (annual demand, peak load, and demand duration)

	West		South		East		North		Core	
	H	C	H	C	H	C	H	C	H	C
Total demand [kWh]	2050	2813	2198	5122	1849	2773	3020	3732	1014	6070
Peak load [kW]	3.3	4.2	5.1	4.4	3.3	3.8	5.3	3.4	4.2	3.7
Demand duration [h]	3692	2482	2263	4074	3352	2816	2585	3722	1267	4885

Modelling approach

The system is modelled component-by-component using the same compressor, heat exchanger and loop models that were developed and experimentally validated in Gholamrezaie et al. [14]. Only the main features are summarized here; elements that differ from the previous study (dual compressors and the local heat pump archetypes) are described in more detail. The main components of the system are two semi-hermetic reciprocating compressors in parallel (one variable-speed and one fixed-speed), a desuperheater (DSPHTR) in line for heating mode and bypassed in cooling mode, an internal heat exchanger (IHE), LHPs, and the CO_2–water plate heat exchanger outdoor unit connected to a geothermal borefield.

In this study, pressure drops in pipes and across components are neglected and all expansion valves are modelled as isenthalpic throttling devices, consistent with the validated model.

Compressor

Compressors are modelled with the third-order polynomial mapping originally developed and validated in Gholamrezaie et al. [14]. This model extends the AHRI 540 approach to a three-variable polynomial fitted to manufacturer data for a transcritical semi-hermetic reciprocating CO_2 compressor. The inputs are suction pressure P_{suc}, discharge pressure P_{dis}, and compressor speed S (Hz); the outputs are the compressor power input $\dot{W}_{comp}$ and the CO_2 mass flow rate $\dot{m}_{CO_2}$. Both quantities are expressed through a general third-order polynomial in the three variables:

$$X = f(P_{suc}, P_{dis}, S) \tag{1}$$

where X represents either $\dot{W}_{comp}$ or $\dot{m}_{CO_2}$ using two distinct sets of coefficients. The polynomial contains up to cubic terms and cross-terms in P_{suc}, P_{dis} and S; its 22 coefficients were obtained by regression on 100 operating points covering 30–75 Hz, 2–5.8 MPa suction pressure and 6–12 MPa discharge pressure and presented in Gholamrezaie et al. [14].

The discharge state is then obtained from the energy balance as follows:

$$\dot{W}_{comp} = \dot{m}_{CO_2}.(h_{dis} - h_{suc}) \tag{2}$$

where h_{dis} and h_{suc} are discharge and suction enthalpies, respectively. In the previous study, a single compressor was used. In the present work, two identical compressors are installed in parallel to increase turndown and part-load performance. Using similarity laws, each compressor is modeled as a half-size version of the reference machine: the same polynomial form is retained, but the power and mass-flow maps are scaled by a factor of 1/2.

Heat exchangers

Two types of plate heat exchangers are used in the system: CO_2-to-CO_2 plate heat exchanger used as the internal heat exchanger (IHE), and CO_2-to-water plate heat exchangers used as the gas cooler (GC) or condenser (COND), and evaporator (EVAP).

CO_2 –CO_2 plate heat exchangers (Internal heat exchanger)

The IHE is treated as an ideal counter-flow heat exchanger with no external losses. It transfers heat from the discharge line to the suction line until the required superheat at compressor inlet is obtained. Consistent with the previous model, it is represented as a perfect heat exchanger with a fixed pinch constraint, such that the enthalpy at the compressor suction is adjusted to provide the target superheat while conserving energy between the hot and cold sides.

Water–CO_2 plate heat exchangers (GC/COND, EVAP)

The water-to-CO_2 plate heat exchanger model developed in Gholamrezaie et al. [14] is reused here for the GC/COND and EVAP. Water glycol 30% mixture flows in counter-flow to CO_2. Depending on the thermodynamic region of CO_2, three different models are used. All plate heat exchangers are assumed adiabatic with negligible pressure loss on both CO_2 and water–glycol sides, as in the validation work.

In the transcritical/superheated region, the thermophysical properties of CO_2 vary rapidly and the heat exchanger is discretized into n cells along the flow direction. In each cell, the water–glycol properties are assumed constant and equal to their value at the outlet of the cell, while CO_2 properties are evaluated with CoolProp. Segment-wise energy balances are solved with convective heat transfer coefficients obtained from standard correlations for turbulent water–glycol flow and for superheated/supercritical CO_2. This discretized model captures the strong variation of CO_2 properties near the critical region and was previously validated against experimental data in Gholamrezaie et al. [14].

When the discharge pressure is below the critical point, the outdoor heat exchanger operates as a condenser. It is modelled with a moving-boundary approach that divides the plate into three zones (superheated, two-phase and sub-cooled). Each zone is treated as a lumped element, and the moving interfaces between zones are determined from energy balances in each region. This provides a computationally efficient representation of phase change while retaining sensitivity to inlet conditions and mass flow rate.

When the outdoor unit operates as an evaporator, an $\varepsilon - NTU$ method is used. The overall heat transfer coefficient and area are taken from the validated model, and effectiveness is evaluated as a function of the number of transfer units and capacity-rate ratio.

CO_2 loop

The single-pipe CO_2 loop is modelled as a near-isothermal two-phase stream that passes sequentially by the LHP interfaces. Rather than resolving detailed pipe-side heat transfer, the model tracks the enthalpy of the loop at the inlet and outlet of each LHP. At a given loop pressure, the saturation temperature is fixed, so the local CO_2 quality changes as zones reject or absorb heat. The loop pressure is controlled and assumed uniform along the loop. This simplification is justified because loop pressure losses are small relative to the compressor pressure rise and cause only minor shifts in two-phase saturation temperature, so their impact on LHP performance is negligible.The loop enthalpy after each LHP in the sequence is obtained from an energy balance, where the LHP capacity and power consumption are used to determine the CO_2 outlet enthalpy as follows:

In heating mode:

$$\dot{Q}_{HP,H,i} - \dot{W}_{HP,i} = \dot{m}_{CO_2}.(h_{HP,in,i} - h_{HP,out,i}) \tag{3}$$

In cooling mode:

$$\dot{Q}_{HP,C,i} + \dot{W}_{HP,i} = \dot{m}_{CO_2}.(h_{HP,out,i} - h_{HP,in,i}) \tag{4}$$

where $\dot{Q}_{HP,H/C,i}$, and $\dot{W}_{HP,i}$ are the heating/cooling capacity and power of the *i-th* LHP, and $h_{HP,in,i}$, $h_{HP,out,i}$ are the CO_2 enthalpies at its inlet and outlet.

Ground heat exchanger and borefield sizing

On the source/sink side, the RVCC exchanges heat with the ground via a CO_2–water plate heat exchanger connected to a secondary hydronic loop circulating 30% water-glycol mixture (the outdoor unit). The vertical borefield simulated with TRNSYS Type 557a, which accounts for borehole thermal resistance and both short- and long-term ground response. Undisturbed ground temperature (10.5 $°C$), thermal conductivity (2.65 $W/m - k$) and diffusivity (0.08 m^2/day) are taken from the literature [134, 135]. The borefield size (number and length of boreholes) is determined with the Alternative ASHRAE sizing method [130] and then kept fixed for all dynamic simulations. During the simulations, the pump in the secondary loop is controlled to maintain the desired temperature approach between the borefield outlet and CO_2 inlet to the outdoor unit plate heat exchanger. This ensures that the outdoor unit can supply (or absorb) the total thermal load required by the CO_2 thermal network while keeping the borehole outlet temperature within a target range (typically 5–25 °C). Table A.2 is the result of borehole sizing for the case study introduced earlier.

Table A.2 Borefield sizing for the case study

Borefield layout	Value
Layout $N_{bx} \times N_{by}$	5×1
Bore spacing s	7.5 m
Per-bore depth H	127 m
Total length L_{tot}	635 m

Local heat pump (LHP)

Each LHP is represented by compact performance maps that link its heating/cooling capacity and power consumption to the source temperature provided by the CO_2 loop and to the internal temperature lift between source and sink. Three different LHP archetypes are considered in this study: a baseline modified “commercial” unit used in the CanmetENERGY CO_2TN prototype [24], a low-lift reciprocating-compressor unit, and a low-lift turbo-compressor unit. All three archetypes are normalized to provide the same nominal zone load at a common reference point, so that system-level comparisons reflect differences in intrinsic HP performance rather than sizing.

Modified commercial local heat pump

For the baseline unit used and modified in the prototype, we reuse the identified COP surfaces and implementation from the validated model [14]. Experimental data from modified CO_2-to-air HPs tested at CanmetENERGY were regressed as functions of the CO_2 loop temperature (T_{loop}) for both heating and cooling modes:

$$COP_{HP,C} = -0.08.\ T_{loop} + 5.04 \tag{5}$$

$$COP_{HP,H} = -0.05.\ T_{loop} + 2.77 \tag{6}$$

where T_{loop} is in °C.

For a given mode j (heating or cooling), the electrical power is obtained from the following relation:

$$\dot{W}_{HP,j} = \frac{\dot{Q}_{HP,j}}{COP_{HP,j}} \tag{7}$$

Low-lift reciprocating-compressor local heat pump

The low-lift reciprocating LHP archetype is based on the prototype described by Gasser et al. [129], in which a positive-displacement reciprocating compressor uses propane (R290) as refrigerant and is optimized for operation with small internal temperature lifts. The prototype is intended for applications with relatively high source temperatures (e.g., deep geothermal or ambient-assisted sources) and low-temperature heating distribution, so that the internal lift typically lies in the range of about 15 to 30 K. In this context, the internal temperature lift is defined as the difference between the condensation and evaporation saturation temperatures of the refrigerant inside the cycle as follows:

$$\Delta T_{lift} = T_{cond} - T_{evap} \tag{8}$$

Here T_{evap}, and T_{cond} (in K) are the saturation temperatures at the evaporator and condenser pressure levels respectively. In the CO_2TN, depending on the operating mode, the evaporation temperature of the local R290 LHP in heating mode is tied to the CO_2 loop saturation temperature, while the condensation temperature follows the supply temperature required by the zone. In cooling mode, the condensation temperature of the LHP is tied to the CO_2 loop, whereas the evaporation temperature follows the supply temperature required for cooling. For the reciprocating low-lift archetype, the COP is written as a Carnot COP multiplied by a lift-dependent Carnot efficiency. The real COPs of the low-lift reciprocating unit are then expressed as:

$$COP_{HP,C} = \eta_{rec} \cdot \frac{T_{evap}}{\Delta T_{lift}} \tag{9}$$

$$COP_{HP,H} = \eta_{rec} \cdot \frac{T_{cond}}{\Delta T_{lift}} \tag{10}$$

where η_{rec} is the Carnot efficiency of the reciprocating prototype, modelled as a function of the temperature lift. Based on the experimental analysis of Gasser et al. [129], the Carnot efficiency is captured with the following piecewise-linear correlation:

$$\eta_{rec} = \begin{cases} 0.50, & \Delta T_{lift} \leq 10K \\ 0.50 + 0.01\left(\Delta T_{lift} - 10\right), & 10K < \Delta T_{lift} < 20K \\ 0.60, & \Delta T_{lift} \geq 20K \end{cases} \tag{11}$$

The heating or cooling capacity is then obtained from the COP and the electrical power. The entire map is scaled such that at a chosen reference operating point (loop temperature and design lift) the reciprocating LHP delivers the same nominal zone capacity as the commercial LHP.

Low-lift turbo-compressor local heat pump

The low-lift turbo-compressor LHP archetype represents the second prototype in Gasser et al. [129], where a small oil-free radial turbo compressor uses butane (R600) as refrigerant. This machine is specifically designed for low-lift operation, with compressor aerodynamics and heat-exchanger design chosen to minimise internal losses for lifts of roughly 10 to 25 K. The experimental results show very high COPs and, more importantly, a Carnot efficiency that is both high and nearly constant over the investigated range of ΔT_{lift}:

$$COP_{HP,C} = \eta_{turbo} \cdot \frac{T_{evap}}{\Delta T_{lift}} \tag{12}$$

$$COP_{HP,H} = \eta_{turbo} \cdot \frac{T_{cond}}{\Delta T_{lift}} \tag{13}$$

where η_{turbo} is the Carnot efficiency of the turbo prototype, modelled as a simple function of the temperature lift. Based on the experimental analysis of Gasser et al. [129], the Carnot efficiency is captured with the following piecewise-linear correlation:

$$\eta_{turbo} = \begin{cases} 0.64, & \Delta T_{lift} \leq 13K \\ 0.64 + 0.003\left(\Delta T_{lift} - 13\right), & 13K < \Delta T_{lift} < 26K \\ 0.60, & \Delta T_{lift} \geq 26K \end{cases} \tag{14}$$

Supervisory control

The current system requires a supervisory controller to specify the variables needed to operate the CO_2 loop, including the compressor configuration, compressor speed, suction and discharge pressures, and the loop pressure. The supervisory strategy follows a temperature-bounded (TB) approach in which the CO_2 loop is no longer constrained to remain strictly two-phase. Instead, for a given loop pressure, the bulk CO_2 state is confined to a narrow band of $\pm 10°C$ around the saturation temperature $T_{sat}(P_{loop})$. This defines maximum allowable heat exchange in the subcooled, two-phase, and superheated regions. The supervisory optimization problem can therefore be formulated as

$$\begin{aligned}
\max_{\theta} \quad & COP_{system} \\
\text{subject to} \quad & P_{suc}, P_{dis} \in \text{compressor envelope} \\
& S \in [30, 75] \text{ Hz} \\
& fix_on \in \{0, 1\} \\
& T_{\min} \leq T_{loop} \leq T_{\max}
\end{aligned} \tag{15}$$

where $T_{\min}$, and $T_{\max}$ are the loop-temperature limits defined as $\pm 10°C$ around $T_{sat}(P_{loop})$. The net exchange between the loop and all LHPs is represented by a six-component vector Q collecting heating and cooling contributions in each of these regions as follows:

$$Q = [Q_{C,sub},\ Q_{C,2\varphi}, Q_{C,sup}, Q_{H,sub}, Q_{H,2\varphi}, Q_{H,sup}] \tag{16}$$

where $Q_C \geq 0$ denotes heat rejected to the loop by cooling LHPs, and $Q_H \leq 0$ denotes heat extracted from the loop by heating LHPs in the subcooled (sub), two-phase (2φ), and superheated (sup) regions. To generate the control parameters, the proposed method is divided into two stages: an offline stage and an online stage. The offline stage builds a "base table" by enumerating feasible combinations of compressor setpoints and six-segment exchanges. The decision tuple is defined as follows:

$$\theta = (S, P_{suc},\ P_{dis},\ P_{loop},\ fix\_on) \tag{17}$$

where S (Hz) is the variable-speed setpoint, P_{suc} and P_{dis} are suction and discharge pressures, and P_{loop} is the CO_2 loop pressure. Under the present assumption of negligible pressure drops in the loop, $P_{loop} = P_{suc}$ in cooling-dominant operation and $P_{loop} = P_{dis}$ in heating-dominant operation. Finally, $fix\_on \in \{0, 1\}$ indicates whether the fixed-speed unit operates at 60 Hz. A discrete grid in $(S, P_{suc},\ P_{dis},\ P_{loop},\ fix\_on)$ is swept; for each grid point within the compressor envelope, loop mass flow is obtained from the dual-compressor maps, the enthalpy bounds and the regional caps are evaluated, all admissible six-segment vectors Q (quantized in 1 kW steps and limited by the enthalpy bounds) are enumerated, and the corresponding system COP is calculated as follows:

$$COP_{system}(\theta; Q) = \frac{Q_c(Q) + |Q_H(Q)|}{\dot{W}_{HP}(\theta, Q) + \dot{W}_{comp}(\theta)} \tag{18}$$

Each combination that respects the constraints and the circulation compressor envelope is stored as a row $(Q, \theta, COP_{system})$ in the base table.

Online, the controller receives the zone command vector $u \in \{-1, 0, +1\}^{n_{HP}}$ (-1 for heating/ +1 for cooling/ 0 off) and the outdoor-unit inlet water temperature ($T_{w,OU,in}$). Using an initial guess tuple $\theta^{(0)}$, the full model solves the appropriate scalar residual (cooling or heating) to obtain a feasible circulation state. The resulting single-pipe traversal yields a continuous six-segment vector Q_{model}, which is then rounded to a discrete key Q_{target}. This key is used to query the base table for all entries with $= Q_{target}$. Candidates are tested in order of decreasing stored COP: for each one, the full model is re-run to close the loop enthalpy balance within the constraints and to verify the compressor envelope and equipment limits. The first candidate that passes these checks provides the accepted tuple $(S, P_{suc}, P_{dis}, P_{loop},\ fix\_on)$, which is then used to drive the circulation compressor and stored in a runtime table for analysis.

Results and discussion

To capture the transient behaviour of the system, the CO_2TN is implemented in TRNSYS for the case study. The system coefficient of performance (COP_{system}) is used as the metric to compare the results and is defined as follows:

$$COP_{system}(t) = \frac{\dot{Q}_{HP}(t)}{\dot{W}_{tot}(t)} \tag{19}$$

where $\dot{Q}_{HP}(t)$, denotes the total useful thermal rate provided by the LHPs at each time step and $\dot{W}_{tot}(t)$, denotes the total electrical power consumed by the RVCC and all LHPs.

Figure A.4 (left) compares the distribution of hourly COP values for the three datasets. The base case ($\mathrm{COP_{base}}$) is tightly clustered around low values, with first quartile $\mathrm{Q_1} = 2.078$, a median of 2.232, third quartile $\mathrm{Q_3} = 2.278$, and a mean of 2.129, indicating that most operating points remain close to a COP of 2.2. In contrast, the reciprocating low-lift local heat pump configuration ($\mathrm{COP_{recp}}$) exhibits a much wider spread and higher central tendency, with $\mathrm{Q_1} = 2.697$, median 4.268, $\mathrm{Q_3} = 4.674$, and a mean of 3.812, showing that at least half of the hours achieve COP values above about 4. Finally, the turbo-compressor low-lift LHP configuration ($\mathrm{COP_{turbo}}$) further shifts the distribution towards higher efficiencies, with $\mathrm{Q_1} = 2.823$, median 4.440, $\mathrm{Q_3} = 4.908$, and a mean of 3.995. Overall, the violin plots highlight not only the increase in average COP when moving from the base case to the two local heat pump configurations, but also the slight yet consistent improvement of the turbo configuration over the reciprocating one across the entire distribution.

Figure A.4 (right) compares the annual electrical energy consumption of the CO_2TN for cooling-only and heating-only operation, partitioned between the circulation compressor

$\dot{W}_{comp}$and the LHPs. The labels C and H denote cooling-only and heating-only modes, respectively. In the base configuration, the LHPs represent a considerable fraction of the total electricity use (about 38% in cooling mode and 41% in heating mode). Moreover, changes in LHP electrical demand also affect the circulation compressor consumption, because the required CO_2 mass flow (and thus compressor work) depends on the net heat exchanged between the active LHPs and the CO_2 loop. Moving from the base case to the reciprocating and turbo compressor configurations, the LHPs become more efficient; therefore, for the same imposed building load, the electricity required by the LHPs decreases, which is consistent with the lower LHP contributions observed in the figure. In cooling-only operation, a more efficient LHP draws less electrical power to meet the same cooling load, and consequently rejects less total heat to the CO_2 loop. This reduced heat rejection lowers the mass-flow requirement for maintaining the loop operating conditions, leading to a decrease in circulation compressor energy. In heating-only operation, the trend is reversed for the compressor: for a fixed heating load, improving the LHP efficiency reduces the electrical input, which increases the portion of heat that must be absorbed from the CO_2 loop. As a result, the circulation system must transport slightly more heat through the loop, which increases the required CO_2 mass flow and yields a modest increase in circulation compressor energy. Despite this increase, the total annual energy consumption in heating-only operation still decreases because the reduction in LHP electricity dominates.

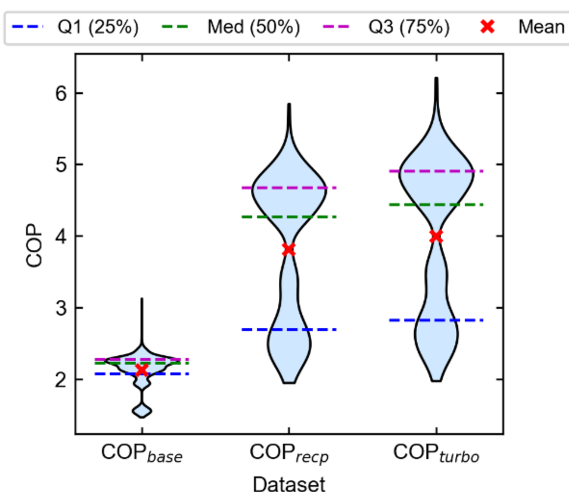

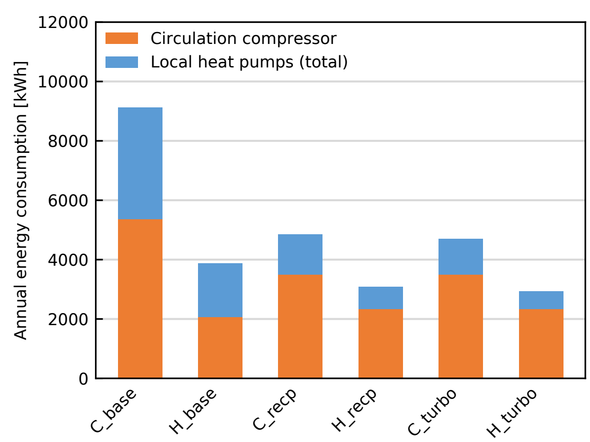

Figure A.4 Violin plots of hourly COP (left) and total energy consumption (right)

To delve deeper into the shape of the violin plots in Figure A.4, we focus on the turbo-compressor results. The operating hours are separated according to whether the system is in heating- or cooling-dominant mode, and COP violin plots are drawn for each mode (Figure A.5). Figure A.5 shows that COP values in cooling mode are systematically higher and less dispersed than in heating mode, which explains the shape of the total COP distribution observed in Figure A.4. This behavior arises from the design points of the turbo-compressor LHPs in heating and cooling modes and from the design and operating envelope of the RVCC components, which are more favourable under cooling-dominant conditions.

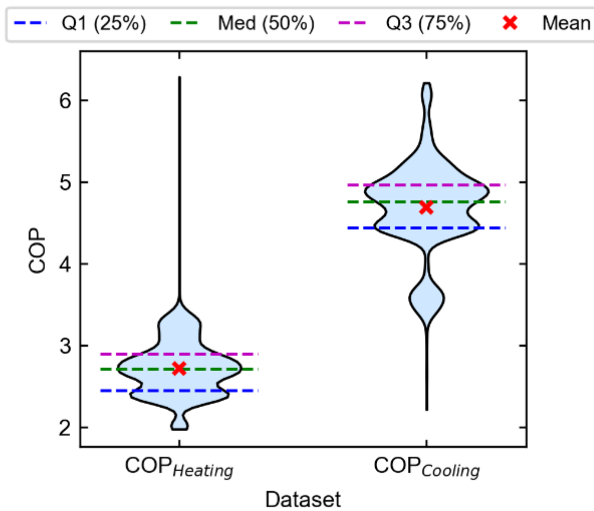

Figure A.5 Violin plots of COP in heating-dominant and cooling-dominant operation for the turbo-compressor case

Conclusions

This work examined how the characteristics of local heat pumps influence the overall performance of a CO_2-based thermal network supplying year-round heating and cooling to a five-zone office building. Using a component-based model of the system integrated with a new supervisory control strategy, heating and cooling demand of an office building in Montreal were simulated for three LHP archetypes: a commercially available unit, and two heat pumps specifically designed for low-lift applications.

Results show that the choice of local heat pump designed for low-lift applications has a decisive impact on system efficiency. With the commercial LHPs, the system COP distribution is narrowly clustered around low values, with most operating hours near COP
approx 2.2. Replacing the commercial units with low-lift heat pumps approximately doubles the typical COP, shifting the median COP to above 4 for both low-lift configurations and substantially broadening the high-performance tail. The turbo-compressor archetype provides a further, albeit more modest, improvement over the reciprocating concept, with slightly higher median and mean COP and a larger fraction of hours operating at the highest

COP levels.

Overall, the study confirms that the benefits of a CO_2 thermal network cannot be fully realized with conventional heat pumps designed for large temperature lifts. Low-lift LHPs that maintain high Carnot efficiency over 10 to 30 K lifts enable much higher system-level COPs under the same plant and control constraints. From a design standpoint, the primary step change in performance arises from adopting any suitably optimized low-lift LHP; the incremental advantage of turbo- over reciprocating-based designs must then be weighed against differences in cost, complexity, and reliability.

Acknowledgements

The authors acknowledge the Natural Sciences and Engineering Research Council of Canada (NSERC) for funding the Ph.D. student contributing to this work through discovery grant. (Funding application number: RGPIN-2020-06556)